1997

Large eddy simulation of turbulent flows with variable property heat transfer using a compressible finite volume formulation

Lyle Douglas Dailey
Iowa State University

INFORMATION TO USERS

This manuscript has been reproduced from the microfilm master. UMI films the text directly from the original or copy submitted. Thus, some thesis and dissertation copies are in typewriter face, while others may be from any type of computer printer.

The quality of this reproduction is dependent upon the quality of the copy submitted. Broken or indistinct print, colored or poor quality illustrations and photographs, print bleedthrough, substandard margins, and improper alignment can adversely affect reproduction.

In the unlikely event that the author did not send UMI a complete manuscript and there are missing pages, these will be noted. Also, if unauthorized copyright material had to be removed, a note will indicate the deletion.

Oversize materials (e.g., maps, drawings, charts) are reproduced by sectioning the original, beginning at the upper left-hand corner and continuing from left to right in equal sections with small overlaps. Each original is also photographed in one exposure and is included in reduced form at the back of the book.

Photographs included in the original manuscript have been reproduced xerographically in this copy. Higher quality 6" x 9" black and white photographic prints are available for any photographs or illustrations appearing in this copy for an additional charge. Contact UMI directly to order.

UMI

A Bell & Howell Information Company
300 North Zeeb Road, Ann Arbor MI 48106-1346 USA
313/761-4700 800/521-0600

Large eddy simulation of turbulent flows with variable property heat transfer using a compressible finite volume formulation

by

Lyle Douglas Dailey

A dissertation submitted to the graduate faculty

in partial fulfillment of the requirements for the degree of

DOCTOR OF PHILOSOPHY

Major: Mechanical Engineering

Major Professor: Richard H. Pletcher

Iowa State University

Ames, Iowa

1997

Graduate College
Iowa State University

This is to certify that the Doctoral dissertation of

Lyle Douglas Dailey

has met the dissertation requirements of Iowa State University

Signature was redacted for privacy.

Committee Member

Signature was redacted for privacy.

Committee Member

Signature was redacted for privacy.

Committee Member

Signature was redacted for privacy.

Committee Member

Signature was redacted for privacy.

Major Professor

Signature was redacted for privacy.

For the Major Program

Signature was redacted for privacy.

For the Graduate College

TABLE OF CONTENTS

LIST OF FIGURES

LIST OF TABLES

NOMENCLATURE

Roman Symbols

$[A], [B], [C]$	inviscid flux Jacobians
A^+	constant in Van Driest damping formula
A_c	channel cross-sectional area ($= L_y L_z$)
$\mathbf{C}$	discretized convective and viscous flux vector
C_d, C_i	dynamic subgrid-scale model coefficients
C_f or f	friction coefficient ($= 2\tau_w/(\rho_b u_b^2)$)
C_s	Smagorinsky subgrid-scale model coefficient
c	speed of sound ($= \sqrt{\gamma RT}$)
c_p	constant pressure specific heat
c_v	constant volume specific heat
D	Van Driest damping function
$\mathbf{D}$	artificial dissipation operator vector
D_h	hydraulic diameter ($= 4\delta$)
$\mathbf{d}$	artificial dissipation flux vector
E	specific total energy ($= e + u_i u_i/2$)
$\mathbf{E}, \mathbf{F}, \mathbf{G}$	flux vectors
$E(k)$	turbulent energy spectrum
ϵ	specific internal energy ($= c_v T$)
F	flatness factor
F_i	Fourier coefficients

f or C_f	friction coefficient $(= 2\tau_w/(\rho_b u_b^2))$
G	filter function
g	gravitational constant
H	total enthalpy $(= h + u_i u_i/2)$ or channel height $(= 2\delta)$
h	rib height, heat transfer coefficient, or specific enthalpy
$\vec{i}, \vec{j}, \vec{k}$	unit vectors
K	subgrid-scale term in energy equation
k	wave number, thermal conductivity, or turbulent kinetic energy
$[L], [D], [U]$	approximate factorization matrices for LU-SGS scheme
$L_{i,j}$	resolved or Leonard turbulent stress tensor
L_r	reference length
L_x, L_y, L_z	dimensions of channel
M	Mach number or mesh spacing for grid generated turbulence
$M_{i,j}$	anisotropic part of subgrid-scale stress tensor
m	pseudo time index
$\dot{m}$	mass flow rate
NBLK	number of blocks
NMG	number of multigrid levels
NPROC	number of processors
N_{stat}	number of time steps for turbulent statistics
Nu	generic Nusselt number
Nu_D	Nusselt number based on hydraulic diameter $(= hD_h/k_b)$
n	physical time index
$\vec{n}$	unit normal vector
n_x, n_y, n_z	components of unit normal vector
P	rib spacing or pitch
$\mathbf{P}$	forcing function vector for multigrid acceleration
Pr	Prandtl number $(= \mu c_p/k)$

Pr_t	turbulent Prandtl number
p	thermodynamic pressure
Q_j	subgrid-scale turbulent heat flux vector
Q^+	nondimensional wall heat flux ($= q_w D_h/(k_b T_b)$)
q_j	heat flux vector
q^2	subgrid-scale turbulent kinetic energy
R	gas constant or cross-correlation coefficient
$\mathbf{R}$	residual vector
$\boldsymbol{\mathcal{R}}$	preconditioned residual vector
Ra	Rayleigh number
Re	generic Reynolds number
Re_D	bulk Re based on hydraulic diameter ($= \rho_b u_b D_h/\mu_b$)
Re_H	bulk Re based on channel height ($= \rho_b u_b H/\mu_b$)
Re_r	Re based on reference quantities ($= \rho_r V_r L_r/\mu_r$)
Re_δ	bulk Re based on channel half-height ($= \rho_b u_b \delta/\mu_b$)
r_A, r_B, r_C	relaxation factors in LU-SGS scheme
S	magnitude of cell face area vector or skewness factor
$\vec{S}$	cell face area vector
$S_{i,j}$	strain rate tensor
T	thermodynamic temperature
$[T]$	time derivative Jacobian ($= \partial\mathbf{U}/\partial\mathbf{W}$)
TKE	turbulent kinetic energy
T_τ	friction temperature ($= q_w/(\rho_w c_p u_\tau)$)
t	physical time
t_e	large eddy turnover time ($= \delta/u_\tau$)
U	contravariant velocity
$\mathbf{U}$	vector of conserved variables $(\rho, \rho u, \rho v, \rho w, \rho E)^T$
U_0	mean velocity for grid generated decaying turbulence

u_τ	friction velocity ($= \sqrt{\tau_w/\rho_w}$)
u_τ^*	semi-local friction velocity ($= \sqrt{\tau_w/\rho(y)}$)
u, v, w	Cartesian velocity components in x, y, z directions
u^+	velocity in wall coordinates ($= u/u_\tau$)
u^*	velocity in semi-local coordinates ($= u/u_\tau^*$)
V_r	reference velocity
$\mathbf{W}$	vector of primitive variables $(p, u, v, w, T)^T$
x, y, z	Cartesian coordinates
y^+	distance to wall in wall coordinates ($= \delta_y u_\tau/\nu_w$)
y^*	distance to wall in semi-local coordinates ($= \delta_y u_\tau^*/\nu(y)$)

Greek Symbols

α, π, ϵ	subgrid-scale terms in energy equation
α_i	constants in Runge-Kutta scheme
β	pressure gradient parameter
$\beta_x, \beta_y, \beta_z$	scale factors in implicit residual averaging
$[\Gamma]$	time derivative preconditioning matrix
γ	ratio of specific heats
$\gamma_A, \gamma_B, \gamma_C$	eigenvalue scaling factors in LU-SGS scheme
Δ	grid filter width
Δ_t	test filter width
δ	channel half-height or Dirac delta
δ_y	distance to closest wall
$\epsilon^{(2)}, \epsilon^{(4)}$	constants for artificial dissipation
θ	temperature difference ($= T_w - T$)
θ^+	temperature in wall coordinates ($= \theta/T_\tau$)
κ	von Karman constant

κ_θ	von Karman constant for temperature log-law
$\kappa^{(2)}, \kappa^{(4)}$	constants for artificial dissipation
Λ	eigenvalue scaling term for artificial dissipation
λ	bulk viscosity or eigenvalue
$\lambda_\xi, \lambda_\eta, \lambda_\zeta$	eigenvalues for artificial dissipation
μ	molecular dynamic viscosity
μ_t	subgrid-scale turbulent viscosity
ν	molecular kinematic viscosity ($= \mu/\rho$)
ν_t	subgrid-scale turbulent kinematic viscosity ($= \mu_t/\rho$)
ρ	thermodynamic density
$\sigma_{i,j}$	shear stress tensor
τ	pseudo time
$\tau_{i,j}$	subgrid-scale stress tensor
Φ	temperature gradient parameter
$\Phi_\xi, \Phi_\eta, \Phi_\zeta$	scaling factors for artificial dissipation
Ω	cell volume
ω	relaxation factor in LU-SGS scheme

Subscripts

b	bulk property
con	conduction contribution
g	ghost cell quantity
i	inviscid contribution
i, j, k	indices for Cartesian coordinates
nw	near wall cell quantity
p	periodic component
r	reference quantity

res	resolved contribution
rms	root-mean-square
s or sgs	subgrid-scale contribution
VD	Van Driest transformation
v or vis	viscous contribution
w	wall value
x, y, z	associated with Cartesian direction
β	cell face index
ξ, η, ζ	associated with i, j, k directions

Superscripts and Other Symbols

$*$	dimensional variable or semi-local coordinates
$+$	wall coordinates
$'$	fluctuation with respect to ensemble average, or unresolved or subgrid-scale component of filtered quantity
$''$	fluctuation with respect to Favre ensemble average, or unresolved or subgrid-scale component of Favre filtered quantity
$\vec{}$	vector quantity
$\overline{}$	resolved or large scale component of filtered quantity
$\widetilde{}$	resolved or large scale component of Favre filtered quantity
$\widehat{}$	quantity that is nonlinear function of Favre filtered quantities
$\frown$	test filtered quantity
$< >$	ensemble averaged quantity
$< >_{x,z}$	ensemble averaged in x and z directions and time
$< >_z$	ensemble averaged in z direction and time

Abbreviations

CFD	computational fluid dynamics
DNS	direct numerical simulation
FD	finite difference
FV	finite volume
LES	large eddy simulation
LU-SGS	lower-upper symmetric-Gauss-Seidel
MPI	Message Passing Interface
PVM	Parallel Virtual Machine
RANS	Reynolds-averaged Navier-Stokes
RK	Runge-Kutta
SGS	subgrid-scale

ABSTRACT

A compressible finite volume formulation has been developed to solve the Favre filtered Navier-Stokes equations to perform the large eddy simulation (LES) of turbulent flows with variable property heat transfer. The efficient finite volume formulation was developed using a dual time stepping approach with time derivative preconditioning and multigrid acceleration. Time marching was done with either an explicit Runge-Kutta scheme or an implicit lower-upper symmetric-Gauss-Seidel (LU-SGS) scheme. The code was developed in a multiblock framework so it could be applied to complex geometries and to provide a means for parallelization.

The second-order accurate finite volume LES formulation was validated with simulations of turbulent incompressible benchmark flows. The results were compared to experimental data and incompressible direct numerical simulation (DNS) results. The LES formulation was subsequently applied to a plane channel flow with constant wall heating rates of magnitudes large enough to cause significant property variations across the channel. The effects of high heating versus high cooling on the turbulence quantities and turbulent structure were studied. Finally, the LES formulation was evaluated for a complex geometry by attempting to simulate the turbulent flow and heat transfer for a plane channel with transverse square ribs on one wall.

Multigrid acceleration and time derivative preconditioning were very effective for steady and unsteady laminar flows. However, multigrid provided no benefit for LES, most likely due to insufficient numerical damping to drive the multigrid since artificial dissipation was not used.

The LES formulation provided excellent agreement with DNS and experimental results for simple turbulent flows (i.e. homogeneous, isotropic, decaying turbulence and smooth wall

channel flows). For the constant heat flux channel flows, high heating tended to reduce the velocity fluctuations, while high cooling tended to promote the fluctuations. The mean and fluctuation velocity profiles collapsed towards the incompressible results when normalized by local properties, as opposed to wall values. The temperature fluctuation profiles were largely independent of the heating rate when normalized by the wall-to-bulk temperature difference. Problems related to significant odd-even decoupling, grid distributions, and SGS modeling were identified for the rib-roughened channel.

CHAPTER 1 INTRODUCTION

1.1 Motivation

The computation of complex turbulent flows of practical interest to engineers continues to be a challenge. These flows commonly contain a variety of complex features such as separation, reattachment, recirculation zones, stagnation points, shocks, mixing, unsteadiness, laminar-to-turbulent transition, heat transfer, and large gradients. Moreover, a wide range of length and time scales may exist. Most present computational fluid dynamics (CFD) tools utilize the Reynolds averaging approach to model turbulence. Reynolds averaging involves ensemble averaging the governing equations, which results in additional terms, the Reynolds shear stresses and Reynolds heat fluxes. The system of equations must be closed with turbulence models for the new terms. Most turbulence models attempt to describe the turbulence in terms of a single characteristic length and velocity (or time) scale. The more complex features that exist, or the wider the range in time and length scales in the flow, the more likely that conventional techniques such as Reynolds averaging will fail or provide inaccurate results.

The most accurate method for the computation of turbulent flows is direct numerical simulation (DNS), where the unsteady Navier-Stokes equations are solved in a time accurate manner with sufficient temporal and spatial resolution to resolve all the time and length scales. The largest scales are bounded by the geometry, and the smallest scales are bounded by the Kolmogorov scales, where viscous dissipation of the turbulent fluctuations occurs. The range in scales is directly related to the Reynolds number. At high Reynolds numbers, where inertial effects dominate viscous effects, the range in scales is large. At lower Reynolds numbers, viscous effects are increasingly important, and the range in turbulence length scales is smaller. Consequently, DNS requires more computational resources for higher Reynolds numbers in

order to resolve all the scales. In general, DNS requires exceptionally large resources, and its application to turbulent flows has been limited to simple geometries and low Reynolds numbers.

Large eddy simulation (LES) is a method that provides nearly the same capability as DNS at a fraction of the cost; typically, one to two orders of magnitude less computational resources are required. For LES, a spatial filtering (or averaging) operation is applied to the governing equations to remove the effects of the small-scale motion. The resulting filtered, unsteady Navier-Stokes equations are solved in a time accurate manner to resolve the large scale turbulent motion. The small-scale motion is mostly isotropic and independent of geometry; hence, it is more likely to be universally modeled. The large scale motion, which can be highly anisotropic and dependent on the geometry, is resolved. The transport of momentum and heat is primarily due to the large scale motion, and is therefore resolved with LES.

Despite its reduced computational cost compared to DNS, large computational resources are still required. The application of LES has also been limited to simple geometries and low Reynolds numbers, although the limitations are not as restrictive as for DNS. Several other issues have impeded the application of LES to practical problems. Nonperiodic inflow and outflow boundary conditions that can sustain a realistic turbulent simulation have been elusive. Simulations have had to rely on periodic boundary conditions, where the turbulence exiting the domain is fed back into the inlet of the domain. There are many deficiencies in the subgrid-scale modeling. The present models tend to break down for complex geometries, the models do not work well with low-order accuracy numerical schemes, and models have not been developed or adequately evaluated for many subgrid-scale contributions to the compressible form of the filtered energy equation. Moreover, the subgrid-scale models that have been developed to overcome some of these shortcomings have become increasingly complex and have added significant overhead to the computational cost of LES, diminishing the advantage of LES compared to DNS.

1.2 Objectives

Some of the issues hindering the usefulness of LES are addressed in the thesis. The four main objectives of this thesis, meant to advance LES capability toward more practical problems, are listed below and discussed in more detail in the subsections that follow.

1. Develop an efficient, time-accurate finite volume scheme to solve the Favre filtered governing equations.

2. Validate a second-order accurate compressible finite volume formulation for LES by simulating turbulent incompressible benchmark flows.

3. Study the capability of the compressible LES formulation to simulate turbulent flows with variable properties resulting from high heat transfer.

4. Evaluate the effectiveness of the LES formulation for a complex geometry.

1.2.1 Develop an Efficient Finite Volume Scheme

As alluded to above, LES and DNS require large computational resources, including both memory and CPU time, and this has been a limiting factor in the application of these two methods to practical problems. The first objective of the thesis was to address this issue by developing an efficient, time-accurate finite volume formulation to solve the Favre filtered Navier-Stokes equations. Several algorithmic and computational methods were combined in a unique way to develop a scheme that used less CPU time and required less memory than most currently available formulations. For instance, multigrid acceleration was evaluated for time accurate computations. A low operation count and low memory implicit scheme was developed in a dual time stepping approach. Time derivative preconditioning was incorporated to allow the computation of low Mach number flows with the compressible formulation. Finally, the code was parallelized to reduce wall clock times, and to maximize the size of the problem that can be handled by distributing the problem over multiple processors.

1.2.2 Validate Second-Order Accurate Finite Volume Formulation for LES

Most early research in LES employed spectral methods due to the high accuracy offered for a moderate amount of grid. However, spectral methods are not easily amenable to complex geometries. Finite volume methods, on the other hand, can handle complex geometries quite well, and are commonly utilized in many engineering CFD codes that are used extensively in industry. These codes typically rely on the Reynolds averaging approach with turbulence models of varying complexity.

As LES technology matures, it would be desirable to add LES capability to existing CFD packages with minimal modifications. Therefore, standard finite volume methods need to be evaluated for their capabilities in computing turbulent flows with LES. A majority of practical CFD packages are spatially second-order accurate finite volume schemes that reduce to central differencing for Cartesian grids. Low-order accuracy is used because of difficulties that arise in maintaining higher order accuracy for complex geometries near boundaries or at the block interfaces of multiblock codes.

Therefore, a second objective of the thesis was to validate a second-order accurate compressible finite volume formulation for the LES of turbulent flows. Two incompressible "benchmark" turbulent flows were simulated: homogeneous, isotropic decaying turbulence and plane turbulent channel flow. Extensive experimental and DNS results were used to validate the simulations. A review and discussion of the issues related to finite volume schemes for LES, including accuracy and discretization methods, is given in Section 1.3.

1.2.3 Study Capability of LES Formulation for Variable Property Flow

Both LES and DNS provide a means for determining detailed information about turbulent flows that may be difficult to obtain experimentally. One such class of flows was considered for this work: turbulent plane channel flow with constant heating rates at the walls of magnitudes large enough to cause significant property variations. Experimental studies of this type of flow have been limited to determining wall and bulk parameters only, e.g. friction factors and Nusselt numbers. This is because the test sections were too small to obtain detailed

measurements of velocity and temperature mean and fluctuating profiles since small tube diameters or channel heights were required to measure dominant forced convection. This thesis was the first known turbulent simulation (LES or DNS) of such a flow.

A significant amount of research was conducted for this class of flows in the late 60's and early 70's (McEligot et al., 1965; Swearingen and McEligot, 1971; Bankston and McEligot, 1970). The efforts primarily employed boundary layer codes and simple mixing length turbulence models for the Reynolds averaged equations. The thermal entry region was studied extensively. Interest in gas-cooled nuclear reactors and nuclear propulsion systems necessitated the understanding of forced convection heat transfer with strongly varying properties.

This particular class of flows is of current interest in the CFD community for several reasons. LES has been used for a very limited set of turbulent flows including heat transfer, especially using the compressible form of the governing equations. An increasing number of such problems need to be investigated to develop and discern the limits of subgrid-scale modeling for these flows. More importantly, recent concerns have been raised about the validity of the commonly used law-of-the-wall for both the velocity and especially the temperature (Bradshaw and Huang, 1995). The simulation of flows with strong heating and variable properties will help to determine the validity and/or limits of these basic relationships that are used extensively in many design and analysis CFD codes.

1.2.4 Evaluate Effectiveness of LES Formulation for a Complex Geometry

The fourth objective was to evaluate the finite volume LES formulation for a more complex geometry that results in complex flow features. The rib-roughened channel was chosen as a test case because the ribbed wall provides complex flow features, such as flow separation, recirculation zones, and reattachment, and yet allows the use of periodic boundary conditions in the streamwise direction. The rib-roughened channel is of practical interest for cooling in gas turbine blades and computer components, as well as other applications. The backward facing step provides similar complex flow features, but requires the specification of nonperiodic inflow conditions, which remains a challenge for LES. This was the first known application of

a compressible finite volume LES formulation to this flow.

1.3 Review of Finite Volume LES Formulations

An extensive literature review of all topics related to the four objectives given in the previous section was not included in this chapter because the objectives, although related, deal with very different topics. The thesis was organized such that additional, more specific references are cited in the appropriate chapters. However, a review of finite volume LES formulations is provided here for background.

The use of finite volume methods for LES has been steadily increasing over time, with incompressible formulations being most common. For example, incompressible finite volume formulations have been used to simulate turbulent lid driven cavity flows (Zang et al., 1993), turbulent flow around circular cylinders (Mittal, 1996), plane channel and rectangular duct flows (Wang, 1995), square ducts (Breuer and Rodi, 1994), and plane channel flows with rib-roughened walls (Ciofalo and Collins, 1992; Yang and Ferziger, 1993). The formulations have ranged from second-order accurate central-difference schemes to higher-order accurate upwind based schemes. The success of the computations has varied, but for the most part they have been promising.

LES with compressible finite volume formulations has been less common. Vreman et al. (1992) used a compressible cell-vertex finite volume formulation to compute homogeneous, isotropic decaying turbulence. Wang and Pletcher (1996) used a staggered grid scheme with third-order upwinding for the convective terms, and fourth-order central differences for the viscous terms to compute turbulent channel flows with significant heat transfer. They had limited success with a colocated grid formulation, which would be better suited to complex geometries compared to a staggered grid formulation. Calhoon and Menon (1996) used a compressible finite volume formulation to compute reacting mixing layers. A fifth-order accurate flux splitting scheme was used for the inviscid fluxes, and viscous stresses were computed with a central-differenced fourth-order accurate scheme. Ansari and Strang (1996) computed turbulent mixing layers using a second-order accurate unstructured finite volume scheme that used

an approximate Riemann solver for the inviscid terms.

Many of the compressible formulations used upwind schemes. However, several researchers have reported that first and second-order accurate upwind schemes, hybrid upwind, and higher-order upwind schemes were too dissipative, leading to rapid decay of the turbulent fluctuations (Ciofalo and Collins, 1992; Breuer and Rodi, 1994; Mittal, 1995).

Another issue of contention for finite volume and finite difference schemes is the required spatial order of accuracy for LES. Second-order accurate finite difference or finite volume schemes have been used with varying degrees of success by many researches, including Yang and Ferziger (1993), Breuer and Rodi (1994), Manhart and Wengle (1994), Wang (1995), Balaras et al. (1996), Ansari and Strang (1996), and Wu and Squires (1997). As long as the grid was sufficiently refined, satisfactory results were obtained.

In terms of computational resources, Rai and Chakravarthy (1993) showed that second-order accurate schemes required two orders of magnitude more computing time than fourth-order accurate schemes. This was possible because much less grid was required for the same level of accuracy. On the other hand, Ridder (1992) showed no significant advantage to fourth-order spatial terms, and a 76 percent increase in CPU time was observed compared to second-order accuracy.

It is possible to obtain the same absolute level of accuracy with either second or fourth order accuracy. Of course, the second-order accurate scheme will require more grid refinement. Fourth-order accurate methods are difficult to generalize to non-Cartesian grids, and it is difficult to maintain fourth-order accuracy across block interfaces in multiblock and parallel codes. Increased communication costs associated with message passing in parallel codes are also likely. It may also be difficult to ensure the subgrid-scale modeling is discretized with the same level of high-order accuracy. For a parallel code, the additional grid points required for a second-order accurate formulation can be partially offset by using additional processors, if available.

1.4 Dissertation Organization

The mathematical formulation for the LES of compressible turbulent flows is presented in Chapter 2. The nondimensional compressible Navier-Stokes equations are Favre filtered, and then cast in an integral-vector form amenable to the development of finite volume formulations. The mathematical formulation of the subgrid-scale modeling is also discussed.

In Chapter 3, the details of the finite volume formulation are given. This includes a discussion of the selected solution variables, the second-order accurate spatial discretization of the inviscid and viscous fluxes, and the temporal discretization of the time derivative terms. The need for and implementation of time derivative preconditioning is mentioned. Two time integration schemes, an explicit Runge-Kutta scheme and implicit lower-upper symmetric-Gauss-Seidel (LU-SGS) scheme, are developed in the framework of the present formulation. Convergence acceleration techniques that were used, such as multigrid acceleration, are described. The various boundary condition options that were implemented are also discussed. In the latter part of Chapter 3, the multiblock and parallelization strategy of the code is discussed. The convergence behavior is shown for multigrid acceleration, multiple blocks, and parallel computations.

A laminar, two-dimensional variant of the finite volume formulation was evaluated extensively and is presented in Chapter 4, which is a journal article that was published in *Computers & Fluids* (Dailey and Pletcher, 1996). The effectiveness of preconditioning was demonstrated for low Mach number steady and unsteady flows. The speedups provided by multigrid acceleration for steady and unsteady flows were also studied.

Chapter 5 includes the LES results for the homogeneous, isotropic decay of turbulence. Two different subgrid-scale models were compared, and the grid requirements for LES with a second-order accurate finite volume scheme were assessed for the two models. Comparisons were made to available experimental data.

The LES formulation was further evaluated with a standard turbulent incompressible benchmark flow in Chapter 6. The incompressible, turbulent plane channel flow was computed, and the velocity statistics were compared to detailed incompressible DNS results and

experimental results. Constant wall heating was applied at low rates such that the velocity and temperature field were essentially decoupled. The temperature statistics were compared to incompressible DNS results for a turbulent channel flow where the temperature was treated as a passive scalar.

Chapter 7 presents the simulation of turbulent plane channel flow with constant wall heating rates of magnitudes large enough to cause significant property variations. This was the first known LES or DNS simulation of a variable property channel flow with a bulk temperature rise. The modeling assumptions for this flow, which was treated in a "quasi-developed" manner, were validated with a laminar test case. Turbulent simulations with high cooling and high heating rates were compared to the simulations in Chapter 6 with low heating rates. Comparisons were also made to empirically based correlations for the friction coefficients and Nusselt numbers. The effect of high heating versus cooling on the turbulence statistics are shown.

In Chapter 8, the LES formulation was used to attempt the simulation of turbulent flow and heat transfer for a plane channel with square transverse ribs on one wall. This complex geometry produces a turbulent flow with stagnation points, separation, recirculation zones, and reattachment. The results are compared to experimental measurements of the velocity and temperature fields, as well as to previous LES performed with an incompressible finite volume formulation.

The thesis is summarized in Chapter 9, including a discussion of the significant contributions of this work. Conclusions from this research, as well as recommendations for future work, are also given.

CHAPTER 2 MATHEMATICAL FORMULATION

In this chapter, the filtered set of nondimensional governing equations used for LES are derived. The subgrid-scale models required to close the system of equations is discussed. The equations are recast in integral-vector form so they can be numerically solved with a finite volume formulation that is presented in Chapter 3.

2.1 Compressible Navier-Stokes Equations

The conservation of mass, momentum, and energy for a fluid is expressed in summation notation as

$$\frac{\partial \rho}{\partial t} + \frac{\partial (\rho u_i)}{\partial x_i} = 0 \tag{2.1}$$

$$\frac{\partial (\rho u_i)}{\partial t} + \frac{\partial (\rho u_i u_j)}{\partial x_j} = -\frac{\partial p}{\partial x_i} + \frac{\partial \sigma_{ij}}{\partial x_j} \tag{2.2}$$

$$\frac{\partial (\rho E)}{\partial t} + \frac{\partial (\rho E u_j)}{\partial x_j} = -\frac{\partial (p u_j)}{\partial x_j} - \frac{\partial q_j}{\partial x_j} + \frac{\partial (\sigma_{ij} u_i)}{\partial x_j}, \tag{2.3}$$

respectively, where the total specific energy is $E = e + \frac{1}{2} u_i u_i$. The variables have been nondimensionalized with respect to dimensional reference quantities, denoted with a subscript r, as

$$x_i = \frac{x_i^*}{L_r} \qquad t = \frac{t^*}{L_r / V_r} \qquad u_i = \frac{u_i^*}{V_r} \tag{2.4}$$

$$p = \frac{p^*}{\rho_r V_r^2} \qquad \rho = \frac{\rho^*}{\rho_r} \qquad T = \frac{T^*}{T_r} \qquad e = \frac{e^*}{V_r^2} \tag{2.5}$$

$$R = \frac{R^*}{(V_r^2 / T_r)} \qquad c_p = \frac{c_p^*}{(V_r^2 / T_r)} \qquad c_v = \frac{c_v^*}{(V_r^2 / T_r)} \qquad \mu = \frac{\mu^*}{\mu_r}. \tag{2.6}$$

Dimensional variables are denoted with a superscript asterisk, and all other variables are nondimensional.

For a Newtonian fluid, the shear stress tensor is

$$\sigma_{ij} = \frac{2\mu}{\mathrm{Re}_r}(S_{ij} - \frac{1}{3}S_{kk}\delta_{ij}) \tag{2.7}$$

where the strain rate tensor is

$$S_{ij} = \frac{1}{2}\left(\frac{\partial u_i}{\partial x_j} + \frac{\partial u_j}{\partial x_i}\right). \tag{2.8}$$

and the Reynolds number based on reference quantities is $\mathrm{Re}_r = \rho_r V_r L_r/\mu_r$. Equation 2.7 makes use of Stokes' hypothesis, $\lambda + \frac{2}{3}\mu = 0$, where λ is the coefficient of bulk viscosity. The heat flux vector is given by Fourier's law of heat conduction as

$$q_j = -\frac{\mu}{(\gamma-1)M_r^2\,\mathrm{Re}_r\,\mathrm{Pr}}\frac{\partial T}{\partial x_j} = -\frac{c_p\,\mu}{\mathrm{Re}_r\,\mathrm{Pr}}\frac{\partial T}{\partial x_j}, \tag{2.9}$$

where the molecular Prandtl number is $\mathrm{Pr} = \mu^* c_p^*/\kappa^*$ and the reference Mach number is $M_r = V_r/\sqrt{\gamma R^* T_r}$. For an ideal gas, the pressure, temperature, and density are related by the equation of state as

$$p = \rho RT = \frac{\rho T}{\gamma M_r^2} = (\gamma-1)\rho e. \tag{2.10}$$

For air, the nondimensional molecular viscosity is given as a function of temperature by Sutherland's law as

$$\mu = \frac{1+S}{T+S}\,T^{3/2} \;:\; S = \frac{S^*}{T_r} \tag{2.11}$$

where $S^* = 111K$, or by the power law as

$$\mu = T^n. \tag{2.12}$$

where typically $n = 0.7$. Sutherland's law is slightly more accurate over a larger temperature range, but the power law is less computationally demanding. The power law or a constant molecular viscosity was used for this thesis. A perfect gas was assumed such that the specific heats, c_p and c_v, were constant, and the molecular Prandtl number was assumed to have a constant value of 0.71.

An alternate form of the energy equation, the thermal energy equation, can be obtained by manipulation of Eqs. 2.1 through 2.3 (Currie, 1974). The mechanical energy contributions are removed from the energy equation yielding

$$\frac{\partial(\rho c_v T)}{\partial t} + \frac{\partial(\rho c_v T u_j)}{\partial x_j} = -p\frac{\partial u_i}{\partial x_i} - \frac{\partial q_j}{\partial x_j} + \sigma_{ij}\frac{\partial u_j}{\partial x_i}. \tag{2.13}$$

The total energy equation, given by Eq. 2.3, is preferred for finite volume formulations because it is in conservation law form.

2.2 Filtering

For large eddy simulation, a filtering operation is applied to the compressible Navier-Stokes equations to separate the effects of the large-scale and small-scale motions. The filtering operation is applied to local, instantaneous quantities in terms of a convolution integral as

$$\bar{f}(\vec{x}, t) = \int_D G(\vec{x}, \vec{\xi})\, f(\vec{\xi}, t)\, d\vec{\xi}, \tag{2.14}$$

where G is the filter function and the integration is performed over the entire domain. The quantity f is decomposed as $f = \bar{f} + f'$, where $\bar{f}$ is the large-scale, or resolved component, and f' is the small-scale, unresolved, or subgrid-scale component.

The most commonly used filters for LES are the spectral cut-off filter, Gaussian filter, and top-hat filter. The simplest is the spectral cut-off filter, defined in wavenumber, or $\vec{k}$ space, as

$$G(\vec{k}) = \begin{cases} 1 & \text{for } |k_i| < k_c \\ 0 & \text{for } |k_i| > k_c, \end{cases} \tag{2.15}$$

where k_c is the cut-off wave number, and k_i is the *ith* component of the wavenumber vector, $\vec{k}$. This filter eliminates the contributions of the high wave numbers (or small scales). It is used often with spectral methods; however, it is difficult to implement for finite difference or finite volume methods because it is not easily defined in physical, or $\vec{x}$ space.

The Gaussian filter is preferred by some researchers because it approximates the cut-off filter, yet has very similar definitions in both wavenumber and physical space. In physical space, it is given by

$$G(\vec{x}, \vec{\xi}) = \left[\frac{\sqrt{c/\pi}}{\Delta}\right]^n \exp\left\{-\left[\frac{\sqrt{c}}{\Delta}\right]^n (\vec{x} - \vec{\xi})^2\right\} \tag{2.16}$$

where c is a constant, Δ is the filter width, and n is the number of dimensions to be filtered. In wavenumber space, the same filter is

$$G(\vec{k}) = \exp\left[-\frac{\Delta^2 k^2}{4c}\right] \tag{2.17}$$

where k is the magnitude of the wavenumber vector, $\vec{\mathbf{k}}$.

The top-hat, or box filter, is defined in physical space as

$$G(\vec{x},\vec{\xi}) = \begin{cases} 1/\Delta^3 & \text{for } |x_i - \xi_i| \le \Delta/2 \quad (i = 1,2,3) \\ 0 & \text{otherwise.} \end{cases} \tag{2.18}$$

The top-hat filter reduces to volume averaging, and is the logical choice for LES employing finite volume methods.

2.3 Favre Filtered Governing Equations

The filtering operation in Eq. 2.14 is applied to the nondimensional continuity, momentum, and thermal energy equations (Eqs. 2.1, 2.2, and 2.13, respectively). It can be shown that if G is a function of $\vec{x} - \vec{\xi}$ only, then differentiation and the filtering operation commute (Leonard, 1974) as

$$\overline{\frac{\partial f}{\partial t}} = \frac{\partial \bar{f}}{\partial t} \quad ; \quad \overline{\frac{\partial f}{\partial x}} = \frac{\partial \bar{f}}{\partial x}. \tag{2.19}$$

This leads to the following set of filtered governing equations:

$$\frac{\partial \bar{\rho}}{\partial t} + \frac{\partial (\overline{\rho u_i})}{\partial x_i} = 0 \tag{2.20}$$

$$\frac{\partial (\overline{\rho u_i})}{\partial t} + \frac{\partial (\overline{\rho u_i u_j})}{\partial x_j} = -\frac{\partial \bar{p}}{\partial x_i} + \frac{\partial \bar{\sigma}_{ij}}{\partial x_j} \tag{2.21}$$

$$\frac{\partial (\overline{\rho c_v T})}{\partial t} + \frac{\partial (\overline{\rho c_v T u_j})}{\partial x_j} = -\overline{p \frac{\partial u_i}{\partial x_i}} - \frac{\partial \bar{q}_j}{\partial x_j} + \overline{\sigma_{ij} \frac{\partial u_j}{\partial x_i}}, \tag{2.22}$$

where

$$\bar{\sigma}_{ij} = \overline{\frac{2\mu}{\mathrm{Re}_r}(S_{ij} - \frac{1}{3} S_{kk}\delta_{ij})}, \tag{2.23}$$

$$\bar{q}_j = -\overline{\frac{c_p \mu}{\mathrm{Re}_r \, \mathrm{Pr}} \frac{\partial T}{\partial x_j}}, \tag{2.24}$$

and the equation of state becomes

$$\bar{p} = R \, \overline{\rho T}. \tag{2.25}$$

For compressible flows, it is advantageous to use the filter introduced by Favre (1983), defined by

$$\tilde{f} = \frac{\overline{\rho f}}{\bar{\rho}}. \tag{2.26}$$

which implies the decomposition $f = \tilde{f} + f''$, where $\tilde{f}$ is the resolved component, and f'' is the unresolved component. As a result of the Favre filter,

$$\overline{\bar{\rho}\tilde{u}_i} = \bar{\rho}\tilde{u}_i, \quad : \quad \overline{\bar{\rho}\tilde{u}_i\tilde{u}_j} = \bar{\rho}\widetilde{u_i u_j}, \quad : \quad \overline{\rho u_i \tilde{T}} = \bar{\rho}\widetilde{u_i T}. \tag{2.27}$$

Consequently, the Favre filtered governing equations are

$$\frac{\partial \bar{\rho}}{\partial t} + \frac{\partial(\bar{\rho}\tilde{u}_i)}{\partial x_i} = 0 \tag{2.28}$$

$$\frac{\partial(\bar{\rho}\tilde{u}_i)}{\partial t} + \frac{\partial(\bar{\rho}\tilde{u}_i\tilde{u}_j)}{\partial x_j} = -\frac{\partial \bar{p}}{\partial x_i} + \frac{\partial \bar{\sigma}_{ij}}{\partial x_j} - \frac{\partial \tau_{ij}}{\partial x_j} \tag{2.29}$$

$$\frac{\partial(\bar{\rho}c_v\tilde{T})}{\partial t} + \frac{\partial(\bar{\rho}c_v\tilde{T}\tilde{u}_j)}{\partial x_j} = \frac{\partial \bar{q}_j}{\partial x_j} - \frac{\partial Q_j}{\partial x_j} - \overline{p\frac{\partial u_i}{\partial x_i}} + \overline{\sigma_{ij}\frac{\partial u_j}{\partial x_i}} \tag{2.30}$$

and

$$\bar{p} = R\,\bar{\rho}\tilde{T}. \tag{2.31}$$

The viscous stress tensor and heat flux vector in Eqs. 2.29 and 2.30 are approximated by neglecting the subgrid-scale contributions yielding

$$\overline{\sigma}_{ij} \approx \bar{\sigma}_{ij} = \frac{2\bar{\mu}}{\mathrm{Re}_r}(\tilde{S}_{ij} - \frac{1}{3}\tilde{S}_{kk}\delta_{ij}) \tag{2.32}$$

and

$$\bar{q}_j \approx \bar{q}_j = -\frac{c_p\,\bar{\mu}}{\mathrm{Re}_r\,\mathrm{Pr}}\frac{\partial \tilde{T}}{\partial x_j} \tag{2.33}$$

where the strain rate tensor is

$$\tilde{S}_{ij} = \frac{1}{2}\left(\frac{\partial \tilde{u}_i}{\partial x_j} + \frac{\partial \tilde{u}_j}{\partial x_i}\right) \tag{2.34}$$

and $\bar{\mu} = \bar{\mu}(\tilde{T})$ is given by Sutherland's law or the power law. Note that the 'hat'-symbol, $\widehat{\ }$, does not denote a filter operation, but instead denotes that the quantity is based on filtered variables. The approximations in Eqs. 2.32 and 2.33 require the assumption that the correlation between the fluid properties and the derivatives of the velocity and temperature are weak (Cebeci and Smith, 1974).

The effects of the small-scale motion are present in the above equations through the subgrid-scale (SGS) stress tensor in the Favre filtered momentum equation,

$$\tau_{ij} = \bar{\rho}(\widetilde{u_i u_j} - \tilde{u}_i\tilde{u}_j). \tag{2.35}$$

and the SGS terms in the thermal energy equation, including the SGS heat flux

$$Q_j = \bar{\rho} c_v (\widetilde{T u_j} - \tilde{T}\tilde{u}_j), \tag{2.36}$$

and the third and fourth terms on the right hand side of Eq. 2.30, which represent the pressure work and viscous work.

Finite volume methods were used for this work to numerically solve the resulting Favre filtered governing equations. The thermal energy equation, Eq. 2.30, is not directly amenable to finite volume methods since it is not in conservation law or divergence form. There are at least two methods for obtaining a conservation law form of the filtered energy equation. The first method is to derive an equation for the resolved total energy,

$$\hat{E} = c_v \tilde{T} + \frac{1}{2}\tilde{u}_i\tilde{u}_i \neq c_v \tilde{T} + \frac{1}{2}\widetilde{u_i u_i}, \tag{2.37}$$

and the second method is to directly filter the total energy equation, Eq. 2.3.

The first method was used for the present work. The equation for the resolved total energy, derived following Vreman et al. (1995) in Appendix A, is given by

$$\frac{\partial(\bar{\rho}\hat{E})}{\partial t} + \frac{\partial[(\bar{\rho}\hat{E} + \bar{p})\tilde{u}_j]}{\partial x_j} = \frac{\partial(\tilde{u}_i\hat{\sigma}_{ij})}{\partial x_j} - \frac{\partial \hat{q}_j}{\partial x_j} - \frac{\partial Q_j}{\partial x_j} - \alpha - \pi + \epsilon \tag{2.38}$$

where

$$\alpha = \tilde{u}_i \frac{\partial(\tau_{ij})}{\partial x_j}. \tag{2.39}$$

$$\pi = \overline{p\frac{\partial u_j}{\partial x_j}} - \bar{p}\frac{\partial \tilde{u}_j}{\partial x_j}. \tag{2.40}$$

$$\epsilon = \overline{\sigma_{ij}\frac{\partial u_i}{\partial x_j}} - \hat{\sigma}_{ij}\frac{\partial \tilde{u}_i}{\partial x_j}. \tag{2.41}$$

The second method, described in Appendix B, follows the work of Ragab and Sheen (1993). The total energy equation, Eq. 2.3, is directly filtered yielding

$$\frac{\partial(\bar{\rho}\hat{E} + q^2/2)}{\partial t} + \frac{\partial[(\bar{\rho}\hat{E} + \bar{p})\tilde{u}_j]}{\partial x_j} = -\frac{\partial K_j}{\partial x_j} - \frac{\partial(\gamma Q_j)}{\partial x_j} - \frac{\partial \hat{q}_j}{\partial x_j} + \frac{\partial(\overline{\sigma_{ij}u_i})}{\partial x_j}, \tag{2.42}$$

where

$$K_j = \frac{1}{2}\bar{\rho}\left[(\widetilde{u_i u_i u_j}) - \tilde{u}_i\tilde{u}_i\tilde{u}_j\right] \tag{2.43}$$

and $q^2/2$ is the unresolved, or SGS kinetic energy, as defined in Appendix B.

Equation 2.38 was used for the present work because it is more similar to the form of the energy equation used by most compressible finite volume formulations for the RANS equations. Equation 2.42 has the drawback that the SGS kinetic energy, q^2, appears in the time derivative term. Also, modeling for the SGS terms is more complex for Eq. 2.42 compared to Eq. 2.38.

The resolved total energy equation, Eq. 2.38, is similar to the thermal energy equation, Eq. 2.30, except that the resolved pressure work and viscous work terms are included in the former, and the total energy equation is in conservation law form. The total energy equation has the advantage that it is preferred for flows with shocks due to its conservative nature.

2.4 Subgrid-Scale Modeling

Subgrid-scale modeling for LES is analogous to turbulence modeling for the Reynolds averaged Navier-Stokes (RANS) equations. The advantage for LES is that the simulations should be much less sensitive to the modeling compared to RANS methods. In LES, it is only the small-scale effects that must be accounted for by the model. Since the small-scale motion is mostly isotropic, especially compared to the wide range of scales and anisotropy that must be completely captured in RANS modeling, SGS models should be more universal.

A myriad of techniques exists to model the SGS terms in LES, similar to the situation for modeling for the RANS equations. The models range from simple algebraic methods to complex multi-equation methods. A thorough review of SGS modeling techniques can be found in Ciofalo (1994) and Piomelli (1994).

2.4.1 Gradient-Diffusion Models

The most widely used SGS modeling approach is the gradient-diffusion, or eddy viscosity methodology. The SGS stress tensor is parameterized with an eddy viscosity or gradient-diffusion formulation, similar to the Boussinesq approximation for RANS turbulence models. The model consists of assuming that the anisotropic part of the SGS stress tensor is propor-

tional to the strain rate tensor as

$$\tau_{ij} - \frac{1}{3}q^2\delta_{ij} = -2\mu_t\left(\tilde{S}_{ij} - \frac{1}{3}\tilde{S}_{kk}\delta_{ij}\right). \tag{2.44}$$

where $q^2 = \tau_{kk}$ is the isotropic part of τ_{ij}. The turbulent, or eddy viscosity is

$$\mu_t = C_d\bar{\rho}\Delta^2|\tilde{S}| \tag{2.45}$$

where the magnitude of the strain rate tensor is

$$|\tilde{S}| = \left(2\tilde{S}_{ij}\tilde{S}_{ij}\right)^{1/2}. \tag{2.46}$$

The filter width, Δ, is typically given by $\Delta = (\Delta_x\Delta_y\Delta_z)^{1/3}$, where $\Delta_x, \Delta_y, \Delta_z$ are the control volume dimensions in the x, y, z directions, respectively, and C_d is a coefficient to be determined.

Other forms of the gradient-diffusion model have been proposed in the literature. Alternate formulations are based on the SGS stress tensor being proportional to a quantity other than the strain rate tensor, such as the vorticity or unresolved SGS energy, as discussed by Ciofalo (1994).

Higher order models include solving individual transport equations for each of the subgrid stresses, resulting in seven additional equations, similar to Reynolds stress RANS models. Algebraic approximated equations for the subgrid stresses have also been attempted, similar to algebraic stress models for the RANS equations. These models involve a relevant number of empirical constants and ad hoc assumptions which work well for specific problems, but are difficult to generalize to many different problems and complex geometries.

The gradient-diffusion strain rate model, or eddy viscosity model, is the most widely used variant in the literature, and was used exclusively for this research.

2.4.2 Smagorinsky SGS Model

The strain rate gradient-diffusion model is further classified depending on the method for determining the anisotropic coefficient, C_d. For the Smagorinsky (Smagorinsky, 1963) or Smagorinsky-Lilly (Lilly, 1966) SGS model, the coefficient is specified and held constant

during the simulation. The Smagorinsky model was derived by imposing equilibrium between the energy transfer from large-to-small scale structures and the energy dissipation by the small-scale motion. This required the assumption that the cutoff between the resolved and subgrid scales lies in the inertial subrange where the -5/3 law holds.

There are several problems with the Smagorinsky model that have limited its use. The model coefficients are highly dependent on the problem, numerical algorithm, and grid size, among other factors or variables. This is an obvious drawback, especially for applying the model to complex geometries. The model also predicts the incorrect asymptotic behavior near a wall or in laminar flow, making the model inappropriate for wall bounded or transitional flows unless ad hoc damping functions are incorporated into the model. Finally, the Smagorinsky model does not allow for the backscatter of SGS energy to the resolved scales since the model is purely dissipative. Backscatter has been shown to be significant for many classes of flows, such as transitional flows.

One strategy to improve the Smagorinsky model is to use damping functions to account for the near-wall effect (Moin and Kim, 1982; Piomelli, Moin, and Ferziger, 1988; Ciofalo and Collins, 1992). Ciofalo and Collins (1992), for example, used

$$\tau_{ij} - \frac{1}{3}q^2\delta_{ij} = -2\mu_t\left(\tilde{S}_{ij} - \frac{1}{3}\tilde{S}_{kk}\delta_{ij}\right), \tag{2.47}$$

$$\mu_t = C_d\bar{\rho}D^2\Delta^2|\tilde{S}|, \tag{2.48}$$

where the Van Driest damping function is given by

$$D = 1 - \exp\left[-\left(\frac{y^+}{A^+}\right)\right]. \tag{2.49}$$

$A^+ = 25$ is a constant, and y^+ is the distance to the nearest wall, expressed in wall units.

2.4.3 Isotropic Part of SGS Model

The isotropic part of the SGS stress tensor, $\tau_{kk} = q^2$, is treated separately from the anisotropic part. For incompressible flows, q^2 is typically absorbed into the pressure. For compressible flows, a commonly used parameterization given by Yoshizawa (1986) is

$$q^2 = \tau_{kk} = 2C_I\bar{\rho}\Delta^2|\tilde{S}|^2. \tag{2.50}$$

There is much uncertainty surrounding the parameterization of q^2. For example, Speziale et al. (1988) showed that Yoshizawa's model for q^2 correlated very poorly with results of DNS of compressible isotropic turbulence. In another study, Squires (1991) compared Yoshizawa's parameterization, a parameterization given by Squires and Zeman (1990) as

$$q^2 = 2\beta\bar{\rho}\Delta^2|\tilde{S}|^2 + \beta\Delta^2\frac{\nabla\tilde{p}\cdot\nabla\tilde{T}}{\tilde{T}\mathrm{Pr}_t} - \frac{\sqrt{2\beta}}{3}\bar{\rho}\Delta^2|\tilde{S}|\tilde{S}_{kk}. \tag{2.51}$$

and simply setting $q^2 = 0$. Squires observed negligible difference between the parameterizations for the LES of compressible decaying turbulence.

Many researchers neglect q^2 on the grounds that it is negligible compared to the thermodynamic pressure (Moin et al., 1991; Spyropoulas and Blaisdell, 1995). Erlebacher et al. (1992) quantified this assumption, claiming q^2 can be neglected for

$$M_{sgs} = \left(\frac{q^2}{\gamma RT}\right)^{1/2} < 0.4. \tag{2.52}$$

Finally, q^2 has been neglected for numerical reasons. Vreman et al. (1995) found that the dynamic SGS model was unstable with the box filter and a finite volume scheme if q^2 was not neglected. Simulations in the present study (Chapter 5) confirmed the finding of Vreman et al.

For all of the simulations in the present work, except those noted in Chapter 5, q^2 was neglected for the above reasons.

2.4.4 Dynamic SGS Model

Germano et al. (1991) introduced a dynamic version of the eddy viscosity model in an attempt to alleviate the problems with the Smagorinsky model. For this model, the coefficient (C_d) is computed dynamically as the simulation progresses rather than input *a priori*. The model is based on an algebraic identity between the SGS stresses at two different filtered levels and the resolved turbulent stresses. The SGS stresses obtained using the dynamic model vanish in laminar flow and at solid boundaries, and have the correct asymptotic behavior in the near-wall region of wall-bounded flows. In addition, the model allows for the backscatter

of SGS energy to the resolved field. The introduction of the dynamic model has since greatly renewed interest in LES research.

The dynamic model used for this research was based on the dynamic model proposed for compressible turbulence by Moin et al. (1991). A test filter, with filter width $\Delta_t > \Delta$, was applied to the resolved turbulence field to obtain information about the resolved field. Using the modification to Moin's closure method recommended by Lilly (1992), the coefficients were determined as

$$C_d = \frac{\langle L_{ij} M_{ij} \rangle}{\langle M_{kl} M_{kl} \rangle}, \tag{2.53}$$

and

$$C_i = \frac{\langle L_{kk} \rangle}{\left\langle 2\widehat{\bar{\rho}}\,\Delta_t^2 |\widehat{\tilde{S}}|^2 - 2\Delta^2 \widehat{(\bar{\rho}|\tilde{S}|^2)} \right\rangle} \tag{2.54}$$

where the tensors L_{ij} and M_{ij} are given by

$$L_{ij} = \widehat{\bar{\rho}\tilde{u}_i\tilde{u}_j} - (\widehat{\bar{\rho}\tilde{u}_i})(\widehat{\bar{\rho}\tilde{u}_j})/\widehat{\bar{\rho}} \tag{2.55}$$

$$M_{ij} = -2\Delta_t^2 \widehat{\bar{\rho}}\,|\widehat{\tilde{S}}| \left(\widehat{\tilde{S}_{ij} - \frac{1}{3}\tilde{S}_{kk}\delta_{ij}} \right) + 2\Delta^2 \widehat{\bar{\rho}|\tilde{S}| \left(\tilde{S}_{ij} - \frac{1}{3}\tilde{S}_{kk}\delta_{ij} \right)}. \tag{2.56}$$

The over-parenthesis, $\widehat{\ }$, denotes a test filtered quantity, and $\langle\rangle$ denotes a spatial averaging procedure. The spatial averaging is performed along the homogeneous directions of the flow. It is an ad hoc procedure necessary due to instabilities that arise from using local values of the dynamic coefficients.

For isotropic decaying turbulence, which is assumed to be homogeneous in all three coordinate directions, the spatial averaging results in volume averaging. Consequently, the model coefficient only varies with time. For turbulent channel flows with smooth walls, which are homogeneous in the streamwise and spanwise directions, the spatial averaging reduces to planar averaging, and the coefficient varies in the cross-stream direction and with time. For a ribbed channel, the flow is no longer homogeneous in the streamwise direction, so averaging

can only be performed in the spanwise direction: consequently, the coefficient varies in two spatial directions and time.

The dynamic model was only used in this thesis for simulations of homogeneous, isotropic decaying turbulence presented in Chapter 5. All other simulations utilized the Smagorinsky model.

2.4.5 SGS Modeling for the Energy Equation

The SGS terms in the energy equation must also be modeled. To date, SGS modeling for the energy equation has not received as much attention as modeling for the momentum equations. A brief review of modeling approaches for the energy equation follows.

Some of the earliest LES research for compressible turbulent flows was done by Erlebacher et al. (1992). They used the Favre filtered thermal energy equation, and generalized the Smagorinsky model and scale-similarity model of Bardina et al. (1980) to include compressibility effects and energy transport. The method used a gradient transport hypothesis to model the turbulent heat flux, while the pressure gradient-velocity correlation and viscous dissipation dissipation terms were neglected.

Ragab and Sheen (1993) applied the Favre filter to the total energy equation, and then utilized modeling techniques similar to Erlebacher et al. (1992) for the SGS terms. Again, several terms were neglected.

Moin et al. (1991) generalized the dynamic SGS model for compressible flows. They also used the Favre filtered thermal energy equation with the gradient transport hypothesis for the turbulent heat flux term. However, a turbulent Prandtl number was defined and dynamically computed. Other terms in the energy equation were again neglected. Others, including Spyropoulos and Blaisdell (1995) and Wang (1995) have used similar approaches.

Vreman et al. (1992), and later Vreman et al. (1995), utilized an equation for the resolved total energy. In their 1992 work, a Smagorinsky model was used with the gradient transport formulation for the turbulent heat flux term, and all other terms were neglected. The 1995 work utilized a dynamic mixed model, which combines the dynamic SGS model with Bardina's

(1984) scale similarity model. The modeling of the SGS energy terms was studied extensively in this paper for various Mach numbers. They determined that no modeling was required for the energy terms for Mach numbers of 0.2 and below.

Since only low Mach number flows were considered in the present study, all SGS energy terms except the SGS heat flux were neglected. If higher Mach number flows were to be considered, models for the other SGS terms would need to be developed.

The SGS heat flux was modeled with a gradient-diffusion model as

$$Q_j = \bar{\rho} c_v (\widetilde{T u_j} - \tilde{T}\tilde{u}_j) \approx -\frac{c_v \mu_t}{\mathrm{Pr}_t} \frac{\partial \tilde{T}}{\partial x_j} \tag{2.57}$$

where Pr_t is the turbulent Prandtl number.

For the dynamic SGS model, Pr_t can be determined dynamically as the simulation progresses. The dynamic model was only used here for nearly incompressible simulations without heat transfer, for which Pr_t was not important. All simulations with heat transfer utilized the Smagorinsky model, for which Pr_t was assigned a constant value of 0.9. The reader is referred to Moin et al. (1991) or Wang and Pletcher (1996) for the details of dynamically determining the turbulent Prandtl number.

2.5 Integral-Vector Form of Equations

The nondimensional Favre filtered governing equations, with the resolved total energy equation, were recast in terms of primitive variables ($\bar{p}, \tilde{u}, \tilde{v}, \tilde{w}$, and $\tilde{T}$) by multiplying the equations by the gas constant, removing density with the equation of state, and writing the equations in vector form as

$$\frac{\partial \mathbf{U}}{\partial \mathbf{W}} \frac{\partial \mathbf{W}}{\partial t} + \frac{\partial \mathbf{E}}{\partial x} + \frac{\partial \mathbf{F}}{\partial y} + \frac{\partial \mathbf{G}}{\partial z} = 0. \tag{2.58}$$

Equation 2.58 can also be written in conservation law integral form in terms of the primitive variables as

$$\int_\Omega [T] \frac{\partial \mathbf{W}}{\partial t} d\Omega + \int_{\partial\Omega} \left(\mathbf{E}\vec{\imath} + \mathbf{F}\vec{\jmath} + \mathbf{G}\vec{k} \right) \cdot d\vec{S} = 0 \tag{2.59}$$

where Ω is the control volume, $[T] = \partial \mathbf{U}/\partial \mathbf{W}$ is the time derivative Jacobian matrix given in Appendix C, and the flux vectors are

$$\mathbf{E} = \mathbf{E}_i - \mathbf{E}_v + \mathbf{E}_s \tag{2.60}$$

$$\mathbf{F} = \mathbf{F}_i - \mathbf{F}_v + \mathbf{F}_s \tag{2.61}$$

$$\mathbf{G} = \mathbf{G}_i - \mathbf{G}_v + \mathbf{G}_s \tag{2.62}$$

where the subscript i denotes the inviscid contributions to the flux vectors, the subscript v denotes the viscous contributions, and the subscript s denotes the subgrid-scale contributions. The vector quantities are defined as

$$\mathbf{W} = \begin{bmatrix} \bar{p} \\ \tilde{u} \\ \tilde{v} \\ \tilde{w} \\ \tilde{T} \end{bmatrix} \quad : \quad \mathbf{U} = \begin{bmatrix} \bar{p}/\tilde{T} \\ \bar{p}\tilde{u}/\tilde{T} \\ \bar{p}\tilde{v}/\tilde{T} \\ \bar{p}\tilde{w}/\tilde{T} \\ (\bar{p}/\tilde{T})[c_v\tilde{T} + \frac{1}{2}(\tilde{u}^2 + \tilde{v}^2 + \tilde{w}^2)] \end{bmatrix} \tag{2.63}$$

$$\mathbf{E}_i = \begin{bmatrix} \bar{p}\tilde{u}/\tilde{T} \\ \bar{p}\tilde{u}^2/\tilde{T} + R\bar{p} \\ \bar{p}\tilde{u}\tilde{v}/\tilde{T} \\ \bar{p}\tilde{u}\tilde{w}/\tilde{T} \\ (\bar{p}\tilde{u}/\tilde{T})\hat{H} \end{bmatrix} \quad : \quad \mathbf{F}_i = \begin{bmatrix} \bar{p}\tilde{v}/\tilde{T} \\ \bar{p}\tilde{u}\tilde{v}/\tilde{T} \\ \bar{p}\tilde{v}^2/\tilde{T} + R\bar{p} \\ \bar{p}\tilde{v}\tilde{w}/\tilde{T} \\ (\bar{p}\tilde{v}/\tilde{T})\hat{H} \end{bmatrix} \quad : \quad \mathbf{G}_i = \begin{bmatrix} \bar{p}\tilde{w}/\tilde{T} \\ \bar{p}\tilde{u}\tilde{w}/\tilde{T} \\ \bar{p}v\tilde{w}/\tilde{T} \\ \bar{p}\tilde{w}^2/\tilde{T} + R\bar{p} \\ (\bar{p}\tilde{w}/\tilde{T})\hat{H} \end{bmatrix} \tag{2.64}$$

$$\mathbf{E}_v = \begin{bmatrix} 0 \\ \hat{\sigma}_{xx} \\ \hat{\sigma}_{xy} \\ \hat{\sigma}_{xz} \\ \tilde{u}\hat{\sigma}_{xx} + \tilde{v}\hat{\sigma}_{xy} + \tilde{w}\hat{\sigma}_{xz} - \hat{q}_x \end{bmatrix} \quad : \quad \mathbf{F}_v = \begin{bmatrix} 0 \\ \hat{\sigma}_{xy} \\ \hat{\sigma}_{yy} \\ \hat{\sigma}_{yz} \\ \tilde{u}\hat{\sigma}_{xy} + \tilde{v}\hat{\sigma}_{yy} + \tilde{w}\hat{\sigma}_{yz} - \hat{q}_y \end{bmatrix} \tag{2.65}$$

$$\mathbf{G}_v = \begin{bmatrix} 0 \\ \hat{\sigma}_{xz} \\ \hat{\sigma}_{yz} \\ \hat{\sigma}_{zz} \\ \tilde{u}\hat{\sigma}_{xz} + \tilde{v}\hat{\sigma}_{yz} + \tilde{w}\hat{\sigma}_{zz} - \hat{q}_z \end{bmatrix} \tag{2.66}$$

$$\mathbf{E}_s = \begin{bmatrix} 0 \\ \tau_{xx} \\ \tau_{xy} \\ \tau_{xz} \\ Q_x \end{bmatrix} \quad ; \quad \mathbf{F}_s = \begin{bmatrix} 0 \\ \tau_{xy} \\ \tau_{yy} \\ \tau_{yz} \\ Q_y \end{bmatrix} \quad ; \quad \mathbf{G}_s = \begin{bmatrix} 0 \\ \tau_{xz} \\ \tau_{yz} \\ \tau_{zz} \\ Q_z \end{bmatrix} \tag{2.67}$$

where the resolved total enthalpy is

$$\tilde{H} = c_p\tilde{T} + \frac{1}{2}(\tilde{u}^2 + \tilde{v}^2 + \tilde{w}^2). \tag{2.68}$$

The viscous stress tensors are

$$\hat{\sigma}_{xx} = \frac{2\mu R}{3\mathrm{Re}_r}\left(2\frac{\partial\tilde{u}}{\partial x} - \frac{\partial\tilde{v}}{\partial y} - \frac{\partial\tilde{w}}{\partial z}\right) \tag{2.69}$$

$$\hat{\sigma}_{yy} = \frac{2\mu R}{3\mathrm{Re}_r}\left(2\frac{\partial\tilde{v}}{\partial y} - \frac{\partial\tilde{u}}{\partial x} - \frac{\partial\tilde{w}}{\partial z}\right) \tag{2.70}$$

$$\hat{\sigma}_{zz} = \frac{2\mu R}{3\mathrm{Re}_r}\left(2\frac{\partial\tilde{w}}{\partial z} - \frac{\partial\tilde{u}}{\partial x} - \frac{\partial\tilde{v}}{\partial y}\right) \tag{2.71}$$

$$\hat{\sigma}_{xy} = \frac{\mu R}{\mathrm{Re}_r}\left(\frac{\partial\tilde{u}}{\partial y} + \frac{\partial\tilde{v}}{\partial x}\right) \tag{2.72}$$

$$\hat{\sigma}_{xz} = \frac{\mu R}{\mathrm{Re}_r}\left(\frac{\partial\tilde{u}}{\partial z} + \frac{\partial\tilde{w}}{\partial x}\right) \tag{2.73}$$

$$\hat{\sigma}_{yz} = \frac{\mu R}{\mathrm{Re}_r}\left(\frac{\partial\tilde{v}}{\partial z} + \frac{\partial\tilde{w}}{\partial y}\right) \tag{2.74}$$

and the heat flux vectors are

$$\hat{q}_x = -\frac{c_p\mu R}{\mathrm{Re}_r\mathrm{Pr}}\frac{\partial\tilde{T}}{\partial x} \; ; \; \hat{q}_y = -\frac{c_p\mu R}{\mathrm{Re}_r\mathrm{Pr}}\frac{\partial\tilde{T}}{\partial y} \tag{2.75}$$

$$\hat{q}_z = -\frac{c_p\mu R}{\mathrm{Re}_r\mathrm{Pr}}\frac{\partial\tilde{T}}{\partial z}. \tag{2.76}$$

Finally, the SGS stress tensors are

$$\tau_{xx} = \frac{1}{3}q^2 R - \frac{2\mu_t R}{3}\left(2\frac{\partial \tilde{u}}{\partial x} - \frac{\partial \tilde{v}}{\partial y} - \frac{\partial \tilde{w}}{\partial z}\right) \tag{2.77}$$

$$\tau_{yy} = \frac{1}{3}q^2 R - \frac{2\mu_t R}{3}\left(2\frac{\partial \tilde{v}}{\partial y} - \frac{\partial \tilde{u}}{\partial x} - \frac{\partial \tilde{w}}{\partial z}\right) \tag{2.78}$$

$$\tau_{zz} = \frac{1}{3}q^2 R - \frac{2\mu_t R}{3}\left(2\frac{\partial \tilde{w}}{\partial z} - \frac{\partial \tilde{u}}{\partial x} - \frac{\partial \tilde{v}}{\partial y}\right) \tag{2.79}$$

$$\tau_{xy} = \mu_t R\left(\frac{\partial \tilde{u}}{\partial y} + \frac{\partial \tilde{v}}{\partial x}\right) \tag{2.80}$$

$$\tau_{xz} = \mu_t R\left(\frac{\partial \tilde{u}}{\partial z} + \frac{\partial \tilde{w}}{\partial x}\right) \tag{2.81}$$

$$\tau_{yz} = \mu_t R\left(\frac{\partial \tilde{v}}{\partial z} + \frac{\partial \tilde{w}}{\partial y}\right) \tag{2.82}$$

and the SGS heat flux vectors are

$$Q_x = -\frac{c_v \mu_t R}{\mathrm{Pr}_t}\frac{\partial \tilde{T}}{\partial x}\ ;\ Q_y = -\frac{c_v \mu_t R}{\mathrm{Pr}_t}\frac{\partial \tilde{T}}{\partial y} \tag{2.83}$$

$$Q_z = -\frac{c_v \mu_t R}{\mathrm{Pr}_t}\frac{\partial \tilde{T}}{\partial z}. \tag{2.84}$$

A finite volume formulation, described in the next chapter, was used to numerically solve the governing equations given above.

CHAPTER 3 FINITE VOLUME FORMULATION

The finite volume formulation used for this research is described in this chapter. The spatial and temporal discretization procedures are explained in detail. The multiblock and parallelization strategies are also discussed. Finally, some laminar computations that were done to validate the code and to study its convergence and parallel performance are presented.

3.1 Spatial Discretization

3.1.1 Dependent Variables

Most computational fluid dynamics codes use the conserved variables $(\rho, \rho u_i, \rho E_t)$ as the dependent variables since the governing equations are conveniently derived in terms of these variables. Other sets of variables may be used: in fact, the conserved variables are not always the optimal choice. Chwalowski and Taylor (1991) have shown that there is no penalty for using other sets of variables compared to the conserved variables. For preconditioned codes, such as the present code, the primitive variables (p, u_i, T) are typically used (Pletcher and Chen, 1993; Choi and Merkle, 1993). The derivation of the preconditioned governing equations is usually done with these variables.

The pressure is used as a dependent variable instead of density because the variation of pressure is generally significant for all flow regimes. It is the natural choice when solving incompressible flows, and it allows the propagation of acoustic waves in systems to be singled out. Also, at low Mach numbers, computing the pressure from the equation of state with codes that use the conserved variables can result in significant roundoff errors (Shuen, Chen, and Choi, 1992).

The use of primitive variables is also advantageous because higher order reconstructions

and gradients in the governing equations are based on the primitive variables. The primitive variables were used for the present code for the above reasons.

3.1.2 Cartesian Restriction

The finite volume formulation described in the following paragraphs was derived beginning with relationships valid for general, non-Cartesian hexahedral control volumes. The relationships were then simplified, if possible, assuming Cartesian hexahedrons to simplify coding and to minimize operation counts. In this way, extension of the formulation to non-Cartesian hexahedrons in the future should be straightforward.

3.1.3 Integral Approximations

The integral-vector form of the filtered governing equations, given by Eq. 2.59, were discretized in a finite volume framework. The solution domain was divided into rectangular control volumes of generally unequal dimensions, and the solution variables (p, u_i and T) were stored at the geometric centers of the control volumes, or cells. This is termed the cell center approach. An alternative method is to store the variables at the cell vertices. Cell vertex schemes have been shown to be slightly more accurate on nonuniform meshes, but both provide second-order accuracy on smoothly stretched meshes (Swanson and Radespiel, 1991). The cell center approach has three possible decoupling modes, while the cell vertex approach has only one possible mode. Storage of image cells for the cell center approach is an additional cost. Conversely, the solution domain for a cell center based approach is easier to decompose for multiblock formulations, an important consideration for complex geometries. Also, many upwinding techniques are developed in a cell center framework. Since multiblock and complex geometry capabilities were primary issues for this work, the cell center approach was utilized.

A typical control volume is depicted in Fig. 3.1, showing the main control volume, its cell center (labeled as C), and the cell centers of its six neighboring control volumes (labeled as E,W,N,S,U, and D).

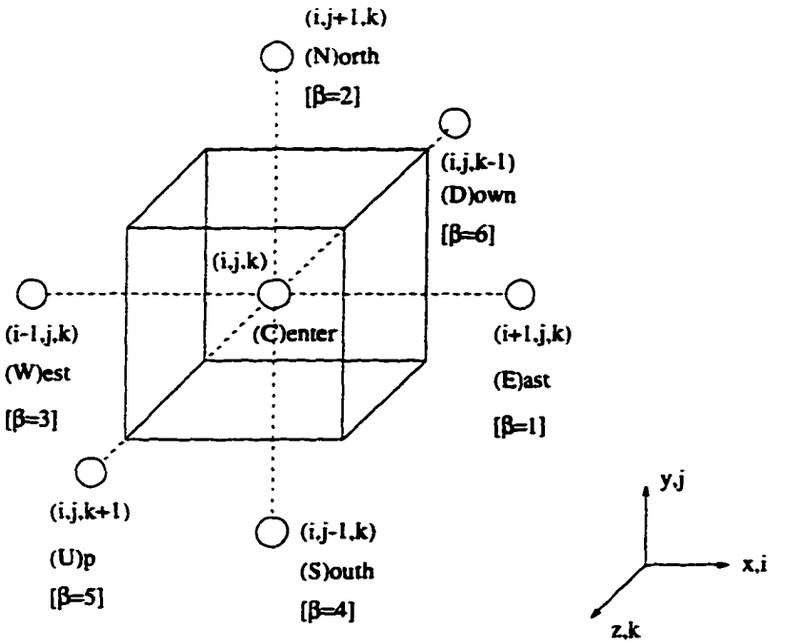

Figure 3.1 Main control volume with cell center, (i, j, k), and six neighboring cell centers, labeled as E,W,N,S,U, and D

The volume integrals in Eq. 2.59 were approximated using the mean value theorem as

$$\int_{\Omega} [T] \frac{\partial \mathbf{W}}{\partial t} d\Omega \approx \left([T] \frac{\partial \mathbf{W}}{\partial t} \right)_{i,j,k} \Omega_{i,j,k}. \tag{3.1}$$

Consequently, a solution variable stored at the cell center was assumed to be the average value for the control volume.

The surface integrals were approximated with the mid-point rule as

$$\int_{\partial\Omega} \left(\mathbf{E}\vec{\imath} + \mathbf{F}\vec{\jmath} + \mathbf{G}\vec{k} \right) \cdot d\vec{S} \approx \mathbf{C}(\mathbf{W}) \tag{3.2}$$

where

$$\mathbf{C}(\mathbf{W}) = \sum_{\beta=1}^{6} \left\{ \left(\mathbf{E}n_x + \mathbf{F}n_y + \mathbf{G}n_z \right) S \right\}_{\beta}, \tag{3.3}$$

and β denotes the six faces of the control volume. The cell face area vector is $d\vec{S} = S\vec{n}$, where S is the magnitude and $\vec{n}$ is the unit normal.

The flux vector on a cell face between the cell centers (i, j, k) and $(i+1, j, k)$, for example,

was determined as

$$\mathbf{E}_{\mathcal{B}} = \mathbf{E}(\mathbf{W}_{i+1/2,j,k}) \tag{3.4}$$

where

$$\mathbf{W}_{i+1/2,j,k} = \frac{1}{2}(\mathbf{W}_{i,j,k} + \mathbf{W}_{i+1,j,k}). \tag{3.5}$$

With these approximations to the integrals, Eq. 2.59 becomes

$$[T]\frac{\mathrm{d}\mathbf{W}}{\mathrm{d}t}\Omega + \mathbf{C}(\mathbf{W}) = 0. \tag{3.6}$$

3.1.4 Gradients

The viscous contributions to the flux vectors require the gradients of u, v, w and T at the cell faces. Two possible techniques for obtaining the gradients are the face based and vertex based approaches. For the vertex based approach, the gradients are calculated and stored at vertices of the main control volumes. The gradients are calculated using the Gauss divergence theorem on an auxiliary control volume with vertices that are the cell centers of the main control volumes surrounding the vertex. The vertex values of the gradients must be interpolated to the cell faces when the fluxes are computed. For the face based approach, the gradients are calculated and stored on all six faces of the control volumes. The gradients are calculated using the Gauss divergence theorem on an auxiliary control volume obtained by shifting the main control volume a half index in the direction of the particular cell face. The face based approach requires three times the storage of the vertex based method. The vertex method is more difficult to implement for multiblock formulations. The vertex method may also be less accurate due to the required interpolations to the cell faces. The face based approach was used here for the above reasons.

The auxiliary control volume used to compute the gradients on the east/west (E/W) faces, for example, of the main control volume is shown in Fig. 3.2. The auxiliary control volume was constructed such that the east/west faces of the auxiliary control volume coincided with the cell centers of the main control volumes. Thus, the volume of the auxiliary control volume is given by

$$\Omega' = \frac{1}{2}\left[\Omega_{i,j,k} + \Omega_{i+1,j,k}\right]. \tag{3.7}$$

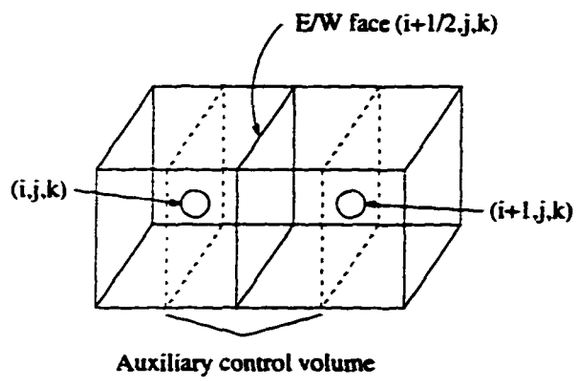

Figure 3.2 Auxiliary control volume for calculation of gradients on east/west (E/W) faces of main control volume

The gradient of a scalar o is given as

$$\int_{\Omega'} \nabla o \; d\Omega' = \int_{\partial\Omega'} o d\vec{S}'. \tag{3.8}$$

where for a Cartesian control volume, $\nabla o = o_x\vec{i} + o_y\vec{j} + o_z\vec{k}$. Equation 3.8 is approximated as

$$(\nabla o)_{i+1/2,j,k}\Omega' = \sum_{\beta'=1}^{6} \left(o\vec{S}'\right)_{\beta'} \tag{3.9}$$

where β' denotes the six faces of the auxiliary control volume. The solution variables on the auxiliary cell faces are defined as

$$o_{E'} = o_{i+1,j,k} \tag{3.10}$$

$$o_{W'} = o_{i,j,k} \tag{3.11}$$

$$o_{N'} = \frac{1}{2}\left\{\left[\alpha_y^+ o_{i+1,j+1,k} + (1-\alpha_y^+)o_{i+1,j,k}\right] + \left[\alpha_y^+ o_{i,j+1,k} + (1-\alpha_y^+)o_{i,j,k}\right]\right\} \tag{3.12}$$

$$o_{S'} = \frac{1}{2}\left\{\left[\alpha_y^- o_{i+1,j-1,k} + (1-\alpha_y^-)o_{i+1,j,k}\right] + \left[\alpha_y^- o_{i,j-1,k} + (1-\alpha_y^-)o_{i,j,k}\right]\right\} \tag{3.13}$$

$$o_{U'} = \frac{1}{2}\left\{\left[\alpha_z^+ o_{i+1,j,k+1} + (1-\alpha_z^+)o_{i+1,j,k}\right] + \left[\alpha_z^+ o_{i,j,k+1} + (1-\alpha_z^+)o_{i,j,k}\right]\right\} \tag{3.14}$$

$$o_{D'} = \frac{1}{2}\left\{\left[\alpha_z^- o_{i+1,j,k-1} + (1-\alpha_z^-)o_{i+1,j,k}\right] + \left[\alpha_z^- o_{i,j,k-1} + (1-\alpha_z^-)o_{i,j,k}\right]\right\} \tag{3.15}$$

where the weighting functions are

$$\alpha_y^+ = \frac{\Delta y'/2}{y_{i,j+1,k} - y_{i,j,k}} \quad ; \quad \alpha_y^- = \frac{\Delta y'/2}{y_{i,j,k} - y_{i,j-1,k}} \tag{3.16}$$

$$\alpha_z^+ = \frac{\Delta z'/2}{z_{i,j,k+1} - z_{i,j,k}} \quad ; \quad \alpha_z^- = \frac{\Delta z'/2}{z_{i,j,k} - z_{i,j,k-1}} \tag{3.17}$$

and $\Delta y'$ and $\Delta z'$ are the dimensions of the auxiliary control volume in the y and z directions, respectively. The auxiliary cell face areas are given by

$$S'_{EW} = S_{EW} \tag{3.18}$$

$$S'_{NS} = \frac{1}{2}[S_{NS}(i,j,k) + S_{NS}(i+1,j,k)] \tag{3.19}$$

$$S'_{UD} = \frac{1}{2}[S_{UD}(i,j,k) + S_{UD}(i+1,j,k)], \tag{3.20}$$

where the main control volume face areas are

$$S_{EW} = \Delta y\, \Delta z \qquad S_{NS} = \Delta x\, \Delta z \qquad S_{UD} = \Delta x\, \Delta y \tag{3.21}$$

and $\Delta x, \Delta y, \Delta z$ are the dimensions of the main control volume in the x, y, z directions, respectively.

Gradients on the north/south (N/S) and up/down (U/D) faces are defined in a corresponding manner. The gradients computed in this way are second-order accurate for a smoothly varying, nonuniform grid distribution. This was confirmed with quadratic test functions on nonuniform grids.

3.1.5 Time Derivative Preconditioning

This research was concerned with computing flows with significant regions of low Mach number. This could occur from recirculation zones, flows near stagnation points, low speed flows with high heat transfer, or flows with chemical reactions. These flows lead to significant density and property variations, such that the compressible form of the governing equations must be retained. Moreover, flows used to validate compressible formulations are often incompressible benchmark computations or low speed experimental data. Compressible flow solvers exhibit convergence problems at low Mach numbers due to the wide disparity between the

convective and acoustic signal speeds leading to large differences in the magnitude of system eigenvalues.

Time derivative preconditioning is a method which attempts to reduce the difference in the magnitude of the eigenvalues, and leads to convergence rates nearly independent of Mach number. Turkel (1987) was one of the first to discuss preconditioning, specifically for the Euler equations. Feng and Merkle (1990) later applied preconditioning methods to the Euler equations using the conserved variables with an approximate factorization scheme. Choi and Merkle extended preconditioning to viscous flows (Choi and Merkle, 1993). Withington et al. (1991) applied preconditioning to chemically reacting flows using a dual time step formulation for time accuracy. Pletcher and Chen (1993) developed a similar preconditioning formulation, which was adopted here.

Preconditioning is employed by adding a pseudo time derivative that is premultiplied by a preconditioning matrix to the governing equations. The preconditioning matrix is constructed in such a way to modify the system eigenvalues. The goal is to make the magnitude of the eigenvalues closer together, at speeds closer to the convective speed, thereby improving convergence rates for the time marching algorithm.

For the present formulation, the preconditioning was incorporated by adding a pseudo time derivative to the left hand side of Eq. 3.6 as

$$[\Gamma]\frac{d\mathbf{W}}{d\tau}\Omega + [T]\frac{d\mathbf{W}}{dt}\Omega + \mathbf{C}(\mathbf{W}) = 0 \tag{3.22}$$

where τ is the pseudo time, and $[\Gamma]$ is the preconditioning matrix. The preconditioning matrix used here is given in Appendix C. The addition of the pseudo time derivative is termed the dual time step approach, and involves iterating in pseudo time for each step in physical time. Upon convergence of the subiteration process in pseudo time, the pseudo time term vanishes, and the original unsteady governing equations are satisfied.

3.2 Artificial Dissipation

For a uniform grid, the spatial discretization outlined above reduces to central differencing. Consequently, artificial dissipation may be necessary for some flow conditions to suppress odd-

even decoupling and to maintain stability near stagnation points. The artificial dissipation employed here was the Jameson type blend of adaptive second and fourth order differences with eigenvalue scaling for viscous shear layers (Martinelli and Jameson. 1988: Swanson and Turkel. 1987).

The dissipation was incorporated by adding a dissipation operator. $\mathbf{D(W)}$. to Eq.3.22 yielding

$$[\Gamma]\frac{d\mathbf{W}}{d\tau}\Omega + [T]\frac{d\mathbf{W}}{dt}\Omega + \mathbf{C(W)} - \mathbf{D(W)} = 0. \tag{3.23}$$

The fully conservative dissipation operator, which was modified to fit into the framework of the preconditioned set of equations is

$$\mathbf{D(W)} = \mathbf{d}_{i+1/2,j,k} - \mathbf{d}_{i-1/2,j,k} + \mathbf{d}_{i,j+1/2,k} - \mathbf{d}_{i,j-1/2,k} + \mathbf{d}_{i,j,k+1/2} - \mathbf{d}_{i,j,k-1/2} \tag{3.24}$$

where the dissipation flux for face $(i+1/2, j, k)$, for example, is

$$\begin{aligned}\mathbf{d}_{i+1/2,j,k} = [\Gamma]_{i+1/2,j,k}\Lambda_{i+1/2,j,k}\Big[&\epsilon^{(2)}_{i+1/2,j,k}(\mathbf{W}_{i+1,j,k} - \mathbf{W}_{i,j,k}) - \\ &\epsilon^{(4)}_{i+1/2,j,k}(\mathbf{W}_{i+2,j,k} - 3\mathbf{W}_{i+1,j,k} + 3\mathbf{W}_{i,j,k} - \mathbf{W}_{i-1,j,k})\Big].\end{aligned} \tag{3.25}$$

The preconditioning matrix, $[\Gamma]_{i+1/2,j,k}$, was included in the dissipation flux to ensure that the global summation of fluxes for the steady-state nonpreconditioned residual. $\mathbf{C} - \mathbf{D}$. is fully conservative.

The variable scaling factors based on the maximum eigenvalues of the discretized equations are

$$\Lambda_{i+1/2,j,k} = \frac{1}{2}[(\bar{\lambda}_\xi)_{i,j,k} + (\bar{\lambda}_\xi)_{i+1,j,k}] \tag{3.26}$$

$$\Lambda_{i,j+1/2,k} = \frac{1}{2}[(\bar{\lambda}_\eta)_{i,j,k} + (\bar{\lambda}_\eta)_{i,j+1,k}] \tag{3.27}$$

$$\Lambda_{i,j,k+1/2} = \frac{1}{2}[(\bar{\lambda}_\zeta)_{i,j,k} + (\bar{\lambda}_\zeta)_{i,j,k+1}] \tag{3.28}$$

where ξ, η, and ζ refer to the i, j, and k directions, respectively, and

$$\bar{\lambda}_\xi = \lambda_\xi \Phi_\xi \;\; ; \;\; \bar{\lambda}_\eta = \lambda_\eta \Phi_\eta \;\; : \;\; \bar{\lambda}_\zeta = \lambda_\zeta \Phi_\zeta \tag{3.29}$$

and

$$\Phi_\xi = 1 + \left(\frac{\lambda_\eta}{\lambda_\xi}\right)^\sigma + \left(\frac{\lambda_\zeta}{\lambda_\xi}\right)^\sigma$$

$$\Phi_\eta = 1 + \left(\frac{\lambda_\xi}{\lambda_\eta}\right)^\sigma + \left(\frac{\lambda_\zeta}{\lambda_\eta}\right)^\sigma \tag{3.30}$$
$$\Phi_\eta = 1 + \left(\frac{\lambda_\xi}{\lambda_\zeta}\right)^\sigma + \left(\frac{\lambda_\eta}{\lambda_\zeta}\right)^\sigma .$$

For the system without preconditioning, the maximum eigenvalue is

$$\lambda = U + cS \tag{3.31}$$

and for the preconditioned system, the maximum eigenvalue is

$$\lambda = \frac{1}{2R}\left[(R+1)U + \sqrt{(R-1)^2U^2 + 4Rc^2S^2}\right] \tag{3.32}$$

where $U = \left|\vec{V}\cdot d\vec{S}\right|$ is the contravariant velocity, $S = \left|d\vec{S}\right|$, and $c = \sqrt{\gamma RT}$ is the speed of sound. The preconditioning matrix was computed as

$$[\Gamma]_{i+1/2,j,k} = \frac{1}{2}\left([\Gamma]_{i,j,k} + [\Gamma]_{i+1,j,k}\right), \tag{3.33}$$

the dissipation coefficients are

$$\epsilon^{(2)}_{i+1/2,j,k} = \kappa^{(2)}\max(\nu_{i,j,k}, \nu_{i+1,j,k}) \tag{3.34}$$

$$\epsilon^{(4)}_{i+1/2,j,k} = \max[0.,(\kappa^{(4)} - \epsilon^{(2)}_{i+1/2,j,k})] \tag{3.35}$$

and the pressure sensor is

$$\nu_{i,j,k} = \frac{|p_{i+1,j,k} - 2p_{i,j,k} + p_{i-1,j,k}|}{p_{i+1,j,k} + 2p_{i,j,k} + p_{i-1,j,k}}. \tag{3.36}$$

The user specified constants were typically $\sigma = 1/2$, $\kappa^{(2)} = 1/2$ and $\kappa^{(4)} = 1/64$.

For this research, artificial dissipation was used primarily for laminar test cases. In general, it was not used for LES cases unless otherwise noted.

3.3 Time Marching Schemes

Two different schemes, described in the following sections, were used to integrate the governing equations in time. Both the Runge-Kutta (RK) scheme and lower-upper symmetric-Gauss-Seidel (LU-SGS) scheme were used in a dual time stepping approach to provide for time derivative preconditioning in a time accurate formulation.

3.3.1 Runge-Kutta Scheme

Jameson (1991) utilized a dual time stepping, implicit Runge-Kutta (RK) scheme to solve the unsteady Euler equations. The method was later applied to time-accurate viscous flows by Arnone et al. (1993), Melson et al. (1993), and later Wang and Yang (1994). Liu and Ji (1995) also used Jameson's dual time stepping approach for a Navier-Stokes solver. They concluded that the implicit RK dual time stepping scheme had great benefits over the pure explicit RK scheme for low frequency unsteadiness and small grid sizes. Turbulent fluctuations are not necessarily of low frequency, but the required grid sizes were definitely small, so that this approach should work well with LES. All of the above work was done with the nonpreconditioned Navier-Stokes equations. The RK scheme was extended here to march in pseudo time for the preconditioned, three-dimensional, Favre filtered governing equations in a dual time stepping manner.

The physical time derivative in Eq. 3.23 was discretized with a second-order accurate three point backward difference as

$$[\Gamma]\frac{d\mathbf{W}}{d\tau}\Omega + [T]\frac{\Omega}{2\Delta t}(3\mathbf{W}^{n+1} - 4\mathbf{W}^{n} + \mathbf{W}^{n-1}) + \mathbf{C}(\mathbf{W}^{n+1}) - \mathbf{D}(\mathbf{W}^{n+1}) = 0. \tag{3.37}$$

Eq. 3.37 can be rewritten as

$$\Omega\frac{d\mathbf{W}}{d\tau} = -[\Gamma]^{-1}\mathbf{R}^{n+1} \tag{3.38}$$

where the residual is

$$\mathbf{R}^{k} = \mathbf{T}(\mathbf{W}^{k}) + \mathbf{C}(\mathbf{W}^{k}) - \mathbf{D}(\mathbf{W}^{k}) \tag{3.39}$$

and $\mathbf{T}$ is the physical time derivative term

$$\mathbf{T}(\mathbf{W}^{k}) = [T]^{k}\frac{\Omega}{2\Delta t}(3\mathbf{W}^{k} - 4\mathbf{W}^{n} + \mathbf{W}^{n-1}). \tag{3.40}$$

Equation 3.38 was solved using either a four or five stage Jameson type Runge-Kutta scheme, where an l-stage scheme is given by

$$\mathbf{W}^{(0)} = \mathbf{W}^{m} \tag{3.41}$$

$$\mathbf{W}^{(1)} = \mathbf{W}^{(0)} - \frac{\Delta\tau}{\Omega}\alpha_1[\Gamma]^{-1}\mathbf{R}^{(0)} \tag{3.42}$$

$$\mathbf{W}^{(2)} = \mathbf{W}^{(0)} - \frac{\Delta\tau}{\Omega}\alpha_1[\Gamma]^{-1}\mathbf{R}^{(0)} \tag{3.43}$$

$$\vdots \tag{3.44}$$

$$\mathbf{W}^{(l)} = \mathbf{W}^{(0)} - \frac{\Delta\tau}{\Omega}\alpha_{l-1}[\Gamma]^{-1}\mathbf{R}^{(l-1)} \tag{3.45}$$

$$\mathbf{W}^{m+1} = \mathbf{W}^{(l)}. \tag{3.46}$$

For the four stage scheme, the coefficients are

$$\alpha_1 = \frac{1}{4}, \quad \alpha_2 = \frac{1}{3}, \quad \alpha_3 = \frac{1}{2}, \quad \alpha_4 = 1 \tag{3.47}$$

and for the five stage scheme, the coefficients are

$$\alpha_1 = 0.449182. \quad \alpha_2 = 0.163954. \quad \alpha_3 = 0.635112, \quad \alpha_4 = 0.5. \quad \alpha_5 = 1. \tag{3.48}$$

The five stage scheme was used most often for this work due do its large stability bound for viscous flows (Vatsa and Wedan, 1990) and good damping properties to drive multigrid acceleration. The four stage scheme was sometimes used for its less dissipative properties.

At each step in physical time, with index n, the RK scheme was used to march in pseudo time, with index m, until the average residual, R_2^{avg}, was less than some tolerance.

$$R_2^{avg} = \frac{\sum_{i,j}|R_2|}{N_{\text{cells}}} < TOL. \tag{3.49}$$

where R_2 is the second component of the residual vector, $\mathbf{R}$, corresponding to the $x-$component of the momentum equation, and N_{cells} is the total number of interior grid cells. Throughout the subiterations in pseudo time, the values of $\mathbf{W}^n$ and $\mathbf{W}^{n-1}$ were frozen in the evaluation of $\mathbf{T}(\mathbf{W}^m)$. As the iteration in pseudo time converged, then $m \to n+1$, and the implicit equation given by the residual, Eq. 3.39, was satisfied, independent of the pseudo time step and the preconditioning matrix.

To reduce the computational effort, the artificial dissipation operator was only evaluated on the first two stages of the RK scheme. Local time stepping, variable coefficient implicit residual smoothing, and multigrid acceleration were used to accelerate the convergence in pseudo time at each physical time step. The first two acceleration techniques are described below, and multigrid acceleration is described in Section 3.5.

3.3.2 Local Time Stepping

Local time stepping involves using the locally maximum allowable time step. For this work, the pseudo time step was computed as

$$\Delta\tau = \mathrm{CFL}\frac{\Omega}{\lambda_{EW} + \lambda_{NS} + \lambda_{UD}} \tag{3.50}$$

where CFL is the Courant-Friedrichs-Lewy stability parameter. The eigenvalues were given by Eqs. 3.31 and 3.32 for the system without and with preconditioning, respectively. The subscripts EW, NS, and UD denote that the area vectors in the eigenvalue equations were for the east/west, north/south, and up/down faces of the control volume, respectively.

With the dual time step formulation, the physical time step, Δt, is only limited by the desired numerical temporal accuracy. As stated by Arnone et al. (1993), the pseudo time step must be further limited as $\Delta\tau < \Delta t$ to maintain stability. This condition can become restrictive for multigrid acceleration. On the coarse grids, larger pseudo time steps are allowed by the CFL condition due to the larger cell volumes. This is one of the reasons for enhanced convergence with multigrid. However, the limitation $\Delta\tau < \Delta t$ can restrict the pseudo time step, and reduce the convergence rate on the coarse grids. This can greatly reduce the effectiveness of multigrid if $\Delta\tau$ and Δt are similar in magnitude.

3.3.3 Implicit Residual Smoothing

Implicit smoothing of the residuals was used to extend the stability limit and robustness of the basic RK scheme. The residual smoothing operator is

$$(1 - \beta_\xi \nabla_\xi \Delta_\xi)(1 - \beta_\eta \nabla_\eta \Delta_\eta)(1 - \beta_\zeta \nabla_\zeta \Delta_\zeta)\bar{R} = R \tag{3.51}$$

where Δ_ξ and ∇_ξ are forward and backward difference operators in the i direction, Δ_η and ∇_η are in the j direction, and Δ_ζ and ∇_ζ are in the k direction. The unsmoothed residual, R, is given by Eq. 3.39 and $\bar{R}$ is the residual after smoothing. Equation 3.51 was solved in three steps, once in each direction, using a Thomas algorithm. For the three-dimensional code, only constant coefficient residual smoothing was implemented, where $\beta_\xi, \beta_\eta, \beta_\zeta$ are constants input by the user.

3.4 LU-SGS Scheme

The lower-upper symmetric Gauss-Seidel (LU-SGS) scheme is an implicit algorithm that provides low operation count per time step — lower than most explicit schemes (Yoon, 1995). The scheme also uses much less memory compared to most implicit schemes and some explicit schemes. The LU-SGS scheme was originally developed by Yoon and Jameson (1987) for the Euler and Navier-Stokes equations without preconditioning. Rieger and Jameson (1988) extended the LU-SGS scheme to three dimensions to solve the steady compressible Navier-Stokes equations in a finite volume framework. Grasso and Marini (1991) applied the LU-SGS method in a finite volume formulation to the solution of two-dimensional high speed flow using an upwind biased TVD spatial discretization. Chen and Shuen (1994) applied the LU-SGS scheme to the preconditioned Navier-Stokes equations using a finite difference discretization. The scheme has also been shown to be an effective driver for multigrid acceleration (Blazek, 1994; Yoon et al., 1995). The methodology incorporated here combines aspects of these LU-SGS based codes to solve the preconditioned, time accurate, Favre filtered governing equations in a dual time stepping approach.

Beginning with Eq. 3.23, the pseudo time derivative was discretized with an Euler backward difference, and the physical time derivative was discretized with a second-order accurate three point backward difference, yielding

$$[\Gamma]\frac{\Delta \mathbf{W}}{\Delta \tau}\Omega + [T]\frac{\Omega}{2\Delta t}(3\mathbf{W}^{n+1} - 4\mathbf{W}^{n} + \mathbf{W}^{n-1}) + \mathbf{C}(\mathbf{W}^{n+1}) - \mathbf{D}(\mathbf{W}^{n+1}) = 0. \tag{3.52}$$

where $\Delta \mathbf{W} = \mathbf{W}^{m+1} - \mathbf{W}^{m}$ and $\Delta \tau = \tau^{m+1} - \tau^{m}$. The inviscid flux vectors were linearized about pseudo time level m as

$$\mathbf{E}_i^{m+1} \approx \mathbf{E}_i^{m} + [A]^{m}\Delta \mathbf{W} \;\; ; \;\; [A] = \partial \mathbf{E}_i / \partial \mathbf{W} \tag{3.53}$$

$$\mathbf{F}_i^{m+1} \approx \mathbf{F}_i^{m} + [B]^{m}\Delta \mathbf{W} \;\; ; \;\; [B] = \partial \mathbf{F}_i / \partial \mathbf{W} \tag{3.54}$$

$$\mathbf{G}_i^{m+1} \approx \mathbf{G}_i^{m} + [C]^{m}\Delta \mathbf{W} \;\; : \;\; [C] = \partial \mathbf{G}_i / \partial \mathbf{W} \tag{3.55}$$

where the inviscid flux Jacobians ([A],[B], and [C]) are given in Appendix C.

The linearized fluxes were substituted into Eq. 3.52. and the entire equation was multiplied by $[\Gamma]^{-1}$ to give

$$\left\{\frac{\Omega}{\Delta\tau}[I]+[\Gamma]^{-1}[T]\frac{3}{2}\frac{\Omega}{\Delta t}+[\Gamma]^{-1}\sum_{\beta=1}^{6}\left[([A]n_x+[B]n_y+[C]n_z)\,S\right]_\beta\right\}^m \Delta\mathbf{W}=-\boldsymbol{\mathcal{R}}^{\,m}. \quad (3.56)$$

where $[I]$ is the identity matrix and the preconditioned residual is defined as

$$\boldsymbol{\mathcal{R}}=[\Gamma]^{-1}\mathbf{R}. \quad (3.57)$$

The viscous and subgrid-scale terms and artificial dissipation were only included in the explicit operator or right hand side of Eq. 3.56. Robustness and stability may be improved for some problems by including viscous terms and artificial dissipation in the implicit operator (Rieger and Jameson, 1988; Yoon, 1985). No problems were encountered for this research, so the additional complexity was not added. Addition of such terms could have an adverse affect on the LU-SGS scheme, since the implicit operator may no longer be strictly diagonal. The importance of the diagonal implicit operator is further discussed later in this section.

For a given control volume with the cell center located at (i,j,k), the east/west control volume faces at $(i\pm 1/2,j,k)$ are labeled as $\beta=1$ and 3, respectively, as depicted in Fig. 3.1. Similarly, the north/south faces at $(i,j\pm 1/2,k)$ are labeled as $\beta=2$ and 4, and the up/down faces at $(i,j,k\pm 1/2)$ are labeled as $\beta=5$ and 6, respectively. The inviscid flux Jacobians on faces 1 and 3 are denoted as $[\hat{A}]$, Jacobians on faces 2 and 4 are denoted as $[\hat{B}]$, and Jacobians on faces 5 and 6 are denoted as $[\hat{C}]$, where

$$\begin{aligned}[\hat{A}]&=([A]n_x+[B]n_y+[C]n_z)_{\beta=1,3}\\ [\hat{B}]&=([A]n_x+[B]n_y+[C]n_z)_{\beta=2,4}\\ [\hat{C}]&=([A]n_x+[B]n_y+[C]n_z)_{\beta=5,6}.\end{aligned} \quad (3.58)$$

For a Cartesian grid with rectangular control volumes, the matrices are simply $[\hat{A}]=[A]$, $[\hat{B}]=[B]$ and $[\hat{C}]=[C]$.

Utilizing Eq. 3.58 and letting $\Delta\tau\to\infty$, Eq. 3.56 becomes

$$\left\{[\Gamma]^{-1}[T]\frac{3}{2}\frac{\Omega}{\Delta t}+[\Gamma]^{-1}\left[[\hat{A}]_1S_1+[\hat{A}]_3S_3+[\hat{B}]_2S_2+[\hat{B}]_4S_4+[\hat{C}]_5S_5+[\hat{C}]_6S_6\right]\right\}\Delta\mathbf{W}=-\boldsymbol{\mathcal{R}}\,. \quad (3.59)$$

To apply the LU-SGS algorithm to the preconditioned system of equations, the flux Jacobians were modified (Chen and Shuen, 1994) to accommodate the preconditioning matrix as

$$[\tilde{A}] = [\Gamma][\Gamma]^{-1}[\tilde{A}] = [\Gamma][\hat{A}] \quad ; \quad [\hat{A}] = [\Gamma]^{-1}[\hat{A}]. \tag{3.60}$$

The flux Jacobian, $[\tilde{A}]$, was split as

$$[\tilde{A}] = [\tilde{A}]^{+} + [\tilde{A}]^{-} \tag{3.61}$$

where

$$[\tilde{A}]^{\pm} = \frac{1}{2}\omega([\tilde{A}] \pm \gamma_A[I]), \tag{3.62}$$

$$\gamma_A = r_A \max\left|\lambda_{[\tilde{A}]}\right|. \tag{3.63}$$

$\lambda_{[\tilde{A}]}$ is the maximum eigenvalue of $[\tilde{A}]S$, and ω and r_A were relaxation factors of $O(\geq 1)$. This splitting of the flux Jacobians was made to ensure diagonal dominance. Multiplying Eq. 3.62 by $[\Gamma]$ yields

$$[\Gamma][\tilde{A}]^{\pm} = \frac{1}{2}\omega([\Gamma][\tilde{A}] \pm \gamma_A[\Gamma]) = \frac{1}{2}\omega([\hat{A}] \pm \gamma_A[\Gamma]). \tag{3.64}$$

The flux Jacobians on the control volume faces were approximated as

$$\begin{aligned}
([\Gamma][\tilde{A}]\Delta\mathbf{W})_1 &= ([\Gamma][\tilde{A}]^{+}\Delta\mathbf{W})_{i,j,k} + ([\Gamma][\tilde{A}]^{-}\Delta\mathbf{W})_{i+1,j,k} \\
([\Gamma][\tilde{A}]\Delta\mathbf{W})_3 &= ([\Gamma][\tilde{A}]^{+}\Delta\mathbf{W})_{i-1,j,k} + ([\Gamma][\tilde{A}]^{-}\Delta\mathbf{W})_{i,j,k} \\
([\Gamma][\tilde{B}]\Delta\mathbf{W})_2 &= ([\Gamma][\tilde{B}]^{+}\Delta\mathbf{W})_{i,j,k} + ([\Gamma][\tilde{B}]^{-}\Delta\mathbf{W})_{i,j+1,k} \\
([\Gamma][\tilde{B}]\Delta\mathbf{W})_4 &= ([\Gamma][\tilde{B}]^{+}\Delta\mathbf{W})_{i,j-1,k} + ([\Gamma][\tilde{B}]^{-}\Delta\mathbf{W})_{i,j,k} \\
([\Gamma][\tilde{C}]\Delta\mathbf{W})_5 &= ([\Gamma][\tilde{C}]^{+}\Delta\mathbf{W})_{i,j,k} + ([\Gamma][\tilde{C}]^{-}\Delta\mathbf{W})_{i,j,k+1} \\
([\Gamma][\tilde{C}]\Delta\mathbf{W})_6 &= ([\Gamma][\tilde{C}]^{+}\Delta\mathbf{W})_{i,j,k-1} + ([\Gamma][\tilde{C}]^{-}\Delta\mathbf{W})_{i,j,k}.
\end{aligned} \tag{3.65}$$

Equations 3.64 and 3.65 were substituted into Eq. 3.59 and result is written as

$$([L] + [D] + [U])\Delta\mathbf{W} = -\boldsymbol{\mathcal{R}} \tag{3.66}$$

where the matrices $[L]$, $[D]$ and $[U]$ are

$$[L] = -[\Gamma]^{-1}\left[([\Gamma][\tilde{A}]^{+})_{i-1,j,k}S_3 + ([\Gamma][\tilde{B}]^{+})_{i,j-1,k}S_4 + ([\Gamma][\tilde{C}]^{+})_{i,j,k-1}S_6\right] \tag{3.67}$$

$$[D] = [\Gamma]^{-1}[T]\frac{3}{2}\frac{\Omega}{\Delta t} + [\Gamma]^{-1}_{i,j}\left[([\Gamma][\tilde{A}]^{+})_{i,j,k}S_1 - ([\Gamma][\tilde{A}]^{-})_{i,j,k}S_3\right.$$

$$\left.+([\Gamma][\tilde{B}]^{+})_{i,j,k}S_2 - ([\Gamma][\tilde{B}]^{-})_{i,j,k}S_4 + ([\Gamma][\tilde{C}]^{+})_{i,j,k}S_5 - ([\Gamma][\tilde{C}]^{-})_{i,j,k}S_6\right] \tag{3.68}$$

$$[L] = [\Gamma]^{-1}\left[([\Gamma][\tilde{A}]^{-})_{i+1,j,k}S_1 + ([\Gamma][\tilde{B}]^{-})_{i,j+1,k}S_2 + ([\Gamma][\tilde{C}]^{-})_{i,j,k+1}S_5\right]. \tag{3.69}$$

Note that $[D]$ was only a function of quantities defined at the center point, (i, j, k), $[L]$ was only a function of quantities at the lower points, and $[U]$ was only a function of quantities at the upper points. These facts were utilized in the solution procedure described in the following paragraphs.

Due to the splitting of the flux Jacobians,

$$[\Gamma][\tilde{A}]^{+} - [\Gamma][\tilde{A}]^{-} = \omega\gamma_A[\Gamma] \tag{3.70}$$

$$[\Gamma][\tilde{B}]^{+} - [\Gamma][\tilde{B}]^{-} = \omega\gamma_B[\Gamma] \tag{3.71}$$

$$[\Gamma][\tilde{C}]^{+} - [\Gamma][\tilde{C}]^{-} = \omega\gamma_C[\Gamma]. \tag{3.72}$$

Furthermore, it was assumed that $S_1 \approx S_3$, $S_2 \approx S_4$, and $S_5 \approx S_6$, such that Eq. 3.68 reduced to

$$[D] = \frac{3}{2}\frac{\Omega}{\Delta t}[\Gamma]^{-1}[T] + \Omega\left(\gamma_A S_{13} + \gamma_B S_{24} + \gamma_C S_{56}\right)[I] \tag{3.73}$$

where

$$S_{13} = \frac{1}{2}(S_1 + S_3)\ ;\ S_{24} = \frac{1}{2}(S_2 + S_4)\ :\ S_{56} = \frac{1}{2}(S_5 + S_6). \tag{3.74}$$

For a Cartesian grid, the approximate equalities above become strict equalities. Due to the nature of the preconditioning matrix employed here, the product $[\Gamma]^{-1}[T]$ is a diagonal matrix; hence, the matrix $[D]$ given by Eq. 3.73 is also diagonal. This is not generally true for other preconditioners, such as those of Choi and Merkle (1993) or Lee and van Leer (1993).

To efficiently solve Eq. 3.66, it was approximately factored as

$$([L] + [D])[D]^{-1}([D] + [U])\Delta\mathbf{W} = -\boldsymbol{\mathcal{R}} \tag{3.75}$$

and solved in three steps as follows:

$$\text{Step 1:} \qquad ([L]+[D])\Delta\mathbf{W}^* = -\boldsymbol{\mathcal{R}}$$
$$\Delta\mathbf{W}^* = [D]^{-1}(-\boldsymbol{\mathcal{R}} - [L]\Delta\mathbf{W}^*)$$

$$\text{Step 2:} \qquad ([D]+[U])\Delta\mathbf{W} = [D]\Delta\mathbf{W}^*$$
$$\Delta\mathbf{W} = \Delta\mathbf{W}^* - [D]^{-1}[U]\Delta\mathbf{W}$$

$$\text{Step 3:} \qquad \mathbf{W}^{m+1} = \mathbf{W}^m + \Delta\mathbf{W}$$

The solution process for Step 1 involved sweeping on $i+j+k = constant$ planes from the lower corner, $(i,j,k) = (1,1,1)$, to the upper corner, $(i,j,k) = (ni, nj, nk)$, of the grid, where ni, nj, nk are the number of interior control volumes in the x, y, z directions, respectively. Since $[L]\Delta\mathbf{W}^*$ was always known during this process, it was moved to the right hand side in Step 1. Similarly, for Step 2 the solution was swept from the upper corner to the lower corner of the grid. Since $[U]\Delta\mathbf{W}$ was always known during this process, it was moved to the right hand side in Step 2. Since $[D]$ is diagonal, as mentioned previously, the inversion of $[D]$ in Steps 1 and 2 required a trivial amount of work. This is one of the key reasons that the LU-SGS scheme is so efficient compared to other implicit schemes.

A simple algorithm to sweep through the grid cells on $i+j+k = constant$ planes is shown in Fig. 3.3, where `nplane` is the plane index, and `numpnts` is the number of grid cells contained in a plane. This algorithm is valid for any general domain size (i.e., $ni \neq nj \neq nk$).

Boundary conditions for the LU-SGS scheme were handled by setting $\Delta\mathbf{W} = 0$ at ghost cells and explicitly setting $\mathbf{W}$ at the beginning of each iteration. Boundary conditions, in general, are discussed in more detail in Section 3.6.

3.5 Multigrid Acceleration

Multigrid acceleration was implemented to improve the rate of convergence for both the RK and LU-SGS schemes. Multigrid is a technique that uses a series of coarse grids to provide corrections to the solution on the finest grid. A thorough and introductory review of multigrid is provided by Brandt (1977).

```
numplanes=ni+nj+nk-2
do nplane=1,numplanes
    ijksum=nplane+2
    numpnts=0
    ibeg=max(ijksum-nj-nk,1)
    iend=min(ijksum-2,ni)
    do i=ibeg,iend
        jksum=ijksum-i
        jbeg=max(jksum-nk,1)
        jend=min(jksum-1,nj)
        do j=jbeg,jend
            k=jksum-j
            numpnts=numpnts+1
        end do
    end do
end do
```

Figure 3.3 Algorithm for looping through indices on $i+j+k=$ constant planes in LU-SGS scheme

For this work, multigrid was implemented with the Full Approximation Storage (FAS) scheme, as discussed in Arnone et al. (1993) or Martinelli and Jameson (1988), for example. Successively coarser grids were obtained by removing every other grid line in the directions being coarsened. Usually, the grid was coarsened in all three dimensions. However, for some problems, such as a channel flow with a large length-to-height ratio, it was advantageous to coarsen in only one or two dimensions. This is termed semi-coarsening multigrid, and was implemented for this research.

The multigrid procedure involved first updating the solution on the fine grid for a specified number of iterations. The grid levels were numbered $L = 1, 2, \ldots, NMG$, where $L = 1$ was the finest grid, and $L = NMG$ was the coarsest grid. After updating the solution on the fine grid, the solution was restricted from the fine grid (level L-1) to the next coarsest grid (level L) by a volume weighted average as

$$\mathbf{W}_0^{(L)} = \frac{1}{\Omega^{(L)}} \sum_{icv=1}^{8} \left[\Omega^{(L-1)}\mathbf{W}^{(L-1)}\right]_{icv} \tag{3.76}$$

where the sum was over the eight fine grid control volumes that comprised the coarse grid control volume (or four control volumes for semi-coarsening in two dimensions, or two control volumes for semi-coarsening in one dimension).

A forcing function was defined for coarse grid level 2 as

$$\mathbf{P}^{(2)} = \sum_{icv=1}^{8} \left[[\Gamma]^{-1} \mathbf{R}^{(1)} \right]_{icv} - [\Gamma]^{-1} \mathbf{R}^{(2)} \tag{3.77}$$

where the residual was given by Eq. 3.39 and the coarse grid residual was based on $\mathbf{W}_0^{(1)}$.

The forcing function was added to the right hand side (RHS) of Eq. 3.38 as

$$\text{RHS} = -([\Gamma]^{-1}\mathbf{R})^{(L)} + \mathbf{P}^{(L)} \tag{3.78}$$

where $P^{(L)}$ was frozen for a given grid level throughout a multigrid cycle. The solution was updated for a specified number of iterations on the coarse grid level L. Recall that $\mathbf{W}^n$ and $\mathbf{W}^{n-1}$ do not change throughout the iteration in m. Values of $\mathbf{W}^n$ and $\mathbf{W}^{n-1}$ were found on the coarse grid levels by restriction using Eq. 3.76. The same physical time step, Δt, was used on all grid levels.

On coarser grid levels ($L > 2$) the forcing function included the collection of the residuals *and* forcing functions from level L

$$\mathbf{P}^{(L+1)} = \sum_{icv=1}^{8} \left[[\Gamma]^{-1} \mathbf{R}^{(L)} + \mathbf{P}^{(L)} \right]_{icv} - [\Gamma]^{-1} \mathbf{R}^{(L+1)}. \tag{3.79}$$

This process was repeated until the coarsest grid was reached.

After updating the solution on the coarsest grid (level L) for a specified number of iterations, the corrections were prolongated to the next finer grid ($L-1$) as follows:

$$\mathbf{W}^{(L-1)} = \tilde{\mathbf{W}}^{(L-1)} + I_{(L)}^{(L-1)} (\tilde{\mathbf{W}}^{(L)} - \mathbf{W}_0^{(L)}) \tag{3.80}$$

where $\tilde{\mathbf{W}}^{(L-1)}$ is the solution on grid $L-1$ before the restriction to grid L, $\mathbf{W}_0^{(L)}$ is the solution restricted to grid L before any iterations were performed on grid L, and $I_{(L)}^{(L-1)}$ is a trilinear interpolation operator (or bilinear interpolation for semi-coarsening in two dimensions and linear interpolation for semi-coarsening in one dimension).

The boundary conditions on the coarse grids were enforced in the same way as for the fine grid. A typical multigrid cycle consisted of performing two iterations of the scheme on each grid level on the way up and down a V cycle. Local time stepping and residual averaging were applied on all grid levels for the RK scheme.

3.6 Boundary Conditions

Boundary conditions were enforced in this code by using "ghost" or "image" cells, as depicted in Fig. 3.4. These cells are reflections of the near wall control volume about the grid boundary. The ghost cells have the same volume and cell face areas as the near wall control volume. The purpose of the ghost cells is to ensure that the desired fluxes of mass, momentum, and energy are obtained for the cell faces lying on the boundaries. The various boundary condition options used for this research are described below.

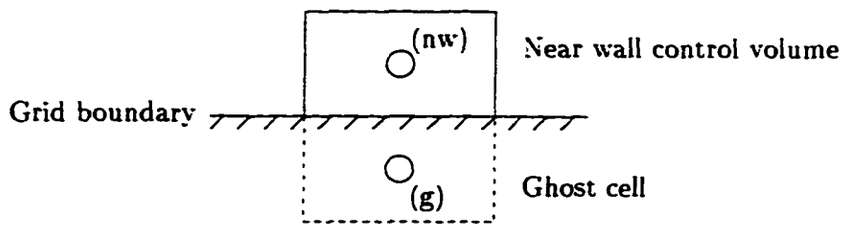

Figure 3.4 Ghost cells for boundary conditions

3.6.1 Solid Wall Boundary Conditions

For solid walls, the no slip condition was enforced for the velocity components. For stationary walls, all three components were zero, which was enforced with the ghost cell as $u_g = -u_{nw}$, $v_g = -v_{nw}$, and $w_g = -w_{nw}$, where the subscript g refers to the ghost cell and the subscript nw refers to the near wall control volume. For a wall moving at a given velocity, V_w, in the x direction, for example, the ghost cell value was set as $u_g = 2V_w - u_{nw}$.

For moving or stationary solid walls, the approximate boundary condition $\partial p/\partial n = 0$ at the wall was enforced by setting $p_g = p_{nw}$.

Two different temperature conditions were used: fixed wall temperature or fixed wall heat flux. In general, the specified wall temperature or heat flux could vary in space. A fixed wall temperature, T_w, was enforced by setting the ghost cell value as $T_g = 2T_w - T_{nw}$. A fixed nondimensional wall heat flux condition, q_w, was enforced by setting the ghost cell value as

$$T_g = T_{nw} + \frac{q_w \mathrm{RePr}}{\mu_w}(y_{nw} - y_g) \tag{3.81}$$

where μ_w is the nondimensional molecular viscosity at the wall. The nondimensional heat flux is given in terms of dimensional quantities as

$$q_w = \frac{q_w^*}{\rho_r V_r T_r c_p^*}. \tag{3.82}$$

For variable property flows, where the molecular viscosity at the wall was a nonlinear function of temperature, $\mu_w = \mu_w(T_w)$, an iterative procedure was required in the boundary condition routine to obtain the correct value of the wall, and hence, ghost cell temperatures.

3.6.2 Periodic Boundary Conditions

Periodic boundary conditions were used extensively for many of the test cases presented in this thesis. For periodic boundaries, the ghost cells are no longer a reflection of the near wall control volume, but are a periodic copy of the near wall control volume from the opposite boundary.

As an example, to enforce periodicity of the u-velocity in the z-direction, the ghost cell values for the $k = 1$ boundary would be set as

$$u_g = u(i, j, 0) = u(i, j, nk) \tag{3.83}$$

as depicted by the shaded cells in Fig. 3.5, and the ghost cell values for the $k = nk$ boundary would be set as

$$u_g = u(i, j, nk + 1) = u_{nw} = u(i, j, 1). \tag{3.84}$$

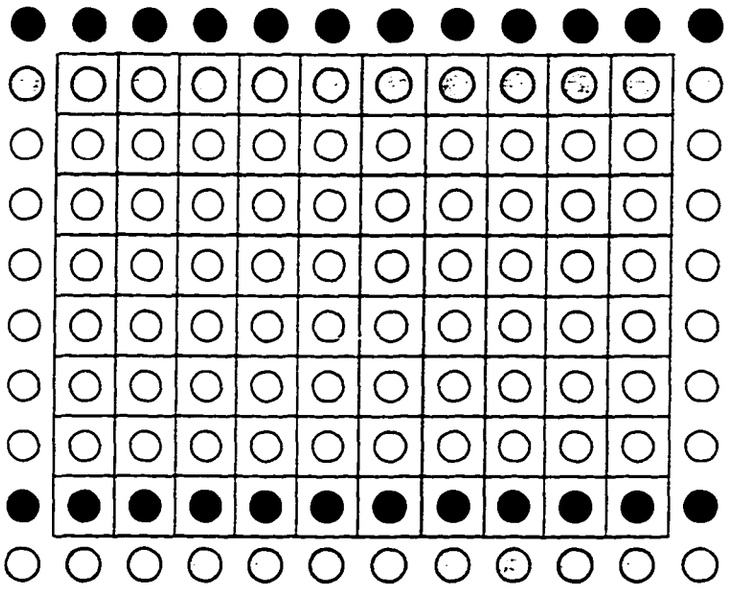

Figure 3.5 Ghost cells for periodicity in one direction

as depicted by the solid filled cells in Fig. 3.5. The interior control volumes are denoted by $k = 1, \ldots, nk$ and the ghost cells are denoted by $k = 0$ and $k = nk + 1$. For periodicity in two directions, the corner cells require special treatment. The periodicity of the control volumes is depicted in Fig. 3.6 for this situation.

3.6.3 Inflow and Outflow Boundary Conditions

Some of the laminar flow test cases, such as developing channel flow, required the specification of inflow and outflow boundary conditions. Only subsonic conditions were used for this work. For inflow boundaries, the total temperature, total pressure, and two velocity components (or some other combination of four quantities) were specified. The static pressure (or possibly some other quantity) was extrapolated from the interior by first order extrapolation, $p_g = 2\ p(1,j,k) - p(2,j,k)$. The ghost cell values of the primitive solution variables $(p_g, u_g, v_g, w_g, T_g)$ were derived from these quantities.

For outflow boundaries, one quantity was specified at the ghost cells, usually the static

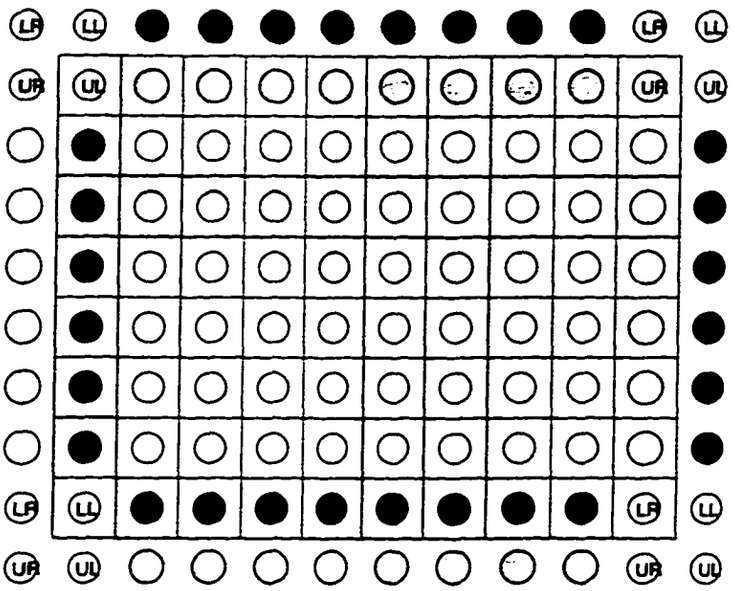

Figure 3.6 Ghost cells for periodicity in two directions

pressure. The other four primitive variables were extrapolated from the interior with a first order extrapolation.

3.7 Multiblock and Parallelization Strategies

The three-dimensional code for this research was developed in a multiblock framework. This enabled the code to handle complex geometries such as step flows and channels with square ribbed walls, and provided a means for parallelization of the code such that multiple processors could be utilized. In this section, the multiblock formulation used for the current code is described. A literature review is provided for multiblock, multigrid explicit and implicit schemes, including parallelization. Finally, the parallelization strategy implemented in the present code is discussed.

3.7.1 Multiblock Formulation

For the multiblock formulation, the computational domain was divided into multiple domains, or blocks. The code can handle any general collection of three-dimensional rectangular blocks with Cartesian grids of generally unequal spacing. In order to simplify coding and minimize complexity, several restrictions were placed on the blocking. Adjoining blocks must share a face with common characteristics: most importantly, grid lines must be continuous across the interface between two blocks. Consequently, the shared face has the same dimensions, same number of control volume faces, and the control volume faces have the same areas.

Each rectangular block has six faces or sides, labeled as EAST, WEST, NORTH, SOUTH, UP, and DOWN, and indexed as IFACE= 1,...,6, respectively, as shown in Fig. 3.7. Two pointers or arrays are needed to provide the block connectivity and boundary condition information, NGB and BCTYPE. The blocks were arbitrarily numbered as IBLK=1,...,NBLK, where NBLK is the total number of blocks. NGB(IBLK,IFACE) identifies the number of the neighboring block, if any, which shares face IFACE. BCTYPE(IBLK,IFACE) identifies the type of boundary condition to be applied on face IFACE, if no neighboring block exists. Only one type of boundary condition is allowed per block face, but each block face can have any of the available boundary condition types. A more general boundary condition treatment, common in more generalized multiblock codes (e.g. Rizzi et al., 1993) is to have boundary condition windows on each face, allowing multiple boundary condition types on a face. However, this more general and complex treatment was not adopted for this work since the test cases considered would not require it. Many generalized multiblock codes also do not have the restriction on shared block faces, i.e. grid lines do not have to be continuous and block interfaces do not have to be coincident. However, complex interpolation techniques are then required at the interfaces.

Two layers of ghost cells surround each block. The ghost cells are used to store data from neighboring blocks or to apply boundary conditions. The overlap provided by two layers of ghost cells allows the use of fourth-difference artificial dissipation or up to third order accurate upwind formulas for the inviscid terms without loss of accuracy. Higher order accurate methods would require more layers of ghost cells, significantly increasing the complexity and memory

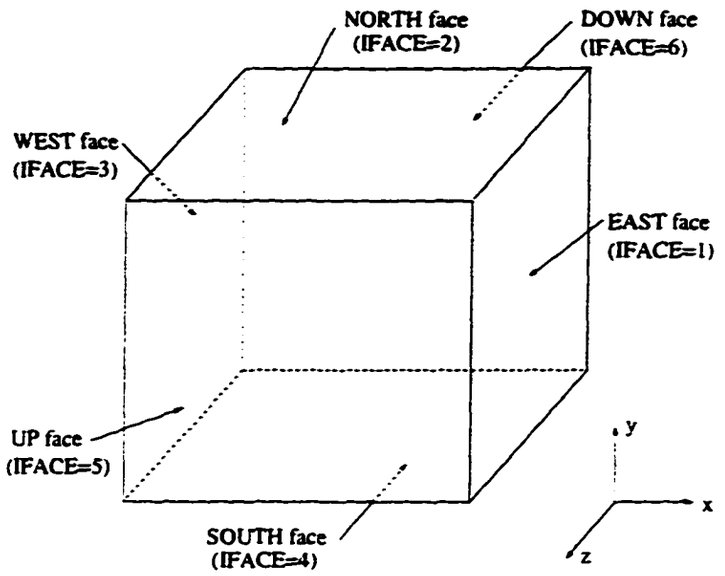

Figure 3.7 Typical grid block showing labeling of sides or faces of block

overhead. Alternatively, lower order accurate discretizations could be used at block interfaces, but this approach is undesirable.

The control volumes interior to each block domain were indexed as $(i, j, k) = (1, 1, 1)$ to (ni, nj, nk), such that the total number of interior control volumes was NCELLS $= ni \times nj \times nk$. The complete domain, including two layers of ghost cells, was indexed as $(i, j, k) = (-1, -1, -1)$ to $(ni+2, nj+2, nk+2)$, such that the total number of cells was the product NTOTAL$=(ni+4) \times (nj+4) \times (nk+4)$. The ghost cells were subdivided and named as face cells, edge cells, and corner cells. For example, the first layer of EAST face ghost cells had indices $(ni+1, 1 : nj, 1 : nk)$, and the second layer of EAST face ghost cells had indices $(ni+2, 1 : nj, 1 : nk)$. The NORTH-EAST edge ghost cells, for example, had indices $(ni+1, nj+1, 1 : nk)$, and the EAST-NORTH-UP corner, for example, had the index $(ni+1, nj+1, nk+1)$. The present schemes required solution variables at two layers of face ghost cells, and only one layer of corner and edge ghost cells, although memory was allocated for two complete layers.

The addition of ghost cells can significantly increase the total required storage. On a per-

centage basis. this is especially detrimental for blocks with a small number of control volumes. This is a serious drawback for the serial multiblock code on a single processor. because all memory must be allocated on the processor. For the parallel code on multiple processors with distributed memory. this is not a serious drawback since the memory can be spread over multiple processors.

The code was written in Fortran 90. which offers several new features compared to Fortran 77. Fortran 90 provides simple dynamic memory allocation capabilities. Due to the extra memory requirements for the ghost cells and multigrid, the ability to allocate the minimum memory required for a particular problem was advantageous. Other features of Fortran 90 that were utilized include the use of array sections, pointers, and modules. These features were very helpful in developing a large, complex code.

3.7.2 Review of Multiblock, Multigrid Schemes

For a purely explicit scheme. such as the Runge-Kutta scheme without implicit residual averaging, no special treatment is required for a multiblock code. It is only necessary to ensure that before each iteration. the ghost cells contain the appropriate values of the solution variables from the neighboring blocks from the previous iteration.

As more implicitness is added to the schemes. such as the Runge-Kutta scheme with implicit residual averaging, multigrid acceleration. or the implicit LU-SGS scheme. convergence deterioration can result when the solution domain is divided into multiple blocks. A review of the literature shows that there are several ways to deal with the multiblock formulation for these schemes.

Yadlin and Caughey (1991) studied multiblock. multigrid algorithms for the solution of the Euler equations. They considered two methods for handling multigrid in a multiblock framework. In the horizontal mode. the multigrid cycle is kept in phase in all blocks. In the vertical mode. the multigrid cycle is advanced independently in each block. and only synchronized at the end of a multigrid cycle. This approach has the potential for high parallel efficiency. For two-dimensional cases presented in Yadlin and Caughey (1991) they found

convergence problems with the vertical mode. They later found that improvements to the vertical mode led to convergence similar to that for the horizontal mode (Yadlin and Caughey, 1992). This involved using asynchronous updating at the interface boundaries, where the interface boundaries were updated with currently available data from adjacent blocks. They also found that no updating on the interpolation steps had no visible effect on convergence.

Rossow (1992) investigated an explicit Runge-Kutta scheme for the Euler equations in a multiblock framework. He found that convergence rates were maintained if a complete RK cycle was completed before exchanging data between blocks. However, information had to be exchanged before residuals were computed for restriction to the next coarsest grid.

Using a three-dimensional incompressible Navier-Stokes code, Sheng et al. (1995) found that both the horizontal and vertical modes gave essentially the same CPU time and number of iterations. They preferred the vertical mode because one can use a different number of multigrid levels and full versus semi-coarsening in each block, and because of its inherent parallelism. For the horizontal mode, the same multigrid strategy must be used in all blocks (same number of grid levels and same level of coarsening in each direction). They even found better convergence for the blocked multigrid compared to the unblocked multigrid for some cases. They used an unsynchronized dependent variable technique, where the latest available information was used to calculate the residuals.

Rizzi et al. (1993) elected to treat all blocks in phase in their multiblock, multigrid code based on the earlier work of Yadlin and Caughey. Steinthorsson and Ameri (1995) also described a three-dimensional multiblock, cell centered finite volume scheme using multigrid and a four stage RK scheme with residual averaging and local time stepping. They exchanged data between blocks only before the first stage of RK, and communicated on all levels of the multigrid cycle at the beginning of each smoothing sweep. Implicit residual smoothing was done independently in each block. They showed no convergence rates for their scheme, but did successfully compute the flows about some very complicated geometries.

Alonso et al. (1994) proposed three methods for implementing multigrid in parallel for a two-dimensional explicit RK Navier-Stokes solver.

- *Full multigrid.* Communicate at all RK levels on all multigrid levels to maintain serial convergence at the expense of poor parallel performance.

- *Implicit multigrid within subdomains.* Completely decouple the subdomains on coarser levels. This restores parallel efficiency at the expense of poorer convergence.

- *"lazy"-"dumb" multigrid.* At a specified grid level, pass the flow and grid information to a single processor, which performs relaxations for all coarser levels. This approach recovers convergence and maintains high parallel efficiency at the expense of coding complexity and extra overhead. The motivation for this approach is that at lower multigrid levels, communication costs are latency driven, so message passing must be avoided at the coarsest levels where the ratio of communication-to-computation is higher than for the finer grid levels.

Lazy-dumb multigrid gave slightly better parallel speedups compared to full multigrid and roughly the same convergence. Alonso et al. stated that full multigrid may be more suited to three-dimensional Navier-Stokes or LES calculations where the ratio of computation-to-communication is increased.

Three methods for implementing residual averaging in parallel were proposed by Alonso and Jameson (1994):

- *Fully implicit.* This method is terribly inefficient in parallel because the tridiagonal solver is inherently serial.

- *Completely decoupled.* This gives rise to severely degraded convergence.

- *Iterated residual averaging.* This approach involves passing residuals at boundaries after each iteration. A minimum of two iterations were required, but usually three were used. They used Jacobi relaxation on all subdomains.

Alonso and Jameson concluded that iterated residual averaging was the only choice. However, in a later paper Jameson and Alonso (1996) concluded that contrary to the two-dimensional

tests presented in 1994, applying residual averaging implicitly in each block (decoupled) resulted in no loss of convergence in three dimensions. They demonstrated that even with multigrid, 80 percent parallel efficiency can be achieved on 16 IBM SP-2 processors for three-dimensional Navier-Stokes calculations.

3.7.3 Parallelization Strategy

For the present code, implicit residual averaging and the implicit LU-SGS scheme were implemented in each block independently. Based on the review of the literature, this should be acceptable for a three-dimensional solver as long as the number of control volumes in each cell does not become too low. For this work, relatively fine grids with coarse-grained parallelism (8 to 16 processors) were expected to be used, so the independent treatment of these algorithms was not expected to pose a problem. This was verified with later calculations as described in Section 3.8.1. Multigrid acceleration was also treated independently in each block. For the RK scheme, the multigrid was implemented synchronously, in the horizontal mode, as described by Yadlin and Caughey above.

The code was parallelized by incorporating message passing between the blocks using Parallel Virtual Machine (PVM) message passing libraries. There are many message passing libraries available. PVM was chosen because of its portability — it is available on most computer architectures. Many other message passing libraries are machine specific, providing increased performance at the expense of portability. A more recent message passing library is the Message Passage Interface (MPI) standard. It provides about the same level of portability as PVM, but gives improved performance on most systems. MPI message passing could be incorporated into the current code with minimal effort by replacing the PVM message passing routines with comparable MPI routines.

The parallel code was written in a single program, multiple data (SPMD) format. This means that only one code was required, the same code being run on all processors with the data distributed across the different processors. One processor starts up initially and becomes the *parent* task. The *parent* then spawns the desired number of *child* tasks. The parallelization

was achieved with domain decomposition utilizing the multiblock features of the code. The domain was divided into blocks, and typically one block was assigned to each processor.

Two approaches were considered for passing messages between blocks at the end of each iteration. For Method A, or *neighbor-to-host-to-neighbor* message passing, each *child* process sends data to the *parent* process. The *parent* process receives the data from all *child* processes, and then sends the appropriate data out to each *child* process. This method minimizes the number of calls to PVM message passing routines. For Method B, or *neighbor-to-neighbor* message passing, message passing is accomplished by having each *child* process send the appropriate data directly to each *child* process that needs the data. This method requires more calls to PVM message passing routines, but minimizes the amount of data that is being transmitted. Early studies conducted with a two-dimensional, inviscid, compressible flow solver using domain decomposition showed that Method B was much more efficient and resulted in less overall wall clock time, and was thus adopted for the three-dimensional LES code.

The solution schemes were implemented for both serial and parallel execution. An attempt was made to maximize the number of routines common to both the serial and parallel codes. The parallel code is comprised of about 45 modules and subroutines, and the serial code is comprised of about 40 modules and subroutines, with 34 being common to both. The code uses a makefile to compile the code on different architectures for either serial or parallel execution. The architecture dependent compiler names, options, and libraries are determined by the makefile depending on the architecture selected.

3.8 Performance Estimates

The convergence properties and parallel performance of the code were studied for a laminar and turbulent flow. Computations of laminar, steady-state, three-dimensional lid driven cavity flow are presented in Section 3.8.1. Limited simulations of the turbulent plane channel flow are discussed in Section 3.8.2. Some limitations of the current formulations are identified.

A two-dimensional, laminar, serial version of this code was tested extensively to assess the effectiveness of time derivative preconditioning and multigrid acceleration for time accurate

flows. The results are presented in Chapter 4, which is a journal article presented in *Computers & Fluids*.

3.8.1 Laminar Lid Driven Cavity Flow

Steady state calculations were made of the three-dimensional, impulsively started lid driven cubic cavity for Re=100 and $M = 0.001$, where Re is based on the cavity dimensions and lid velocity. The flow was started from quiescent conditions, and the lid was instantaneously set in motion at time zero.

The flow was computed with a uniformly spaced $32 \times 32 \times 32$ grid and $48 \times 48 \times 48$ grid. The resulting centerline u—velocity and v-velocity distributions are shown in Figs. 3.8 and 3.9, respectively. The computations of Chen (1990) with a $20 \times 20 \times 20$ grid are shown for comparison purposes. Minimal change in the solution was observed between the $32 \times 32 \times 32$ and $48 \times 48 \times 48$ grid, indicating a nearly grid independent solution. Fair agreement with the computations of Chen (1990) were obtained. This is expected since Chen used a very coarse grid.

Figure 3.10 shows the effectiveness of multigrid acceleration for the three-dimensional calculation with a single block $32 \times 32 \times 32$ grid. Convergence with no multigrid ($NMG = 1$) was compared to convergence with three levels of multigrid ($NMG = 3$). A speedup of more than five was obtained for both schemes, indicating that multigrid was very effective for the three-dimensional code for this type of flow. It is interesting that the LU-SGS scheme without multigrid required about the same amount of work units as the Runge-Kutta scheme with multigrid, where a work unit is defined as the equivalent amount of work required on the fine grid only. Moreover, the LU-SGS scheme was found to require half as much CPU time per work unit compared to the RK scheme. This was also observed for the 2-D version of the schemes (see Chapter 4). The fact that this behavior carried over to the 3-D code is one of the strong points of the LU-SGS scheme.

The flow was subsequently computed with multiple blocks with the two schemes with and without multigrid. The cubic three-dimensional cavity domain was divided into one, two, four,

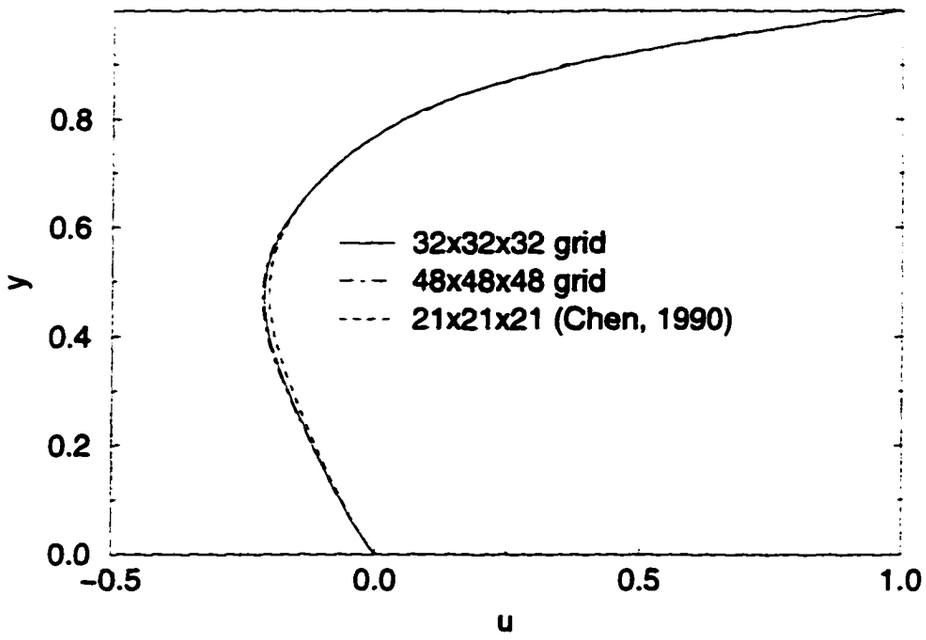

Figure 3.8 u-velocity component along vertical centerline for 3-D laminar lid driven cavity with LU-SGS scheme

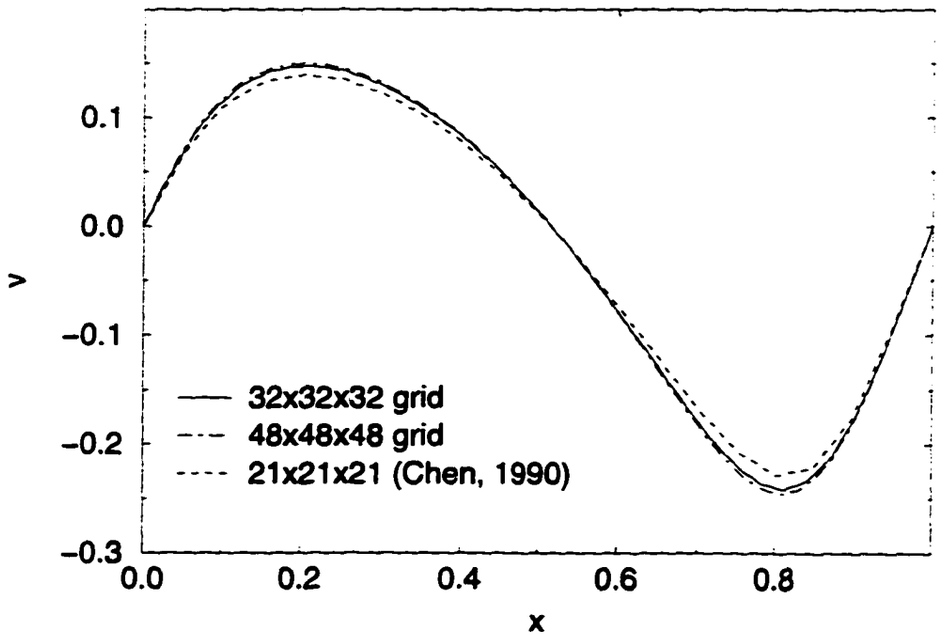

Figure 3.9 v-velocity component along horizontal centerline for 3-D laminar lid driven cavity with LU-SGS scheme

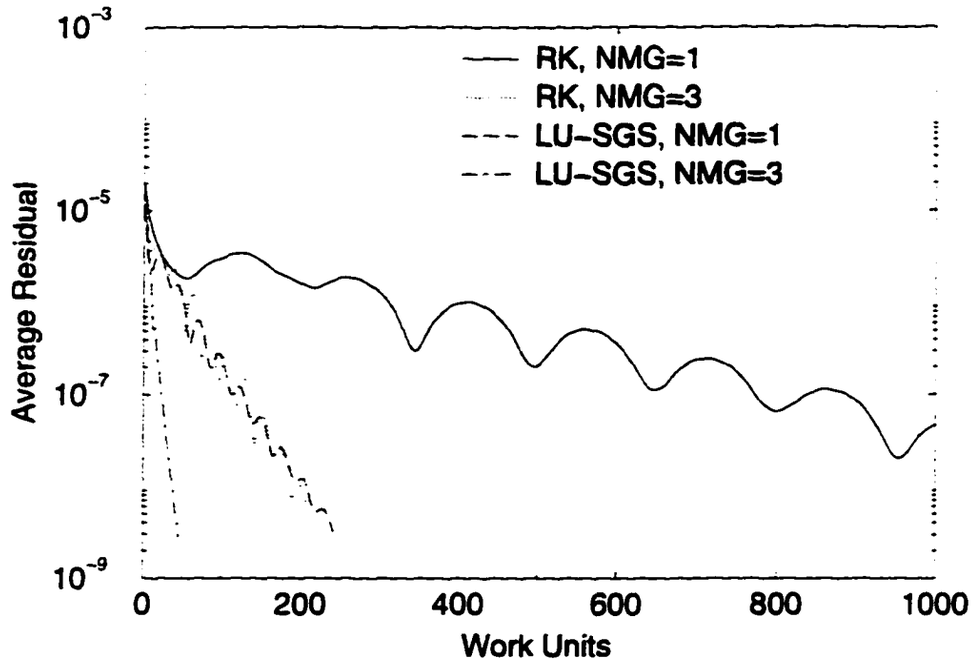

Figure 3.10 Effectiveness of multigrid acceleration for single block convergence ($32 \times 32 \times 32$ grid) for the 3-D laminar lid driven cavity

and eight blocks, as depicted in Fig. 3.11.

Convergence for the RK scheme with implicit residual averaging but without multigrid ($NMG = 1$), shown in Fig. 3.12, indicates that this scheme works well with multiple blocks. Identical convergence was obtained with three levels of multigrid ($NMG = 3$) for one, two, and four blocks. However, convergence for the RK scheme deteriorated for eight blocks. All cases shown in Fig. 3.12 were run with the same CFL number and the same $32 \times 32 \times 32$ grid. The point at which convergence deteriorates for this scheme is dependent on these properties. Lowering the CFL number would cause the eight block configuration to remain stable. In addition, a larger grid size would be able to maintain convergence for a larger number of blocks, while a smaller grid size would diverge for a fewer number of blocks. Methods such as iterated implicit residual averaging mentioned in Section 3.7.2 could be used to recover the same convergence rates. However, these methods increase the coding complexity and computational overhead. Since relatively fine grids and few blocks were anticipated for this research, none of these advanced techniques were incorporated.

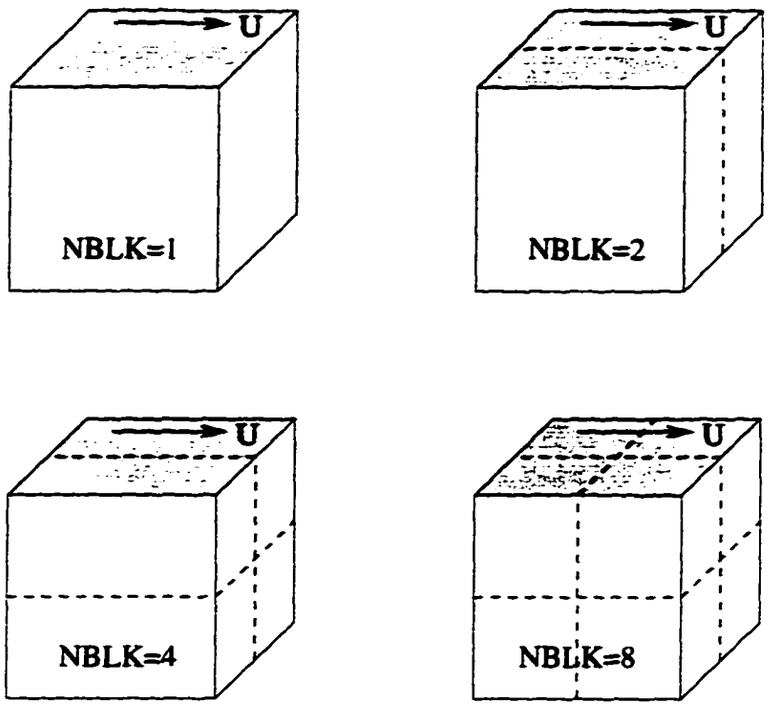

Figure 3.11 Blocking configurations for the 3-D lid driven cavity

The multiblock convergence for the LU-SGS scheme is shown in Fig. 3.13. A slight reduction in the convergence rates were observed with no multigrid. The LU-SGS scheme with multigrid was divergent for all multiblock configurations. The problems were most likely due to the treatment of the scheme and/or boundary conditions at the block interfaces. As will be demonstrated in Section 3.8.2. the deterioration is problem dependent. being nonexistent for the turbulent channel flow simulation.

Tables 3.1 and 3.2 show the speedups obtained for the RK and LU-SGS schemes. As long as the scheme remained stable, good parallel speedups were obtained. The RK scheme with four processors and three levels of multigrid required 20 times less computing time than a single processor. single grid case. Comparison of the results for the two schemes showed that the LU-SGS scheme with multiple processors yielded the smallest wall clock times. even without multigrid acceleration. This will be more pronounced for grids with more refinement and/or stretching. since the RK scheme will require lower CFL numbers and correspondingly more

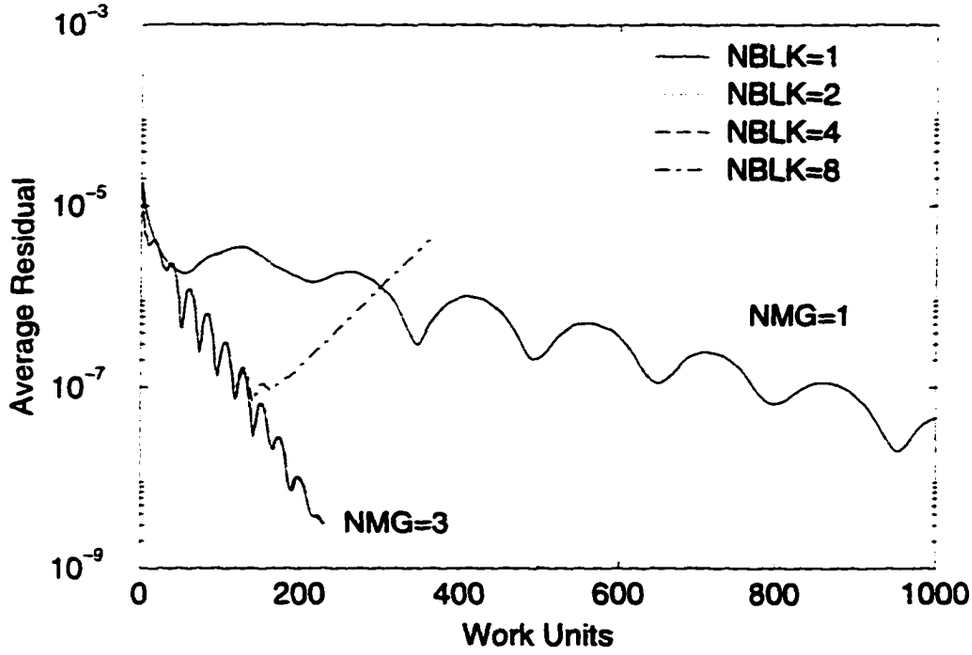

Figure 3.12 Convergence for laminar 3-D lid driven cavity for Runge-Kutta scheme

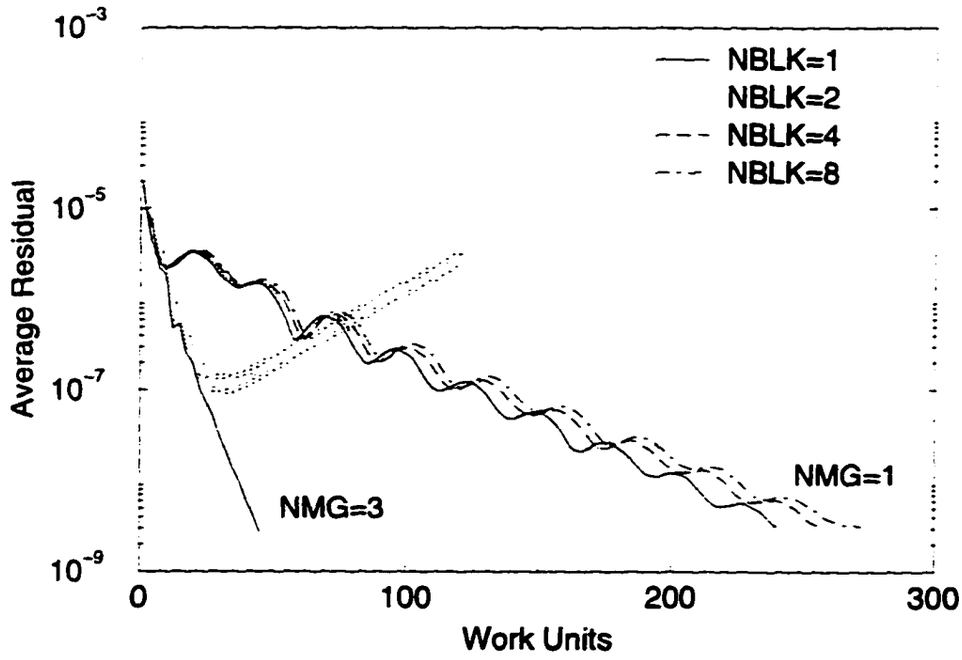

Figure 3.13 Convergence for laminar 3-D lid driven cavity for LU-SGS scheme

Table 3.1 Speedups for 3-D steady-state laminar lid driven cavity with RK scheme

Scheme	NMG	NBLK	Work Units	Wall Clock Time (min.)	Parallel Speedup	Parallel Efficiency	Overall Speedup
RK	1	1	1433.0	67.0	1.0	—	1.0
RK	1	2	1433.0	337.3	2.0	99.4	2.0
RK	1	4	1433.0	175.6	3.8	95.5	3.8
RK	1	8	1433.0	95.6	7.0	87.7	7.0
RK	3	1	227.3	122.3	1.0	—	5.5
RK	3	2	228.8	61.6	2.0	100.0	11.1
RK	3	4	229.8	33.4	3.7	91.5	20.1

Table 3.2 Speedups for 3-D steady-state laminar lid driven cavity with LU-SGS scheme

Scheme	NMG	NBLK	Work Units	Wall Clock Time (min.)	Speedup	Parallel Efficiency
LU-SGS	1	1	241.0	52.2	1.00	—
LU-SGS	1	2	249.0	25.2	2.00	100.0
LU-SGS	1	4	257.0	13.1	3.98	99.6
LU-SGS	1	8	273.0	7.3	7.20	89.4
LU-SGS	3	1	45.0	12.0	4.30	—

work units, while the LU-SGS scheme will continue to converge in about the same number of work units (based on the results in Chapter 4).

3.8.2 Turbulent Channel Flow

Performance estimates were also obtained for the flow of primary interest for this research — the time accurate simulation of a turbulent flow. The plane turbulent channel flow with smooth walls was computed for 50 physical time steps using up to 16 blocks and 16 processors. The simulations were started from a fully developed realization of the turbulent channel flow. All timings were obtained on the IBM SP-2 with IBM RS6000 processors. It should be emphasized that the computed parallel efficiencies are only estimates. Only a single run was used to compute efficiencies, and the wall clock time included initialization and output routines.

The results are summarized in Table 3.3 for the LU-SGS scheme and Table 3.4 for the RK

Table 3.3 Parallel/multigrid performance for plane channel flow simulation with LU-SGS scheme

NMG	NBLK	NPROC	Blocking	Work Units	Wall Clock Time (min.)	Speedup	Parallel Efficiency
1	1	1	$(32 \times 32 \times 24) \times 1$	303	43.9	1.0	-
1	4	4	$(32 \times 16 \times 12) \times 4$	303	11.7	3.8	93.8
1	8	8	$(16 \times 16 \times 12) \times 8$	303	6.3	7.0	87.3
1	16	16	$(8 \times 16 \times 12) \times 16$	303	3.7	11.8	73.9
3	1	1	$(32 \times 32 \times 24) \times 1$	357	63.3	1.0	-
3	4	4	$(32 \times 16 \times 12) \times 4$	357	17.5	3.6	90.3
3	8	8	$(16 \times 16 \times 12) \times 8$	357	9.7	6.6	81.9
3	16	16	$(8 \times 16 \times 12) \times 16$	357	6.1	10.3	64.3

Table 3.4 Parallel/multigrid performance for plane channel flow simulation with Runge-Kutta scheme

NMG	NBLK	NPROC	Blocking	Work Units	Wall Clock Time (min.)	Speedup	Parallel Efficiency
1	1	1	$(32 \times 32 \times 24) \times 1$	251	73.0	1.0	-
1	4	4	$(32 \times 16 \times 12) \times 4$	251	23.3	3.1	78.2
1	8	8	$(16 \times 16 \times 12) \times 8$	251	12.6	5.8	72.5
1	16	16	$(8 \times 16 \times 12) \times 16$	251	7.4	9.8	61.3
3	1	1	$(32 \times 32 \times 24) \times 1$	228	82.7	1.0	-
3	4	4	$(32 \times 16 \times 12) \times 4$	228	23.7	3.5	87.4
3	8	8	$(16 \times 16 \times 12) \times 8$	228	13.2	6.3	78.1
3	16	16	$(8 \times 16 \times 12) \times 16$	228	8.8	9.4	58.9

scheme. The speedups for both schemes are compared in Fig. 3.14. An important observation was that the LU-SGS scheme with multigrid acceleration remained convergent for even 16 blocks. This was unexpected, since as discussed previously, the LU-SGS scheme with multigrid diverged for the laminar lid driven cavity flow with only 8 blocks. This is believed to be due to the different boundary conditions for the two flows. The turbulent channel flow used periodic boundary conditions in both the x and z directions, whereas the lid driven cavity used solid boundaries in all three directions. In any event, the results demonstrate that the convergence properties of the multiblock LU-SGS scheme are problem dependent.

Slightly higher parallel efficiencies were obtained with the LU-SGS scheme compared to

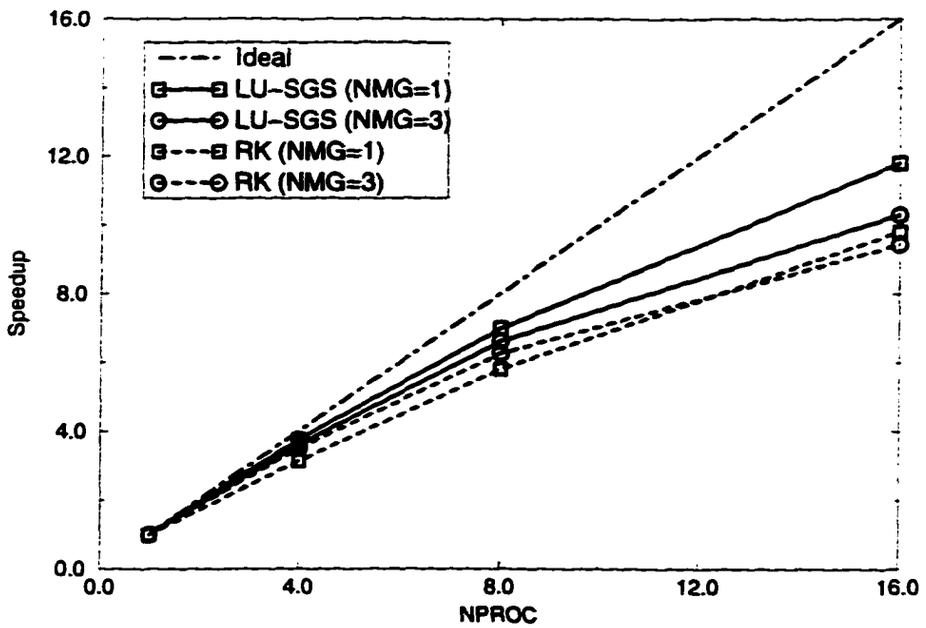

Figure 3.14 Parallel speedup for simulation of turbulent channel flow

the RK scheme. Both schemes have fairly low parallel efficiencies (less than 80 percent) for 16 processors, indicating that the code may not scale very well to higher numbers of processors. On the other hand, the parallel efficiency may be improved for longer simulations where the effects of initialization and post-processing would have less impact on the overall timings. No more than 16 processors were utilized for this research effort. so 73.9 parallel efficiency for the LU-SGS scheme was considered adequate. For larger scale problems, additional effort may be worthwhile to improve the parallel efficiency of the code.

Although it was encouraging that the LU-SGS scheme remained stable with parallel multigrid, it was discouraging to observe that multigrid acceleration for this case provided no benefit. In fact, the simulations with multigrid were more than 50 percent slower than the simulations without multigrid for 16 processors. One possible reason the multigrid was ineffective for this flow was that no artificial dissipation was used. Artificial dissipation provides high frequency damping required to drive multigrid. It cannot be used for the turbulent simulations because it will damp out the turbulent fluctuations. The poor performance of multigrid may also be

related to the size of the time steps and subiteration tolerance level. Multigrid may become effective for significantly larger time steps, lower tolerance levels, or finer grids.

Broeze et al. (1996) investigated the problem of insufficient high frequency damping for the time-accurate DNS of compressible turbulent flow. They applied a filtering operation to the corrections before they were applied to the fine grid. They claimed moderate success in maintaining performance with multigrid for DNS type calculations. Other possibilities are to implicitly average the corrections before applying them to the finest grid, or to apply artificial dissipation on the coarse grids only. The latter two approaches were attempted in the present work, but they did not provide the desired effect. The method of Broeze et al. was not attempted due to time limitations. Consequently, multigrid acceleration was not employed for any of the turbulent simulations for this work.

CHAPTER 4 EVALUATION OF MULTIGRID ACCELERATION FOR PRECONDITIONED TIME-ACCURATE NAVIER-STOKES ALGORITHMS

A paper published in *Computers & Fluids*[1], 1996, Vol. 25, pp. 791-811.

Lyle D. Dailey and Richard H. Pletcher[2]

Abstract

The development of a two-dimensional time accurate dual time step Navier-Stokes flow solver with time-derivative preconditioning and multigrid acceleration is described. The governing equations are integrated in time with both an explicit Runge-Kutta scheme and an implicit lower-upper symmetric-Gauss-Seidel scheme in a finite volume framework, yielding second order accuracy in space and time. Issues concerning the implementation of multigrid for preconditioned, dual time step algorithms are discussed. Steady and unsteady computations were made of lid driven cavity flow, thermally driven cavity flow, and pulsatile channel flow for a variety of conditions to validate the schemes and evaluate the effectiveness of multigrid for time accurate simulations. Significant speedups were observed for steady and unsteady simulations. The speedups for unsteady simulations were problem dependent, a function of how rapidly the flow varied in time and the size of the allowable time step.

[2]Department of Mechanical Engineering, Iowa State University, Ames, IA 50011, U.S.A.

4.1 Introduction

One of the most prohibitive aspects of unsteady Navier-Stokes simulations is the large amount of computer resources required, including both CPU time and memory. Researchers continue to seek methods to reduce these requirements to enable larger and more complex problems, such as direct and large eddy simulation of turbulence, to be tackled. This paper addresses the effectiveness of multigrid acceleration as a strategy for reducing the CPU time required for unsteady simulations, especially as it pertains to the preconditioned Navier-Stokes equations.

The paper describes the development of a Navier-Stokes solver for low speed time accurate flows that may contain heat transfer and flow separation. The compressible form of the equations are retained so that low speed flows with significant property variations can be handled. For instance, flows with heat transfer or chemical reactions could lead to significant variations in density, making the use of an incompressible formulation inappropriate. Time derivative preconditioning is incorporated to alleviate the stiffness and associated convergence problems that occur at low Mach numbers. The preconditioning is applied with a dual time step approach, where a "pseudo" time derivative is added to the governing equations.

Preconditioning has been used successfully by many investigators for solving steady viscous flows, including Choi and Merkle [1], Shuen, Chen, and Choi [2], Lee and van Leer [3], and Jorgenson and Pletcher [4], among others. Several investigators have also used preconditioning for time accurate flows. Shuen et al. [2] applied preconditioning to unsteady laminar combustion flows using a coupled implicit procedure. Pletcher and Chen [5] applied preconditioning in an unsteady finite difference code using generalized coordinates and an implicit procedure. Weiss and Smith [6] applied preconditioning for variable and constant density flows on unstructured meshes for time accurate flows using an explicit multistage scheme. Venkateswaran and Merkle [7] developed an improved preconditioning matrix for the unsteady Euler equations. Here, preconditioning is applied in a finite volume framework, and the equations are integrated in time with both an explicit Runge-Kutta (RK) scheme and implicit lower-upper symmetric-Gauss-Seidel (LU-SGS) scheme.

Multigrid has proven to be one of the most effective methods for accelerating the convergence of steady flow solvers. Several recent investigators have reported the use of multigrid for unsteady solvers, including Arnone et al. [8] and Wang and Yang [9]. However, very few investigators have reported the application of multigrid to preconditioned solvers, especially unsteady solvers. Thus, the purpose of this paper is (1) to describe the implementation of multigrid in an unsteady, preconditioned Runge-Kutta scheme and LU-SGS scheme, and (2) study the effectiveness of multigrid for accelerating time accurate simulations.

Item (2) is of particular importance because although Arnone et al. [8] and Wang and Yang [9] describe multigrid for unsteady flows, they did not discuss or exhibit the effectiveness of multigrid for providing speedups for various flow conditions and grid sizes. Moreover, the effectiveness of multigrid for preconditioned steady and, and more importantly, unsteady flows has not been adequately studied or discussed in the literature.

The paper begins by presenting the nondimensionalized, preconditioned governing equations. The explicit Runge-Kutta and implicit LU-SGS schemes for solving these equations are then described, including the multigrid methodology. The effectiveness of the schemes with and without multigrid for steady and unsteady flows is subsequently demonstrated for lid driven cavity flow, thermally driven cavity flow, and pulsatile channel flow.

4.2 Governing Equations

The solution variables are nondimensionalized as follows:

$$\begin{aligned} x &= \frac{x^*}{L_r} \qquad y = \frac{y^*}{L_r} \qquad p = \frac{p^*}{\rho_r V_r^2} \\ u &= \frac{u^*}{V_r} \qquad v = \frac{v^*}{V_r} \qquad T = \frac{T^*}{T_r} \\ \rho &= \frac{\rho^*}{\rho_r} \qquad t = \frac{t^*}{L_r/V_r} \qquad \mu = \frac{\mu^*}{\mu_r} \end{aligned} \tag{4.1}$$

where the dimensional variables are denoted with a superscript asterisk, and the dimensional reference values are denoted by a subscript r. All other variables are nondimensional. The variables x and y are the space dimensions, t, p, u, v, T, ρ, e, and μ are the time, pressure, x and y velocity components, temperature, density, internal energy, and molecular viscosity.

Nondimensionalization yields the parameters

$$M = \frac{V_r}{\sqrt{\gamma R^* T_r}} \quad ; \quad \mathrm{Re} = \frac{\rho_r V_r L_r}{\mu_r} \quad ; \quad \mathrm{Pr} = \frac{\mu^* c_p^*}{\kappa^*} \tag{4.2}$$

where M is the reference Mach number, Re is the Reynolds number, and Pr is the Prandtl number. In Eq. 4.2. R^* is the dimensional gas constant, c_p^* is the constant pressure specific heat, and κ^* is the thermal conductivity. The nondimensional gas constant and equation of state become

$$R = \frac{1}{\gamma M^2} \; ; \; p = \rho R T. \tag{4.3}$$

The nondimensional governing equations are written in conservation law integral form in terms of primitive variables (p, u, v and T) as follows:

$$\int_\Omega [T] \frac{\partial \mathbf{W}}{\partial t} \mathrm{d}\Omega + \int_{\partial\Omega} [(\mathbf{E} - \mathbf{E}_v)\vec{\imath} + (\mathbf{F} - \mathbf{F}_v)\vec{\jmath}] \cdot \mathrm{d}\vec{S} = \int_\Omega \mathbf{B} \mathrm{d}\Omega \tag{4.4}$$

where Ω is the control volume, $[T] = \partial \mathbf{U}/\partial \mathbf{W}$ is the time derivative Jacobian given in the Appendix. $\mathrm{d}\vec{S} = S\vec{n}$, and

$$\mathbf{W} = \begin{bmatrix} p \\ u \\ v \\ T \end{bmatrix}, \; \mathbf{U} = \begin{bmatrix} p/T \\ pu/T \\ pv/T \\ (p/T)[c_v T + \frac{1}{2}(u^2 + v^2)] \end{bmatrix}, \; \mathbf{B} = \begin{bmatrix} 0 \\ 0 \\ -[\mathrm{Ra}/(2\epsilon \mathrm{Pr} \mathrm{Re}^2)](p/T) \\ -[\mathrm{Ra}/(2\epsilon \mathrm{Pr} \mathrm{Re}^2)](pv/T) \end{bmatrix} \tag{4.5}$$

$$\mathbf{E} = \begin{bmatrix} pu/T \\ pu^2/T + Rp \\ puv/T \\ (pu/T)H \end{bmatrix} \; ; \; \mathbf{F} = \begin{bmatrix} pv/T \\ puv/T \\ pv^2/T + Rp \\ (pv/T)H \end{bmatrix} \tag{4.6}$$

$$\mathbf{E}_v = \begin{bmatrix} 0 \\ \tau_{xx} \\ \tau_{xy} \\ u\tau_{xx} + v\tau_{xy} - q_x \end{bmatrix} \; ; \; \mathbf{F}_v = \begin{bmatrix} 0 \\ \tau_{xy} \\ \tau_{yy} \\ u\tau_{xy} + v\tau_{yy} - q_y \end{bmatrix} \tag{4.7}$$

$$H = c_p T + \frac{1}{2}(u^2 + v^2) \tag{4.8}$$

where the stress and heat flux terms are

$$\tau_{xx} = \frac{2\mu R}{3\mathrm{Re}}\left(2\frac{\partial u}{\partial x} - \frac{\partial v}{\partial y}\right) \tag{4.9}$$

$$\tau_{yy} = \frac{2\mu R}{3\mathrm{Re}}\left(2\frac{\partial v}{\partial y} - \frac{\partial u}{\partial x}\right) \tag{4.10}$$

$$\tau_{xy} = \frac{\mu R}{\mathrm{Re}}\left(\frac{\partial u}{\partial y} + \frac{\partial v}{\partial x}\right) \tag{4.11}$$

$$q_x = -\frac{c_p \mu R}{\mathrm{Re\ Pr}}\frac{\partial T}{\partial x}\ ;\ q_y = -\frac{c_p \mu R}{\mathrm{Re\ Pr}}\frac{\partial T}{\partial y}. \tag{4.12}$$

Also, **B** contains the buoyancy source terms where **Ra** is the Rayleigh number and ϵ is the temperature difference parameter, both defined later in the paper.

4.2.1 Finite Volume Formulation

The governing equations are discretized in a finite volume framework to give second order accuracy in space. The computational domain is decomposed into arbitrary quadrilateral cells, with the solution variables (p, u, v and T) stored at the cell centers. Using the method of lines to separate the space and time discretizations, and approximating the integrals with the mean value theorem yields

$$[T]\frac{\mathrm{d}\mathbf{W}}{\mathrm{d}t}\Omega + \sum_{\beta=1}^{4}\left\{\left[(\mathbf{E}-\mathbf{E}_v)n_x + (\mathbf{F}-\mathbf{F}_v)n_y\right]S\right\}_\beta = \mathbf{B}\Omega. \tag{4.13}$$

where β identifies the four cell faces.

Time derivative preconditioning is applied by adding a pseudo time derivative to the left hand side as

$$[\Gamma]\frac{\mathrm{d}\mathbf{W}}{\mathrm{d}\tau}\Omega + [T]\frac{\mathrm{d}\mathbf{W}}{\mathrm{d}t}\Omega + \mathbf{C}(\mathbf{W}) = \mathbf{B}(\mathbf{W})\Omega \tag{4.14}$$

where

$$\mathbf{C}(\mathbf{W}) = \sum_{\beta=1}^{4}\left\{\left[(\mathbf{E}-\mathbf{E}_v)n_x + (\mathbf{F}-\mathbf{F}_v)n_y\right]S\right\}_\beta, \tag{4.15}$$

τ is the pseudo time, and $[\Gamma]$ is the preconditioning matrix. The preconditioning matrix used here (shown in the Appendix) was developed by Pletcher and Chen [5]. For low Mach numbers, the eigenvalues of the system without preconditioning differ greatly in magnitude, leading to convergence problems. Preconditioning the governing equations is an attempt to

reduce the difference in the magnitude of the eigenvalues, and leads to convergence rates nearly independent of Mach number. The addition of the "pseudo" time step is termed the dual time step approach, and involves iterating in pseudo time for each step in physical time.

4.2.2 Artificial Dissipation

Since central differences were utilized for the spatial terms, artificial dissipation was added in order to suppress odd-even decoupling and maintain stability near stagnation points. The artificial dissipation is a blend of adaptive second and fourth order differences with eigenvalue scaling for viscous shear layers [10,11].

The fully conservative dissipation operator, $\mathbf{D}(\mathbf{W}^m)$, is

$$\mathbf{D}(\mathbf{W}^m) = \mathbf{d}_{i+1/2,j} - \mathbf{d}_{i-1/2,j} + \mathbf{d}_{i,j+1/2} - \mathbf{d}_{i,j-1/2} \tag{4.16}$$

where the dissipation flux for face $(i+1/2, j)$ is

$$\mathbf{d}_{i+1/2,j} = [\Gamma]_{i+1/2,j}\Lambda_{i+1/2,j}\left[\epsilon^{(2)}_{i+1/2,j}(\mathbf{W}_{i+1,j} - \mathbf{W}_{i,j})\right.$$

$$\left. - \epsilon^{(4)}_{i+1/2,j}(\mathbf{W}_{i+2,j} - 3\mathbf{W}_{i+1,j} + 3\mathbf{W}_{i,j} - \mathbf{W}_{i-1,j})\right]. \tag{4.17}$$

The preconditioning matrix, $[\Gamma]_{i+1/2,j}$, was included in the dissipation flux to ensure that the global summation of fluxes for the steady-state nonpreconditioned residual, $\mathbf{C} - \mathbf{D}$, is fully conservative.

The variable scaling factors based on the maximum eigenvalues of the discretized equations are

$$\Lambda_{i+1/2,j} = \frac{1}{2}[(\bar{\lambda}_\xi)_{i,j} + (\bar{\lambda}_\xi)_{i+1,j}] \tag{4.18}$$

$$\Lambda_{i,j+1/2} = \frac{1}{2}[(\bar{\lambda}_\eta)_{i,j} + (\bar{\lambda}_\eta)_{i,j+1}] \tag{4.19}$$

where ξ refers to the i direction and η refers to the j direction, and

$$\bar{\lambda}_\xi = \lambda_\xi \Phi_\xi \;\; ; \;\; \bar{\lambda}_\eta = \lambda_\eta \Phi_\eta \tag{4.20}$$

and

$$\Phi_\xi = 1 + \left(\frac{\lambda_\eta}{\lambda_\xi}\right)^\sigma \;\; : \Phi_\eta = 1 + \left(\frac{\lambda_\xi}{\lambda_\eta}\right)^\sigma . \tag{4.21}$$

For the system without preconditioning, the maximum eigenvalue is

$$\lambda = U + cS \tag{4.22}$$

and for the preconditioned system, the maximum eigenvalue is

$$\lambda = \frac{1}{2R}\left[(R+1)U + \sqrt{(R-1)^2U^2 + 4\gamma R^2 TS^2}\right] \tag{4.23}$$

where $U = \left|\vec{V}\cdot d\vec{S}\right|$ and $S = \left|d\vec{S}\right|$. The preconditioning matrix is computed as

$$[\Gamma]_{i+1/2,j} = \frac{1}{2}\left\{[\Gamma]_{i,j} + [\Gamma]_{i+1,j}\right\} \tag{4.24}$$

and the dissipation coefficients and pressure sensor are

$$\epsilon^{(2)}_{i+1/2,j} = \kappa^{(2)}\max(\nu_{i,j}, \nu_{i+1,j}) \tag{4.25}$$

$$\epsilon^{(4)}_{i+1/2,j} = \max[0, (\kappa^{(4)} - \epsilon^{(2)}_{i+1/2,j})] \tag{4.26}$$

$$\nu_{i,j} = \frac{|p_{i+1,j} - 2p_{i,j} + p_{i-1,j}|}{p_{i+1,j} + 2p_{i,j} + p_{i-1,j}}. \tag{4.27}$$

Typically $\sigma = 1/2$, $\kappa^{(2)} = 1/2$ and $\kappa^{(4)} = 1/64$.

With the addition of the dissipation operator, Eq. 4.14 becomes

$$[\Gamma]\frac{d\mathbf{W}}{d\tau}\Omega + [T]\frac{d\mathbf{W}}{dt}\Omega + \mathbf{C}(\mathbf{W}) - \mathbf{D}(\mathbf{W}) = \mathbf{B}(\mathbf{W})\Omega. \tag{4.28}$$

4.3 Explicit Runge-Kutta Scheme

Jameson [12], Arnone et al. [8], and Melson et al. [13] have used the Runge-Kutta (RK) scheme to march in pseudo time to solve the unsteady 2D Navier-Stokes equations without preconditioning using a dual time step approach. In a similar fashion, the RK scheme was used here to march in pseudo time for a preconditioned system.

The physical time derivative in Eq. 4.28 was discretized with a three point backward difference as

$$[\Gamma]\frac{d\mathbf{W}}{d\tau}\Omega + [T]\frac{\Omega}{2\Delta t}(3\mathbf{W}^{n+1} - 4\mathbf{W}^{n} + \mathbf{W}^{n-1}) + \mathbf{C}(\mathbf{W}^{n+1}) - \mathbf{D}(\mathbf{W}^{n+1}) = \mathbf{B}(\mathbf{W})\Omega. \tag{4.29}$$

which gives an implicit scheme which is second order accurate in physical time. Eq. 4.29 can be rewritten as

$$\Omega \frac{d\mathbf{W}}{d\tau} = -[\Gamma]^{-1}\mathbf{R}^{n+1} \tag{4.30}$$

where the residual, $\mathbf{R}^k$, is

$$\mathbf{R}^k = \mathbf{T}(\mathbf{W}^k) + \mathbf{C}(\mathbf{W}^k) - \mathbf{D}(\mathbf{W}^k) - \mathbf{B}(\mathbf{W})\Omega \tag{4.31}$$

and $\mathbf{T}$ is the physical time derivative term

$$\mathbf{T}(\mathbf{W}^k) = [T]^k \frac{\Omega}{2\Delta t}(3\mathbf{W}^k - 4\mathbf{W}^n + \mathbf{W}^{n-1}). \tag{4.32}$$

Equation 4.30 was solved using a five stage Runge-Kutta scheme. The five stage scheme was selected due do its large stability bound for viscous flows [14] and good damping properties to drive multigrid acceleration.

The RK scheme was used to march in pseudo time, with counter m, until the average u residual, R_2^{avg}, was less than some tolerance,

$$R_2^{avg} = \frac{\sum_{i,j} |R_2|}{N_{\text{cells}}} < TOL. \tag{4.33}$$

where R_2 is the second component of the residual vector, $\mathbf{R}$, corresponding to the $x-$component of the momentum equation, and N_{cells} is the total number of interior grid cells. Throughout the iteration in m, the values of $\mathbf{W}^n$ and $\mathbf{W}^{n-1}$ are frozen in the evaluation of $\mathbf{T}(\mathbf{W}^m)$. As the iteration in m converges, then $m \rightarrow n+1$, and the implicit equation given by the residual, Eq. 4.31, is satisfied, independent of the pseudo time and the preconditioning matrix.

To reduce the computational effort, the artificial dissipation operator was only evaluated on the first two stages of the RK scheme. Local time stepping, variable coefficient implicit residual smoothing, and multigrid acceleration were used to accelerate the convergence in pseudo time at each physical time step.

4.3.1 Multigrid Acceleration

Multigrid was implemented with the Full Approximation Storage (FAS) scheme, as discussed in [8] or [10], for example. Turkel [15] suggested that when using multigrid for preconditioned systems, it was better to transfer the residuals based on the preconditioned system

to the next grid since these residuals are more balanced than the physical residuals. Early tests where the residuals were transferred both ways did not confirm this suggestion, and for steady computations using the preconditioned residuals longer CPU times resulted. However, for the unsteady dual time step formulation, using the preconditioned residual, where the equations have been multiplied through by $[\Gamma]^{-1}$, resulted in reduced CPU times. Therefore, the preconditioned residuals were used throughout the work presented here.

Successively coarser grids were obtained by removing every other grid line in both directions. The solution was updated on the fine grid for a specified number of iterations. The solution was then restricted from the fine grid (level L-1) to the next coarsest grid (level L) by an area weighted average as

$$\mathbf{W}_0^{(L)} = \frac{1}{\Omega^{(L)}} \sum_{icv=1}^{4} \left[\Omega^{(L-1)}\mathbf{W}^{(L-1)}\right]_{icv} \tag{4.34}$$

where the sum is over the four fine grid control volumes comprising the coarse grid control volume.

A forcing function was defined for the coarse grid as

$$\mathbf{P}^{(L)} = \sum_{icv=1}^{4} \left[[\Gamma]^{-1}\mathbf{R}^{(L-1)}\right]_{icv} - [\Gamma]^{-1}\mathbf{R}^{(L)} \tag{4.35}$$

where the residual was given by Eq. 4.31 and the coarse grid residual was based on $\mathbf{W}_0^{(L)}$.

The forcing function was added to the right hand side (RHS) of Eq. 4.30 as follows:

$$RHS = -([\Gamma]^{-1}\mathbf{R})^{(L)} + \mathbf{P}^{(L)} \tag{4.36}$$

where $P^{(L)}$ was frozen for a given grid level throughout a multigrid cycle. The solution was updated for a specified number of iterations on the coarse grid level L. Recall that $\mathbf{W}^n$ and $\mathbf{W}^{n-1}$ do not change throughout the iteration in m. Values of $\mathbf{W}^n$ and $\mathbf{W}^{n-1}$ were found on the coarse grid levels by restriction using Eq. 4.34. The same physical time step, Δt, was used on all grid levels.

On the next coarsest grid (level $L+1$) the collection of the residuals from level L for the forcing function for level $L+1$ included the forcing function from level L as

$$\mathbf{P}^{(L+1)} = \sum_{icv=1}^{4} \left[[\Gamma]^{-1}\mathbf{R}^{(L)} + \mathbf{P}^{(L)}\right]_{icv} - [\Gamma]^{-1}\mathbf{R}^{(L+1)}. \tag{4.37}$$

This process was repeated until the coarsest grid ($L = NMG$) was reached. After updating the solution on the coarsest grid (level L) for a specified number of iterations, the corrections were prolongated to the next finer grid ($L-1$) as follows:

$$\mathbf{W}^{(L-1)} = \tilde{\mathbf{W}}^{(L-1)} + I_{(L)}^{(L-1)}(\tilde{\mathbf{W}}^{(L)} - \mathbf{W}_0^{(L)}) \tag{4.38}$$

where $\tilde{\mathbf{W}}^{(L-1)}$ is the solution on grid $L-1$ before the restriction to grid L, $\mathbf{W}_0^{(L)}$ is the solution restricted to grid L before any iterations were performed on grid L, and $I_{(L)}^{(L-1)}$ is a bilinear interpolation operator.

The boundary conditions on the coarse grids were enforced in the same way as for the fine grid. A typical multigrid cycle consisted of performing two iterations of the scheme on each grid level on the way up and down a V cycle. Local time stepping and residual averaging were applied on all grid levels.

4.4 Implicit LU-SGS Scheme

The lower-upper symmetric Gauss-Seidel (LU-SGS) scheme was originally developed by Yoon and Jameson [16] for the Euler and Navier-Stokes equations without preconditioning. Rieger and Jameson [17] extended the LU-SGS scheme to three dimensions to solve the steady compressible Navier-Stokes equations in a finite volume framework. Grasso and Marini [18] applied the LU-SGS method in a finite volume discretization to the solution of two-dimensional high speed flow using an upwind biased TVD spatial discretization. Chen and Shuen [19] applied the LU-SGS scheme to the preconditioned Navier-Stokes equations, but for a finite difference discretization. The methodology incorporated here combines aspects of these solvers to develop the LU-SGS scheme for the preconditioned unsteady compressible Navier-Stokes equations in a finite volume framework.

Beginning with Eq. 4.28, the pseudo time derivative was discretized with an Euler backward difference, and the physical time derivative was discretized with a three point backward difference, yielding

$$[\Gamma]^m \Omega \frac{\Delta \mathbf{W}}{\Delta \tau} + \mathbf{T}(\mathbf{W}^{n+1}) + \mathbf{C}(\mathbf{W}^{n+1}) - \mathbf{D}(\mathbf{W}^{n+1}) = \mathbf{B}(\mathbf{W}^{n+1})\Omega. \tag{4.39}$$

where $\Delta\mathbf{W} = \mathbf{W}^{m+1} - \mathbf{W}^m$ and $\Delta\tau = \tau^{m+1} - \tau^m$. The inviscid flux vectors were linearized about pseudo time level m as

$$\mathbf{E}^{m+1} \approx \mathbf{E}^m + [A]^m \Delta\mathbf{W} \; ; \; \mathbf{F}^{m+1} \approx \mathbf{F}^m + [B]^m \Delta\mathbf{W} \tag{4.40}$$

where the flux Jacobians ($[A] = \partial\mathbf{E}/\partial\mathbf{W}$ and $[B] = \partial\mathbf{F}/\partial\mathbf{W}$) are given in the Appendix. As $\Delta\tau \to \infty$ then $m+1 \to n+1$, such that $n+1$ was replaced by $m+1$ in Eq. 4.39. Substitution of the linearized fluxes into Eq. 4.39, multiplying by $[\Gamma]^{-1}$, and including the viscous terms only on the right hand side yields

$$\left\{ \frac{\Omega}{\Delta\tau}[I] + [\Gamma]^{-1}[T]\frac{3}{2}\frac{\Omega}{\Delta t} + [\Gamma]^{-1} \sum_{\beta=1}^{4} [([A]n_x + [B]n_y)\, S]_\beta \right\}^m \Delta\mathbf{W} = -([\Gamma]^{-1}\mathbf{R})^m. \tag{4.41}$$

The $(i+1/2, j)$ and $(i-1/2, j)$ faces are labeled as $\beta = 1$ and 3, and the $(i, j+1/2)$ and $(i, j-1/2)$ faces are labeled as $\beta = 2$ and 4. Inviscid flux Jacobians in directions normal to faces 1 and 3 are denoted as $[\hat{A}]$, and Jacobians in directions normal to faces 2 and 4 are denoted as $[\hat{B}]$, where

$$\begin{aligned} [\hat{A}] &= ([A]n_x + [B]n_y)_{\beta=1,3} \\ [\hat{B}] &= ([A]n_x + [B]n_y)_{\beta=2,4}. \end{aligned} \tag{4.42}$$

Using Eq. 4.42 and letting $\Delta\tau \to \infty$, Eq. 4.41 becomes

$$\left\{ [\Gamma]^{-1}[T]\frac{3}{2}\frac{\Omega}{\Delta t} + [\Gamma]^{-1}\left[[\hat{A}]_1 S_1 + [\hat{A}]_3 S_3 + [\hat{B}]_2 S_2 + [\hat{B}]_4 S_4 \right] \right\} \Delta\mathbf{W} = -[\Gamma]^{-1}\mathbf{R}. \tag{4.43}$$

To apply the LU-SGS algorithm to the preconditioned system of equations, the flux Jacobians are modified [19] to accommodate the preconditioning matrix as

$$[\hat{A}] = [\Gamma][\Gamma]^{-1}[\hat{A}] = [\Gamma][\tilde{A}] \; ; \; [\tilde{A}] = [\Gamma]^{-1}[\hat{A}]. \tag{4.44}$$

The flux Jacobian, $[\tilde{A}]$, is split as

$$[\tilde{A}] = [\tilde{A}]^+ + [\tilde{A}]^- \tag{4.45}$$

where

$$[\tilde{A}]^\pm = \frac{1}{2}\omega([\tilde{A}] \pm \gamma_A[I]). \tag{4.46}$$

$\gamma_A = r_A \max\left|\lambda_{[\tilde{A}]}\right|$. $\lambda_{[\tilde{A}]}$ is the maximum eigenvalue of $[\tilde{A}]S$. and ω and r_A are relaxation factors of $O(\geq 1)$. This splitting of the flux Jacobians is made to ensure diagonal dominance. Multiplying Eq. 4.46 by $[\Gamma]$ yields

$$[\Gamma][\tilde{A}]^{\pm} = \frac{1}{2}\omega([\Gamma][\tilde{A}] \pm \gamma_A[\Gamma]) = \frac{1}{2}\omega([\tilde{A}] \pm \gamma_A[\Gamma]). \tag{4.47}$$

The fluxes at the control volume faces are

$$\begin{aligned}([\Gamma][\tilde{A}]\Delta\mathbf{W})_1 &= ([\Gamma][\tilde{A}]^{+}\Delta\mathbf{W})_{i,j} + ([\Gamma][\tilde{A}]^{-}\Delta\mathbf{W})_{i+1,j} \\ ([\Gamma][\tilde{A}]\Delta\mathbf{W})_3 &= ([\Gamma][\tilde{A}]^{+}\Delta\mathbf{W})_{i-1,j} + ([\Gamma][\tilde{A}]^{-}\Delta\mathbf{W})_{i,j}.\end{aligned} \tag{4.48}$$

Equation 4.43 can be written as

$$[M]\Delta\mathbf{W} = ([L] + [D] + [U])\Delta\mathbf{W} = -[\Gamma]^{-1}\mathbf{R} \tag{4.49}$$

where $[L]$ contains the portions of $[M]$ below the block diagonal of $[M]$, $[D]$ is the block diagonal of $[M]$. and $[U]$ is the upper part of $[M]$. Specifically, $[L]$, $[D]$ and $[U]$ are

$$[L] = -[\Gamma]^{-1}\left[([\Gamma][\tilde{A}]^{+})_{i-1,j}S_3 + ([\Gamma][\tilde{B}]^{+})_{i,j-1}S_4\right] \tag{4.50}$$

$$[D] = [\Gamma]^{-1}[T]\frac{3}{2}\frac{\Omega}{\Delta t} + [\Gamma]^{-1}_{i,j}\left[([\Gamma][\tilde{A}]^{+})_{i,j}S_1 - ([\Gamma][\tilde{A}]^{-})_{i,j}S_3 + ([\Gamma][\tilde{B}]^{+})_{i,j}S_2 - ([\Gamma][\tilde{B}]^{-})_{i,j}S_4\right] \tag{4.51}$$

$$[U] = [\Gamma]^{-1}\left[([\Gamma][\tilde{A}]^{-})_{i+1,j}S_1 + ([\Gamma][\tilde{B}]^{-})_{i,j+1}S_2\right]. \tag{4.52}$$

Due to the splitting of the flux Jacobians,

$$[\Gamma][\tilde{A}]^{+} - [\Gamma][\tilde{A}]^{-} = \omega\gamma_A[\Gamma]\ ;\ [\Gamma][\tilde{B}]^{+} - [\Gamma][\tilde{B}]^{-} = \omega\gamma_B[\Gamma], \tag{4.53}$$

and if it is assumed that $S_1 \approx S_3$ and $S_2 \approx S_4$ then Eq. 4.51 reduces to

$$[D] = \frac{3}{2}\frac{\Omega}{\Delta t}[\Gamma]^{-1}[T] + \omega\left(\gamma_A S_{13} + \gamma_B S_{24}\right)[I] \tag{4.54}$$

where

$$S_{13} = \frac{1}{2}(S_1 + S_3)\ :\ S_{24} = \frac{1}{2}(S_2 + S_4). \tag{4.55}$$

Due to the nature of the preconditioning matrix employed in this paper. the product $[\Gamma]^{-1}[T]$ is a diagonal matrix: hence. the matrix $[D]$ given by Eq. 4.54 is also diagonal. This is not

generally true for other preconditioners, such as those of Choi and Merkle [1] or Lee and van Leer [3].

To efficiently solve Eq. 4.49, it is approximately factored as

$$([L]+[D])[D]^{-1}([D]+[U])\Delta\mathbf{W} = -[\Gamma]^{-1}\mathbf{R}. \tag{4.56}$$

Eq. 4.56 is solved in three steps as follows:

Step 1:
$$([L]+[D])\Delta\mathbf{W}^* = -[\Gamma]^{-1}\mathbf{R}$$
$$\Delta\mathbf{W}^* = [D]^{-1}(-[\Gamma]^{-1}\mathbf{R} - [L]\Delta\mathbf{W}^*)$$

Step 2:
$$([D]+[U])\Delta\mathbf{W} = [D]\Delta\mathbf{W}^*$$
$$\Delta\mathbf{W} = \Delta\mathbf{W}^* - [D]^{-1}[U]\Delta\mathbf{W}$$

Step 3:
$$\mathbf{W}^{m+1} = \mathbf{W}^m + \Delta\mathbf{W}$$

Since $[D]$ is diagonal, as mentioned above, the inversion process requires a trivial amount of work compared to other implicit schemes.

In Step 1 the solution at the $(i-1, j-1)$ control volumes are known, so the solution is swept on $i + j = constant$ lines from the lower left to the upper right corner of the grid. Similarly, for Step 2 the solution at the $(i+1, j+1)$ control volumes are known, so the solution is swept from the upper right to the lower left corner of the grid. Boundary conditions are handled by setting $\Delta\mathbf{W} = 0$ at ghost cells and explicitly setting $\mathbf{W}$ at the beginning of each iteration.

4.5 Results

The flow solver was evaluated by computing a shear driven flow, the lid driven cavity; a pressure driven flow, the pulsatile channel; and a buoyancy driven flow, the thermally driven cavity, as described in the following sections.

4.5.1 Steady State Lid Driven Cavity

Steady state calculations were made to verify that the preconditioning and multigrid acceleration were working properly. The impulsively started lid driven square cavity was computed for Re = 100 and 400, where Re is based on the cavity height and lid velocity. The flow was started from stagnant conditions, and the lid velocity was instantaneously set in motion to give $M = 0.001$.

Steady solutions were computed on successively refined grids with 32×32, 48×48, and 64×64 grid cells. The grids were clustered near all four walls of the cavity. The u-velocity component along the vertical centerline is shown in Fig. 4.1, and the v-velocity component along the horizontal centerline is shown in Fig. 4.2. The solution of Ghia et al. [20], which is considered a standard benchmark solution, used a very fine 129×129 point grid, and is also shown for comparison. Based on this grid refinement study, the 48×48 grid was used for all later computations for Re = 100, and the 64×64 grid was used for all Re = 400 cases.

The benefits of preconditioning are demonstrated in Figs. 4.3 and 4.4, which show convergence histories for the RK and LU-SGS schemes for Re = 100 with and without preconditioning for various Mach numbers. The convergence of both schemes without preconditioning was severely degraded as the Mach number was decreased below $M = 0.2$, whereas the convergence for the preconditioned schemes was independent of Mach number.

For higher Mach numbers, the RK scheme without preconditioning was slightly more efficient than the scheme with preconditioning. However, the preconditioned LU-SGS scheme was almost three times faster than the LU-SGS scheme without preconditioning. This was an unexpected result, and is probably due to the conditioning of the system eigenvalues leading to enhanced diagonal dominance and, hence, improved convergence. Consequently, the LU-SGS scheme was much more efficient than the RK scheme in terms of CPU times.

The effectiveness of multigrid is demonstrated in Figs. 4.5 and 4.6 for the RK and LU-SGS schemes, respectively. The LU-SGS convergence with multigrid was nearly grid independent in terms of work units, indicating the success of multigrid. All computations in this paper were made on a DEC AXP 3000 600S workstation with a 175 MHz clock speed and 192 Mb

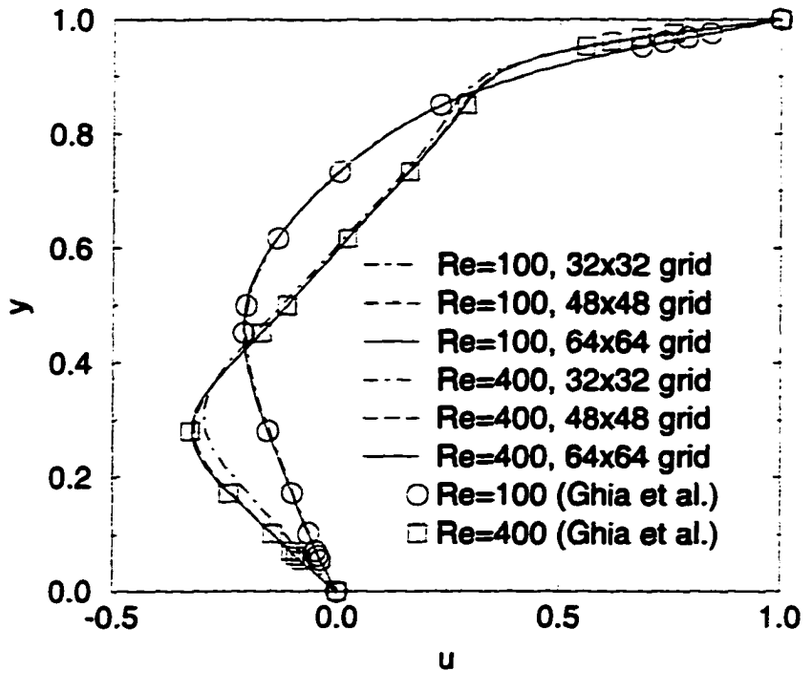

Figure 4.1 u-velocity component along vertical centerline for steady lid driven cavity with LU-SGS scheme

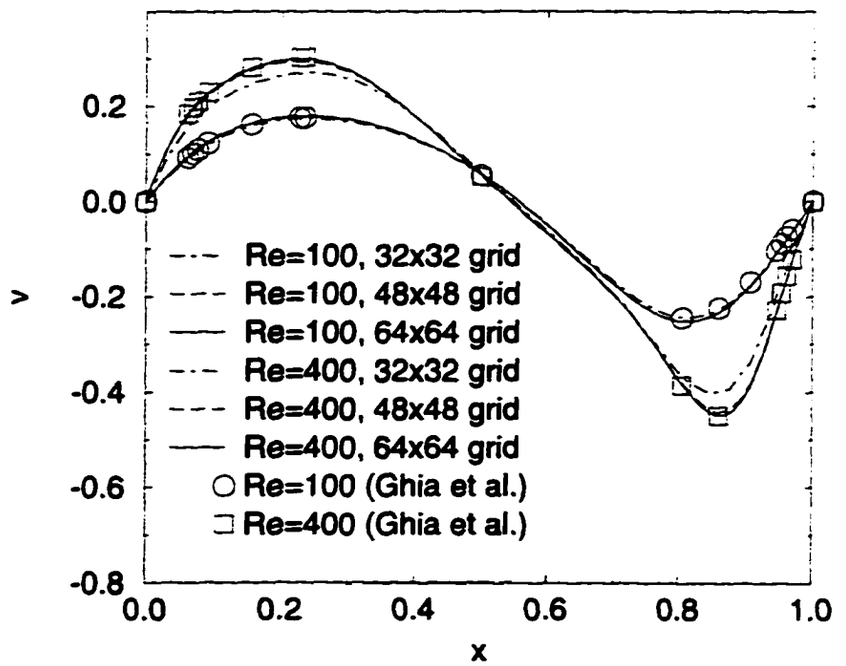

Figure 4.2 v-velocity component along horizontal centerline for steady lid driven cavity with LU-SGS scheme

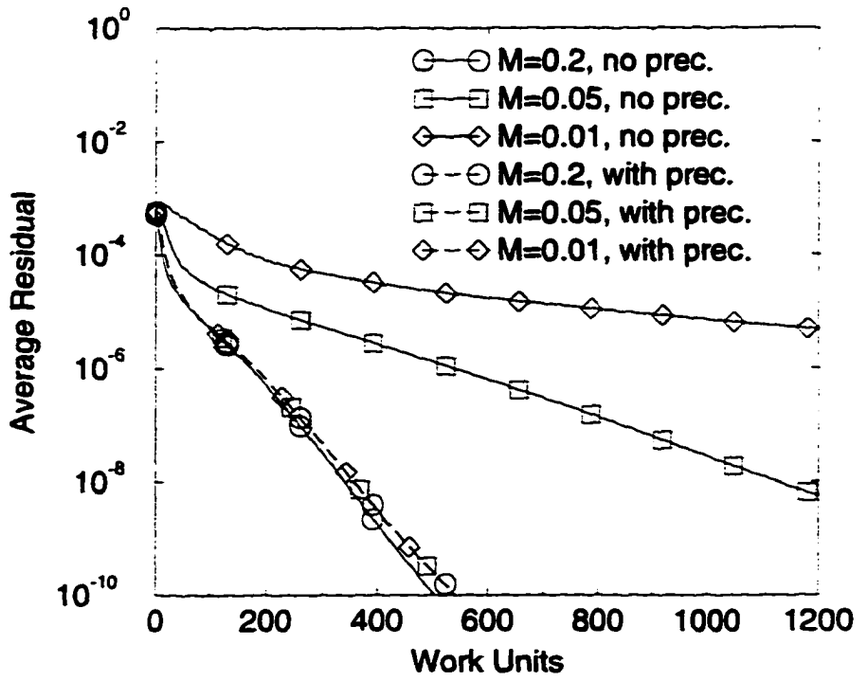

Figure 4.3 Effectiveness of preconditioning for steady lid driven cavity with RK scheme (Re = 100)

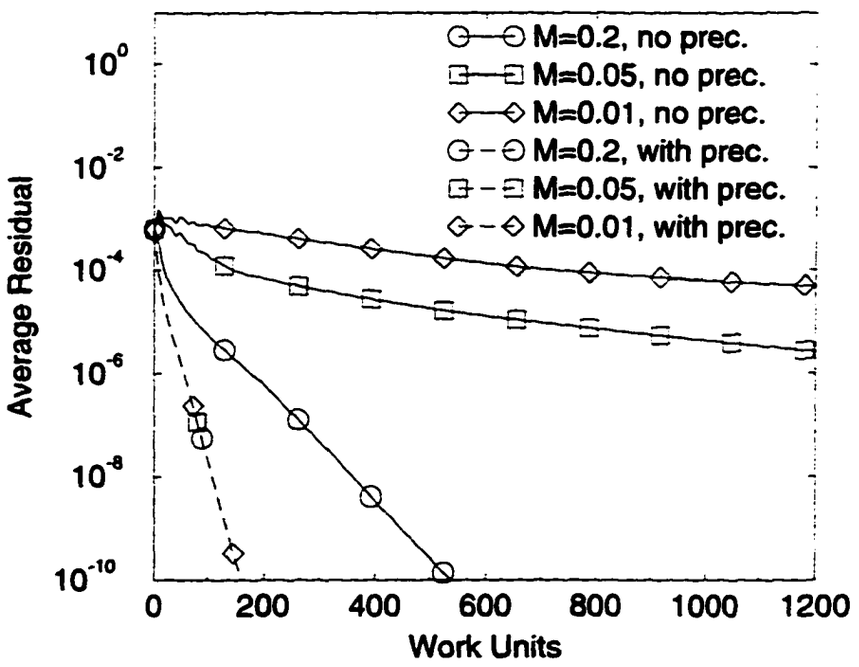

Figure 4.4 Effectiveness of preconditioning for steady lid driven cavity with LU-SGS scheme (Re = 100)

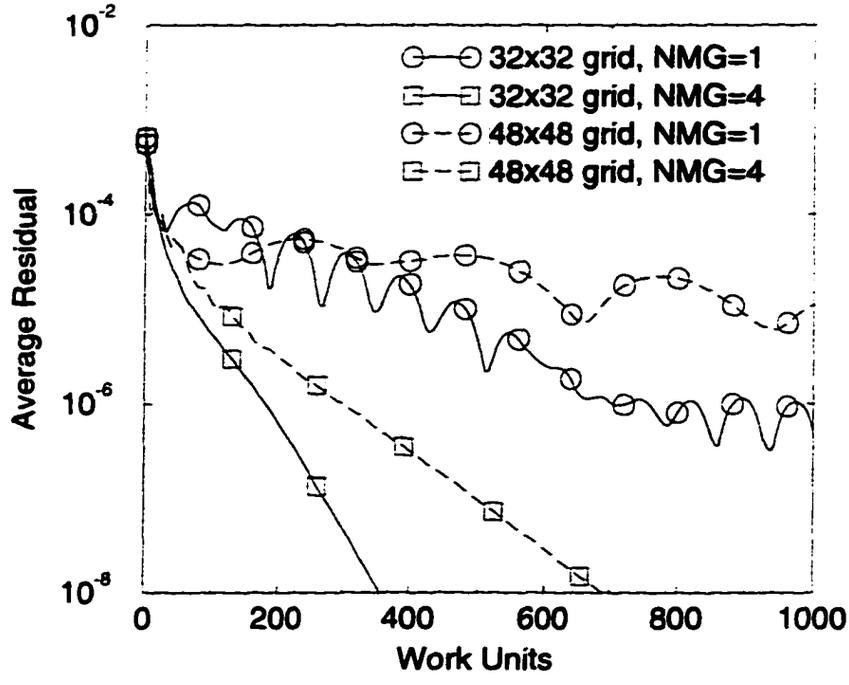

Figure 4.5 Effectiveness of multigrid for steady lid driven cavity with RK scheme (Re = 100)

of memory. With multigrid, the CPU time per work unit per grid cell was about 3.87×10^{-4} seconds for the RK scheme and 1.93×10^{-4} seconds for the LU-SGS scheme.

4.5.2 Unsteady Lid Driven Cavity

The steady state computations demonstrated significant speedups for the multigrid formulation of the preconditioned LU-SGS and RK schemes. The time accurate solution for the impulsively started lid driven cavity was computed to determine the ability of multigrid to provide speedups for unsteady simulations.

Grid refinement studies for the unsteady flow yielded the same conclusions as for the steady flow; the 48×48 grid was required for Re = 100 and the 64×64 grid was required for Re = 400.

The physical time step, Δt, was refined as shown in Fig. 4.7, showing excellent agreement with the results of Pletcher and Chen [5]. A time step of $\Delta t \leq 0.025$ and $TOL \leq 1 \times 10^{-7}$ was required for accurate solutions, which resulted in 2–4 orders of magnitude drop in the residual. This time step and tolerance gave accurate results for Re = 400 as well, as shown in Fig. 4.8.

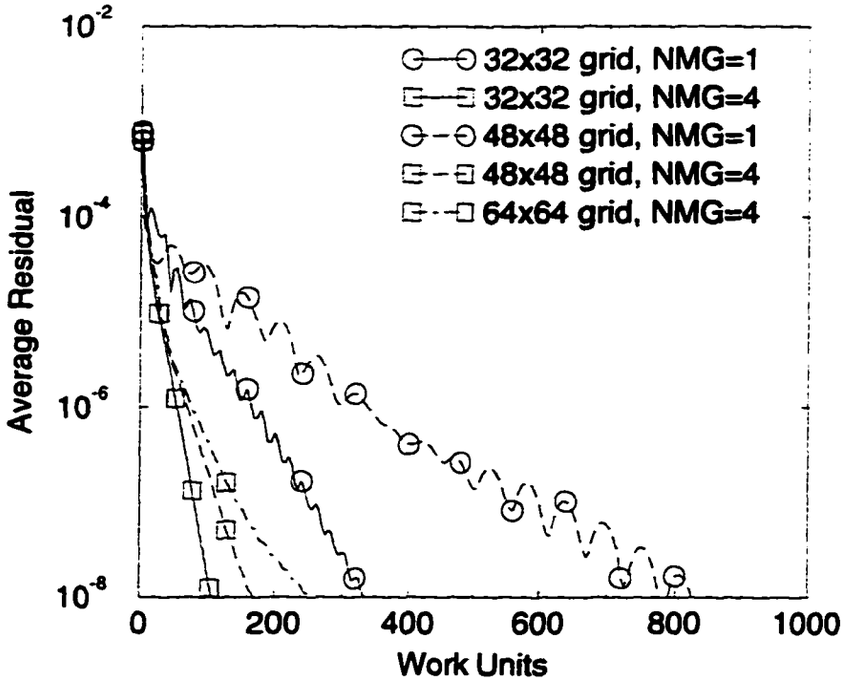

Figure 4.6 Effectiveness of multigrid for steady lid driven cavity with LU-SGS scheme (Re = 100)

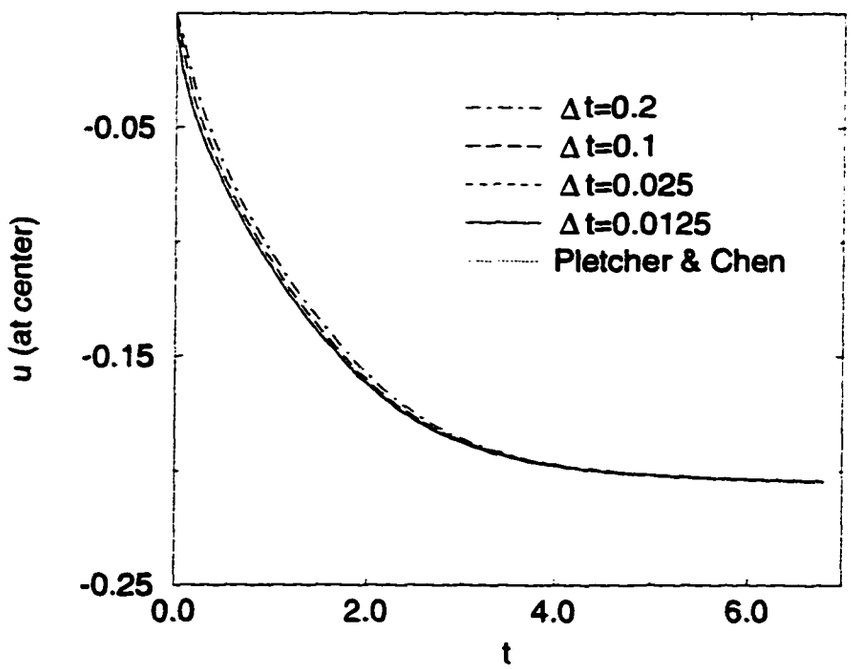

Figure 4.7 Time step refinement for unsteady lid driven cavity with LU-SGS scheme (Re = 100)

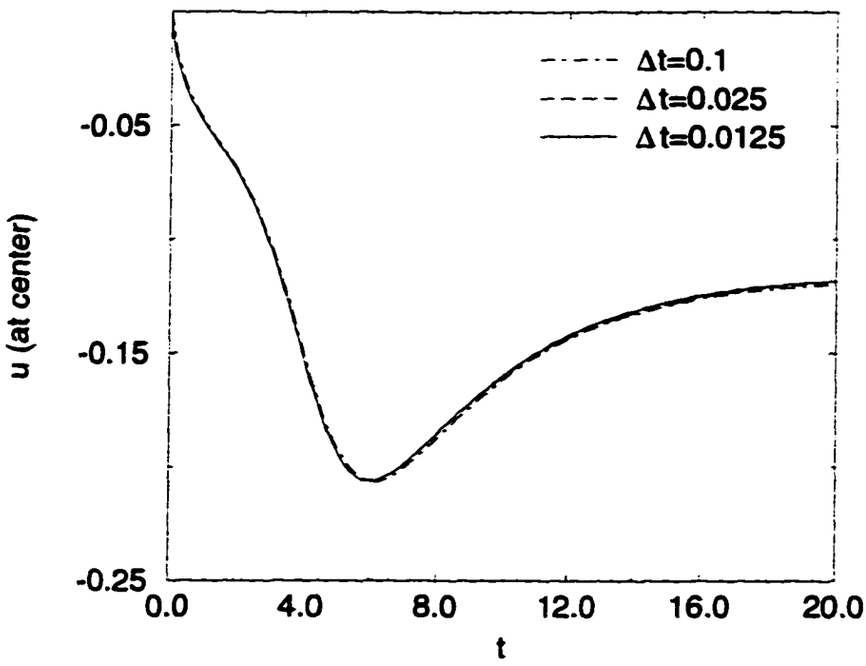

Figure 4.8 Time step refinement for unsteady lid driven cavity with LU-SGS scheme (Re = 400)

The resulting CPU times and work units to reach $t = 6.8$ and $t = 20.0$ for Re = 100 and Re = 400. respectively, are shown in Tables 4.1.4.2. and 4.3. For both the RK and LU-SGS schemes. overall speedups of 2.2–2.7 were obtained for Re = 100, while overall speedups of 1.3–1.7 were obtained for Re = 400. Although these speedups may seem meager for multigrid, they should not be unexpected due to the asymptotic nature of the lid driven cavity flow. During the initial steps in physical time the solution was changing rapidly and multigrid was very effective in reducing the amount of work per time step, yielding speedups of 4–5 as shown in Fig. 4.9. During later time steps the changes in the solution were diminishing, and the speedups for each step in physical time decreased to about 1.5–2. Consequently, the overall speedup was less for Re = 400 compared to Re = 100, because a higher percentage of the time steps had small speedups.

The results also revealed that multigrid was more effective for larger physical time steps. Thus. the speedup for unsteady flows depends on how much the flow varies in time and the size of the time step that will maintain accurate solutions.

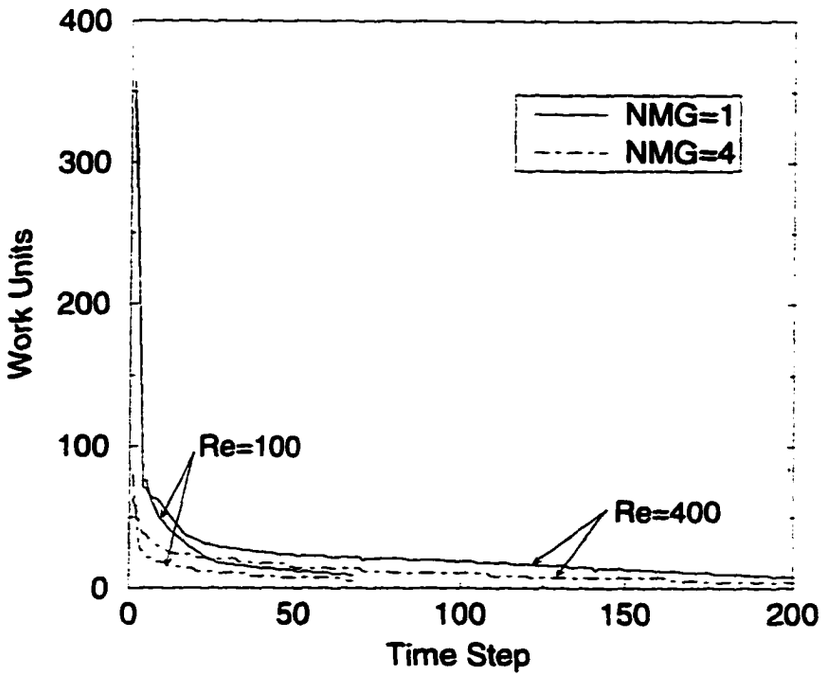

Figure 4.9 Work units per time step for unsteady lid driven cavity ($\Delta t = 0.1$)

4.5.3 Pulsatile Channel Flow

The pulsatile fully developed channel flow was selected to test the effectiveness of multigrid acceleration for a pressure driven, periodic, unsteady flow. The pulsatile channel flow consists of fully developed flow with a mass flow rate, and hence, mean velocity that varies periodically in time as,

$$U(t) = U_s \text{ if } 0 \leq \frac{t}{T_p} \leq \frac{1}{2}$$
$$U(t) = U_s - U_p \sin(2\pi \frac{t}{T_p}) \text{ if } \frac{1}{2} < \frac{t}{T_p} \leq 1, \tag{4.57}$$

where $T_p = 2\pi$ is the period, and $U_s = 1$ and $U_p = 1.23$ are the steady and the oscillating components of the average inflow velocity, respectively; see Fig. 4.10.

The geometry consisted of a straight channel of unit nondimensional height and nondimensional lengths of $L = 1, 2,$ and 4. The boundary conditions at the inlet entailed specifying $u(y,t)$, $v = 0$, $\rho = 1$, and extrapolating p from the interior. The exact solution for $u(y,t)$ for this problem was derived in [21]. However, an error (or misprint) was detected and the correct

Table 4.1 Results for unsteady lid driven cavity for RK scheme (Re = 100)

Grid	Δt	NMG	CPU Time (min)	Speedup (CPU)	Total Work Units	WU per time step min	WU per time step max	WU per time step avg
48 × 48	0.025	1	148.0	1.0	16000	12.0	3180	58.9
48 × 48	0.025	4	66.5	2.2	4080	4.3	383	15.0
48 × 48	0.1	1	120.0	1.0	10500	39.9	1710	154.0
48 × 48	0.1	4	46.2	2.6	2760	14.1	254	40.6

Table 4.2 Results for unsteady lid driven cavity for LU-SGS scheme (Re = 100)

Grid	Δt	NMG	CPU Time (min)	Speedup (CPU)	Total Work Units	WU per time step min	WU per time step max	WU per time step avg
48 × 48	0.0125	4	25.2	—	3170	4.3	222	5.8
48 × 48	0.025	1	33.6	1.0	4280	4.0	875	15.7
48 × 48	0.025	4	15.2	2.2	1910	4.3	140	7.1
48 × 48	0.1	1	18.9	1.0	2300	9.0	358	33.8
48 × 48	0.1	4	7.1	2.7	870	5.3	80.8	12.8
48 × 48	0.2	4	5.1	—	610	7.6	74.2	17.8

solution is given by the real part of

$$u(y,t) = 6M_0 y(1-y) + \sum_{n=1}^{\infty} M_n A_n(y) \exp(-int) \tag{4.58}$$

where $\mathrm{i} = \sqrt{-1}$ and

$$A_n(y) = \left(1 - \frac{\cosh \alpha(y-1/2)}{\cosh(\alpha/2)}\right) / \left(1 - \frac{2\sinh(\alpha/2)}{\alpha\cosh(\alpha/2)}\right) \tag{4.59}$$

$$\alpha = k_n(\mathrm{i}-1) \;:\; k_n = \sqrt{nRe/2} \tag{4.60}$$

$$M_0 = U_s + \frac{U_p}{\pi} \tag{4.61}$$

$$M_1 = -\mathrm{i}\frac{U_p}{2} \tag{4.62}$$

$$M_n = -\frac{2}{n^2-1}\frac{U_p}{\pi} \text{ for } n = 2,4,6,\ldots \tag{4.63}$$

At the outlet, $\partial u/\partial x = \partial v/\partial x = 0$ were enforced and p and T were extrapolated from the interior. At the channel walls, $u = v = 0$ and $\partial p/\partial n = 0$ were enforced, and adiabatic conditions were specified for the temperature, $\partial T/\partial n = 0$. The grids were typically stretched

Table 4.3 Results for unsteady lid driven cavity for LU-SGS scheme (Re = 400)

Grid	Δt	NMG	CPU Time (min)	Speedup (CPU)	Total Work Units	WU per time step min	max	avg
64 × 64	0.0125	4	112	—	7860	2.0	202	4.9
64 × 64	0.025	1	91.2	1.0	7040	3.0	738	8.8
64 × 64	0.025	4	71.8	1.3	5000	4.3	127	6.3
64 × 64	0.1	1	60.8	1.0	4890	8.0	344	24.4
64 × 64	0.1	4	35.2	1.7	2490	4.3	63.3	12.5

to provide moderate clustering of points near the channel walls, but uniform spacing was used in the streamwise direction. The Reynolds number was Re = 131.9 based on the channel height and U_s, and the Mach number was $M = 0.001$.

Refinement studies were first performed to determine the grid density, number of time steps per cycle (N_p), and convergence tolerance in pseudo time, TOL, required for accurate solutions. The studies revealed that $TOL = 1 \times 10^{-6}$, $N_p = 24$, and a 32×32 grid (for L=1) were sufficient. This tolerance level resulted in 2–3.5 orders of magnitude drop in the residuals. The velocity profiles computed at a streamwise location near the outlet for these conditions are shown in Fig. 4.11 at various times in a cycle. The exact solution was matched very well, giving less than 0.5 percent error compared to the exact solution over most of the channel during the entire cycle. The percent error was as high as five percent near the walls when reversed flow occurred.

Only the LU-SGS scheme was used for the channel flow calculations due to its superior performance. Several cases were run with and without multigrid for $N_p = 24, 48$, and 96 on a 32×32 grid for L=1. The results in Table 4.4 show that speedups of 2.5 to 2.9 were obtained, depending on the number of time steps per cycle. The total time to complete a cycle increased as N_p was increased.

The pulsatile channel flow was also computed for channels with increased lengths of L=2 and 4 (see Table 4.5), where the same grid density as for L=1 was maintained. The computational work increased significantly as the channel was lengthened, and the observed speedups from multigrid were larger. The work units per time step for several cases are shown in

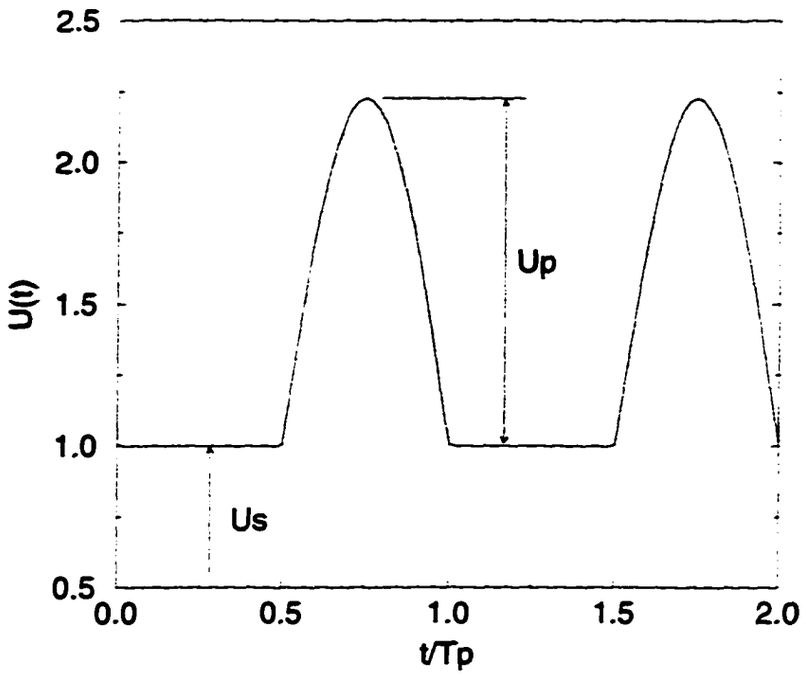

Figure 4.10 Mean velocity for pulsatile channel flow

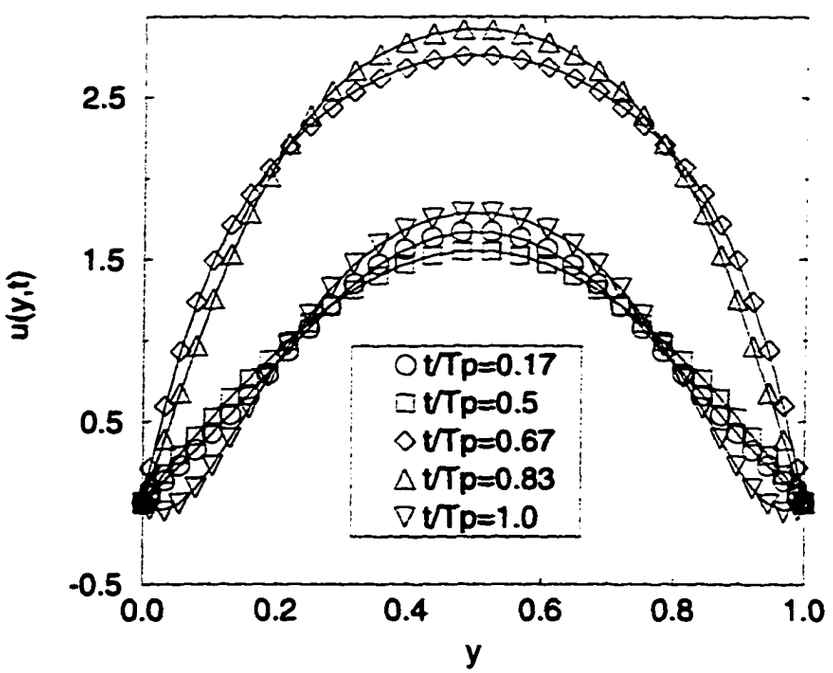

Figure 4.11 Computed velocity profiles (symbols) near outlet for pulsatile channel flow compared to exact solution (solid lines)

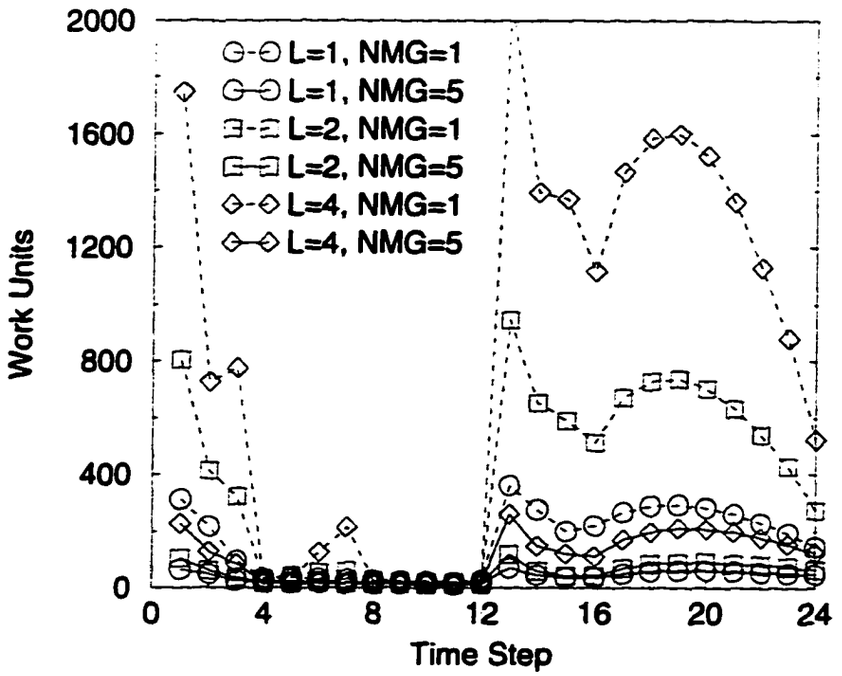

Figure 4.12 Work units per time step for pulsatile channel flow ($N_p = 24$)

Fig. 4.12. The figure shows that, as opposed to the lid driven cavity, multigrid was able to provide speedups over most of the time period, leading to improved overall speedups.

The convergence for these cases could probably be improved by employing semi-coarsening (coarsening the grid more in the streamwise direction than the cross-stream direction), allowing for improved propagation of information along the channel.

4.5.4 Thermally Driven Cavity

The steady state buoyancy driven flow in a square enclosure was computed to demonstrate the capabilities of the flow solver to compute low speed flows with compressibilities arising from density variations induced by heat transfer. The problem consists of two adiabatic horizontal walls (top and bottom) and two isothermal vertical walls, one at a hot temperature T_h (left wall) and the other at a cold temperature T_c (right wall). The temperature difference is defined by the temperature difference parameter, $\epsilon = \Delta T/(2T_r)$, where $\Delta T = T_h - T_c$ and $T_r = (T_h + T_c)/2$. Most studies of this class of flows employ incompressible methods with

Table 4.4 Results for one cycle of pulsatile channel flow (L=1)

Grid	Np	NMG	CPU Time (min)	Speedup (CPU)	Total Work Units	WU per time step min	WU per time step max	WU per time step avg
32 × 32	24	1	16.1	1.0	3900	19.0	361	158
32 × 32	24	5	5.5	2.9	921	12.0	71.7	37.8
32 × 32	48	1	25.7	1.0	6230	10.0	476	126
32 × 32	48	5	9.6	2.7	1600	7.6	95.0	32.7
32 × 32	96	1	36.9	1.0	8640	6.0	648	88.0
32 × 32	96	5	15.0	2.5	2540	5.3	135	26.2

Table 4.5 Results for one cycle of pulsatile channel flow (N_p=24 for all cases)

Grid	L	NMG	CPU Time (min)	Speedup (CPU)	Total Work Units	WU per time step min	WU per time step max	WU per time step avg
64 × 32	2	1	67.6	1.0	9250	18.0	945	370
64 × 32	2	5	11.8	5.7	1240	12.0	118	50.4
64 × 64	2	6	26.7	2.5	1360	12.0	145	55.5
64 × 32	4	1	280	1.0	19800	19.0	2080	790
64 × 32	4	5	25.6	10.9	2690	14.3	261	108
64 × 64	4	6	62.5	4.5	3170	14.3	325	128

the Boussinesq approximation, which is only appropriate for small temperature differences ($\epsilon << 1$). Higher temperature differences require compressible methods, but traditional compressible flow solvers have much difficulty computing this flow due to convergence problems at the associated low speeds. Preconditioned compressible flow solvers, such as the one in this study, are able to easily handle this case with large temperature differences.

In this study, cases were run with $\epsilon = 0.6$ at Rayleigh numbers

$$\mathrm{Ra} = \frac{2\epsilon g \rho_r^2 L_r^3 \mathrm{Pr}}{\mu_r^2} \tag{4.64}$$

of 10^3 and 10^5 with uniform 64 × 64 and 96 × 96 grids, respectively. Convergence with the LU-SGS and RK schemes for $\mathrm{Ra} = 10^3$ and $\mathrm{Ra} = 10^5$ are shown in Figs. 4.13 and 4.14, respectively, with and without multigrid acceleration. As shown, the LU-SGS scheme with multigrid computes this flow very efficiently. Multigrid provided speedups of 6.8 and 11.5 for $\mathrm{Ra} = 10^3$ and $\mathrm{Ra} = 10^5$, respectively, with the LU-SGS scheme. Multigrid provided significant

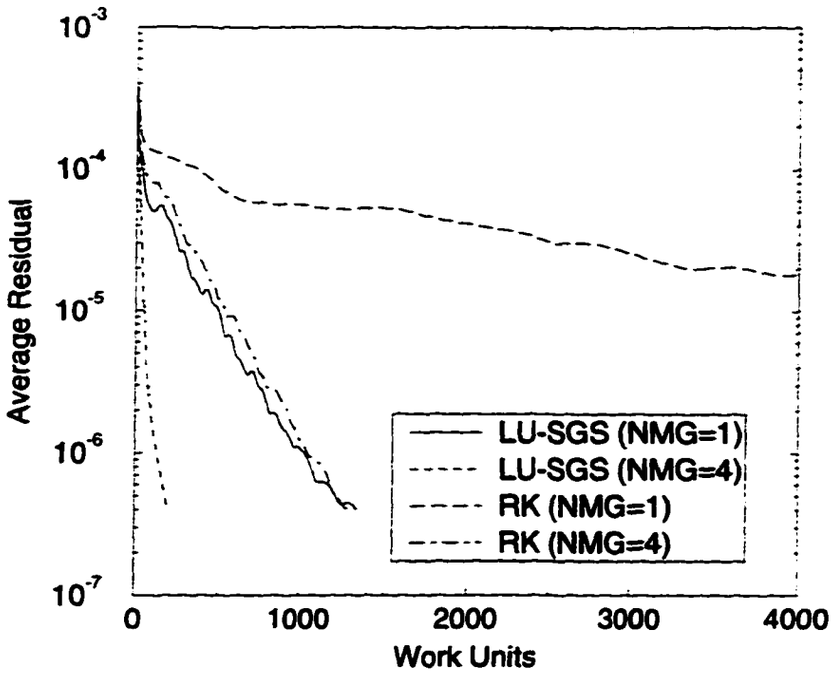

Figure 4.13 Convergence for thermally driven cavity ($Ra = 10^3$, 64×64 grid)

speedups for the RK scheme as well.

Temperature contours and velocity vectors for the two cases are shown in Fig. 4.15. Excellent agreement was obtained with the results presented by Choi and Merkle [1]. Average Nusselt numbers along the left wall were also computed, giving $Nu_L = 1.10$ and $Nu_L = 4.50$ for $Ra = 10^3$ and $Ra = 10^5$, respectively. This resulted in percent errors of 2.3 and 1.8 compared to the correlation by Chenoweth and Paolucci [22].

4.6 Conclusion

A two-dimensional time accurate dual time step Navier-Stokes flow solver with time derivative preconditioning was evaluated to determine the effectiveness of multigrid acceleration for unsteady simulations. Both an explicit Runge-Kutta scheme and an implicit LU-SGS scheme were used to integrate the equations in time.

The convergence for steady calculations was shown to be independent of Mach number, demonstrating the capabilities of the time derivative preconditioning. Multigrid provided sig-

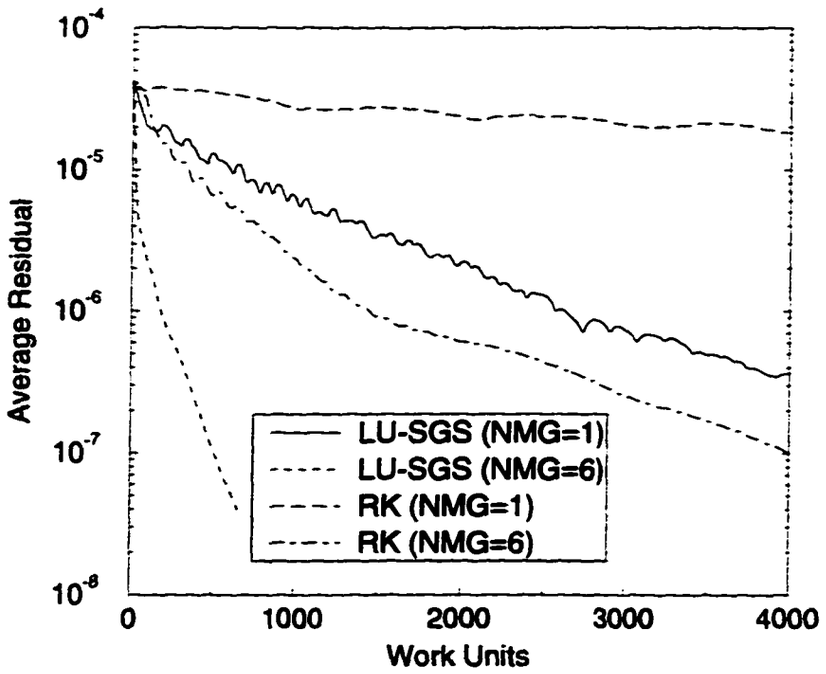

Figure 4.14 Convergence for thermally driven cavity (Ra = 10^5, 96 × 96 grid)

nificant speedups for steady and unsteady computations of the lid driven cavity, thermally driven cavity, and pulsatile channel flows. The speedups for unsteady simulations were problem dependent, a function of how rapidly the flow varied in time and the size of the allowable time step. In addition, the LU-SGS scheme was much more efficient than the Runge-Kutta scheme for most cases.

Acknowledgements

The first author was supported by a Department of Defense National Defense Science and Engineering Graduate Fellowship.

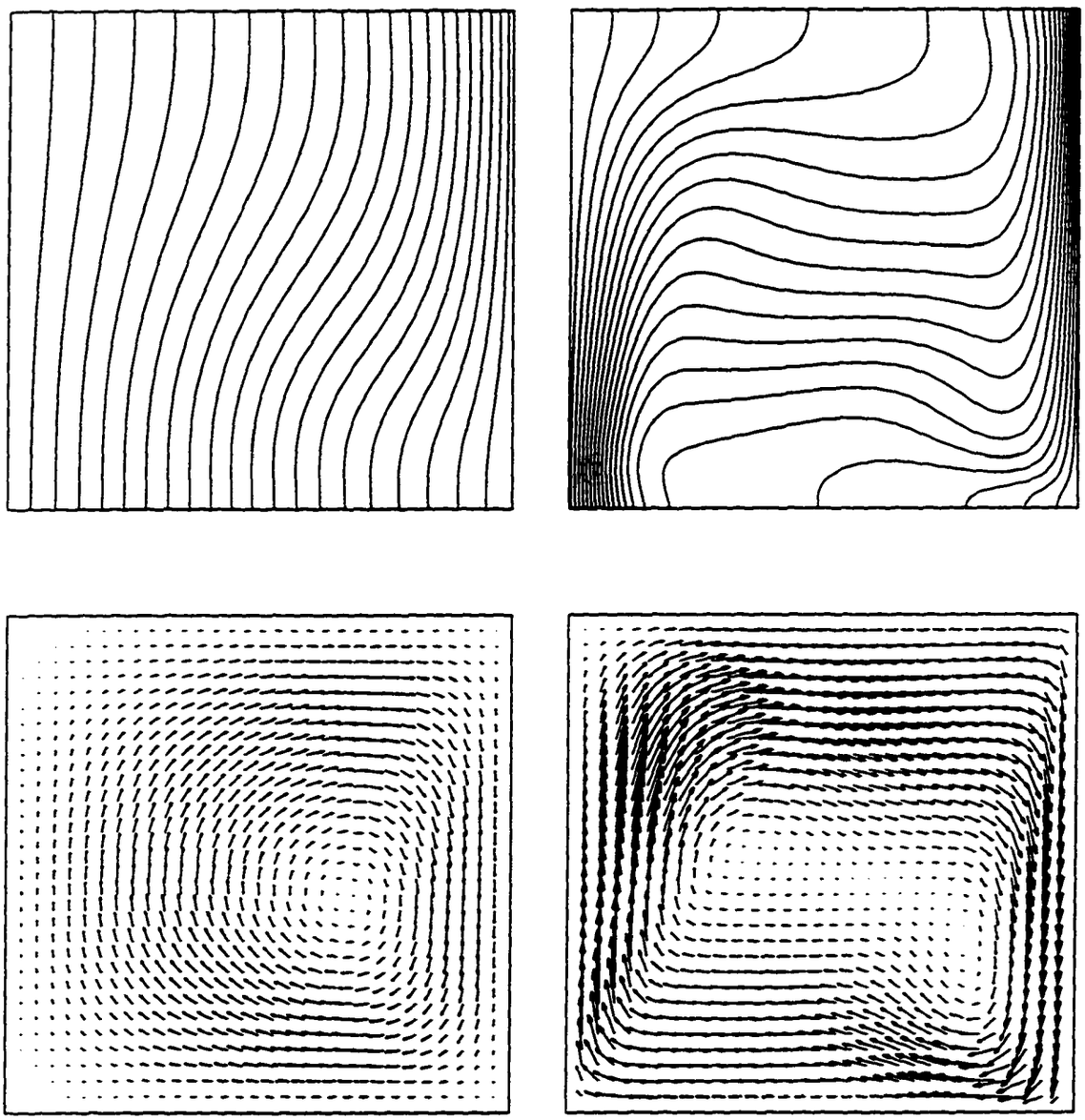

Figure 4.15 Temperature contours and velocity vectors for thermally driven cavity (vectors not shown for all grid points, and vector scales are different for $Ra = 10^3$ and $Ra = 10^5$)

References

1. Y.-H. Choi and C.L. Merkle, The Application of Preconditioning in Viscous Flows. *J. of Comput. Phys.*, 1993, **105**, 207-223.

2. J.-S. Shuen, K.-H. Chen, and Y. Choi, A Coupled Implicit Method for Chemical Non-Equilibrium Flows at All Speeds. *J. of Comput. Phys.*, 1993, **106**, 306-318.

3. D.L. Lee and van Leer, B., Progress in Local Preconditioning of the Euler and Navier-Stokes Equations. AIAA Paper 93-3328-CP. 1993.

4. P.C.E. Jorgenson and R.H. Pletcher. An Implicit Numerical Scheme for the Simulation of Internal Viscous Flows on Unstructured Grids. AIAA Paper 94-0306. 1994.

5. R.H. Pletcher and K.-H. Chen, On Solving the Compressible Navier-Stokes Equations for Unsteady Flows at Very Low Mach Numbers. AIAA Paper 93-3368. 1993.

6. J.M. Weiss and W.A. Smith, Preconditioning Applied to Variable and Constant Density Time Accurate Flows on Unstructured Meshes. AIAA Paper 94-2209. 1994.

7. S. Venkateswaran and C.L. Merkle. Dual Time Stepping and Preconditioning for Unsteady Computations. AIAA Paper 95-0078, 1995.

8. A. Arnone, M.-S. Liou, and L.A. Povinelli. Multigrid Time-Accurate Integration of Navier-Stokes Equations. AIAA Paper 93-3361, 1993.

9. Z.J. Wang and H.Q. Yang, Unsteady Flow Simulation using a Zonal Multi-grid Approach with Moving Boundaries. AIAA Paper 94-0057, 1994.

10. L. Martinelli and A. Jameson, Validation of a Multigrid Method for Reynolds Averaged Equations. AIAA Paper 88-0414, 1988.

11. R.C. Swanson and E. Turkel, Artificial Dissipation and Central Difference Schemes for the Euler and Navier-Stokes Equations. AIAA Paper 87-1107, 1987.

12. A. Jameson. Time Dependent Calculations Using Multigrid. with Applications to Unsteady Flows Past Airfoils and Wings. AIAA Paper 91-1596. 1991.

13. M. Melson, M. Sanetrik, and H. Atkins, Time Accurate Navier-Stokes Calculations with Multigrid Acceleration. Presented at the Sixth Copper Mountain Conference on Multigrid Methods, 4-9 April 1993. Copper Mountain, CO.

14. V.N. Vatsa and B.W. Wedan. Development of a Multigrid Code for 3-D Navier-Stokes Equations and its Applications to a Grid-Refinement Study. *Computers Fluids*, 1990. **18**. 391-403.

15. E. Turkel. Review of Preconditioning Methods for Fluid Dynamics. NASA-CR-189712. 1992.

16. S. Yoon and A. Jameson, An LU-SSOR Scheme for the Euler and Navier-Stokes Equations. AIAA Paper 87-600, 1987.

17. H. Rieger and A. Jameson, Solution of steady three dimensional compressible Euler and Navier Stokes equations by an implicit LU scheme. AIAA Paper 88-0619, 1988.

18. F. Grasso and M. Marini. LU Implicit TVD Scheme for the Solution of Viscous Two Dimensional High Speed Flows. AIAA Paper 91-1573, 1991.

19. K.-H. Chen and J.-S. Shuen, Three Dimensional Coupled Implicit Methods for Spray Combustion Flows at all Speeds. AIAA Paper 94-3047, 1994.

20. U. Ghia, K.N. Ghia, and C.T. Shin, High-Re Solutions for Incompressible Flow Using the Navier-Stokes Equations and a Multigrid Method. *J. of Comput. Phys.*, 1982, **48**, 387-411.

21. M. Rosenfeld, Validation of Numerical Simulation of Incompressible Pulsatile Flow in a Constricted Channel. *Computers Fluids*, 1993, **22**, 139-156.

22. D.R. Chenoweth and S. Paolucci, Natural Convection in an Enclosed Vertical Air Layer with Large Horizontal Temperature Differences. *J. Fluid Mech.*, 1986. **169**. 173-210.

Appendix A. Jacobian Matrices

$$[T] = \begin{bmatrix} \frac{1}{T} & 0 & 0 & -\frac{p}{T^2} \\ \frac{u}{T} & \frac{p}{T} & 0 & -\frac{pu}{T^2} \\ \frac{v}{T} & 0 & \frac{p}{T} & -\frac{pv}{T^2} \\ c_v + \frac{1}{2}\frac{u^2+v^2}{T} & \frac{pu}{T} & \frac{pv}{T} & -\frac{1}{2}\frac{p}{T^2}(u^2+v^2) \end{bmatrix}$$

$$[\Gamma] = \begin{bmatrix} \frac{R}{T} & 0 & 0 & -\frac{p}{T^2} \\ \frac{Ru}{T} & \frac{p}{T} & 0 & -\frac{pu}{T^2} \\ \frac{Rv}{T} & 0 & \frac{p}{T} & -\frac{pv}{T^2} \\ R\left(c_v + \frac{1}{2}\frac{u^2+v^2}{T}\right) & \frac{pu}{T} & \frac{pv}{T} & -\frac{1}{2}\frac{p}{T^2}(u^2+v^2) \end{bmatrix}$$

$$[A] = \begin{bmatrix} \frac{u}{T} & \frac{p}{T} & 0 & -\frac{pu}{T^2} \\ \frac{u^2}{T} + R & 2\frac{pu}{T} & 0 & -\frac{pu^2}{T^2} \\ \frac{uv}{T} & \frac{pv}{T} & \frac{pu}{T} & -\frac{puv}{T^2} \\ \frac{uH}{T} & \frac{pH}{T} + \frac{pu^2}{T} & \frac{puv}{T} & -\frac{1}{2}\frac{pu}{T^2}(u^2+v^2) \end{bmatrix}$$

$$[B] = \begin{bmatrix} \frac{v}{T} & 0 & \frac{p}{T} & -\frac{pv}{T^2} \\ \frac{uv}{T} & \frac{pv}{T} & \frac{pu}{T} & -\frac{puv}{T^2} \\ \frac{v^2}{T} + R & 0 & 2\frac{pv}{T} & -\frac{pv^2}{T^2} \\ \frac{vH}{T} & \frac{puv}{T} & \frac{pH}{T} + \frac{pv^2}{T} & -\frac{1}{2}\frac{pv}{T^2}(u^2+v^2) \end{bmatrix}$$

CHAPTER 5 RESULTS FOR HOMOGENEOUS, ISOTROPIC, DECAYING TURBULENCE

In this chapter, the results for the LES of homogeneous, isotropic, decaying turbulence in a periodic box are presented. This simple flow was used for preliminary analysis of the finite volume formulation before application to more complex flows. Both the Smagorinsky subgrid-scale model and the dynamic subgrid-scale model were evaluated. Comparisons were made to available experimental data.

5.1 Introduction

Before application to complex geometries, the finite volume formulation was evaluated with a simple turbulent flow: homogeneous, isotropic, decaying turbulence. This flow is ideal for preliminary analysis of LES methods because the effects of wall boundary conditions, inflow and outflow boundary conditions, and other nonhomogeneities are not present. This permits a detailed analysis of the discretization methods and initial evaluation of the subgrid-scale model implementation.

The LES of isotropic, decaying turbulence has been carried out by many investigators, a few of whom are mentioned here. Kwak et al. (1975) used incompressible finite difference methods with a Smagorinsky subgrid-scale (SGS) model. Moin et al. (1991), and more recently Spyropoulos and Blaisdell (1995), applied the dynamic SGS model for compressible turbulence using a pseudospectral scheme. All of these researchers made comparisons to the experimental data of Comte-Bellot and Corrsin (1971). Vreman et al. (1992) used a finite volume method to successfully compute compressible isotropic, decaying turbulence using a Smagorinsky SGS model. Vreman et al. (1992) evaluated various discretization methods for a cell vertex finite

volume formulation. They made comparisons to the theoretical Kolmogorov -5/3 law for a low Taylor microscale Reynolds number. The results varied for the different discretization methods, but encouraging results were obtained with even second order accurate methods.

5.2 Problem Description

The simulations presented in this chapter were an attempt to compute the decay of isotropic, grid-generated turbulence in the experiment of Comte-Bellot and Corrsin (1971) (denoted as CBC in the remainder of this chapter). The wind tunnel experiment was of grid-generated turbulence that decayed spatially as the flow proceeded downstream. An observer traveling at the mean speed of the flow would see an isotropic turbulence field decaying in time. The latter situation is the problem considered here, but comparisons are made to the CBC data. This is a common procedure followed by other researchers, such as those mentioned above.

The experimental data includes three-dimensional energy spectra at three different streamwise locations downstream of the turbulence generating grid. The three streamwise spatial locations correspond to three instances of time for the temporally decaying simulation. The time is expressed nondimensionally as tU_0/M, where U_0=10 m/s is the mean streamwise speed of the experimental spatially decaying turbulence, and $M = 5.08$ cm was the size of the turbulence generating grid. The three experimental energy spectra correspond to $tU_0/M = 42$, 98, and 171. The average turbulent kinetic was obtained at each time by integrating the three-dimensional energy spectrum as

$$TKE = \frac{1}{2}u_i u_i = \int_0^\infty E(k)\, dk \tag{5.1}$$

where $E(k)$ is the three-dimensional energy spectrum as a function of the magnitude of the wave number, k. An initial flow field was generated, as described in Section 5.4, to match the filtered experimental energy spectrum at the initial time, $tU_0/M = 42$. Comparisons were then made to the TKE and energy spectra at the two later times.

The initial state resulted in $\mathrm{Re}_L = 13,000$ and $M_r = 0.1$. For the nondimensionalization, L_r was the length of one side of the computational box, and V_r was the L_2-norm of the initial velocity field.

5.3 Test Filtering

The dynamic SGS model requires the spatial filtering of several quantities with a test filter width of Δ_t (see the description of the dynamic SGS model in Section 2.4.4). The filtering operation is given by the convolution integral

$$\widehat{f}(\vec{x},t) = \int_D \widehat{G}(\vec{x},\vec{\xi})\, f(\vec{\xi},t)\, d\vec{\xi} \tag{5.2}$$

where $\widehat{G}$ is the test filter function and the integration is performed over the entire domain. Top hat (or box) filters are used with finite volume formulations since this type of filtering is implied by the finite volume methodology. The top hat filter function is

$$\widehat{G}(\vec{x}-\vec{\xi}) = \begin{cases} \frac{1}{\Delta_t^3} & \text{if } x_i - \Delta_t/2 \le \xi_i \le x_i + \Delta_t/2 \\ 0 & \text{otherwise} \end{cases} \tag{5.3}$$

where Δ_t is the test filter width.

To filter a quantity in physical space, the convolution integral in Eq. 5.2 must be approximated. This can either be done by applying a one-dimensional approximation to the integral successively in each coordinate direction, or by deriving a three-dimensional approximation to the integral. The two approaches are related for some situations, as discussed in Appendix D. For the simulations presented in this chapter, the 27 point filter given by Eq. D.12 was used. The test-to-grid filter width ratio was 2.0, which has been shown to be the optimal value (Germano et al., 1991).

5.4 Initial Conditions

The simulations required the generation of an initial flow field that represented the turbulent kinetic energy and turbulent structure of homogeneous, isotropic turbulence. The methodology for generation of the initial conditions was based upon the procedures used by Kwak et al. (1975) and Erlebacher et al. (1990). The basic idea is to generate a random velocity field that matches some desired energy spectrum. The specific procedure is outlined below.

A random velocity field was generated such that $-0.5 \le u_i \le 0.5$. A fast Fourier transform (FFT) routine was used to find the Fourier coefficients, F_i, of the random velocity field. The

Fourier coefficients were modified to ensure they were divergence free in physical space. In Fourier space, a divergence free velocity field requires that the Fourier coefficients be orthogonal to the wave vectors, $F_i k_i = 0$, where the *ith* component of the nondimensional wave vector is $k_i = n_i$, for $n_i = 0, 1, ..., N/2$, where N is the number of control volumes in the *ith* direction.

However, as pointed out by Kwak et al. (1975), this will not give a divergence free velocity field in physical space. The Fourier coefficients should be made orthogonal to modified wave vectors depending upon the numerical discretization method. For second order accurate central differences, the modified wave vectors are

$$k_i' = \sin(\Delta_i k_i)/\Delta_i, \tag{5.4}$$

where Δ_i is the grid spacing in the ith-direction. The orthogonalization of the Fourier coefficients was accomplished as

$$F_i = F_i - \left(\frac{F_j k_j'}{k_m' k_m'}\right) F_i. \tag{5.5}$$

The velocity coefficients for each wave number were then scaled to match the desired energy spectrum. The three-dimensional energy spectrum can be computed from the Fourier coefficients (Kwak et al., 1975) as

$$E(k_n) = 2\pi(L_{box}/2\pi)^3 k_n^2 \langle F_i(k_n) F_i(k_n) \rangle \tag{5.6}$$

where L_{box} is the length of one side of the computational box, k_n is the magnitude of the wave vector, and <> is an ensemble average. The Fourier coefficients were scaled by solving Eq. 5.6 without the ensemble averaging to give

$$F_i = F_i \left[\frac{E(k_n)}{2\pi(L_{box}/2\pi)^3 k_n^2 F_j F_j}\right]^{1/2}. \tag{5.7}$$

The new physical velocities, u_i, were found by taking the inverse Fourier transform of the Fourier coefficients using an FFT routine.

This complicated procedure for generating the initial conditions does not produce a truly turbulent field, since the coherent structures present in a turbulent flow may not be well represented. Consequently, the simulations were typically run for 250 time steps to allow the turbulent structures to develop. The Fourier coefficients of the resulting velocity field

were rescaled to match the original energy spectrum. This was found necessary to match the experimental decay rates, as discussed in the results below.

The initial pressure field was determined by solving a Poisson equation for pressure, the initial density field was uniform, and the temperature field was determined from the equation of state.

For post-processing, the three-dimensional energy spectra were computed from the Fourier coefficients by replacing the ensemble average in Eq. 5.6 by an average over a shell in k-space. The average was made by taking a mean value over the points between the two shells with radius $(k - \Delta k/2)$ and $(k + \Delta k/2)$, giving

$$E(k_n) = \frac{2\pi k_n^2}{N_k} \left(\frac{L_{box}}{2\pi}\right)^3 \sum_{k_n=k-\Delta k/2}^{k+\Delta k/2} F_i(k_n) F_i(k_n), \tag{5.8}$$

where N_k is the number of points between the two shells with radius $(k-\Delta k/2)$ and $(k+\Delta k/2)$.

5.5 Results

Simulations were performed with the purely explicit Runge-Kutta scheme using the Smagorinsky and dynamic SGS models. For this study, all subgrid-scale contributions to the total energy equation were neglected since only low Mach number cases were considered. Vreman et al. (1995) demonstrated that this assumption was appropriate for Mach numbers below 0.2, as discussed in Chapter 2.

The decay of the resolved turbulent kinetic energy, the skewness component, and the filtered three-dimensional energy spectra were compared to the experimental CBC results. The decay of the resolved turbulent kinetic energy was computed in physical space as

$$TKE = \frac{1}{2} \langle \tilde{u}_i \tilde{u}_i \rangle, \tag{5.9}$$

and skewness tensor of the velocity derivatives was computed as

$$Sk_{ij} = \frac{\langle (\partial u_i/\partial x_j) \rangle^3}{\langle (\partial u_i/\partial x_j)^2 \rangle^{3/2}}. \tag{5.10}$$

Typically, only the component Sk_{11} is considered, and according to Lesieur (1990), experimental values of Sk_{11} found in grid turbulence are of the order of -0.4.

Simulations were performed with a $32 \times 32 \times 32$ grid with $\Delta t = 0.002$ ($\Delta t U_0/M = 0.52$) for 250 time steps, and a $64 \times 64 \times 64$ grid with $\Delta t = 0.001$ ($\Delta t U_0/M = 0.26$) for 500 time steps. The fine grid simulations were done using 8 blocks and 8 processors on an IBM SP-2. and required about 3.8 hours of wall clock time for 500 time steps. An initial velocity field was generated with the methods described in Section 5.4 to match the experimental energy spectrum at $tU_0/M = 42$. This velocity field was filtered using the discrete filter function given by Eq. D.12.

The decay of the resolved turbulent kinetic energy for the two grids is shown in Fig. 5.1. Comparisons were made with the experimental data by integrating the filtered experimental energy spectra over the range of k resolved by the particular grid. The Smagorinsky model with coefficients $C_d = 0.0424$ and $C_i = 0.0$ gave excellent agreement with the CBC data. The dynamic model, however, only matched the CBC data for the finer grid resolution. This indicates that the dynamic model requires more accuracy than the Smagorinsky model to provide acceptable simulations. As shown in Fig. 5.2, the dynamic model asymptotically produced model coefficients of about $C_d = 0.028$ for the $32 \times 32 \times 32$ grid and about $C_d = 0.025$ for the $64 \times 64 \times 64$ grid.

Figure 5.3 shows the skewness component for all cases. The finer grid gave better agreement with the experimental value of -0.4 for both models.

The energy spectra are compared to the filtered CBC energy spectra in Figs. 5.4 and 5.5 for the $32 \times 32 \times 32$ and $64 \times 64 \times 64$ grids, respectively. For the coarser grid, the Smagorinsky model matched the CBC data very well, whereas the dynamic model had too much energy at the high wavenumbers. For the finer grid, however, the dynamic model matched the CBC data while the Smagorinsky model was too dissipative at the higher wavenumbers.

The decay of the root-mean-square (RMS) velocity components in the three coordinate directions are compared to each other in Fig. 5.6. The difference between the three components was insignificant, indicating the simulations were able to maintain isotropy.

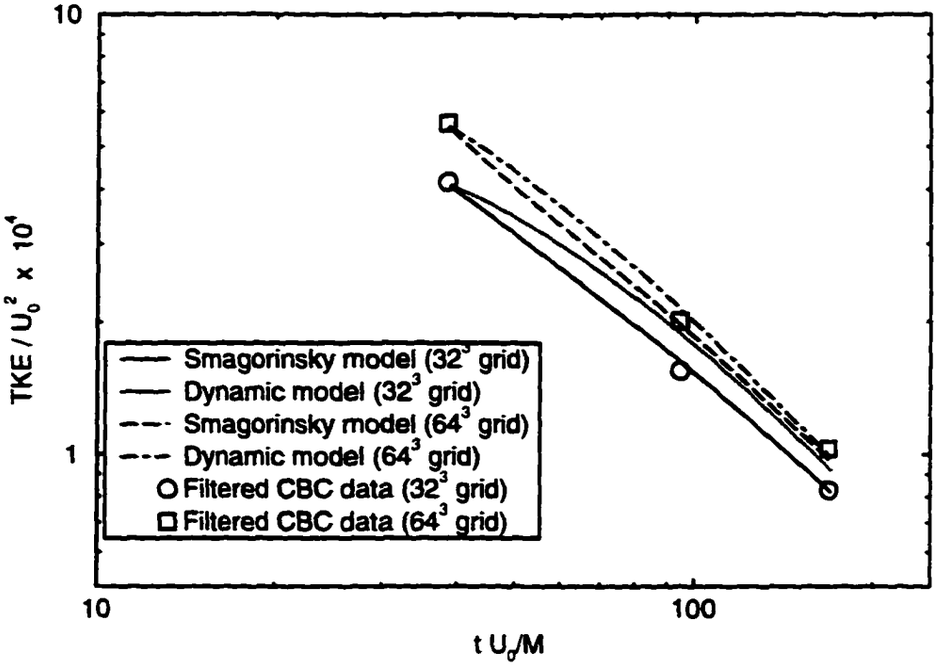

Figure 5.1 Decay of average turbulent kinetic energy

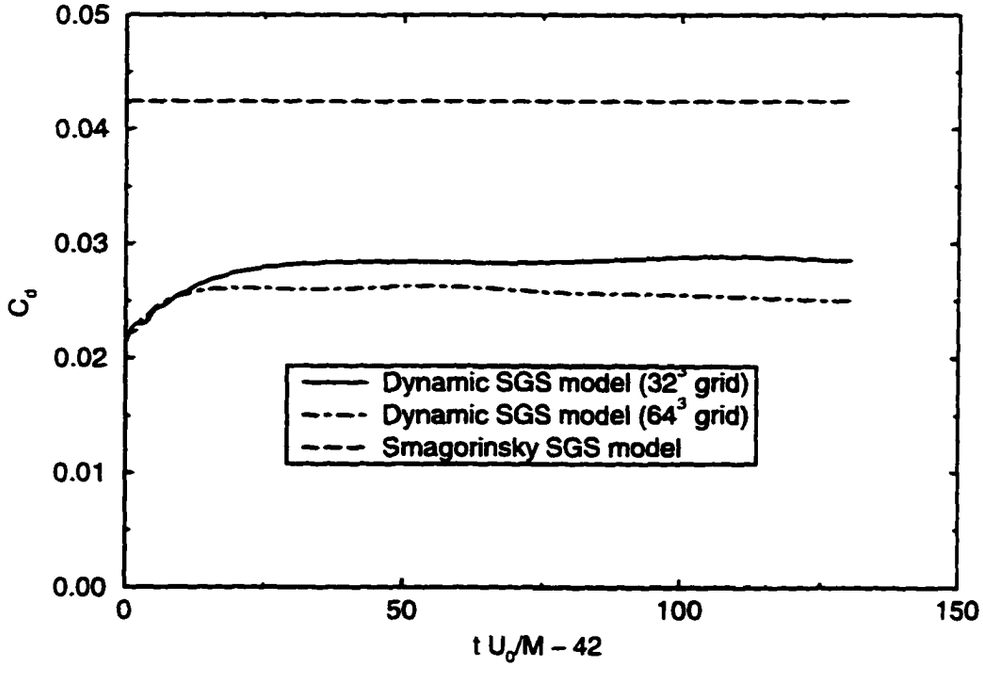

Figure 5.2 Time evolution of average dynamic SGS model coefficient

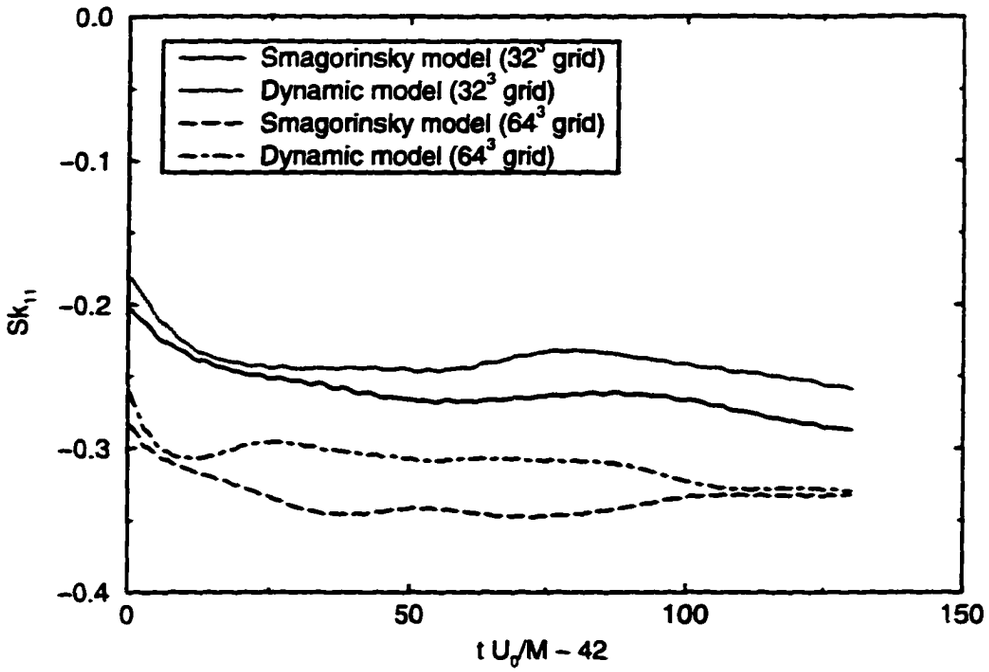

Figure 5.3 Time evolution of average skewness component

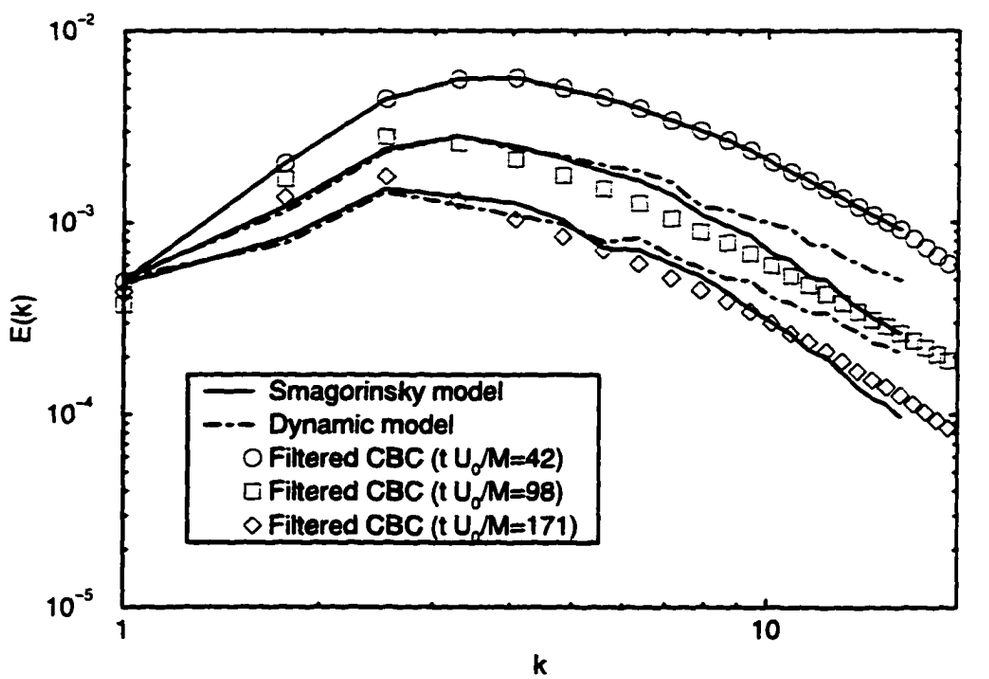

Figure 5.4 Three-dimensional energy spectrums ($32 \times 32 \times 32$ grid)

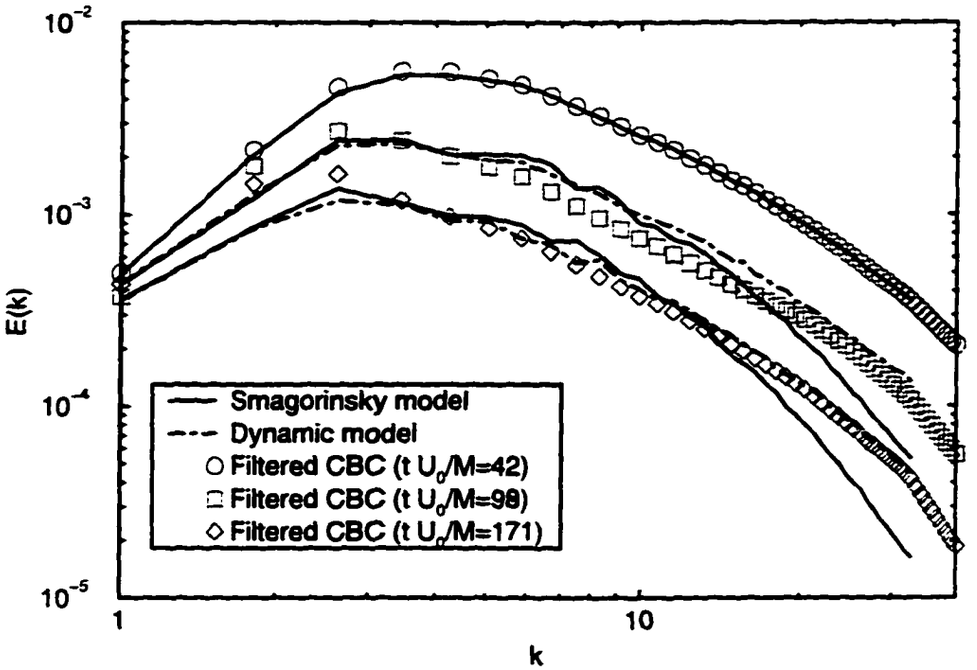

Figure 5.5 Three-dimensional energy spectrums (64 × 64 × 64 grid)

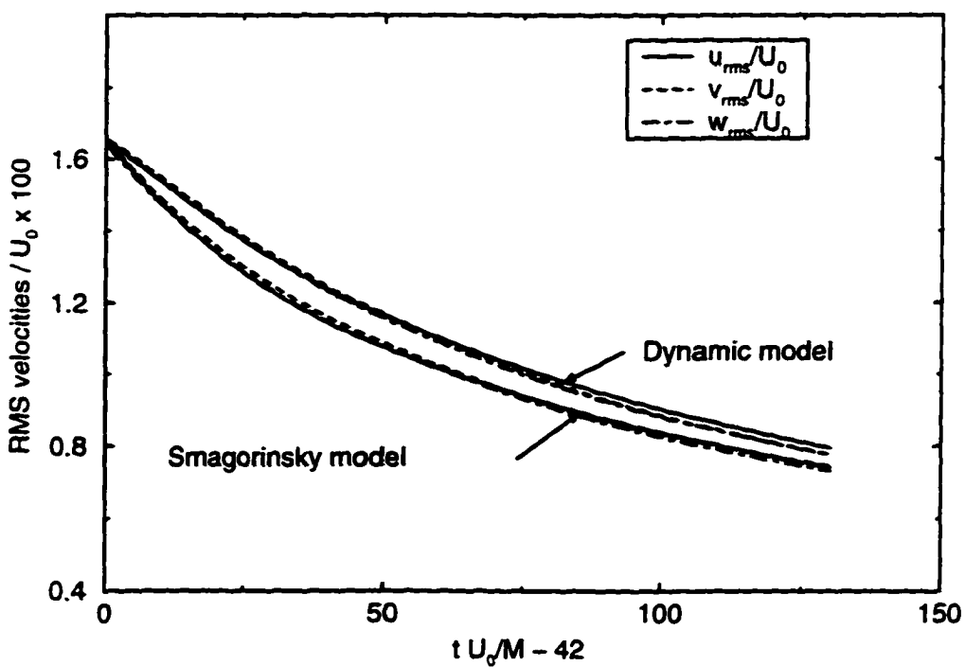

Figure 5.6 Decay of the root-mean-square (RMS) velocity components

5.6 Summary

Excellent agreement was obtained for the decay of turbulent kinetic energy with the Smagorinsky model compared to the filtered experimental data. Good agreement was also obtained with the dynamic model, although finer grid resolutions were required compared to the Smagorinsky model. For both models, better agreement with the experimentally observed skewness component was found with the finer grid. Best agreement with the filtered experimental energy spectra was provided with the dynamic model on the finer grid.

The simulations of isotropic decaying turbulence have demonstrated that second-order accurate finite volume formulations are capable of performing accurate LES with moderate grid resolutions. However, finer grids were required with the dynamic model compared to the Smagorinsky model, and the dynamic model required about 60 percent more CPU time. For these reasons, only the Smagorinsky model was used for the remaining simulations presented in this thesis.

CHAPTER 6 RESULTS FOR TURBULENT PLANE CHANNEL FLOW WITH LOW HEAT TRANSFER AND CONSTANT PROPERTIES

6.1 Introduction

The finite volume LES formulation was used successfully to simulate the simplest of turbulent flows, homogeneous, isotropic, decaying turbulence, as discussed in Chapter 5. The LES formulation was further evaluated by simulating a simple wall bounded flow, turbulent plane channel flow with low heat transfer. This is a benchmark case with extensive experimental and DNS data available in the literature for purposes of comparison. This case highlights the advantage of a preconditioned scheme, for which a compressible formulation can be validated using incompressible benchmark cases by performing analyses at very low Mach numbers.

In the following sections, the channel flow problem and simulation details are described. The resulting velocity statistics are compared to experimental and DNS data for incompressible turbulent channel flow. The temperature statistics are compared to the DNS of a passive scalar field of a turbulent channel flow. Comparisons are also made to empirical correlations for the friction coefficient and Nusselt number.

6.2 Problem Description

The problem of interest was fully developed, turbulent flow of air in a two-dimensional channel with constant wall heat flux, as depicted in Fig. 6.2. The wall heat flux was kept low such that the temperature and density variations were small. Consequently, the velocity and temperature fields were essentially decoupled, and the resulting velocity statistics could be compared to incompressible DNS and low-speed experimental data. The temperature statistics

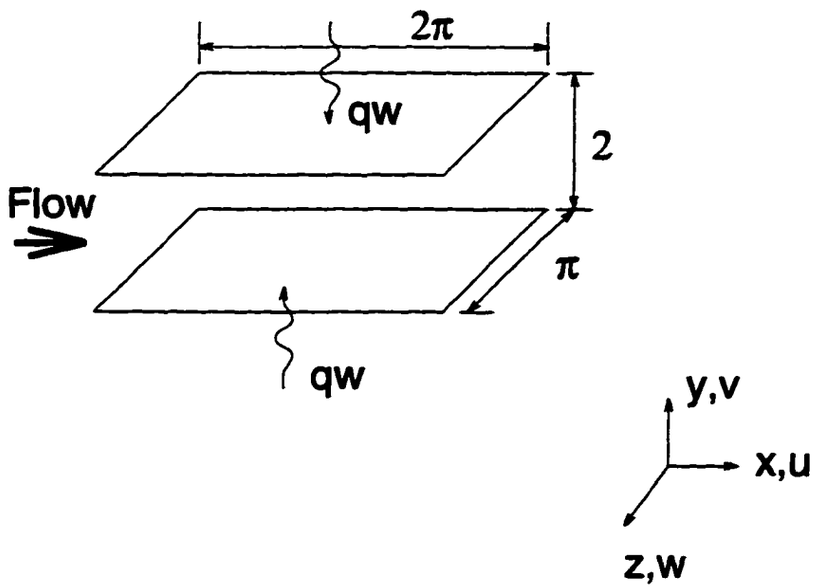

Figure 6.1 Schematic of two-dimensional plane channel with constant wall heating rate, q_w

could be compared to passive scalar DNS and LES results.

For a constant wall heat flux and constant fluid properties, turbulent channel flows approach a fully developed state in which the time averaged streamwise velocity and nondimensional temperature profiles no longer change in the streamwise direction. Consequently, the average local, wall, and bulk streamwise temperature gradients are constant and equal, as

$$\frac{\partial T}{\partial x} = \frac{\partial T_w}{\partial x} = \frac{\partial T_b}{\partial x} = constant. \tag{6.1}$$

Moreover, they are directly related to the amount of heat being added to the flow.

Kasagi et al. (1989) studied the conjugate heat transfer problem taking into account the unsteady heat conduction in a solid wall for various solid-fluid combinations. The problem is characterized by the thermal activity ratio,

$$K = \sqrt{\frac{\rho_f c_{p,f} \kappa_f}{\rho_w c_{p,w} \kappa_w}} \tag{6.2}$$

where the subscript f refers to the fluid, and the subscript w refers to the wall material. The thermal activity ratio for combinations of air and practical structural materials, such as metals,

glass, and plastics, is on the order of 10^{-4} to 10^{-3}. Hence, the wall temperature fluctuations in an air flow should be negligibly small so that the wall can be regarded as isothermal, unless the wall thickness is extremely small. Therefore, isothermal, as opposed to isoflux, boundary conditions should lead to more realistic near wall temperature fluctuations for the LES/DNS of turbulent wall bounded air flows. Due to the condition given by Eq. 6.1 for the problem of interest, isoflux conditions can equivalently be obtained by enforcing a constant streamwise wall temperature gradient. This was accomplished by specifying a fixed wall temperature that varied linearly in the streamwise direction.

No-slip velocity and zero normal pressure gradient boundary conditions were enforced at the upper and lower walls. Two different temperature boundary conditions were attempted, isoflux and a fixed linear temperature distribution, to provide the target isoflux conditions.

All primitive variables ($\bar{p}, \tilde{u}_i, \tilde{T}$) were assumed to be periodic in the spanwise (z) direction. The velocity components, $\tilde{u}_i$, were assumed to be periodic in the streamwise direction as well. The pressure and temperature were not periodic in the streamwise direction due to the negative, linear streamwise pressure gradient that drives the flow and the positive, linear temperature gradient resulting from the heat addition to the channel. Both quantities were decomposed into periodic and aperiodic components as

$$\begin{aligned} \bar{p}(x,y,z,t) &= \beta x + \bar{p}_p(x,y,z,t) \\ \tilde{T}(x,y,z,t) &= \varphi x + \tilde{T}_p(x,y,z,t) \end{aligned} \tag{6.3}$$

where β and φ are the average streamwise pressure and temperature gradients, respectively, and the subscript p indicates the periodic components, which satisfy

$$\begin{aligned} \bar{p}_p(0,y,z,t) &= \bar{p}_p(L_x,y,z,t) \\ \tilde{T}_p(0,y,z,t) &= \tilde{T}_p(L_x,y,z,t), \end{aligned} \tag{6.4}$$

where L_x is the length of the channel in the x-direction. The pressure, $\bar{p}$, in the governing equations was replaced by the decomposition in Eq. 6.3. Recall that the density in the governing equations was replaced by $\bar{p}$ and $\tilde{T}$ with the equation of state. As a result of Eq. 6.3, the

equation of state becomes

$$\tilde{\rho} = \frac{\tilde{p}}{R\tilde{T}} = \frac{\beta x + \bar{p}_p}{R\tilde{T}} = \frac{\beta x}{R\tilde{T}} + \frac{\bar{p}_p}{R\tilde{T}}. \tag{6.5}$$

This substitution would make the equations much too complicated. Fortunately, $\beta x/(R\tilde{T})$ is negligible compared to $\bar{p}_p/(R\tilde{T})$ for moderate Reynolds numbers (and hence pressure gradients, β) and moderate channel lengths. Therefore, it is valid to assume

$$\tilde{\rho} \approx \frac{\bar{p}_p}{R\tilde{T}}. \tag{6.6}$$

The governing equations are consequently unchanged, except that the equations are in terms of $\bar{p}_p$, and the streamwise momentum equation contains the additional pressure gradient parameter, β, as a body force. The equations are solved for the periodic pressure component, $\bar{p}_p$, with a streamwise periodic boundary condition. Note that for fully incompressible formulations, the pressure only appears in the streamwise momentum equation, and the assumption in Eq. 6.6 is no longer required.

As is often done for turbulent channel flow simulations (Benocci and Pinelli, 1990), the streamwise pressure gradient parameter was adjusted at each time step to provide the desired mass flow rate as

$$\beta^{n+1} = \beta^n - \frac{1}{\Delta t}\left[\left(\frac{\dot{m}}{A_c}\right)^0 - 2\left(\frac{\dot{m}}{A_c}\right)^n + \left(\frac{\dot{m}}{A_c}\right)^{n-1}\right]. \tag{6.7}$$

where $\dot{m}^n$ is the average mass flow rate for the channel at time level n, Δt is the physical time step, and A_c is the cross-flow area of the channel. The average mass flow rate is given by

$$\frac{\dot{m}}{A_c} = \frac{1}{L_y L_z}\int_{-1}^{1} < \rho u >_{x,z}\ dy \tag{6.8}$$

where $<>_{x,z}$ denotes an ensemble average in the x and z directions. The desired mass flow rate is $(\dot{m}/A_c)^0$.

The temperature was treated in a "step-periodic" manner in the streamwise direction. Using Eqs. 6.3 and 6.4, the step-periodic condition becomes

$$\begin{aligned} \tilde{T}(0) &= \tilde{T}(L_x) - \Delta\tilde{T}_x \\ \tilde{T}(L_x) &= \tilde{T}(0) + \Delta\tilde{T}_x. \end{aligned} \tag{6.9}$$

The streamwise temperature difference, $\Delta\tilde{T}_x$, was obtained by integrating the energy equation around the boundaries of the solution domain giving

$$\Delta\tilde{T}_x = \frac{q_w L_x}{(\dot{m}/A_c)} \tag{6.10}$$

where q_w is the constant nondimensional heat flux desired at the upper and lower walls.

6.3 Simulation Details

An initial flow field was required for the first turbulent channel simulation attempted. The initial velocity field was constructed by superimposing random velocity fluctuations on a mean flow that matched the DNS results of Kim et al. (1987). The random fluctuating components were scaled at each cross-stream location to match the *rms* velocities from the DNS results. The pressure and temperature were set to linear functions of x.

When the simulation was first started, the flow appeared to completely laminarize, with the average turbulent kinetic energy for the channel, k^+, dropping to near zero, where k^+ is the average turbulent kinetic energy normalized by the square of the friction velocity, as defined in Section 6.4. However, after 8-10,000 time steps, k^+ suddenly increased to a maximum near 8, then decreased and fluctuated about $k^+ \approx 2$. Once the flow was deemed to be statistically stationary, the simulations were run for an additional 8-10,000 time steps to collect the turbulence statistics. Subsequent simulations were started from this developed turbulence field (which in some instances was interpolated onto a different grid).

For the simulations presented in this chapter, the target Reynolds number based on the channel half-height, δ, and bulk velocity, u_b, was $\mathrm{Re}_\delta = 2800$, where $\mathrm{Re}_\delta = u_b\delta/\nu_b$ and ν_b is based on bulk properties. The bulk density, velocity, and temperature are defined as

$$\rho_b = \frac{1}{L_y}\int_{-1}^{1} \rho \, dy, \tag{6.11}$$

$$u_b = \frac{1}{\rho_b L_y}\int_{-1}^{1} \rho u \, dy, \tag{6.12}$$

$$T_b = \frac{1}{\rho_b u_b L_y}\int_{-1}^{1} \rho u T \, dy. \tag{6.13}$$

The nondimensional channel dimensions (with respect to δ) were $2\pi \times 2 \times \pi$ in the x, y, z directions, respectively. The reference Mach number was $M_r = 0.001$, which ensured nearly incompressible results. The nondimensional time step was 0.03112, which corresponded to about 518 time steps per large eddy turnover time, t_e, which is given in terms of nondimensional variables as $t_e = 1/u_\tau$.

Simulations were made with both a $32 \times 32 \times 24$ (coarse) grid and a $48 \times 64 \times 48$ (fine) grid, resulting in 24,576 and 147,456 control volumes, respectively. Both grids were uniformly spaced in the x and z directions, but the grids were clustered towards the walls using algebraic hyperbolic tangent stretching in the y direction, where

$$y_i = \frac{\tanh(a\xi_i)}{\tanh(a)} \tag{6.14}$$

$$\xi_i = -1 + 2\frac{i-1}{imax-1} \quad \text{for} \quad i = 1, \ldots, imax \tag{6.15}$$

$$a = \frac{1}{2}\ln\left[\frac{(1+b)}{(1-b)}\right] \quad \text{for} \quad 0 \leq b < 1. \tag{6.16}$$

The parameter b controls the stretching of the grid, and typically $b = 0.7 - 0.95$.

This resulted in control volume dimensions of 0.131 and 0.0654 with respect to the channel half-height, or 22.7 and 11.4 in wall units, in the x and z directions, respectively. The control volume nearest the wall had a nondimensional height of 0.0133, or 2.29 in wall units, in the y direction. The maximum spacing in the y direction was 0.0462, or 7.95 in wall units.

In order to minimize computational resources, the simulations were performed with the Smagorinsky SGS model with Van Driest damping at the walls. The Smagorinsky constant was $C_s = 0.08$, or $C_d = 0.0064$.

The simulations were typically run with 8 or 16 processors (hence, blocks) on an IBM SP-2. The fine grid simulations, for instance, required about 11 hours per 1000 time steps using 16 processors, or about twice that much with only 8 processors.

6.4 Results for Velocity Statistics

The velocity statistics were compared to the DNS results of Kim et al. (1987) and the experimental results of Niederschulte et al. (1990) for incompressible turbulent plane channel

flow. The DNS results were obtained by Kim et al. by directly solving the incompressible unsteady Navier-Stokes equations with no subgrid-scale model using about 4×10^6 grid points ($192 \times 129 \times 160$ in x, y, z) for nondimensional channel dimensions of $4\pi \times 2 \times 2\pi$. The Reynolds number was $\mathrm{Re}_\delta = 2800$, the same as the present simulations. The experiments of Niederschulte were performed specifically to examine the accuracy of Kim et al.'s DNS results. Therefore, the flow parameters were very similar, with a Reynolds number of $\mathrm{Re}_\delta = 2457$ or 2777 for two different cases. Good, but not exact, agreement was found between the experimental and DNS results.

Several globally averaged (in space and time) parameters for the entire solution domain are provided in Table 6.1 for the fine grid simulations with two different wall temperature boundary conditions. Those parameters available from the DNS and experimental results are also shown for comparison. The shear stress was slightly underpredicted by about 6 percent. The friction coefficient displayed in Table 6.1 is given by $C_f = 2\tau_w/(\rho_b u_b^2)$.

Table 6.1 Simulation parameters (average for entire solution domain) for fine grid

	β	Re_δ	k/V_r^2	k^+	u_τ	u_b/u_τ	C_f
Low heating (Specify $T_w(x)$)	-0.00395	2850	0.00749	1.95	0.0620	16.1	0.00768
Low heating (Specify q_w)	-0.00397	2800	0.00741	1.93	0.0619	16.1	0.00768
DNS	–	2800	–	–	–	15.6	0.00818
Experiments	–	2780	–	–	–	15.6	0.00829

The mean streamwise velocity profiles are shown in Figs. 6.2 and 6.3 in global and wall coordinates, respectively. The mean profile was obtained by averaging in both homogeneous directions (x and z) and in time for 8-10,000 time steps (denoted by <>). The velocity was normalized by the friction velocity as $u^+ = u/u_\tau$, where $u_\tau = \sqrt{\tau_w/\rho_w}$. The dash-dot line in Fig. 6.3 represents the law of the wall and the log law. The additive constant of 5.5 was used in the log law in contrast to the usual value of 5.0. This is a low Reynolds number correction suggested by Kim et al. (1987). As shown in the figures, the coarse grid results underpredicted the shear stress, resulting in large differences in the mean velocity profile. The fine grid results,

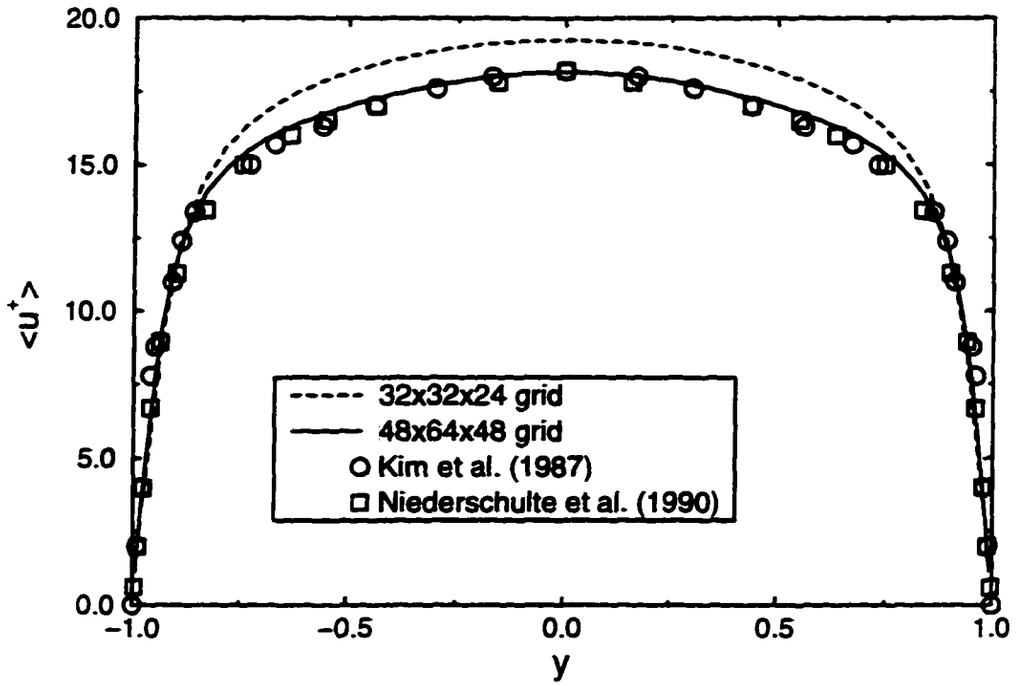

Figure 6.2 Mean velocity profile in global coordinates

however, agreed very well with the DNS and experimental results.

Following the nomenclature of Huang et al. (1995), the conventional Reynolds (or ensemble) average of a quantity is denoted as <>, and the Favre ensemble average as {}, where

$$\{f\} = < \rho f > / < \rho > . \tag{6.17}$$

Furthermore, a single prime,′, and a double prime,″, denote the turbulent fluctuations with respect to the Reynolds or Favre ensemble average, respectively. For the simulations with low heating in this chapter, the density variations were assumed to be small enough that the Reynolds and Favre average were equivalent. Thus, turbulent fluctuations were obtained with respect to simple Reynolds ensemble averages. This is not so in Chapter 7, where channel flows with high heating rates are considered. For the channel flows with low heating, the velocity fluctuations were obtained at each time step as

$$u_i' = u_i - < u_i >_{x,z} \tag{6.18}$$

where $<>_{x,z}$ denotes an average in the x and z directions. The ensemble averaged root-mean-

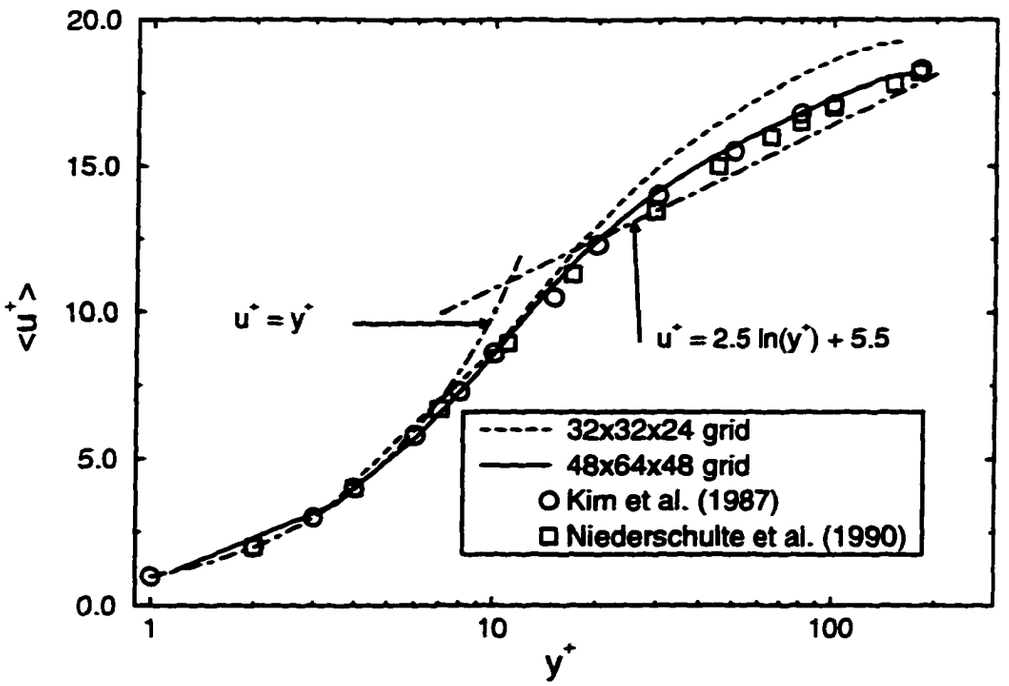

Figure 6.3 Mean velocity profile in wall coordinates

square (rms) values were subsequently obtained as, for example,

$$u'_{rms} = \sqrt{\frac{< u'^2 >}{N_{stat}}} \tag{6.19}$$

where <> denotes an average in x,z and in time, and N_{stat} is the number of time steps used to compute the statistics. The average turbulent kinetic energy is given by

$$k = \frac{1}{2} < u'_i u'_i > \tag{6.20}$$

and $k^+ = k/u_\tau^2$.

The uv velocity cross-correlation coefficient, $R(uv)$, is shown in Fig. 6.4, where

$$R(uv) = \frac{< u'v' >}{u'_{rms} v'_{rms}}. \tag{6.21}$$

Good agreement was obtained between the present coarse and fine grid results and the DNS and experimental results. Slight disagreement between the present, DNS, and experimental results is evident near the wall.

The rms velocity fluctuations are shown in Fig. 6.5. The coarse grid results exhibited the characteristic overprediction of the streamwise velocity fluctuations, and underprediction of

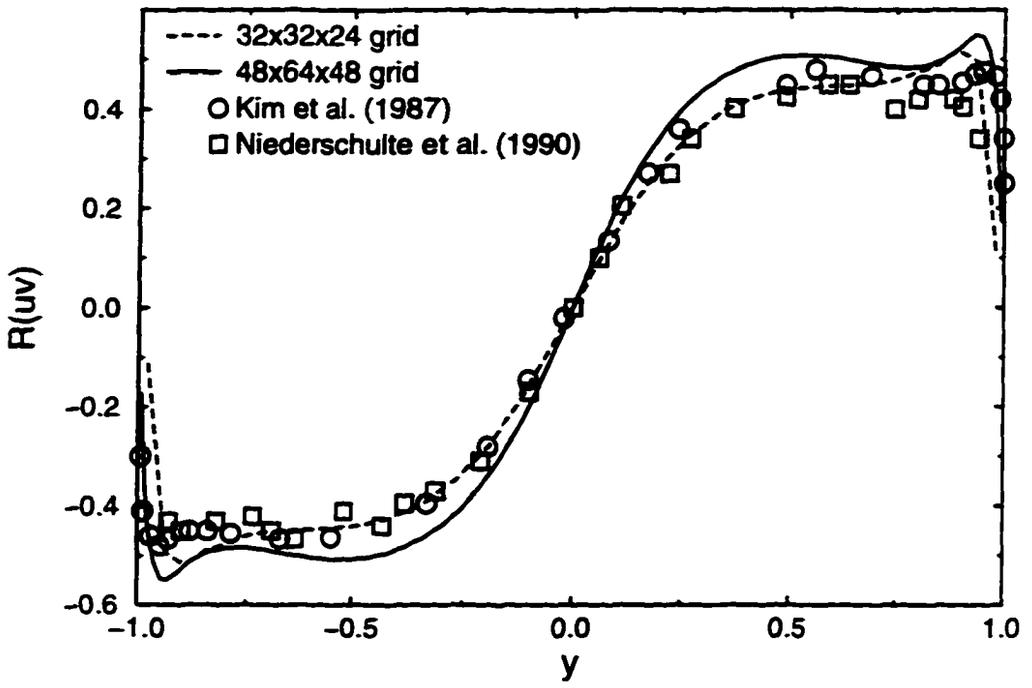

Figure 6.4 Velocity cross-correlation coefficient

the normal velocity fluctuations. The fine grid results show excellent agreement with the DNS and experimental results.

The skewness and flatness factors, which are third and fourth order moments, respectively, were also computed. They are given by

$$S(u_i) = \frac{< u_i'^3 >}{u_{i,rms}'^3} \tag{6.22}$$

and

$$F(u_i) = \frac{< u_i'^4 >}{u_{i,rms}'^4}. \tag{6.23}$$

The skewness represents the asymmetry of the turbulence statistics, and the flatness (or kurtosis) represents the departure of the variable from its *rms* value. The resulting skewness and flatness factors for the velocity fluctuations are shown in Figs. 6.6 and 6.7. More discrepancies are evident between the DNS and experimental results. The present results agree slightly less favorably with these higher order statistics, with the fine grid again showing the best agreement. However, the differences are well within the discrepancies between the experimental and DNS results.

It is not strictly valid to compare the LES resolved turbulence statistics with the DNS or experimental statistics. This is because the small scale contribution to the LES statistics is not included. Two options exist for a precise comparison: 1) attempt to account for the small-scale or unresolved contribution to the LES statistics, or 2) filter the DNS or experimental results to remove the small-scale contributions in a manner consistent with the LES numerical scheme. Option 1) is not possible with the current SGS model because the unresolved scales cannot be recovered. Option 2) is not possible for the DNS and experimental results used here because not enough information is available. The present comparison must rely on the assumption that the subgrid-scale contribution is small compared to the resolved contribution to the statistics.

6.5 Results for Temperature Statistics

The temperature statistics were compared to the passive scalar DNS results of Kasagi et al. (1992) and the LES results of Wang (1995). Kasagi et al. directly solved the unsteady incompressible Navier-Stokes equations for the velocity field. Once the velocity field was obtained at each time step, the scalar field, θ^+, was obtained by integrating the decoupled energy equation, where θ^+ is the dimensionless temperature parameter given by

$$\theta^+(x,y,z,t) = \frac{< T_w > (x) - T(x,y,z,t)}{T_\tau}. \tag{6.24}$$

The friction temperature is $T_\tau = q_w/(\rho_w c_p u_\tau)$, and $< T_w >$ is the average wall temperature.

An isoflux condition was enforced at the upper and lower walls by enforcing $\theta^+ = 0$ at the walls, which also forced the temperature fluctuations at the wall to be zero. When the energy equation is cast in terms of θ^+, a source term is obtained that represents the constant streamwise temperature gradient which is related to isoflux conditions for a fully developed thermal field. In this way, the desired temperature gradient is enforced at each point in the solution domain. For the present simulations, the streamwise temperature gradient is only enforced at the walls (via a fixed linear temperature distribution) and from inlet to outlet (via the step-wise periodic temperature boundary condition). The consequences of these differences will be further discussed later in this section.

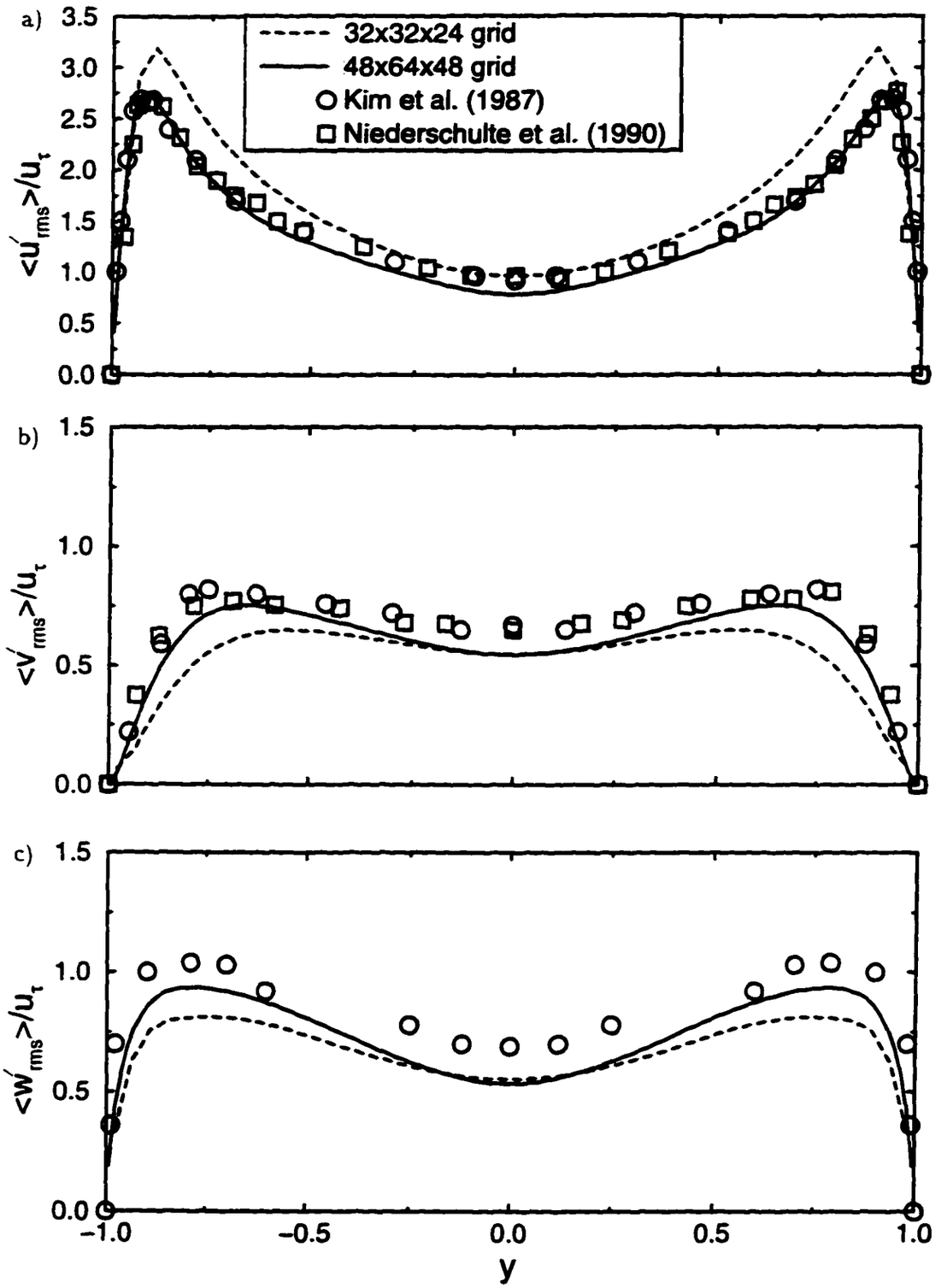

Figure 6.5 Root-mean-square of velocity fluctuations normalized by wall friction velocity

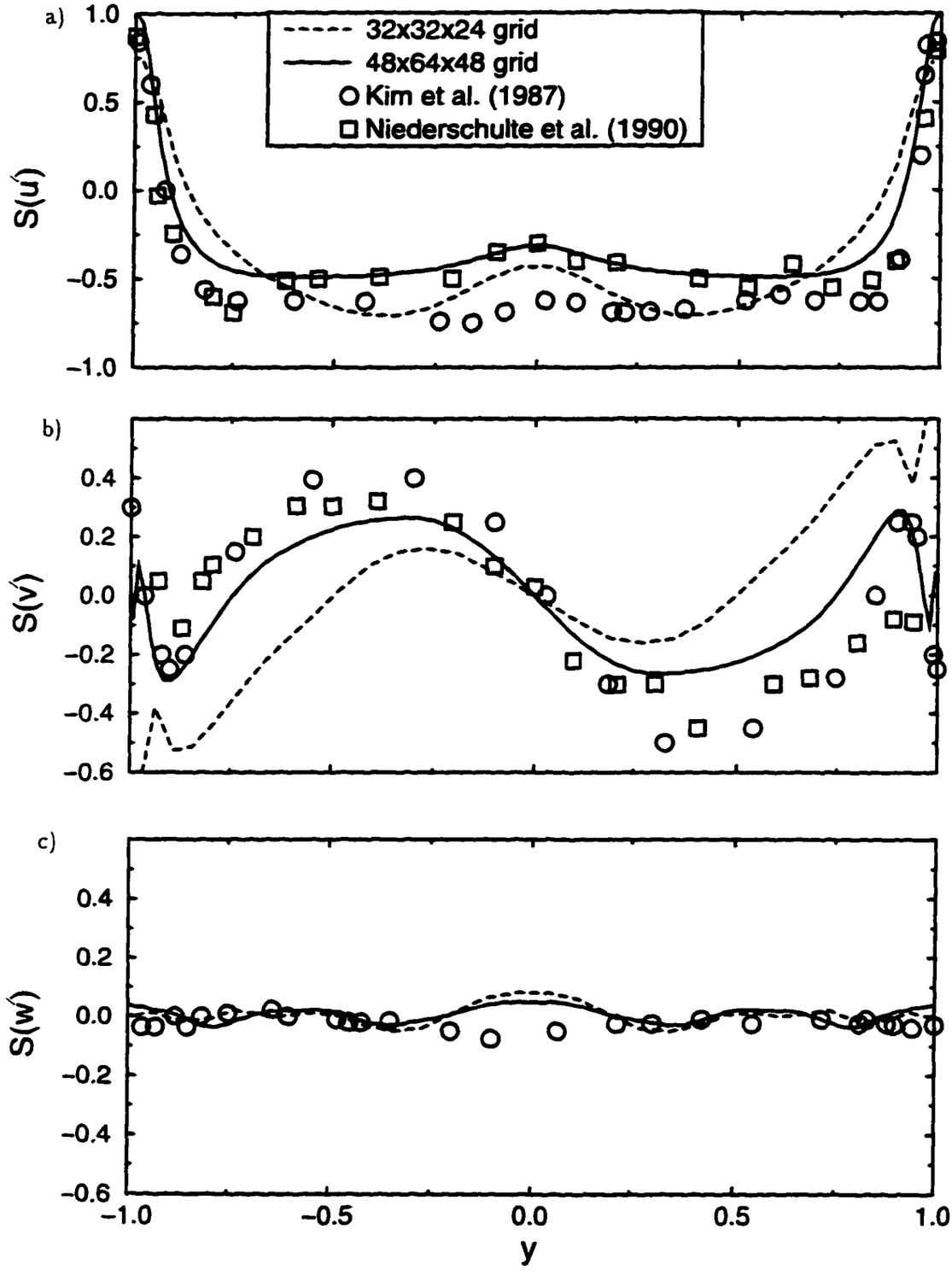

Figure 6.6 Skewness factor of the velocity fluctuations

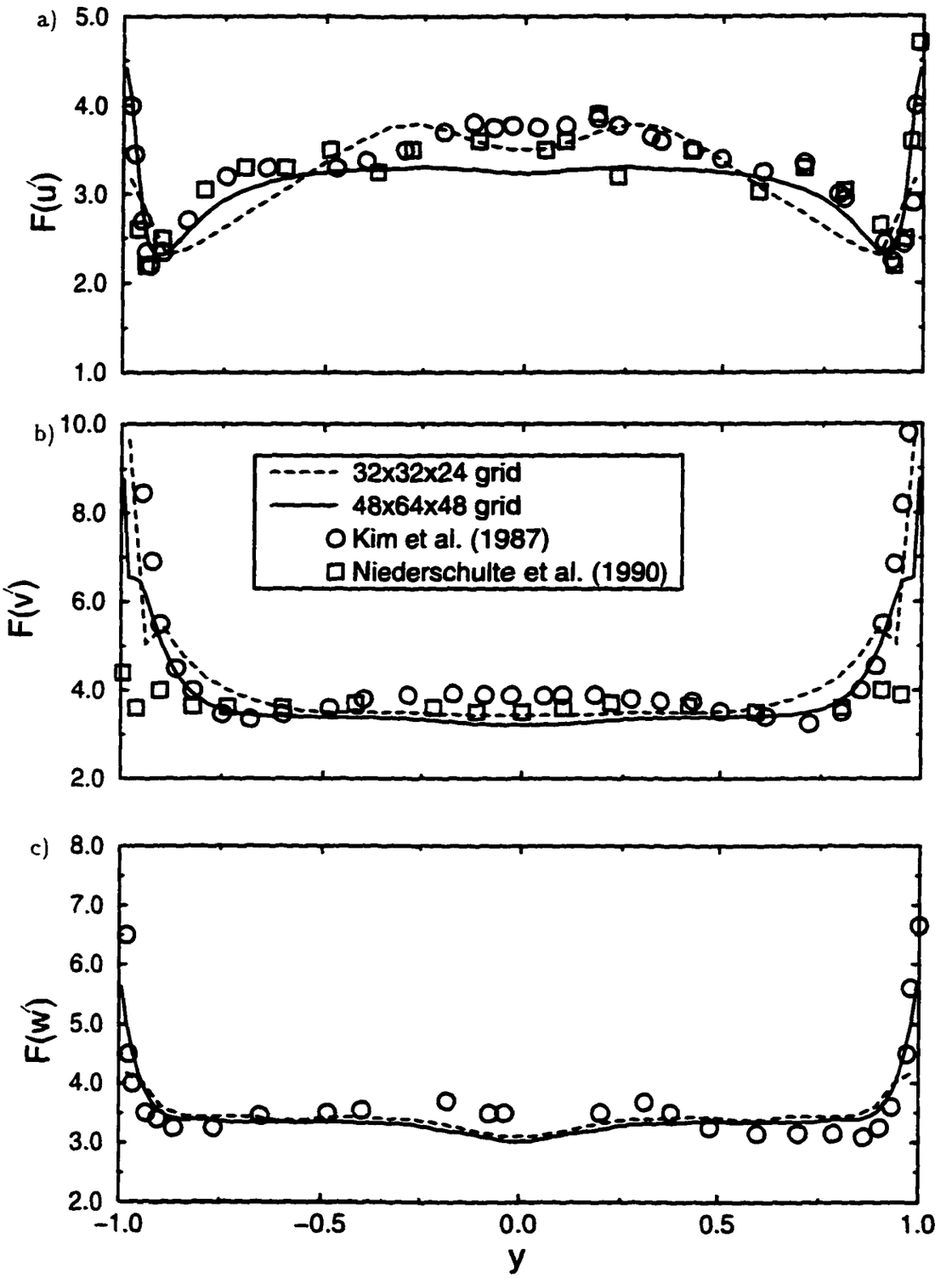

Figure 6.7 Flatness factor of the velocity fluctuations

Kasagi et al. used a 128^3 grid with a $5\pi \times 2 \times 2\pi$ domain. The Reynolds number was $Re_\delta = 2290$. about 18 percent lower than the Reynolds number for the present simulations.

Wang (1995) performed LES of the same isoflux channel flow by solving the filtered unsteady incompressible Navier-Stokes equations. A dynamic SGS model was employed. The energy equation was cast in terms of a nondimensional temperature parameter, again resulting in a source term in the energy equation which enforced the linear streamwise temperature gradient at each point in the solution domain. Wang used a 65^3 grid with a $2\pi \times 2 \times \pi$ domain and $Re_\delta = 2656$.

The present simulation was performed with a very low wall heat flux ($q_w = 1.0 \times 10^{-4}$) in order to minimize the density variations so that the comparison to passive scalar results was valid. This resulted in a wall-to-bulk temperature ratio of $T_w/T_b = 1.024$ and a streamwise temperature difference of $\Delta T_x/T_{b,in} = 6.3 \times 10^{-4}$.

Because the nondimensional temperature parameter, θ^+, is invariant in the streamwise direction for the isoflux conditions, the temperature statistics were computed in the same manner as the velocity statistics, i.e. ensemble averages were performed in the x and z directions and in time.

The mean temperature profiles are plotted in wall coordinates in Fig. 6.8. All simulations agree well with the linear profile, $\theta^+ = \mathrm{Pr}\, y^+$, in the conductive sublayer. The present simulation compares well with the LES of Wang for both the coarse and fine grids, but all overpredict the temperature in the logarithmic region compared to the DNS results of Kasagi et al. and Kader's (1981) empirical log-law ($\theta^+ = 2.78 \ln y^+ + 2.09$) formula. The von Karman constant of Kader's profile, $1/\kappa_\theta = 2.78$ or $\kappa_\theta = 0.36$, is appreciably smaller than the value generally accepted for high Reynolds numbers, $\kappa_\theta = 0.47$. Kader's formula takes into account Reynolds number and Prandtl number effects. The present results, which are in close agreement with Wang's results, do not match Kasagi's results exactly due to differing Reynolds numbers.

The *rms* of the temperature fluctuations, shown in Fig. 6.9, were largely overpredicted by the present simulations. The overprediction is significantly worse for the fine grid compared to the coarse grid. Recall that both Kasagi et al. and Wang were able to enforce the desired

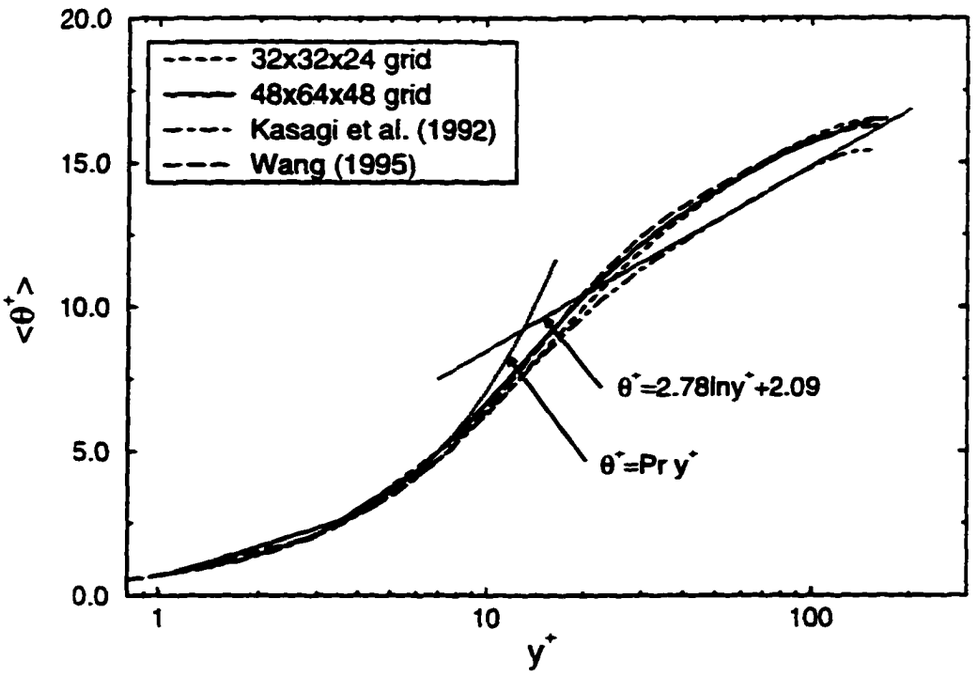

Figure 6.8 Mean temperature distribution in wall coordinates

constant streamwise temperature gradient in the energy equation with a source term. The current approach, however, only enforced the desired temperature gradient via the fixed linear wall temperature and the step-wise periodic temperature boundary condition. Due to the small temperature differences in the streamwise direction, the desired effect was difficult to obtain in the middle regions of the channel, especially considering that ΔT_x is smaller than the temperature fluctuations (T_{rms} is about 1.6×10^{-3} at the channel center). The problem is worse for the fine grid because propagating the temperature differences from the boundaries is more difficult. Later simulations with higher heating levels, presented in Chapter 7, had larger temperature differences, and the desired effect was obtained quite well.

The streamwise and wall-normal turbulent heat fluxes are shown in Figs. 6.10 and 6.11. The present streamwise turbulent heat flux compares better to the DNS results of Kasagi et al. than do the LES results of Wang. The reason for this is not clear. Wang shows better agreement with the DNS results of Kasagi et al. for the wall-normal turbulent heat flux. It is interesting that despite the disagreement in $< \theta'_{rms} >$, fairly good agreement was obtained

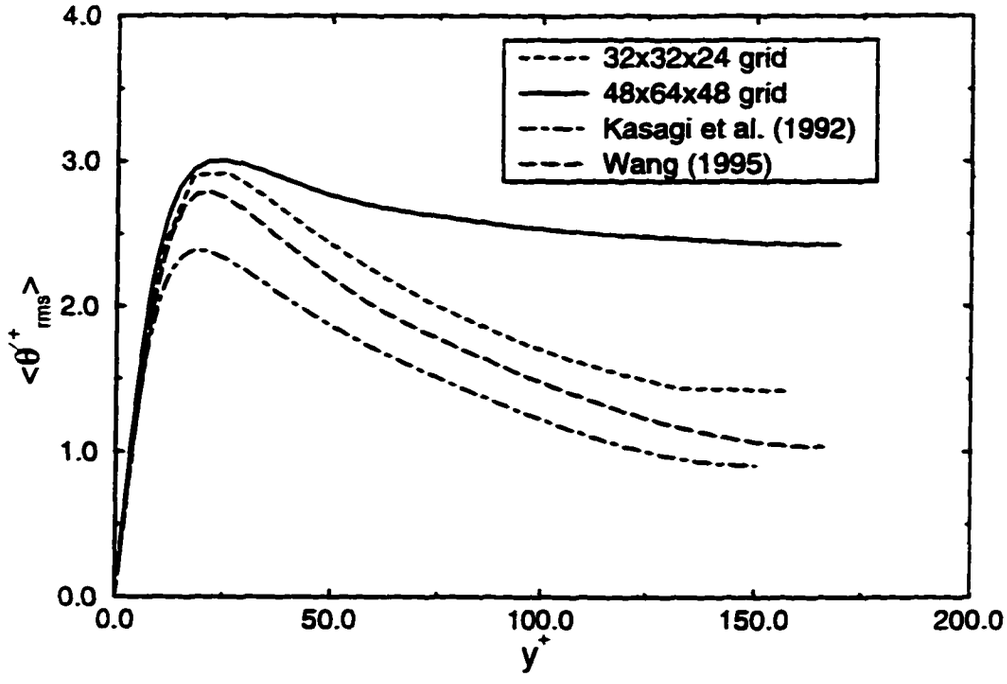

Figure 6.9 Root-mean-square of the temperature fluctuations normalized by friction temperature

between the present results and DNS results for the turbulent heat fluxes. This is most likely because the velocity fluctuations dominate the temperature fluctuations at low heating levels.

The uv and $v\theta$ cross-correlation coefficients are shown in Fig. 6.12. Kasagi et al. observed that these two correlations were nearly identical for their simulations, indicating that the wall-normal turbulent heat flux and the Reynolds shear stress are generated by similar turbulence mechanisms. The present coarse grid results show similar behavior, but the fine grid results do not. Finally, the $u\theta$ cross-correlation coefficient is shown in Fig. 6.13, where the coarse grid results are again superior to the fine grid results for the reasons discussed above.

6.6 Comparison to Empirical Correlations

The average friction coefficients and Nusselt numbers were compared to various empirical correlations. The friction coefficient is defined as

$$C_f = f = \frac{2\tau_w}{\rho_b u_b^2} \tag{6.25}$$

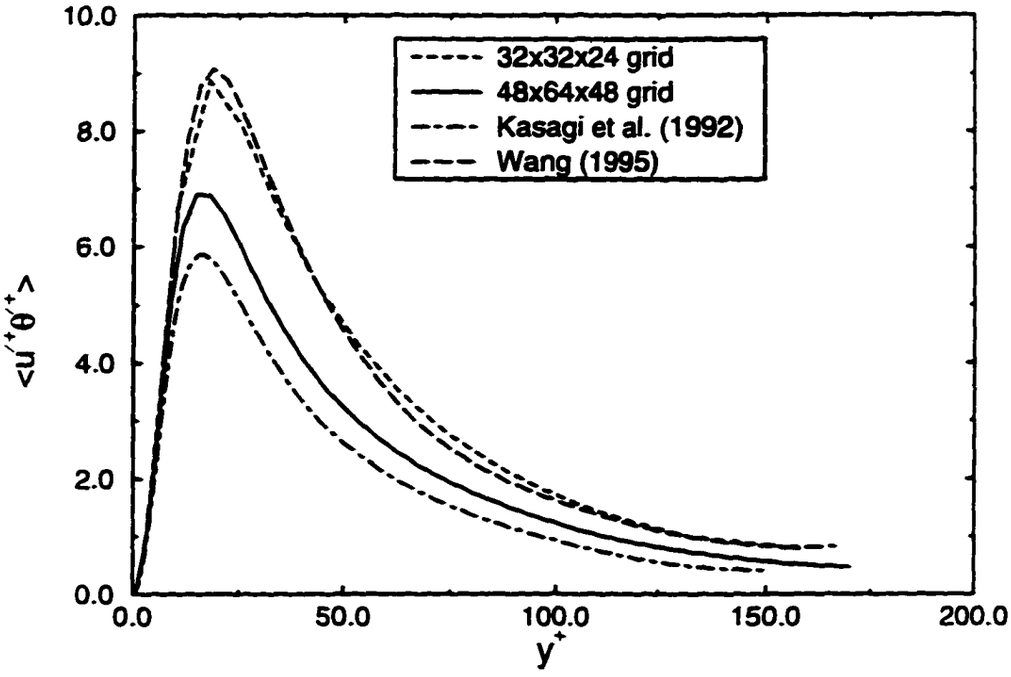

Figure 6.10 Distribution of streamwise turbulent heat flux

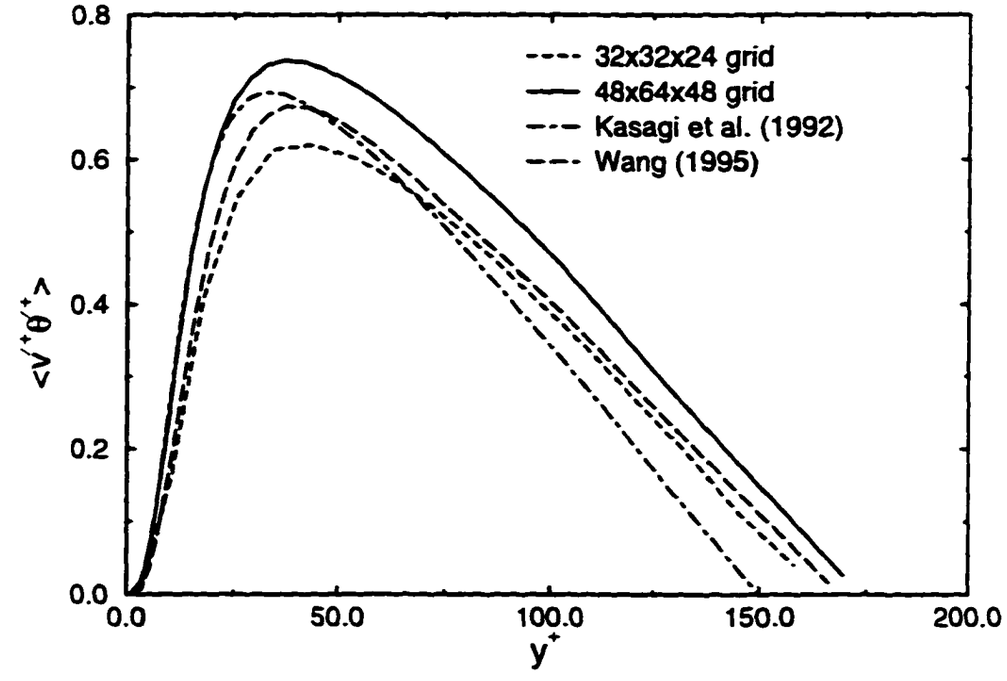

Figure 6.11 Distribution of wall-normal turbulent heat flux

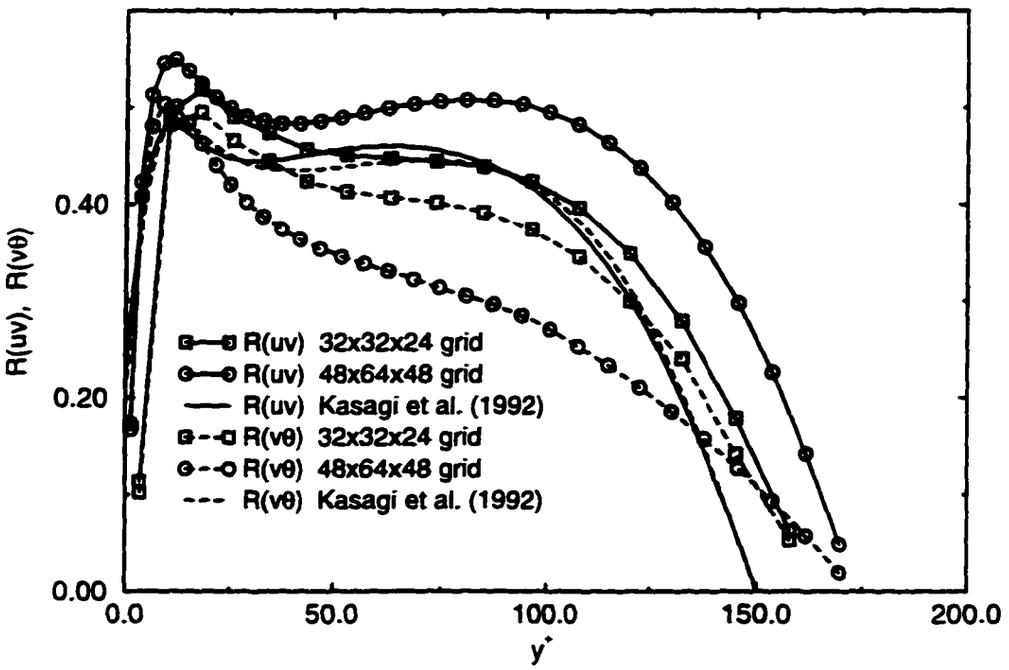

Figure 6.12 Cross-correlation coefficient between wall-normal velocity and temperature

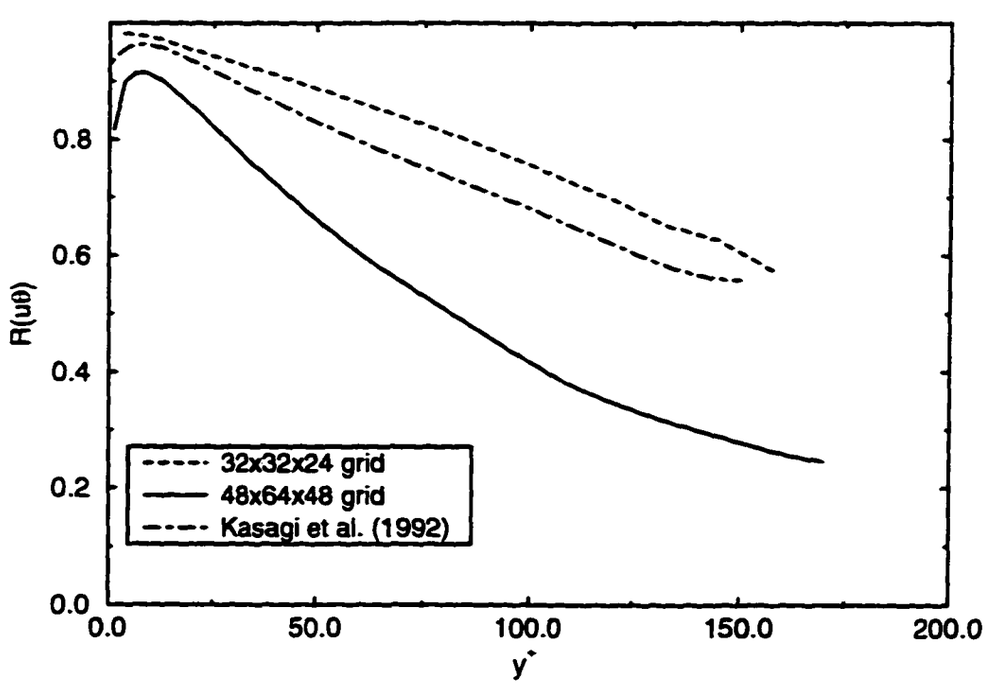

Figure 6.13 Cross-correlation coefficient between streamwise velocity and temperature

and the Nusselt number based on bulk properties and the channel hydraulic diameter, $D_h = 4\delta$, is given by

$$\mathrm{Nu}_D = \frac{hD_h}{k_b}. \tag{6.26}$$

Empirical correlations in the literature have been developed for the friction coefficient and Nusselt number using mostly two methods: 1) find a best fit curve of experimental data or 2) adjust constants in theoretical equations to best fit experimental data. An exhaustive review of correlations for constant and variable property conditions is provided by Kakaç (1987).

An example of the second method is due to Petukhov and Popov (1963). They performed theoretical calculations for fully developed turbulent flow with constant properties in circular tubes with constant heat flux boundary conditions. The resulting correlations are

$$\mathrm{Nu}_D = \frac{(f/2)\mathrm{Re}_D\mathrm{Pr}}{(1 + 13.6f) + (11.7 + 1.8\mathrm{Pr}^{-1/3})(f/2)^{1/2}(\mathrm{Pr}^{2/3} - 1)} \tag{6.27}$$

and

$$f = (3.64 \log_{10} \mathrm{Re}_D - 3.28)^{-2} \tag{6.28}$$

where $\mathrm{Re}_D = u_b D_h/\nu_b$. This correlation is valid for $10^4 < \mathrm{Re}_D < 5 \times 10^5$ and $0.5 < \mathrm{Pr} < 2000$ with 1% error. A simpler form of the above correlation was given by Petukhov and Kirillov (Petukhov, 1970) as

$$\mathrm{Nu}_D = \frac{(f/2)\mathrm{Re}_D\mathrm{Pr}}{1.07 + 12.7(f/2)^{1/2}(\mathrm{Pr}^{2/3} - 1)} \tag{6.29}$$

which is valid for $10^4 < \mathrm{Re}_D < 5 \times 10^6$ and $0.5 < \mathrm{Pr} < 200$ with 5 to 6% error.

Gnielinski (1976) modified the Petukhov-Kirillov correlation to cover a lower Reynolds number range ($2300 < \mathrm{Re}_D < 5 \times 10^6$) as

$$\mathrm{Nu}_D = \frac{(f/2)(\mathrm{Re}_D - 1000)\mathrm{Pr}}{1 + 12.7(f/2)^{1/2}(\mathrm{Pr}^{2/3} - 1)} \tag{6.30}$$

where

$$f = (1.58 \ln \mathrm{Re}_D - 3.28)^{-2}. \tag{6.31}$$

An early and simple correlation was provided by McAdams (1954) as

$$\mathrm{Nu}_D = 0.021\mathrm{Re}_D^{0.8}\mathrm{Pr}^{0.4} \tag{6.32}$$

based on data for common gases and Pr $\approx$ 0.7. Kays and Crawford (1993) recommend the correlations given by

$$\mathrm{Nu}_D = 0.022\mathrm{Re}_D^{0.8}\mathrm{Pr}^{0.5} \tag{6.33}$$

and

$$f = 0.046\mathrm{Re}_D^{-0.2}. \tag{6.34}$$

The Prandtl correlation, due to von Karman and Nikuradse, is an implicit formula for the friction coefficient. An explicit form that agrees with the Prandtl correlation within $\pm 0.1\%$ was developed by Techo, Tickner, and James (Kakaç, 1987), given by

$$\frac{1}{f} = \left(1.7272 \ln \frac{\mathrm{Re}_D}{1.964 \ln \mathrm{Re}_D - 3.8215}\right)^2. \tag{6.35}$$

The majority of the correlations were developed for turbulent flows in circular tubes. Kays and Crawford (1993) claim the correlations are equally valid for noncircular tubes as long as the Reynolds number is based on the hydraulic diameter and there are no sharp corners (as in a square duct or triangular tube). However, as reported by Kakaç (1987), modified correlations have been developed for rectangular channels of various aspect ratios. For infinite parallel plates, for example, the friction coefficients were higher by as much as 11 percent and Nusselt numbers were higher by 7 to 11 percent compared to those for circular tubes at the same Reynolds numbers.

The average Nusselt number for the turbulent simulations discussed in this chapter are compared to the correlation recommended by Kays and Crawford in Table 6.2. Wang obtained the best agreement with the correlation, followed by the present simulation, with Kasagi showing a 12.4 percent difference.

Table 6.2 Comparison of Nusselt numbers for turbulent simulations

Simulation	Re_D	Nu_D	Kays & Crawford Nu_D
LES (present, 48 × 64 × 48 grid)	11,200	33.6	32.2
DNS (Kasagi et al., 1992)	9,160	30.8	27.4
LES (Wang, 1995)	10,620	30.8	30.8

More extensive comparisons to various empirical correlations are presented in Tables 6.3 and 6.4 for the two present simulations with different wall thermal boundary conditions (and slightly different Reynolds numbers). Agreement with the correlations is excellent for the friction coefficient (less than 3 percent error for all) and good for the Nusselt number (less than 8 percent error for all). Overall, the friction coefficient, and especially the Nusselt number, are slightly overpredicted compared to the correlations. Better agreement was obtained with the correlation of Gnielinski (1976), which was modified specifically for lower Reynolds numbers.

Table 6.3 Comparison to constant property correlations for low heating with fixed wall temperature, $T_w(x)$

Correlation	Equation	C_f	% error	Nu_D	% error
Present simulation	—	0.00768	—	34.5	—
Techo, Tickner, and James	6.35	0.00746	3.0	—	—
McAdams (1954)	6.32	—	—	32.2	7.2
Petukhov and Popov (1963)	6.27	0.00758	1.4	32.9	4.8
Petukhov and Kirillov (1970)	6.29	0.00758	1.4	33.7	2.5
Gnielinski (1976)	6.30	0.00759	1.2	33.3	3.6
Kays and Crawford (1993)	6.33	0.00710	8.2	32.6	5.9

Table 6.4 Comparison to constant property correlations for low heating with specified wall heat flux, q_w

Correlation	Equation	C_f	% error	Nu_D	% error
Present simulation	—	0.00768	—	34.28	—
Techo, Tickner, and James	6.35	0.00749	2.5	—	—
McAdams (1954)	6.32	—	—	31.8	7.8
Petukhov and Popov (1963)	6.27	0.00761	0.8	32.6	5.3
Petukhov and Kirillov (1970)	6.29	0.00761	0.8	33.3	3.0
Gnielinski (1976)	6.30	0.00762	0.7	32.9	4.2
Kays and Crawford (1980)	6.33	0.00713	7.7	32.2	6.5

6.7 Summary

The simulation of turbulent plane channel flow with (low) constant wall heating was performed. The velocity statistics were compared to DNS and experimental results, while the

temperature statistics were compared to DNS and LES of a passive scalar field. The $48 \times 64 \times 48$ fine grid was found necessary and sufficient to provide accurate results for the velocity statistics. Both mean and higher order statistics were found to be in good agreement with the DNS and experimental results, even with a moderate amount of grid with a second-order accurate method and simple SGS modeling.

The mean temperature compared well to DNS results, while the temperature fluctuations were grossly overpredicted near the channel center line. The discrepancies in the temperature fluctuations were thought to be related to the treatment of the very small streamwise temperature gradient, and not due to deficiencies in the finite volume formulation or SGS modeling. Good agreement was obtained with various empirical correlations for the friction coefficient and Nusselt number.

CHAPTER 7 RESULTS FOR TURBULENT PLANE CHANNEL FLOW WITH HIGH HEAT TRANSFER AND VARIABLE PROPERTIES

7.1 Introduction

This chapter deals with the LES of turbulent plane channel flow with constant wall heating and cooling rates of magnitudes large enough to cause significant property variations. Comparisons were made to limited experimental data for such flows, which mainly consist of correlations for parameters such as friction factors and Nusselt numbers. Comparisons were also made to simulations of low heating rates, which were discussed in Chapter 6. The effects of high heating and cooling rates on the mean flow and turbulence quantities were investigated.

7.2 Problem Description

The problem of interest was turbulent, nonreacting flow of air in a two-dimensional plane channel. At the upper and lower walls of the channel, a constant heat flux was applied of sufficient magnitude to cause significant variation in the temperature-dependent fluid properties. For gases, the density, thermal conductivity, and molecular viscosity all vary at about the same rate as the absolute temperature. The variation can be represented with a power-law dependence with exponents of 0.7–0.8 for both the thermal conductivity and viscosity. The specific heats vary only slightly with temperature, and the Prandtl number does not vary significantly. Therefore, for the present simulations, the molecular viscosity was specified with the power-law, $\mu = T^{0.7}$, the Prandtl number was assumed to have a constant value of $\mathrm{Pr} = 0.71$, and the specific heats were assumed to be constant. The ratio of specific heats was $\gamma = 1.4$.

The flows were run at low Mach numbers ($M_r = 0.001$) so that the effects of viscous

dissipation were negligible. The Froude number, $Fr = Gr/Re^2$, where Gr is the Grashof number, was small so that buoyancy effects were assumed to be negligible. The Peclet number was small such that axial conduction was negligible. Although the simulation parameters were set up so that viscous dissipation, axial conduction, and buoyancy were negligible, the viscous dissipation and axial conduction terms remained in the governing equations being solved: the buoyancy terms were not included in the governing equations.

For constant wall heating (or cooling) with constant fluid properties under the assumptions given above, turbulent channel flows approach a fully developed state in which the time averaged streamwise velocity, u, and the nondimensional temperature, $\theta = (T_w - T)/(T_w - T_b)$, profiles no longer change in the streamwise direction, and the wall-normal velocity, v, is zero. Consequently, the local, wall, and bulk temperatures increase (or decrease) linearly along the channel at the same rate, which is directly related to the amount of heat being added (or removed) from the flow.

For strong heating or cooling, the assumption of constant fluid properties is no longer valid. For air flows, the large variations in temperature result in significant variations in density, molecular viscosity, and thermal conductivity. In general, a fully developed state is never achieved. The temperature increases (or decreases) in the streamwise direction leading to increasing (or decreasing) density. The velocity must correspondingly increase (or decrease) to maintain a constant mass flow rate in the channel. Also, the temperature variations lead to changes in the the fluid thermal conductivity at the wall, so the temperature gradient at the wall, and hence the nondimensional temperature profiles, changes to maintain the constant wall heat flux.

Performing the LES of a developing channel flow with strong heating or cooling conditions is beyond the capability of current supercomputers. Fortunately, far downstream of the entry region, typically 20 to 40 tube diameters, experiments show that the flow evolves into a "quasi-developed" state (McEligot et al., 1965), where thermal entry effects are no longer important. This is the region of interest for the simulations discussed in this chapter.

7.3 Quasi-Developed Assumption

In this section, two calculations of laminar, two-dimensional, constant heat flux channel flow are compared. The first calculation was of the hydrodynamically and thermodynamically developing channel flow, where the flow develops from uniform conditions at the inlet to the downstream, quasi-developed region. The second calculation used "stepwise" periodic boundary conditions, described later in this section, to compute a short segment of the channel in the downstream, or quasi-developed region. Agreement between the two calculations validated the assumed stepwise periodic boundary conditions, which were subsequently used for turbulent simulations.

7.3.1 Developing Laminar Channel Flow

The first calculation, referred to as the "developing channel" calculation throughout the remainder of this chapter, was initially performed to better understand the downstream region, as well as to validate the stepwise periodic boundary conditions. The bulk Reynolds number based on hydraulic diameter was $Re_D = 80$, and the nondimensional length of the channel was $L_x = 10$ (with respect to the channel half-height). This low Reynolds number was chosen to minimize the length of the channel. The nondimensional wall heat flux was $Q^+ = q_w D_h/(k_b T_b) = 20$, where q_w is the wall heat flux. D_h is the hydraulic diameter, T_b is the bulk temperature, and k_b is the thermal conductivity based on T_b. The inlet flow was uniform, with the total pressure, total temperature, and streamwise velocity being specified, while the static pressure was extrapolated from the interior flow domain. The desired Reynolds number was obtained by specifying the appropriate static pressure at the outlet, while all other variables were extrapolated at the outlet.

The resulting contours of density, streamwise velocity, streamwise momentum, and temperature are shown in Fig. 7.1. The streamwise variation in ρ, u, and T are large due to the low Reynolds number and strong heating. After the initial developing region ($x < 4$) of the channel, it is clear from Fig. 7.1 that the flow asymptotically achieved a quasi-developed state. The profile shapes were essentially unchanged, even though the absolute value was continually

increasing (for u and T) or decreasing (for ρ). The streamwise momentum profile was nearly invariant in the streamwise direction.

Interrogation of the solution revealed that the following conditions held *approximately* in the downstream region ($x > 5$):

$$\frac{\partial(\rho u)}{\partial x} = 0 \tag{7.1}$$

$$\frac{\partial v}{\partial x} = 0 \quad ; \quad v \neq 0 \tag{7.2}$$

$$\frac{\partial p}{\partial x} = \text{constant} \tag{7.3}$$

$$\frac{\partial T}{\partial x} = \text{constant.} \tag{7.4}$$

Thus, it appeared that a short section of the downstream region could be computed in a "stepwise periodic" manner with the following streamwise boundary conditions:

$$\rho u(0, y) = \rho u(L_x, y) \tag{7.5}$$

$$v(0, y) = v(L_x, y) \tag{7.6}$$

$$w(0, y) = w(L_x, y) \tag{7.7}$$

$$p_p(0, y) = p_p(L_x, y) \tag{7.8}$$

$$T(0, y) = T(L_x, y) - \Delta T_x, \tag{7.9}$$

where L_x is the length of the channel in the streamwise direction, and p_p is the periodic component of the pressure, $p(x, y) = 3x + p_p(x, y)$.

The temperature difference, ΔT_x, in Eq. 7.9 is related to the net heat transferred to the flow in the solution domain, and was found by integrating the energy equation around the boundaries. As discussed in Chapter 6, for constant properties ΔT_x is given by

$$\Delta T_x = \frac{q_w}{\dot{m}/A_c} L_x. \tag{7.10}$$

However, for variable properties ΔT_x is a function of y because the streamwise temperature gradient varies in the y direction.

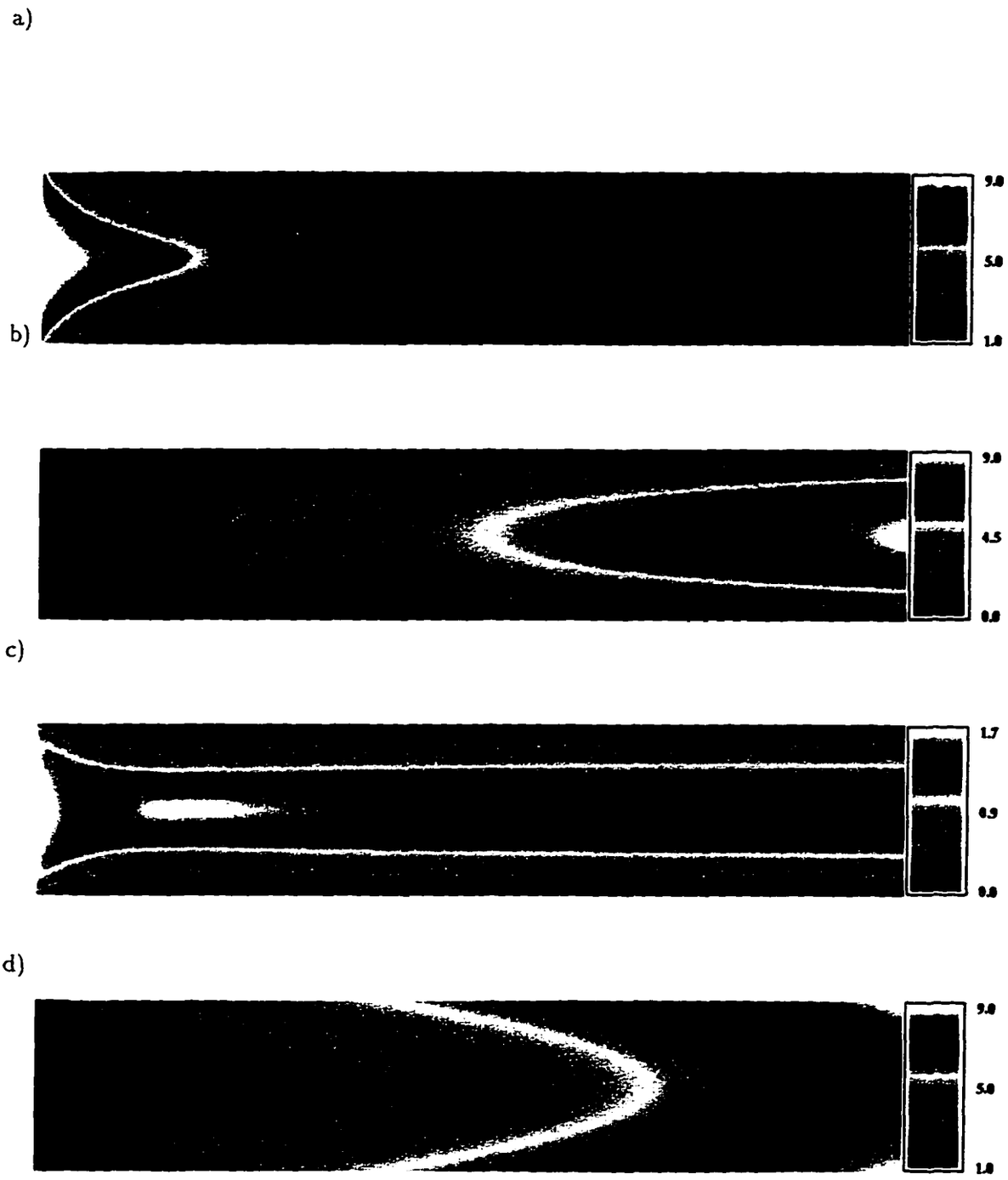

Figure 7.1 Two-dimensional, laminar, developing channel flow with constant wall heat fluxes: a) density, ρ; b) streamwise velocity, u; c) streamwise momentum, ρu; and d) temperature, T

The developing channel calculation indicated that this variation could be approximated by a linear function of y as

$$\Delta T_x(y) = c_1|y| + c_2. \tag{7.11}$$

By specifying the wall streamwise temperature gradient and the bulk temperature rise for the channel, the constants c_1 and c_2 were derived as discussed in Appendix E, giving

$$c_1 = \frac{\Delta T_b - \Delta T_w}{I_{\rho uy} - 1} \tag{7.12}$$

$$c_2 = \frac{I_{\rho uy}\Delta T_w - \Delta T_b}{I_{\rho uy} - 1}, \tag{7.13}$$

where

$$I_{\rho uy} = \frac{1}{2\rho_b u_b}\int_{-1}^{1} \rho u|y|dy. \tag{7.14}$$

7.3.2 Quasi-Developed Laminar Channel Flow

The purpose of the second laminar calculation was to attempt to validate the stepwise periodic boundary conditions for the quasi-developed region given by Eqs. 7.5 through 7.9. A laminar calculation was made of a short section of the downstream region of nondimensional length $L_x = 0.5$. This computation is referred to as the "quasi-developed" channel flow in the remainder of this chapter.

The values of ΔT_b and ΔT_w in Eqs. 7.12 and 7.13 were specified. However, several trials were required to obtain values of these parameters that provided the desired wall heat flux and net heat transfer to the channel. The pressure gradient parameter, β, was adjusted iteratively as in Chapter 6 to provide the desired mass flow rate.

The results for the quasi-developed channel and the developing channel flows are compared in Figs. 7.2 through 7.6. The streamwise variation of the bulk density, velocity, and temperature are shown in Fig. 7.2, and the streamwise variation of the wall-to-bulk temperature ratio, friction coefficient, and Nusselt number, all based on bulk properties, are shown in Fig. 7.3. The results demonstrated excellent agreement between the two computations for these parameters.

Profiles of the streamwise velocity, wall-normal velocity, and temperature, normalized by the local bulk properties, are shown in Figs. 7.4, 7.5, and 7.6, respectively, at a streamwise

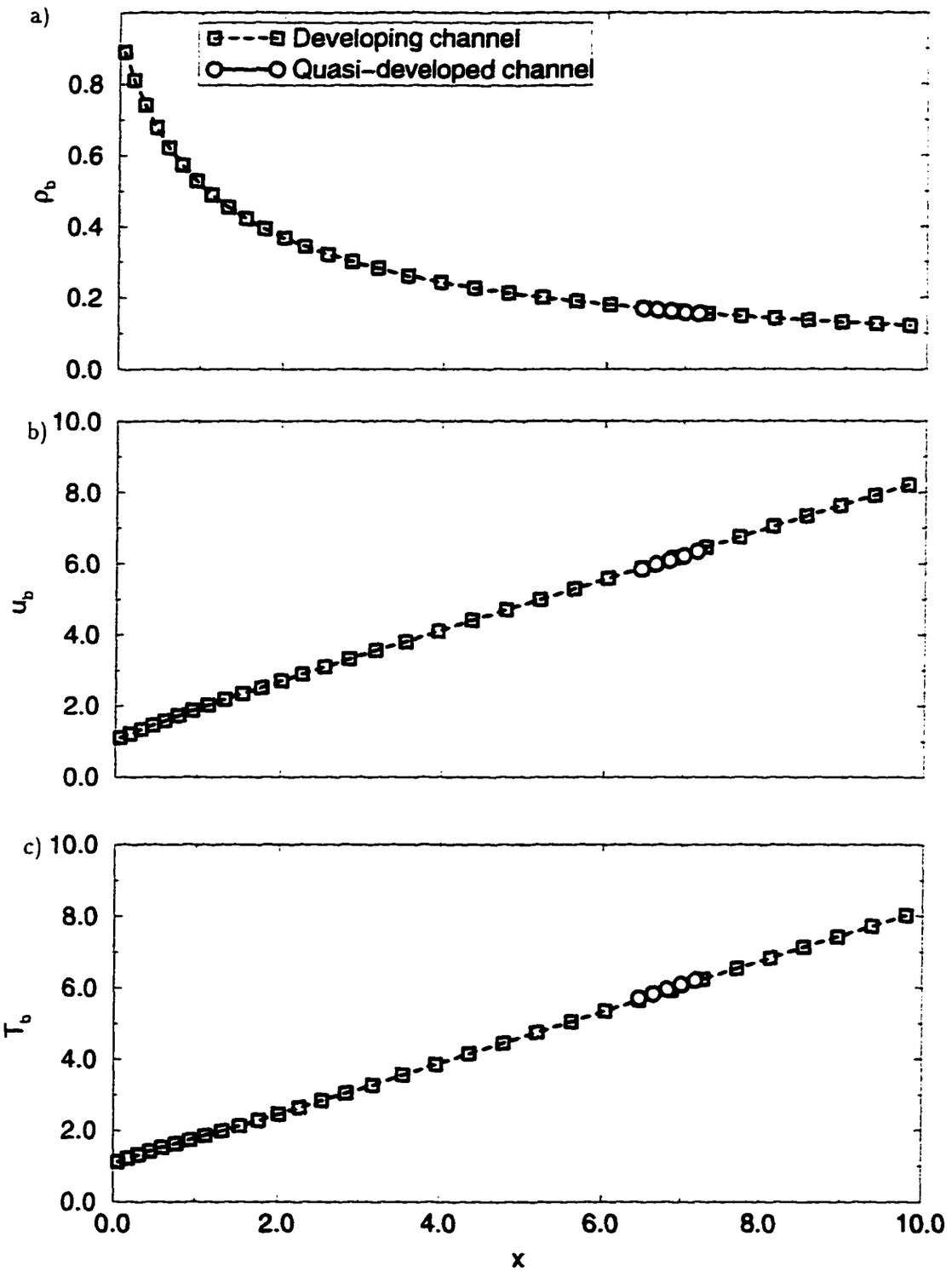

Figure 7.2 Streamwise variation of bulk properties for two-dimensional, laminar, constant heat flux channel flow

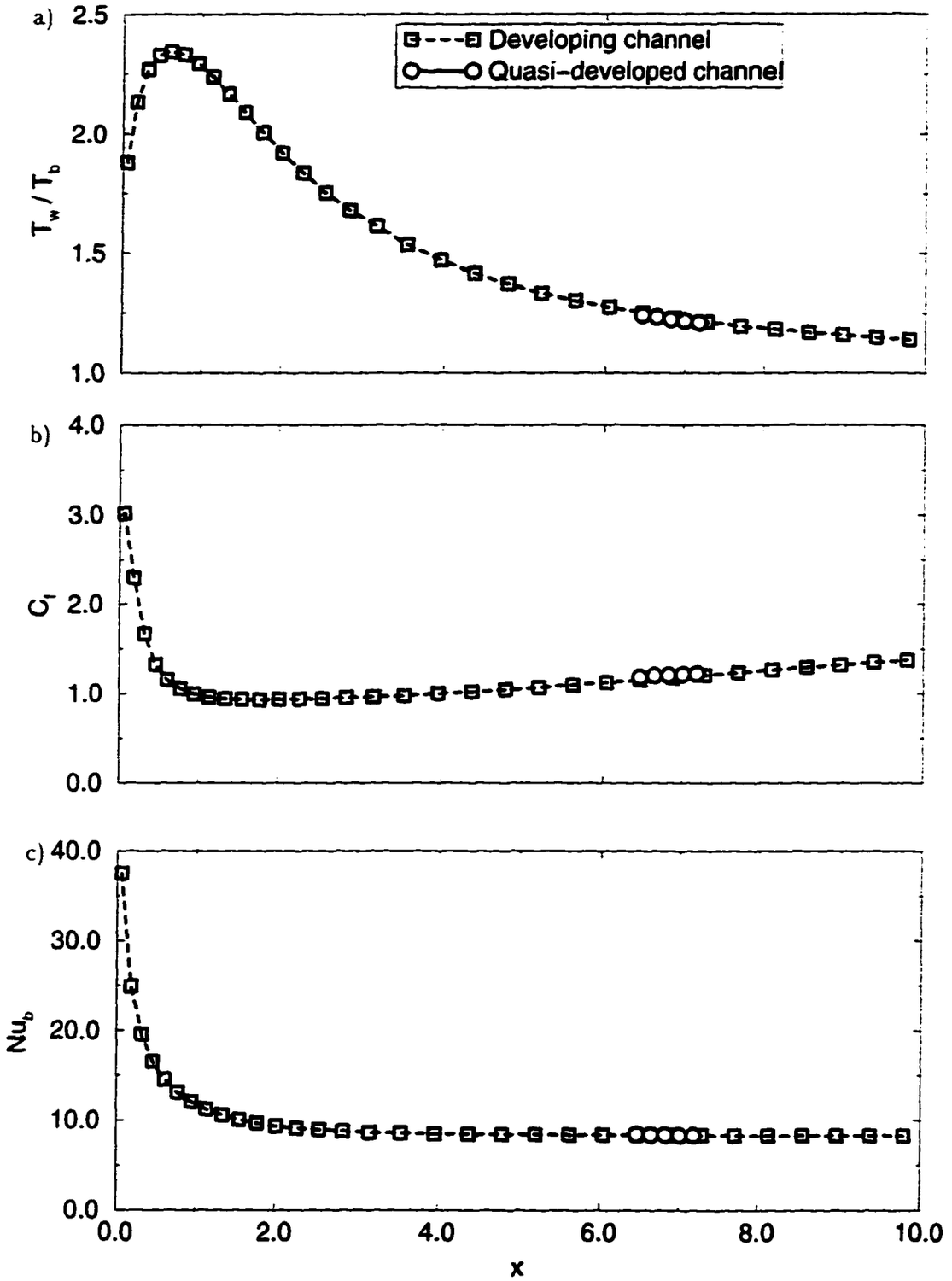

Figure 7.3 Streamwise variation of flow parameters for two-dimensional, laminar, constant heat flux channel flow

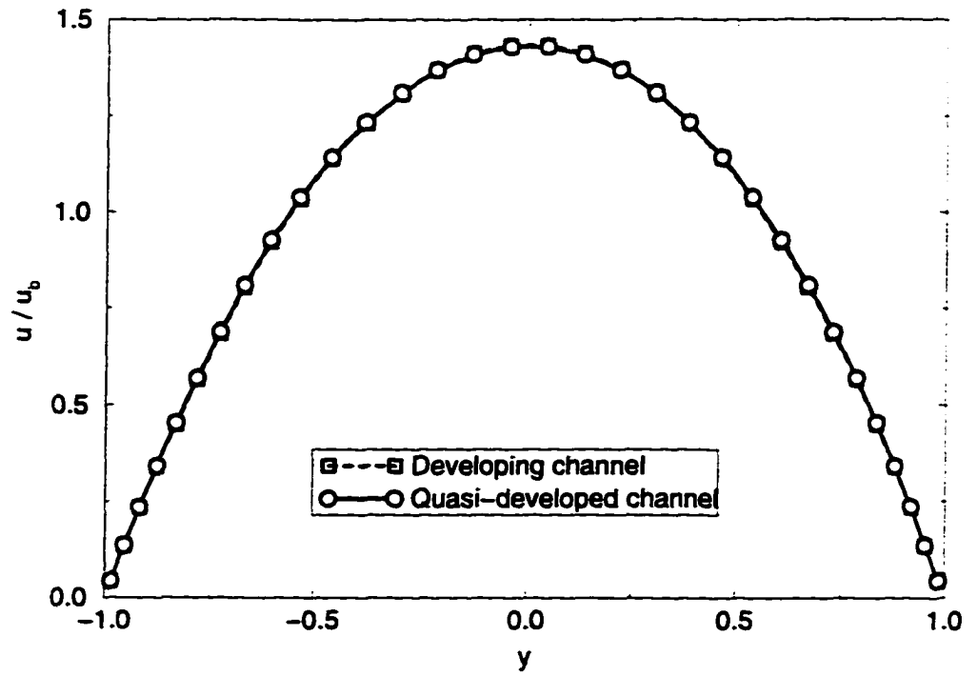

Figure 7.4 Mean streamwise velocity profile normalized by bulk velocity for two-dimensional, laminar, constant heat flux channel flow

location where the Reynolds number based on local bulk properties was the same for both calculations. Excellent agreement was obtained for the streamwise velocity. However, the wall-normal velocity was nearly zero for the quasi-developed computation, whereas a significantly larger, yet negligibly small variation in v across the channel was observed for the developing channel computation. For higher Reynolds numbers, such as those for the turbulent simulations presented later in this chapter, the variation in v is expected to be even less significant based on the results of Swearingen and McEligot (1971), so the current assumptions should be satisfactory. It was also observed by Swearingen and McEligot that as the heating rates were increased, the variation in v was more significant in the developing region of the channel.

The temperature profiles, shown in Fig. 7.6, are in slight disagreement near the walls, even though the Nusselt numbers were in good agreement. The discrepancy is most likely due to slightly different wall temperatures.

Overall, the use of the stepwise periodic boundary conditions, given by Eqs. 7.5 through 7.9, allowed duplicate results to be obtained in the quasi-developed region compared to the

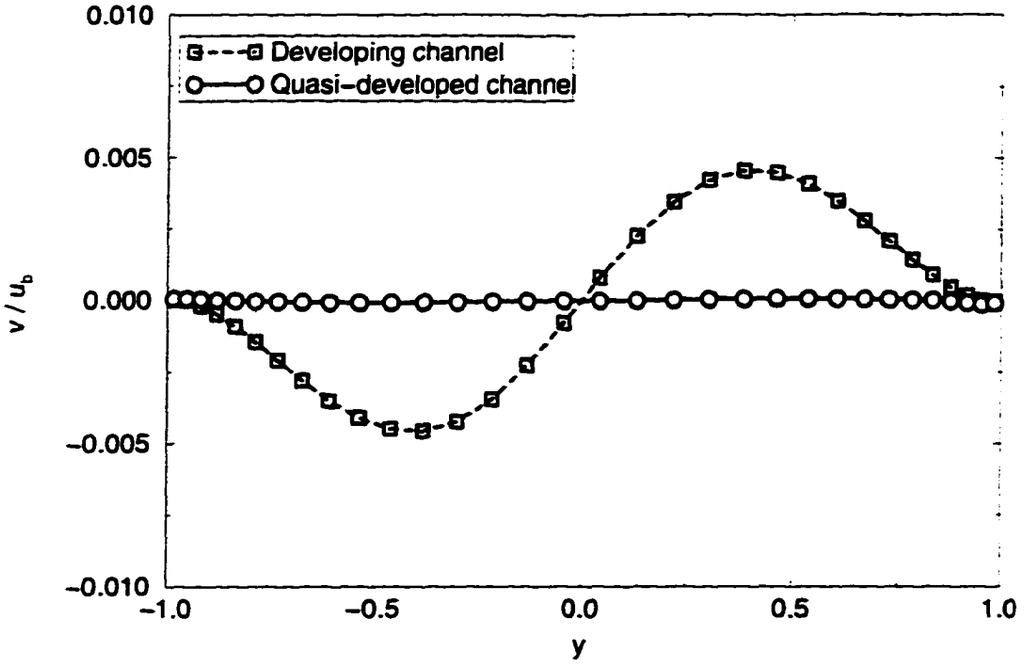

Figure 7.5 Mean wall-normal velocity profile normalized by bulk velocity for two-dimensional, laminar, constant heat flux channel flow

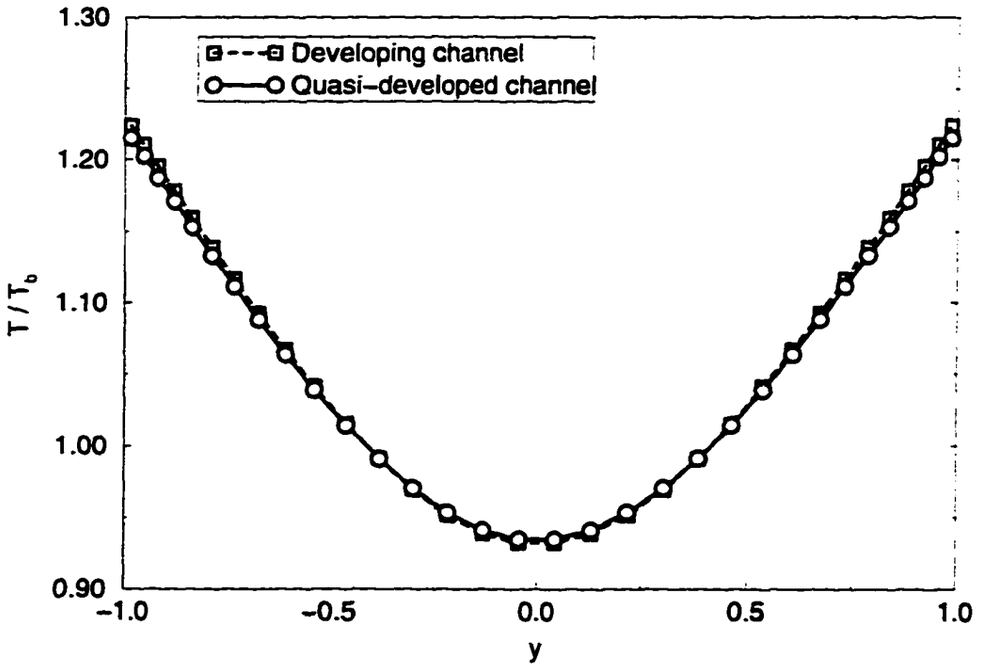

Figure 7.6 Mean temperature profile normalized by bulk temperature for two-dimensional, laminar, constant heat flux channel flow

developing flow calculation for constant wall heat fluxes. The existence of quasi-developed conditions in the downstream region of a channel flow with constant wall heat fluxes has also been observed for turbulent flows (McEligot et al., 1970). Consequently, it was assumed that the stepwise periodic boundary conditions would also be applicable for turbulent simulations.

One slight modification to the stepwise periodic boundary conditions was made for the turbulent simulations presented later in this chapter. The turbulent simulations were performed at much higher Reynolds numbers ($Re_D = 10,800 - 11400$), resulting in less than 1.2 percent variation of the temperature in the streamwise direction. Therefore, it was satisfactory to assume ΔT_x was independent of y, so that Eq. 7.10 could be used instead of Eq. 7.11.

7.4 Turbulent Simulation Details

Details of running the turbulent constant heat flux channel flow simulations are discussed in this section. The cases of interest are described in Section 7.4.1, followed by a discussion of the difficulties in setting up the desired flow conditions in Section 7.4.2. Subgrid-scale modeling and turbulence statistics details for this problem are given in Sections 7.4.3 and 7.4.4, respectively.

7.4.1 Case Descriptions

Four turbulent simulations of quasi-developed turbulent plane channel flow with constant wall heating rates are presented in this chapter. Two cases with "low heating" were discussed in Chapter 6. They are referred to in this chapter as cases LHQW and LHTW, where LHQW was simulated with a specified constant wall heat flux boundary condition, and case LHTW was simulated with a fixed, but linearly varying, wall temperature boundary condition that resulted in a nearly constant wall heat flux. The rate of heat addition, $Q^+ = 0.8$, was low enough that the properties were essentially constant. In many of the figures, the "low heating" cases are referred to collectively as case LH, because many of the mean flow and turbulence statistics, especially for the velocity field, were nearly identical. Case HH, referred to as "high heating" in the figures, was run with constant heat addition ($Q^+ = 15.0$) that resulted in a

wall-to-bulk temperature ratio, T_w/T_b, of 1.5. Finally, case HC, referred to as "high cooling" in the figures, was run with constant cooling ($Q^+ = -15.0$) that resulted in $T_w/T_b = 0.56$. The constant heat flux condition for cases HH and HC were also achieved by specifying a fixed, but linearly varying wall temperature.

All simulations were run with a domain size of $2\pi \times 2 \times \pi$ with the same grid that had $48 \times 64 \times 48$ control volumes in the x, y, z directions, respectively. A grid study in Chapter 6 for the low heating simulations indicated that this grid size provided accurate results compared to DNS and experimental data. The grid spacing was uniform in the x and z directions, but was stretched towards the wall using hyperbolic tangent stretching in the y direction to give $y^+ \approx 1$ for the near-wall control volume. Turbulence statistics were collected using about $N_{stat} = 10,000$ time steps once the flow was deemed to be statistically stationary. The time steps are given in Table 7.1 and the control volume dimensions are given in Table 7.2. The superscript,$^+$, represents a quantity in wall units, where in terms of nondimensional variables, $x^+ = \mathrm{Re}_\tau u_\tau x/\nu_w$ and $t^+ = t u_\tau$.

Table 7.1 Time steps for constant heat flux turbulent channel flows

Case	Δt	Δt^+	$1/\Delta t^+$
LHTW	0.0311	0.00193	518
LHQW	0.0311	0.00193	519
HH	0.0311	0.00240	418
HC	0.0311	0.00153	656

Table 7.2 Control volume dimensions for constant heat flux turbulent channel flows

Case	Δx	Δy_{nw}	Δy_{max}	Δz	Δx^+	Δy^+_{nw}	Δy^+_{max}	Δz^+
LHTW	0.131	0.0133	0.0462	0.0654	22.7	2.3	8.0	11.4
LHQW	0.131	0.0133	0.0462	0.0654	22.6	2.3	8.0	11.3
HH	0.131	0.0133	0.0462	0.0654	14.1	1.4	5.0	7.1
HC	0.131	0.0133	0.0462	0.0654	44.5	4.5	15.6	22.2

The simulations were run with the dual time stepping, preconditioned LU-SGS scheme with relaxation factors $\omega = 1.0$ and $r_A = r_B = r_C = 1.0$. Cases HH and HC were run with

subiteration tolerance levels of $TOL = 1.0 \times 10^{-6}$, which required about 6–7 work units per step in physical time, and resulted in 1–1.5 orders of magnitude drop in the residuals. The LH cases were run with $TOL = 1.0 \times 10^{-7}$, which required about 11–12 work units per step in physical time, and resulted in 1.5-2.5 orders of magnitude drop in the residuals. The lower tolerance was used for the LH cases because of problems resolving the mid-channel temperature fluctuations, as discussed in Section 6.5.

The simulations were typically run with 8 or 16 processors on an IBM SP-2. Using 8 processors. Cases HH and HC required about 12.5–13.5 hours of wall clock time per 1000 time steps, while the LH cases required about 22 hours of wall clock time per 1000 time steps due to the increased number of subiterations.

As discussed in Section 6.2, Kasagi et al. (1989) reported that the specification of a constant wall heat flux boundary condition for LES and DNS leads to unphysically high values of near wall temperature fluctuations. More realistic temperature fluctuations are predicted for turbulent air flows with a fixed wall temperature, as opposed to a fixed wall heat flux, boundary condition. Consequently, the present turbulent simulations were first run 3–4,000 time steps with a constant heat flux boundary condition to determine an estimate of the average wall temperature distribution. The constant heat flux boundary condition was then replaced with a fixed, but linearly varying wall temperature boundary condition, $T_w(x)$, based on the earlier simulations. The resulting wall heat flux, averaged in the z direction and in time, was nearly constant with less than one percent variation in the streamwise direction. The temperature difference, ΔT_x, in Eq. 7.9 was set to the desired heating or cooling level using Eq. 7.10.

7.4.2 Setting the Quasi-Developed State

For the fully developed region of a channel flow with constant properties, downstream of any entrance effects, the bulk density, velocity, and hence, Reynolds number are invariant in the streamwise direction. Consequently, the "state" at each streamwise location is the same, where here the "state" refers to the local values of the bulk density, velocity, and Reynolds number. Conversely, for the quasi-developed region of a channel with variable properties, there

is an infinite number of "states" because of the properties varying in the streamwise direction. Setting the flow parameters to obtain a desired state can be quite difficult, as described in the following section.

The simulation procedure (marching in time with constant heat flux or fixed wall temperature boundary conditions) for the high heat flux cases was no more difficult or time consuming than the low heat flux cases presented in Chapter 6. However, it was somewhat difficult to construct the flow parameters for a given simulation to provide the desired effect. The parameters included the wall temperature distribution, $T_w(x) = T_w(0) + (dT_w/dx)\,x$, initial bulk velocity and temperature distributions (and hence, wall-to-bulk temperature ratio), and the streamwise temperature difference, which is directly related to the wall heat flux. The goal was to adjust these parameters to achieve a desired wall-to-bulk temperature ratio and heating or cooling level.

Recall that the quasi-developed region is far downstream from the entrance region for a developing channel flow. The local bulk Reynolds number provides an indication of how close one is to the entrance region. For instance, in the case of heating, Re_b decreases in the streamwise direction because T_b, and hence ν_b, increases in the streamwise direction.

For the present turbulent high heating simulations, it was found that if Re_b was too large, velocity profiles with dual peaks or maximums were obtained. The dual peak velocity profiles are characteristic of the entry region, as shown by the results of Swearingen and McEligot (1971), for example. In order to study the effects of variable properties, a large value of T_w/T_b was desired. However, as shown in Fig. 7.3(a), the largest values of T_w/T_b occur in the entry region, and T_w/T_b approaches unity far downstream in the channel. Thus, the difficulty of simulating this class of flows lies in setting the appropriate levels of T_w/T_b, ρ_b, u_b, T_b, and Re_b to provide the desired wall-normal temperature variation while remaining in the downstream, or quasi-developed region.

For heating, another possible limit exists for the Reynolds number. As one goes farther downstream, or correspondingly decreases Re_b, there is the potential for relaminarization of the flow (McEligot, 1985). In addition, as higher heating rates are applied, the streamwise

variation in the properties will become more important, and the present assumption that the property variations in the streamwise direction are negligible compared to the wall-normal variations would no longer be appropriate. Thus, corrections such as those given by Eq. 7.11 would be necessary.

7.4.3 Subgrid-Scale Modeling

Only the Smagorinsky SGS model with Van Driest damping was used for the present simulations. The properties in the definition of y^+ in the Van Driest damping formula were evaluated with wall values. One might be inclined to use local values of density and molecular viscosity in evaluating y^+ for flows in which these quantities vary significantly. Bankston and McEligot (1970) used the Van Driest mixing length model to close the Reynolds averaged equations to compute the turbulent thermal entry region for strong heating, and found better agreement when using y^+ with wall values of the properties as opposed to local values. Therefore, the wall values were employed for the simulations presented here. It would be interesting to perform the simulations with the dynamic SGS model, so that the Van Driest damping formulation could be compared with the effective damping implied by the dynamic model.

7.4.4 Turbulence Statistics

As briefly discussed in Section 6.4 of Chapter 6, the conventional Reynolds (or ensemble) average of a quantity is denoted as $<>$, and the Favre ensemble average as $\{\}$, where

$$f = < \rho f > / < \rho > . \tag{7.15}$$

A single prime,$'$, and a double prime,$''$, denote the turbulent fluctuations with respect to the Reynolds or Favre ensemble average, respectively. For the simulations with low heating presented in Chapter 6, the density variations were assumed to be small enough that the Reynolds and Favre averages were equivalent. For the results in this chapter, fluctuations with respect to Reynolds averages were used for *rms* values so that the effect of heat transfer and variable properties on these fluctuations could be studied. The only difference for the turbulence statistics collection procedure compared to the results in Chapter 6 is that ensemble

averaging was only performed in the z direction and time because the flow is generally not homogeneous in the x direction, which results in two-dimensional statistics data. For example, the velocity fluctuations were obtained at each time step as

$$\tilde{u}_i'(x,y) = \tilde{u}_i(x,y) - < \tilde{u}_i >_z (x,y) \tag{7.16}$$

where $<>_z$ denotes an average in the z direction only. The ensemble averaged root-mean-square (rms) values were subsequently obtained as

$$\tilde{u}_{rms}'(x,y) = \sqrt{\frac{< \tilde{u}'(x,y)^2 >}{N_{stat}}} \tag{7.17}$$

where $<>$ denotes an average in z and in time, and N_{stat} is the number of time steps used to compute the statistics.

Shear stress and heat flux distributions were also computed as part of the turbulence statistics. The computed shear stress contributions were

$$\tau_{res} = - < \rho \tilde{u}'' \tilde{v}'' > \tag{7.18}$$

$$\tau_{vis} = - < \frac{\mu}{\mathrm{Re}} \frac{\partial \tilde{u}}{\partial y} > \tag{7.19}$$

$$\tau_{sgs} = - < \mu_t \frac{\partial \tilde{u}}{\partial y} > \tag{7.20}$$

where τ_{res} is the resolvable Reynolds shear stress, τ_{vis} is the viscous shear stress, and τ_{sgs} is the modeled SGS stress. Similarly, the computed heat flux contributions were

$$q_{res} = - < \rho \tilde{v}'' \tilde{T}'' > \tag{7.21}$$

$$q_{con} = - < \frac{\mu c_p}{\mathrm{RePr}} \frac{\partial \tilde{T}}{\partial y} > \tag{7.22}$$

$$q_{sgs} = - < \frac{\mu_t c_v}{\mathrm{Pr}_t} \frac{\partial \tilde{T}}{\partial y} > \tag{7.23}$$

where q_{res} is the resolvable turbulent heat flux, q_{con} is the heat conduction, and q_{sgs} is the modeled SGS heat flux.

7.5 Review of Related Experimental and Numerical Studies

The experimental data available for this class of flows are very limited. Experiments have been limited to determining bulk or wall parameters only, e.g. friction factors and Nusselt numbers. This is because small tube diameters or channel heights are required to measure dominant forced convection. However, in most cases test sections were too small to obtain detailed measurements of temperature and velocity mean and fluctuating profiles. Extensive comparisons to many of the correlations for variable property flows are given in Section 7.8.

Numerical simulations of this class of flows is also practically nonexistent, mainly because of the nonhomogeneity in the streamwise direction. In fact, this research was the first known turbulent simulation of a constant heat flux channel flow with variable properties.

The velocity parameters for the low heating cases can be compared to the incompressible DNS results of Kim et al. (1987) and experimental results of Niederschulte (1990), as presented in Chapter 6. In addition, the temperature profiles for the low heating cases can be compared to the DNS of constant heat flux turbulent channel flow where the temperature field was treated as a passive scalar (Kasagi et al., 1992). In this chapter, the variable property, high heat flux results are compared to the low heating cases to determine the effects of high heating and high cooling.

A similar but distinctly different variable property channel flow was simulated by Wang and Pletcher (1996). They performed the LES of low Mach number isothermal channel flows with one hot wall and one cold wall, with temperature ratios as high as $T_{hot}/T_{cold} = 3$. The hot wall corresponded to heating, and the cold wall corresponded to cooling. However, the heat transferred to the hot wall was removed from the channel through the cold wall, so that unlike the present simulations, there was no bulk temperature rise. The compressible formulation of the dynamic SGS model was utilized in a staggered grid finite volume method that was fully implicit. The trends in the turbulence quantities for heating versus cooling from their simulations were compared to the present results.

Another simulation of interest was the DNS of supersonic isothermal-wall channel flow by Coleman et al. (1995). The Mach numbers, based on the bulk velocity and sound speed at

the walls. were 1.5 and 3.0. resulting in significant density and temperature variations in the channel. The compressible effects were found to be mostly due to these large mean property variations. The heat generated near the walls due to dissipation was transferred out of the channel. so that no bulk temperature rise occurred for this flow.

7.6 Ensemble Averaged Profiles

In this section, ensemble averaged results are presented for the constant heat flux turbulent channel flows. Various flow parameters are given in Section 7.6.1, followed by mean profiles in Section 7.6.2. Profiles of quantities comprised of fluctuations are discussed in Section 7.6.3. Finally. shear stress and heat flux profiles are reviewed in Section 7.6.4.

7.6.1 Average Flow Parameters

Tables 7.3 and 7.4 list globally averaged parameters for the entire solution domain. The pressure gradient parameter, β, was observed to be 56 percent higher for case HH compared to the low heating results, whereas for case HC, β was 51 percent lower. Correspondingly. the friction velocity was 24 percent higher for case HH, and 21 percent lower for case HC compared to the low heating results. The average turbulent kinetic energy, k and k^+, are averages of k at every control volume in the solution domain. The average turbulent kinetic energy, normalized by the square of the reference velocity, was 5.4 percent lower for case HH, and 21 percent higher for case HC.

Table 7.3 Simulation parameters (average for complete solution domain)

Case	β	$u_{\tau,avg}$	k/V_r^2	k^+
LHTW	-0.00395	0.0620	0.00749	1.95
LHQW	-0.00397	0.0619	0.00741	1.93
HH	-0.00618	0.0770	0.00705	1.19
HC	-0.00194	0.0490	0.00904	3.77

The actual average heat flux obtained was computed as

$$q_{w,actual} = \frac{1}{2L_x}\left[\int_0^{L_x} < q_w(x) > \, \mathrm{dx}\Big|_{y=1} + \int_0^{L_x} < q_w(x) > \, \mathrm{dx}\Big|_{y=-1}\right] \qquad (7.24)$$

Table 7.4 Simulation parameters (average for complete solution domain)

Case	$q_{w,actual}$	$T_w(0)$	dT_w/dx	$Nu_{b,avg}$
LHTW	—	1.000	1.00×10^{-4}	34.5
LHQW	1.00×10^{-4}	1.024	1.00×10^{-4}	34.2
HH	2.05×10^{-3}	1.560	1.25×10^{-3}	30.8
HC	-1.99×10^{-3}	0.594	-2.45×10^{-3}	34.0

where <> denotes an ensemble average in z and time. The average friction velocity, $u_{\tau,avg}$, and Nusselt number, $Nu_{b,avg}$, were also found by integrating along the upper and lower walls in this way. For case LHQW, q_w was specified, and the desired value for low heating of 1.0×10^{-4} was obtained. For the other cases (LHTW, HH, and HC), $T_w(x)$ was specified in such a way to provide a nearly constant heat flux. The values of $T_w(0)$, dT_w/dx, and ΔT_x were iterated upon through several trials to obtain the desired heat fluxes, which were 0.002 and -0.002 for cases HH and HC, respectively. The cooling had little effect on the average Nusselt number compared to the low heating results, while high heating reduced the average Nusselt number by 10.5 percent.

Because the high heat flux channel flows are nonhomogeneous in the x direction, profiles are only shown at a single x or streamwise location, which was a plane near mid-channel. The bulk flow parameters at this local position in the channel, averaged in z and time, are given in Table 7.5, and other locally averaged parameters are given in Table 7.6. The bulk properties are defined by Eqs. 6.11, 6.12, and 6.13. The nondimensional heat flux parameter is given by

$$Q^+ = \frac{q_w D_h}{k_b T_b}. \tag{7.25}$$

The low heating cases resulted in wall-to-bulk temperature ratios of 1.025 and 1.023. Case HH resulted in $T_w/T_b = 1.49$ and case HC resulted in $T_w/T_b = 0.56$.

7.6.2 Mean Profiles

The profiles of mean and fluctuating quantities shown throughout the remainder of this chapter are for a streamwise location near mid-channel. The profiles have been ensemble averaged in the z direction and in time.

Table 7.5 Local bulk properties for constant heat flux turbulent channel simulations

Case	ρ_b	u_b	T_b	Re_D	T_w	T_w/T_b
LHTW	—	—	0.98	11.390	1.00	1.03
LHQW	1.001	1.00	1.00	11.210	1.02	1.02
HH	0.965	1.04	1.05	10.810	1.56	1.49
HC	0.953	1.05	1.04	10.900	0.59	0.56

Table 7.6 Local parameters for constant heat flux turbulent channel simulations

Case	u_τ	C_f	q_w	Q^+	Nu_D
LHTW	—	0.00768	—	0.832	34.5
LHQW	0.0620	0.00768	1.00×10^{-4}	0.796	34.3
HH	0.0770	0.00782	2.05×10^{-3}	14.9	30.8
HC	0.0490	0.00779	-1.99×10^{-3}	-14.8	34.0

The mean temperature profiles are shown in Figs. 7.7 and 7.8. normalized by the bulk temperature and wall temperature. respectively. The mean density profile, normalized by the bulk density. is shown in Fig. 7.9. The figures show the significant variation in temperature leading to significant variations in density, viscosity. and thermal conductivity. The distribution of the mean streamwise momentum, $< \rho u >$, is shown in Fig. 7.10. which reveals the redistribution of the mass flow (compared to low heating) towards the center of the channel for high heating. and towards the wall for high cooling. This is because the density is higher in the center of the channel for high heating, while the density is higher near the wall for high cooling.

The mean streamwise velocity profile is plotted in wall coordinates in Fig. 7.11. where

$$u^+ = \frac{u}{u_\tau} \; : \; u_\tau = \sqrt{\frac{\tau_w}{\rho_w}} \tag{7.26}$$

and

$$y^+ = \mathrm{Re}_\tau \frac{\delta_y \, u_\tau}{\nu_w} \tag{7.27}$$

where δ_y is the distance to the wall. The incompressible DNS results of Kim et al. (1987) and experimental results of Niederschulte (1990) are shown for comparison purposes. Also shown is the linear law, $u^+ = y^+$. and the log-law recommended by Kim et al. at these low Reynolds

numbers. $u^+ = 2.5 \ln y^+ + 5.5$. As shown, the high heating and high cooling velocity profiles depart markedly from the incompressible results.

For flows with significant variations in the density, Huang et al. (1995) recommended the use of semi-local coordinates, u^* versus y^*, where local values of density and molecular viscosity are used instead of wall values, giving

$$u^* = \frac{u}{u_\tau^*} \; ; \; u_\tau^* = \sqrt{\frac{\tau_w}{\rho(y)}} \tag{7.28}$$

and

$$y^* = \mathrm{Re}_\tau \frac{\delta_y \, u_\tau^*}{\nu(y)}. \tag{7.29}$$

Figure 7.12 shows the mean streamwise velocity plotted in semi-local coordinates. The velocity profiles have nearly collapsed to a single curve matching the incompressible results. However, the slopes in the logarithmic region do not match perfectly.

Van Driest (1951) proposed a density weighted transformation of the mean velocity profile for compressible turbulent boundary layers as

$$u_{VD}^+ = \int_0^{u^+} \left(\frac{\rho}{\rho_w} \right) du^+ \tag{7.30}$$

which was found to agree with the incompressible log-law, $u^+ = (1/\kappa) \ln y^+ + C$, with κ and C similar to the incompressible values. Huang and Coleman (1994) used a mixing-length formula for the temperature to write u_{VD}^+ as a function of u^+ only, given by

$$u_{VD}^+ = \frac{1}{R} \left\{ \sin^{-1} \left[\frac{R(u^+ + H)}{D} \right] - \sin^{-1} \left[\frac{RH}{D} \right] \right\} \tag{7.31}$$

where $R = M_\tau \sqrt{(\gamma - 1)\mathrm{Pr}_t / 2}$, $H = B_q / [(\gamma - 1) M_\tau^2]$, and $D = \sqrt{1 + R^2 H^2}$. The nondimensional wall parameters are given by

$$M_\tau = \frac{u_\tau}{\sqrt{(\gamma - 1) c_p T_w}} \quad : \quad B_q = \frac{q_w}{\rho_w c_p u_\tau T_w}. \tag{7.32}$$

The values of M_τ and B_q for the present simulations are given in Table 7.7. The values from the LES of a turbulent channel flow with $T_{hot}/T_{cold} = 3$ (Wang and Pletcher, 1996) and from the DNS of supersonic channel flow (Coleman et al., 1995) with $M = 1.5$ (case A) and $M = 3.0$ (case B) are also given for purposes of comparison.

Table 7.7 Nondimensional wall parameters for Van Driest transformation

Simulation	Conditions	M_τ	B_q
Present	Case LH	6.13×10^{-5}	0.0158
Present	Case HH	6.16×10^{-5}	0.0249
Present	Case HC	6.39×10^{-5}	-0.0407
Wang and Pletcher (1996)	Hot wall	5.4×10^{-4}	0.0127
Wang and Pletcher (1996)	Cold wall	5.0×10^{-4}	-0.0684
Coleman et al. (1995)	Case A (M=1.5)	0.082	-0.049
Coleman et al. (1995)	Case B (M=3.0)	0.116	-0.137

The present mean velocity profiles are plotted with the Van Driest transformation given by Eq. 7.31 in Fig. 7.13. The profiles are in much better agreement with the incompressible log-law, especially the slope of the profiles in the logarithmic region. Coleman et al. (1995) also observed a good collapse of the velocity profiles with the Van Driest transformation, while Wang and Pletcher (1996) observed only a fair collapse for their simulation.

The mean temperature difference is given in wall coordinates as

$$\theta^+ = \frac{< T_w > - < T >}{T_\tau} \; : \; T_\tau = \frac{q_w}{\rho_w c_p u_\tau} \tag{7.33}$$

and in semi-local coordinates as

$$\theta^* = \frac{< T_w > - < T >}{T_\tau^*} \; : \; T_\tau^* = \frac{q_w}{\rho(y) c_p u_\tau^*}. \tag{7.34}$$

The mean temperature profiles are plotted in wall coordinates and semi-local coordinates in Figs. 7.14 and 7.15, respectively. The incompressible passive scalar DNS results of Kasagi et al. (1992) and the thermal law-of-the-wall are shown for comparison purposes. The thermal linear law is $\theta^+ = \mathrm{Pr}\ y^+$, and the thermal log-law is $\theta^+ = 2.78 \ln y^+ + 2.09$. As for the velocity profiles, the high heating and high cooling profiles in wall coordinates departed from the incompressible results. However, the curves did not agree as well with the incompressible results with semi-local coordinates as they did for the velocity profiles.

Figure 7.16 shows the mean temperature difference normalized by the bulk temperature difference, where

$$\frac{\theta}{\theta_b} = \frac{T_w - T}{T_w - T_b}. \tag{7.35}$$

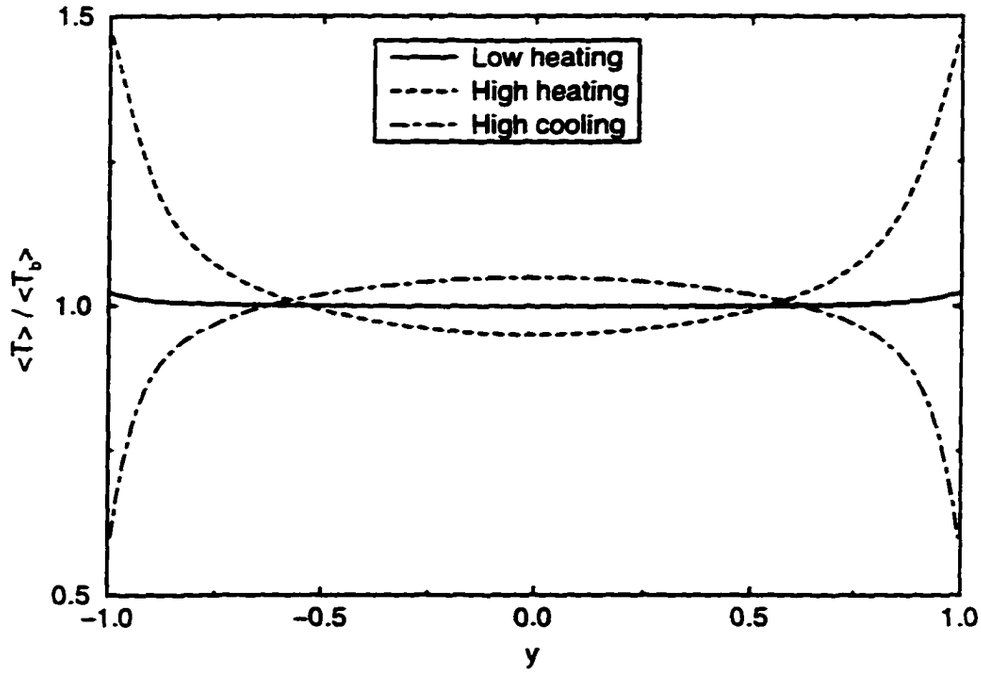

Figure 7.7 Mean temperature profile normalized by bulk temperature

The curves are very similar, but slight differences are evident, especially the slopes near the wall.

7.6.3 Fluctuation Profiles

The root-mean-square of the velocity fluctuations with respect to Reynolds ensemble averages are shown in Figs. 7.17 through 7.20 with four different normalizations. In Fig. 7.17, the velocity fluctuations are normalized by the bulk velocity, while in Fig. 7.18 they are normalized by the local average streamwise velocity, $< u(y) >$. Both figures suggest that the fluctuations are slightly enhanced for high cooling and suppressed for high heating, especially near the center of the channel. However, the differences are small, especially for the normalization by the local velocity.

The trend mentioned above can be plausibly explained by the fact that the local Reynolds number is lower for high heating versus high cooling due to the higher temperatures near the wall. This thickens the viscous sublayer, which is where the maximum production of turbulent

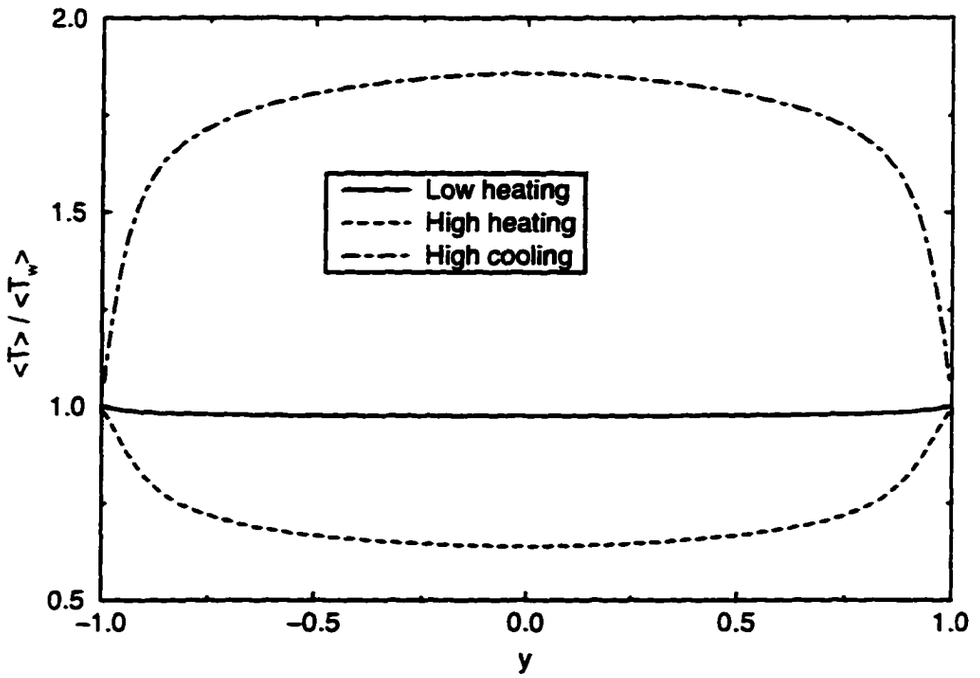

Figure 7.8 Mean temperature profile normalized by wall temperature

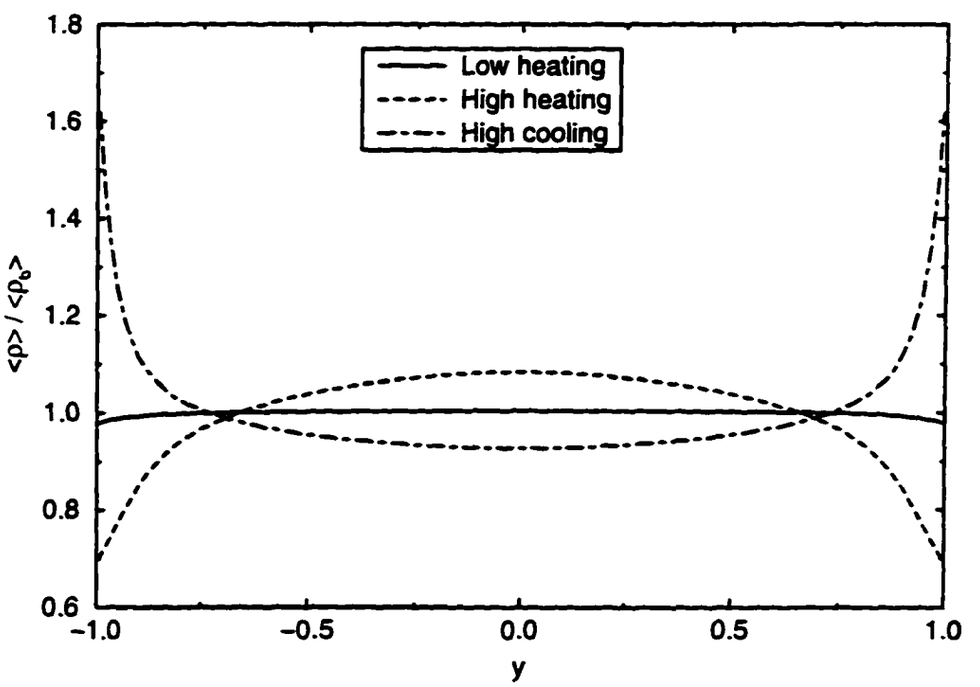

Figure 7.9 Mean density profile normalized by bulk density

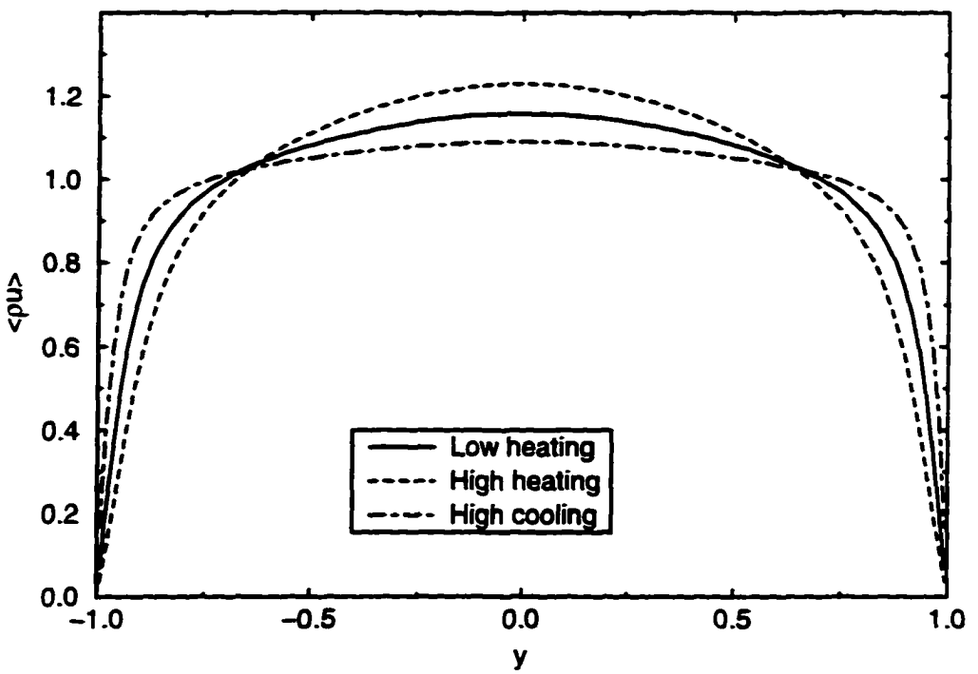

Figure 7.10 Mean streamwise momentum

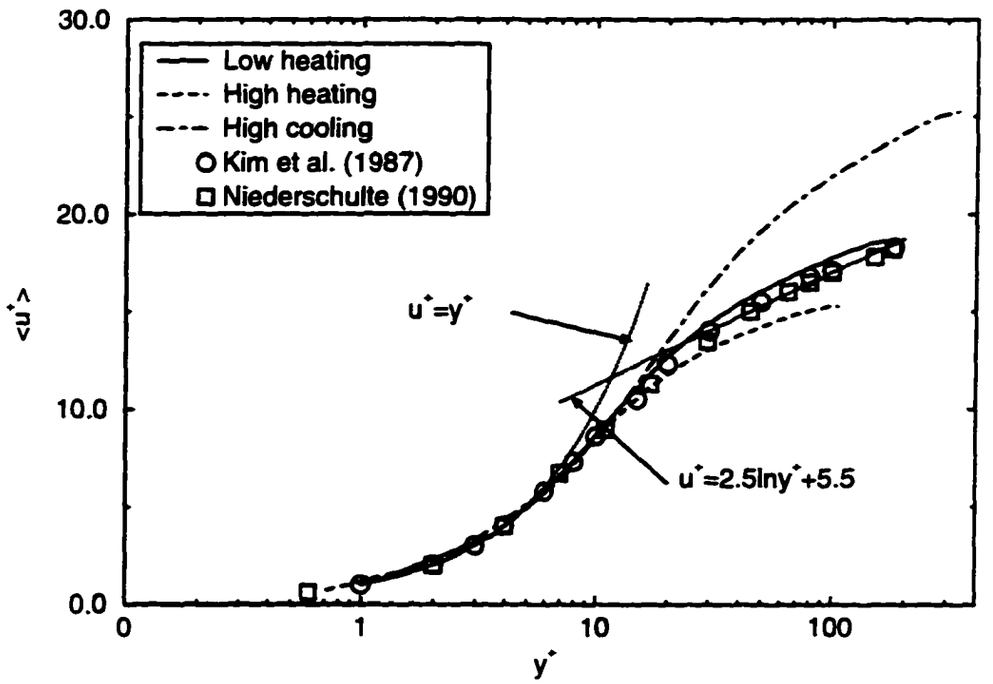

Figure 7.11 Mean streamwise velocity in wall coordinates

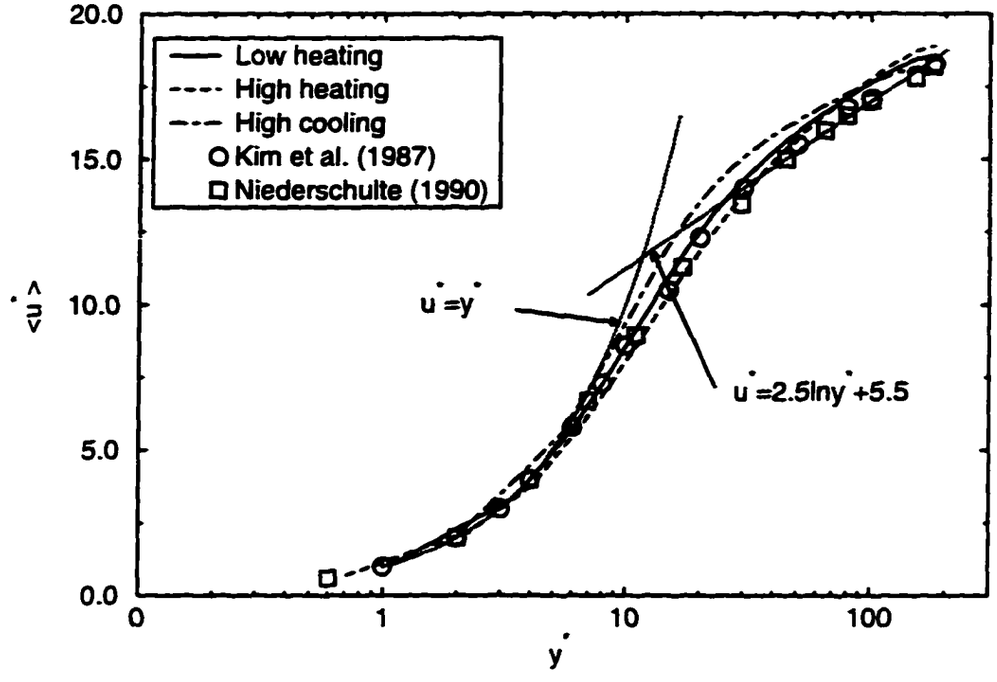

Figure 7.12 Mean streamwise velocity in semi-local coordinates

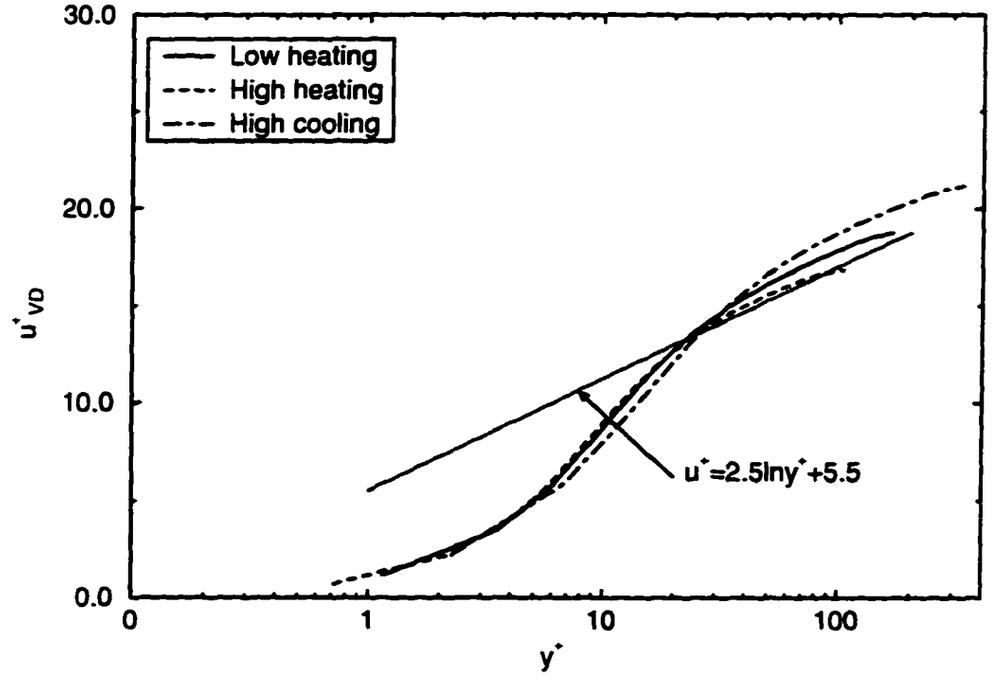

Figure 7.13 Mean streamwise velocity from the Van Driest transformation

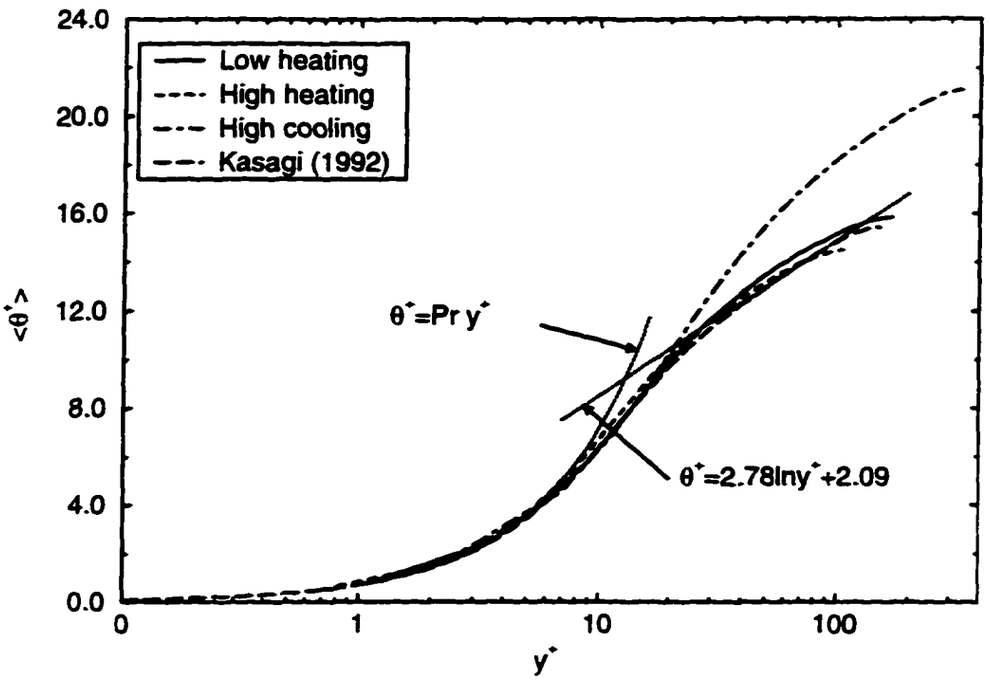

Figure 7.14 Thermal law of the wall in wall coordinates

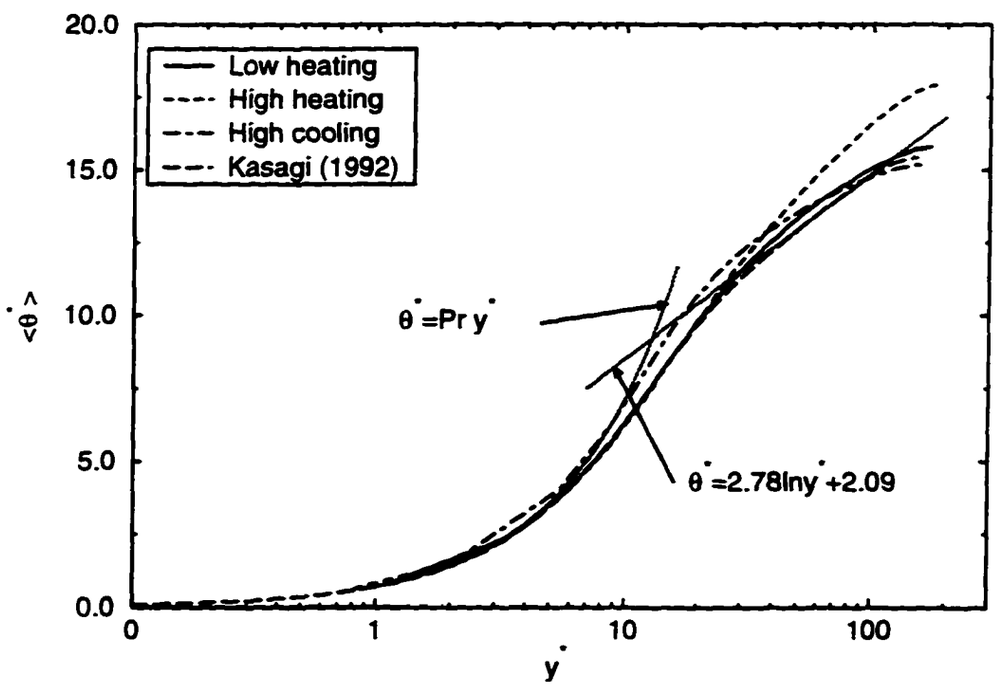

Figure 7.15 Thermal law of the wall in semi-local coordinates

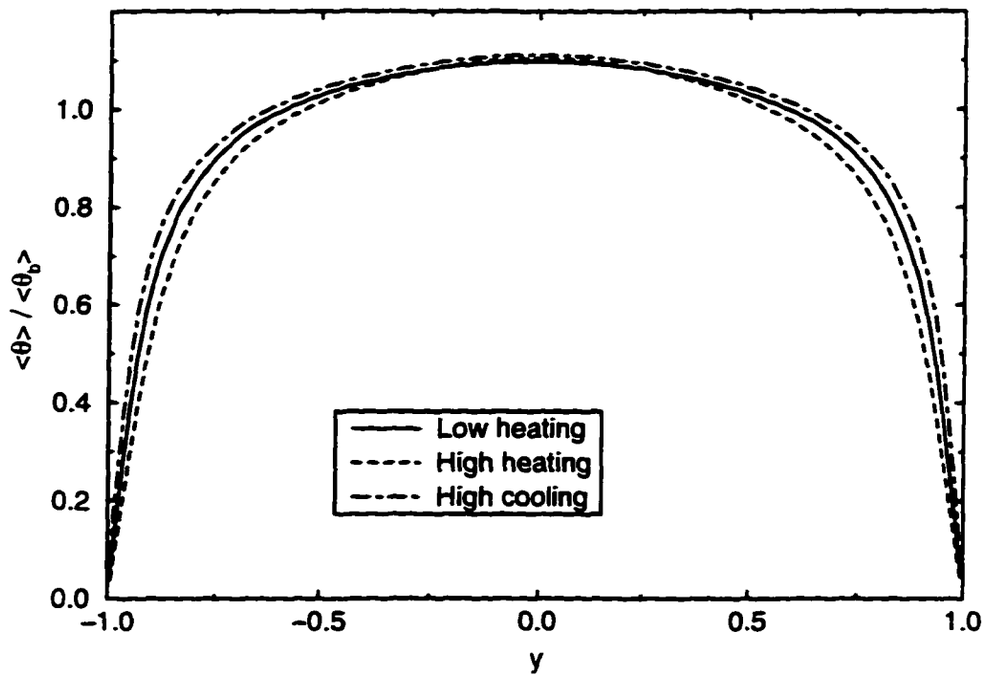

Figure 7.16 Mean temperature difference normalized by bulk temperature difference

kinetic energy occurs, thereby suppressing the velocity fluctuations. It has been observed experimentally that the acceleration of a turbulent flow reduces the apparent turbulent bursting rate near the wall, which would also lead to suppressed velocity fluctuations (McEligot, 1985). The simulations of Wang (1995) showed trends opposite of those observed here. The turbulent velocity fluctuations were enhanced near the hot or heated wall, while the velocity fluctuations were suppressed near the cold or cooled wall. The trends in the temperature and density fluctuations agreed with the observations of the present study. In contrast to the present study, Wang's turbulent channel simulation had no acceleration in the streamwise direction. The streamwise acceleration levels were small for the present simulations, so the trends were most likely due to variations in the mean properties due to heating versus cooling. The DNS of supersonic channel flow reported by Coleman et al. (1995) observed significantly enhanced turbulent fluctuations as the Mach number was increased. As the Mach number increased, the "cooling" of the channel increased. However, it is not clear if their observed trends were due to increasing Mach numbers or to mean property variations.

The velocity fluctuations are plotted in wall coordinates in Fig. 7.19, where $u^+_{rms} = u'_{rms}/u_\tau$. The low heating case agreed well with the DNS and experimental data. However, there was a large departure from the incompressible results for high heating and cooling. Figure 7.20 shows the velocity fluctuations plotted in semi-local coordinates, where $u^*_{rms} = u'_{rms}/u^*_\tau$. The profiles dramatically collapsed toward the incompressible results, although slight differences still exist near the peak values. This collapse was also observed for the DNS of supersonic channel flow (Coleman et al., 1995).

The corresponding turbulent kinetic energy is shown in Figs. 7.21 and 7.22 normalized by the square of the bulk velocity and the square of the local streamwise velocity, respectively. The turbulent kinetic energy is also plotted in wall coordinates and semi-local coordinates in Figs. 7.23 and 7.24. The same trends were observed as for the *rms* velocity components, except that the differences in the peak value with the semi-local coordinates were more pronounced. Also, on a local percentage basis with respect to the local streamwise velocity, the turbulent kinetic energy appeared to be nearly independent of heating or cooling.

The temperature and density fluctuations, scaled by their respective local averages, are shown in Figs. 7.25 and 7.26, respectively. On a local percentage basis, the density and temperature fluctuations were significantly larger for high heating and cooling compared to low heating, demonstrating the "compressible" effects (large density fluctuations) obtained with large variations in the mean properties even though the Mach number is very small. Over most of the channel, the temperature and density fluctuations were larger for high heating compared to high cooling. However, the peak value was larger and shifted towards the wall for high cooling. The difference in the peak value is more dramatic if one considers that the the peak value of the mean density occurs at the wall for high cooling, so the absolute level of the density fluctuations is much larger for high cooling.

The temperature fluctuations are also shown in Fig. 7.27 normalized by the wall-to-bulk temperature difference. Compared to local scaling, the differences in the temperature fluctuations scaled in this manner are not as marked. In fact, the high cooling and heating results have collapsed towards the results of Kasagi et al. (1989). Fig. 7.27 also exaggerates the

overprediction of the temperature fluctuations in the center of the channel for the low heating simulations. The agreement of the present high heating and high cooling results with the profile of Kasagi et al. (1992) confirms that the streamwise temperature boundary condition was effective for large streamwise temperature differences, but ineffective for small streamwise temperature differences.

The difference in the temperature fluctuations in the near wall region is demonstrated for the two low heating cases with the isoflux (case LHQW) and specified $T_w(x)$ (case LHTW) boundary conditions. Case LHQW approaches nonzero values of the fluctuations at the wall, which as pointed out by Kasagi et al. (1989), is unphysical for the combination of air and most practical wall materials.

The density fluctuations are shown in Fig. 7.28 normalized by the wall-to-bulk density difference. As opposed to the temperature fluctuations, the density fluctuations scaled in this manner showed significant differences for high heating versus cooling, with the high heating case resulting in larger fluctuations.

7.6.4 Shear Stress and Heat Flux Profiles

Figure 7.29 shows the resolved, viscous, and modeled SGS shear stress distributions normalized by the wall shear stress. The stresses are defined in Section 7.4.4. The results indicate that high cooling increased the turbulent resolved shear stress, while the viscous shear stress decreased slightly. The opposite trends were observed for high heating. The effect on the turbulent shear stress for heating versus cooling was opposite to the trend observed by Wang and Pletcher (1996). For instance, in the present simulations, the peak value of $\tau_{res} = < \rho u'' v'' >$ was 0.693 for low heating, decreased to 0.590 for high heating, and increased to 0.734 for high cooling. Wang and Pletcher obtained peak values of 0.658 for a low temperature ratio case. For a large temperature ratio case, the hot (or heated) wall peak value increased to 0.757 and the cold (or cooled) wall peak value decreased to 0.627. The reason for the disagreement between the present results and Wang and Pletcher's results is not well understood, but could be due to the different nature of the flows being simulated.

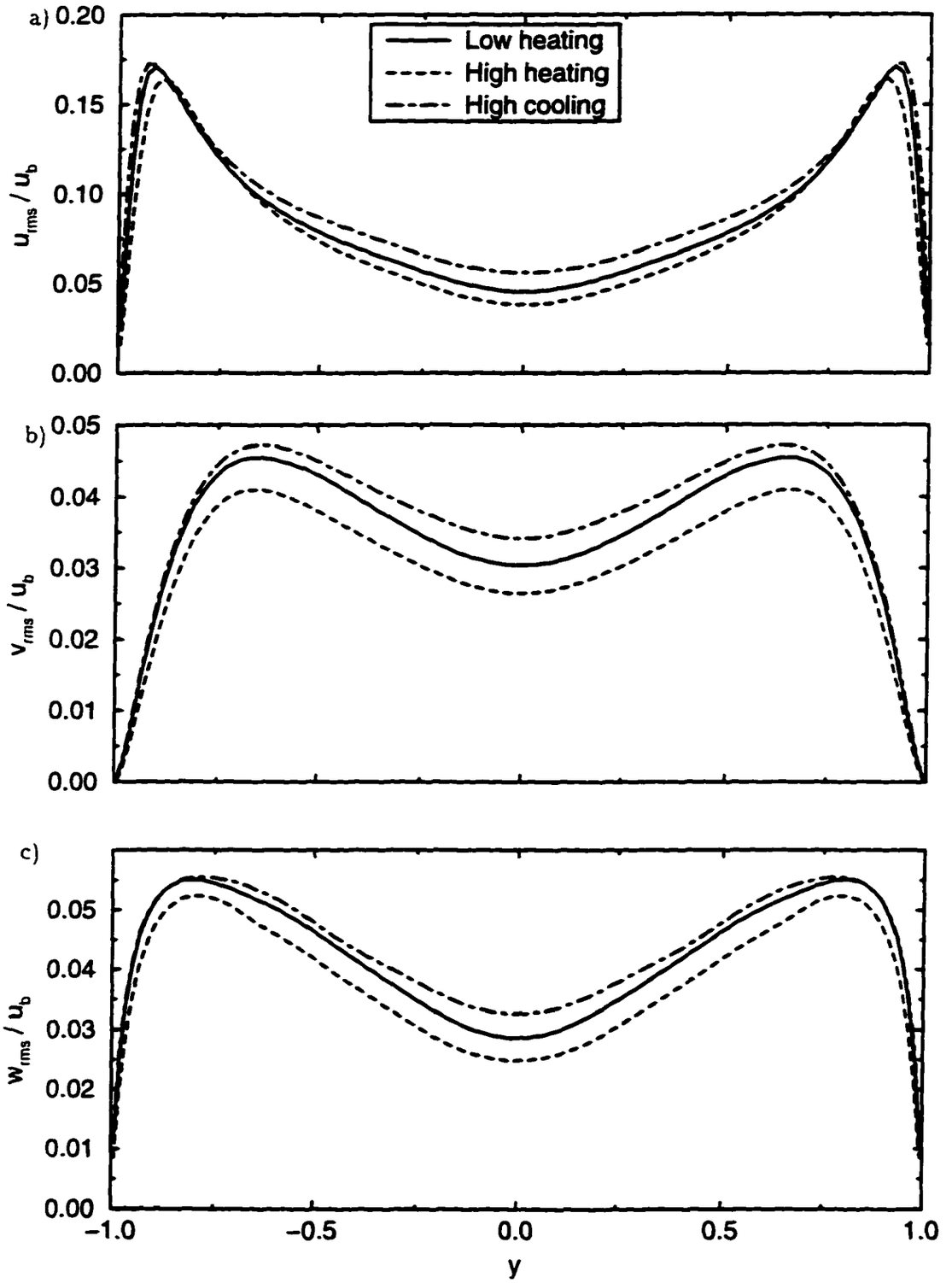

Figure 7.17 Velocity fluctuations scaled by bulk velocity

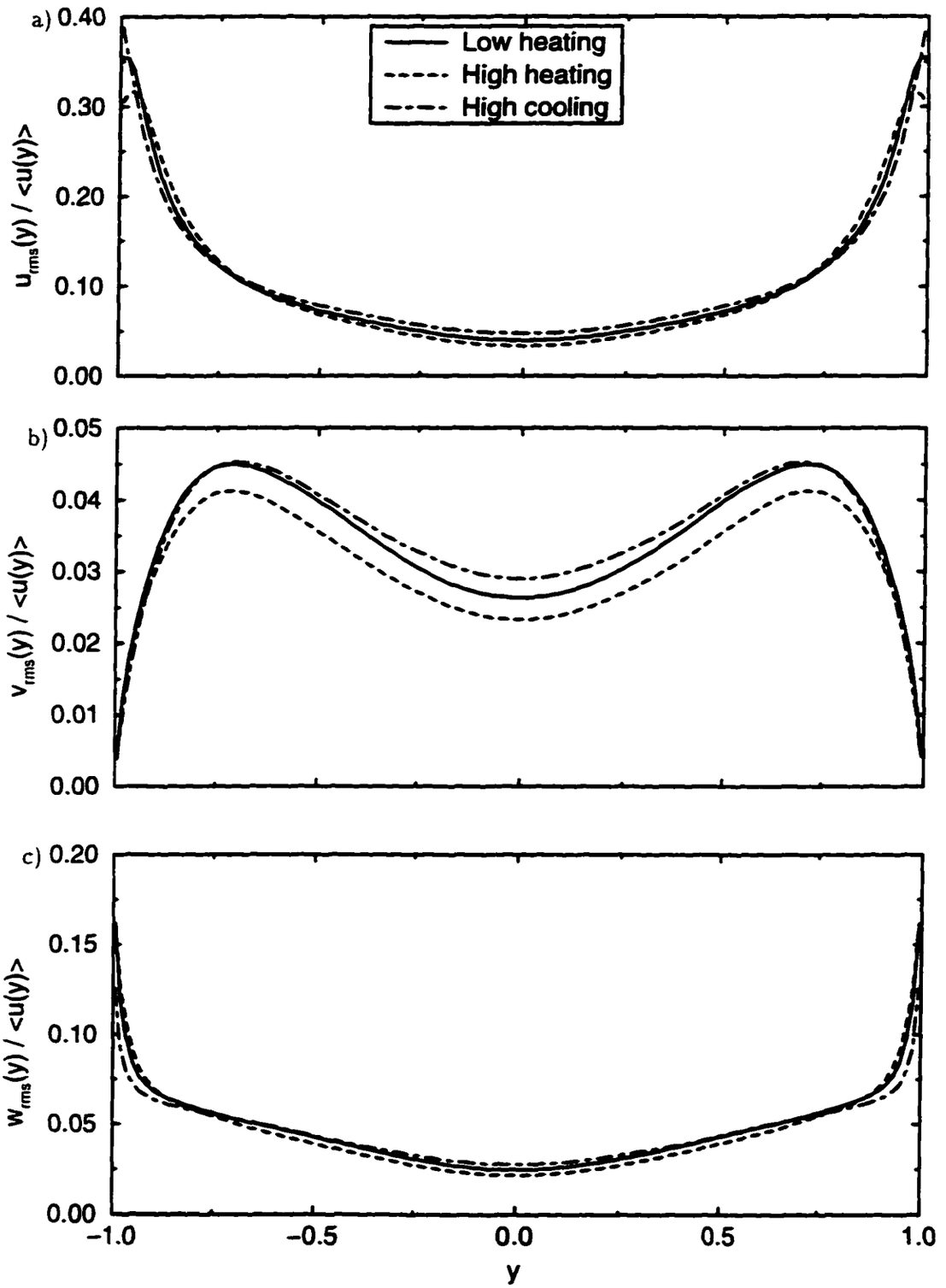

Figure 7.18 Velocity fluctuations scaled by local mean streamwise velocity

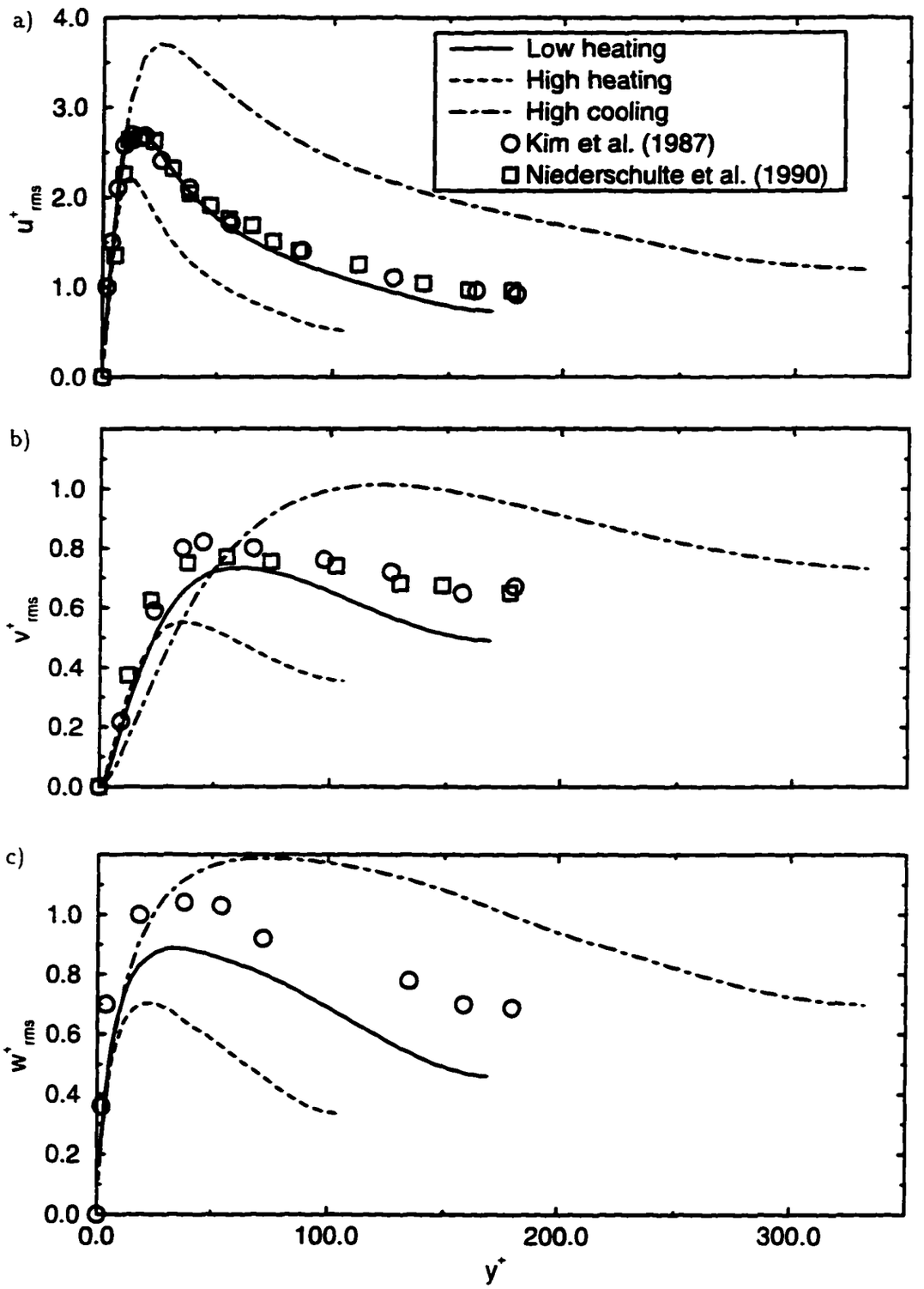

Figure 7.19 Velocity fluctuations in wall coordinates

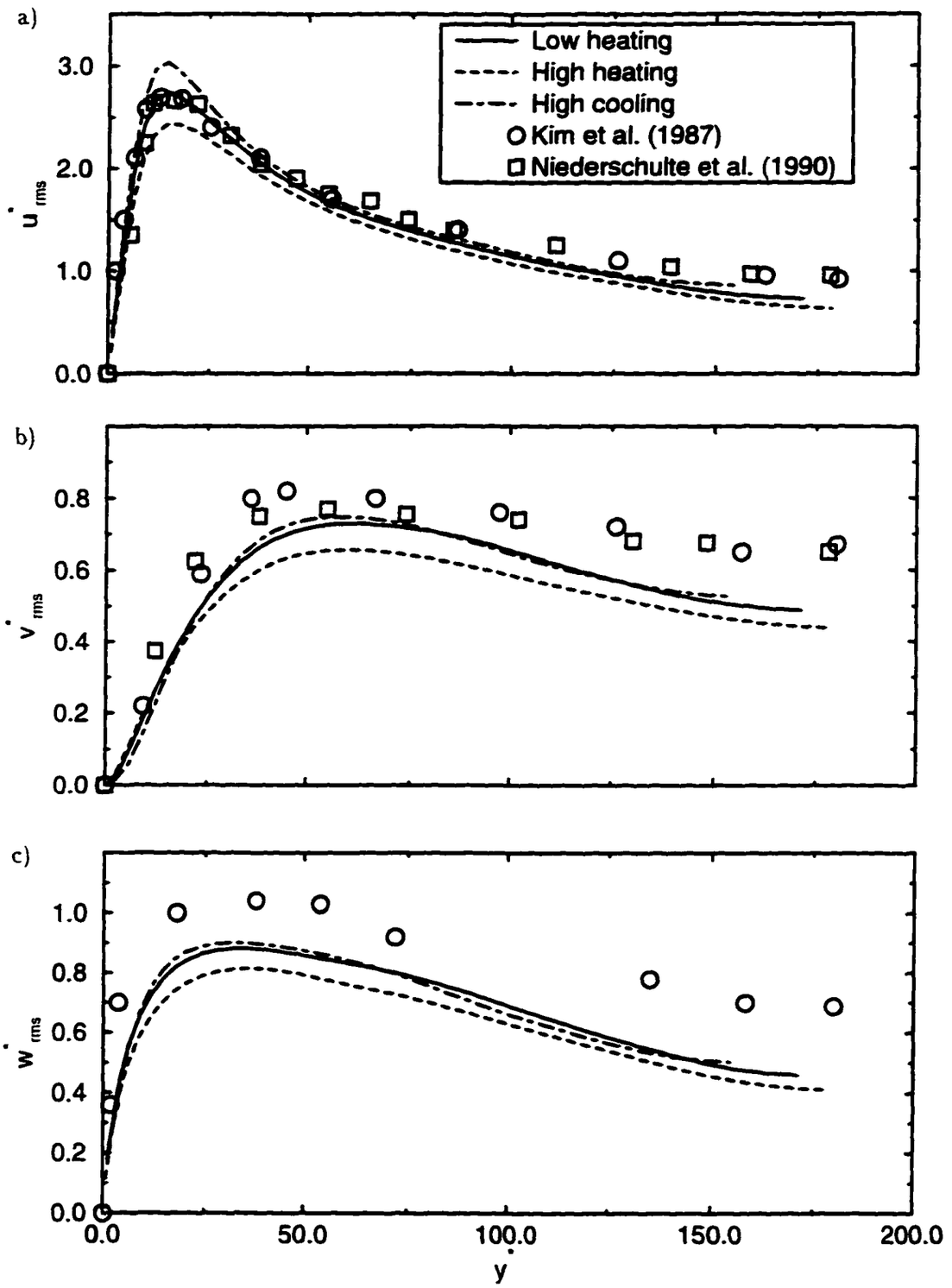

Figure 7.20 Velocity fluctuations in semi-local coordinates

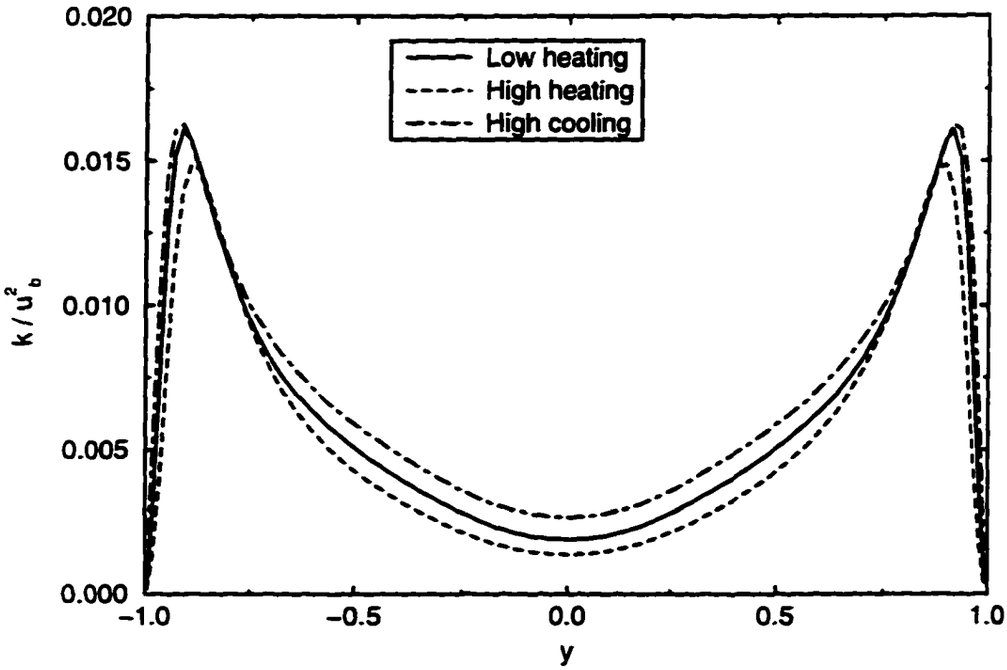

Figure 7.21 Turbulent kinetic energy scaled by bulk velocity

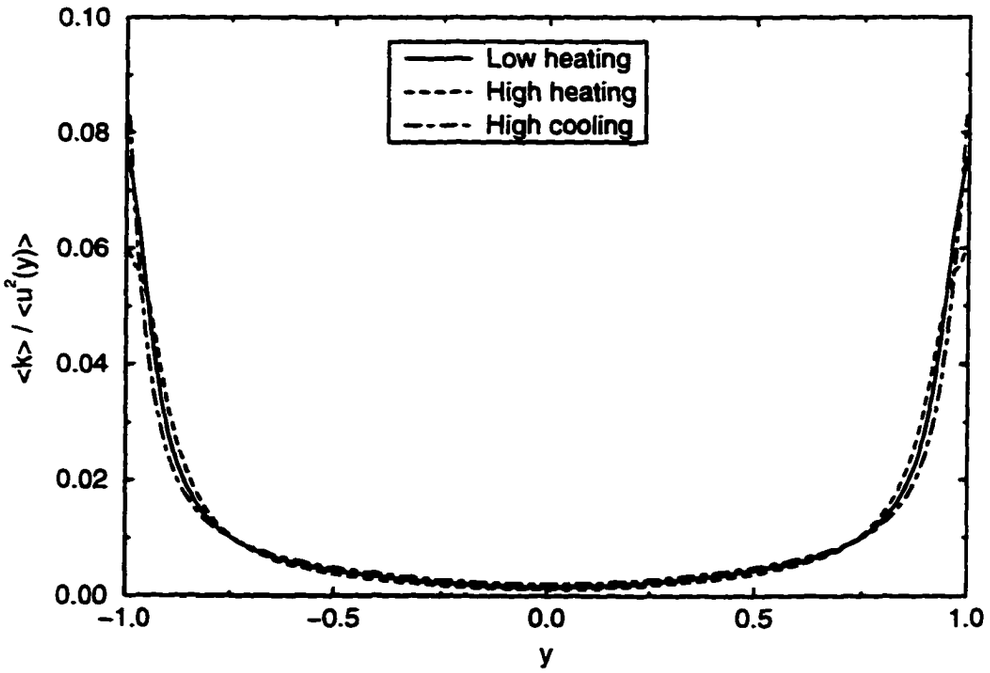

Figure 7.22 Turbulent kinetic energy scaled by mean streamwise velocity

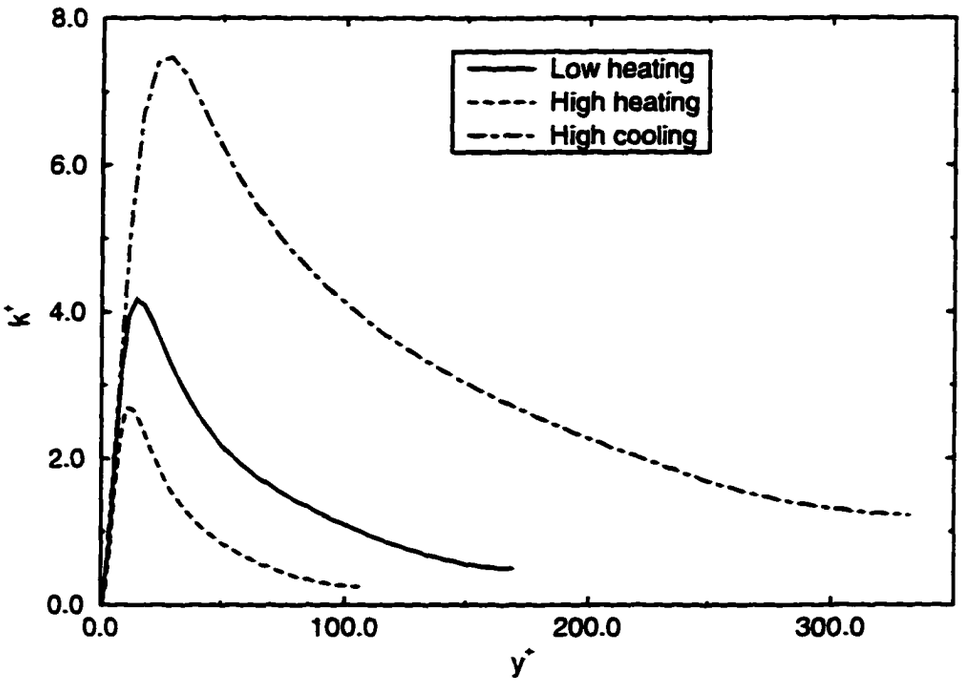

Figure 7.23 Turbulent kinetic energy in wall coordinates

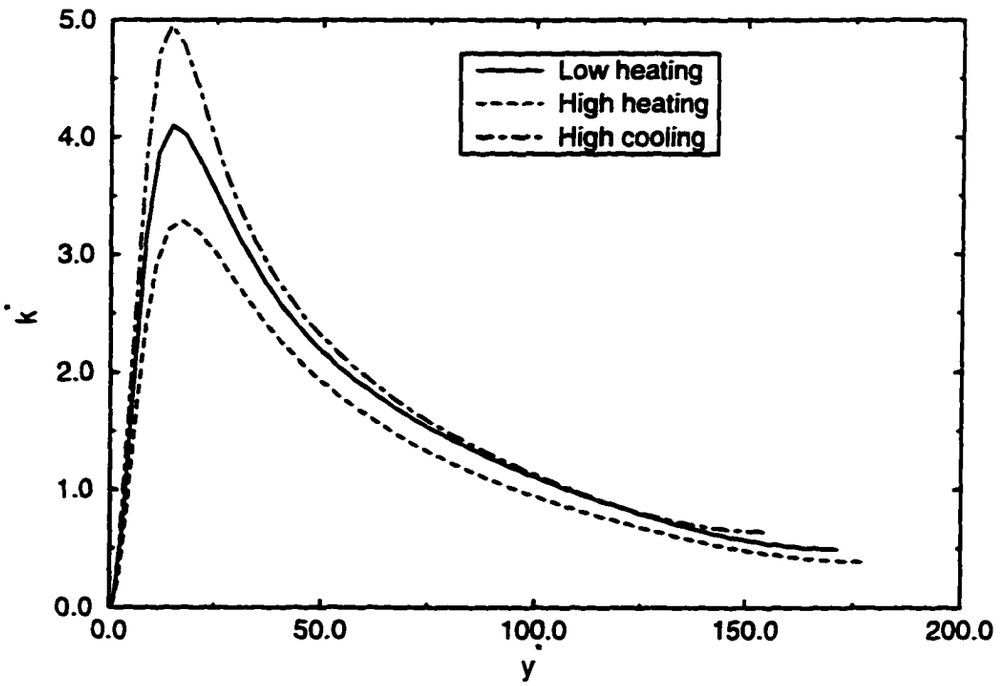

Figure 7.24 Turbulent kinetic energy in semi-local coordinates

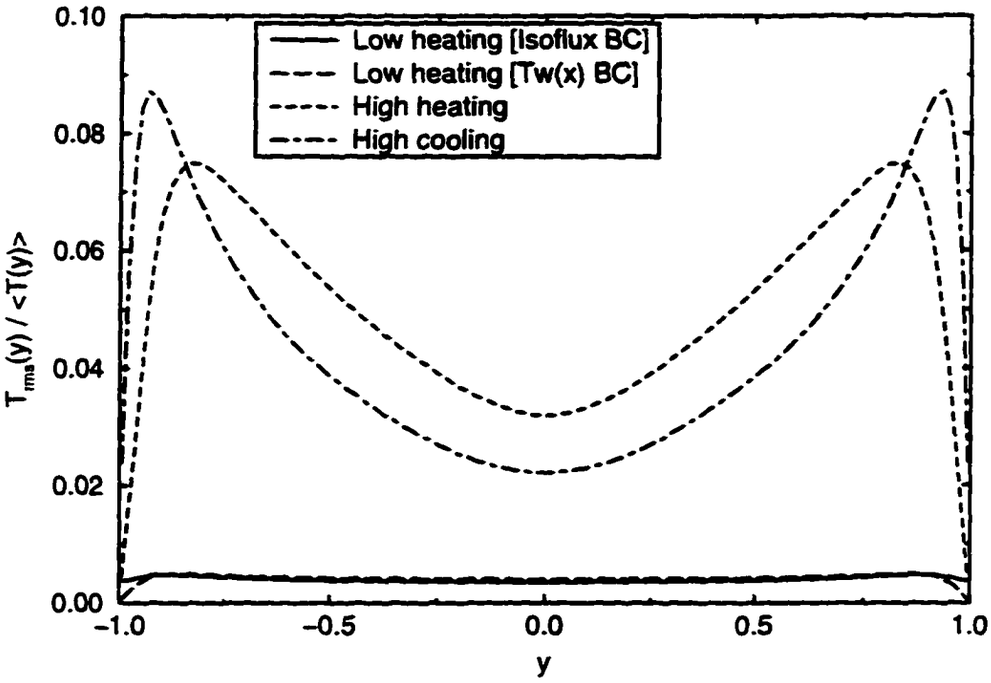

Figure 7.25 Temperature fluctuations scaled by local mean temperature

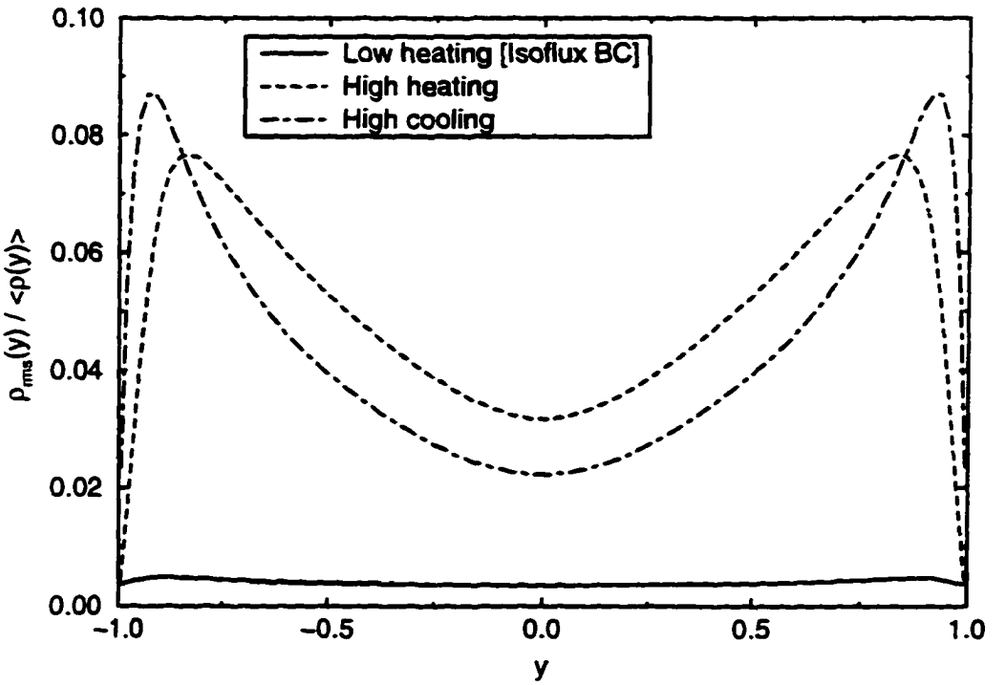

Figure 7.26 Density fluctuations scaled by local mean density

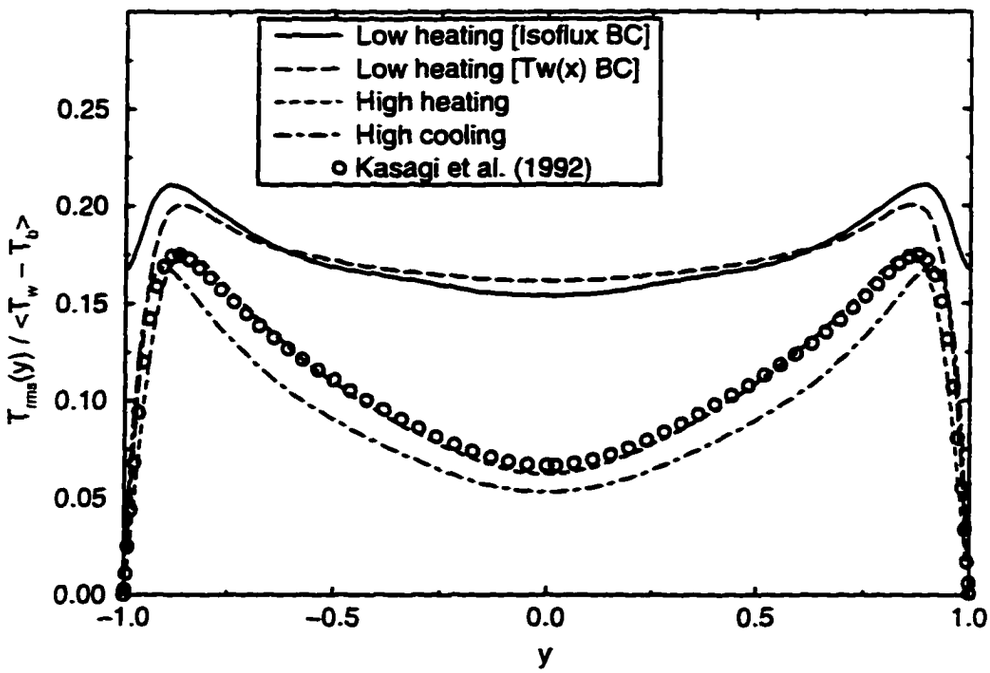

Figure 7.27 Temperature fluctuations scaled by wall-to-bulk temperature difference

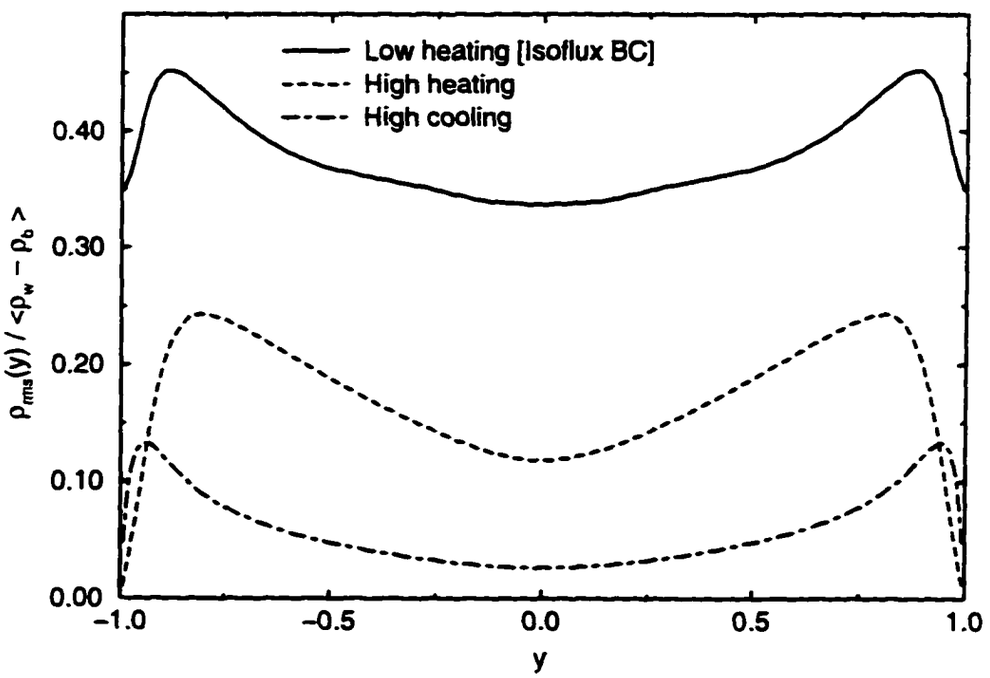

Figure 7.28 Density fluctuations scaled by wall-to-bulk density difference

For low heating, the peak modeled SGS stress was only 2.5 percent of the wall shear stress. For high heating, the peak value decreased to 1.03 percent, and for high cooling the peak value increased to 7.28 percent of the wall shear stress.

Figure 7.30 shows the resolved heat flux, heat conduction, and modeled SGS heat flux distributions normalized by the wall heat flux, as defined in Section 7.4.4. The same trends were observed as for the shear stress distributions, with the exception that the increase of the resolved heat flux with high cooling was not as pronounced. However, the heat conduction was decreased and the and modeled SGS heat flux was increased with high cooling.

The sum of the three shear stress contributions is shown in Fig 7.31, while the sum of the three heat flux contributions is shown in Fig 7.32. For fully developed turbulent flows, such as incompressible turbulent channel flow, these represent the complete contributions to the total shear stress or heat flux, which are linear distributions. For the quasi-developed flows computed here, other terms could be contributing to the shear stress and heat flux balance. This could explain the departure from a linear profile, especially for the high heating shear stress distribution, for example.

The modeled SGS turbulent viscosity is shown normalized by the reference viscosity in Fig 7.33, and normalized by the local molecular viscosity in Fig. 7.34. The figures show that the modeled contribution to the total "effective" viscosity was less than 8.3 percent for low heating, but increased to as much 12.8 percent for high cooling. For high heating, the peak value fell to 5.9 percent.

7.7 Instantaneous Turbulence Contours

In this section, instantaneous contours of several quantities are compared for the low heating, high heating, and high cooling channel flows, which are denoted as cases LH, HH, and HC, respectively. The instantaneous quantities shown in this section were normalized by the reference quantities. For the channel flow simulations, the reference density, velocity and temperature were nearly equal to the bulk values at the inlet. Differences in the structure of the turbulence were sought to help explain some of the trends observed in the ensemble averaged

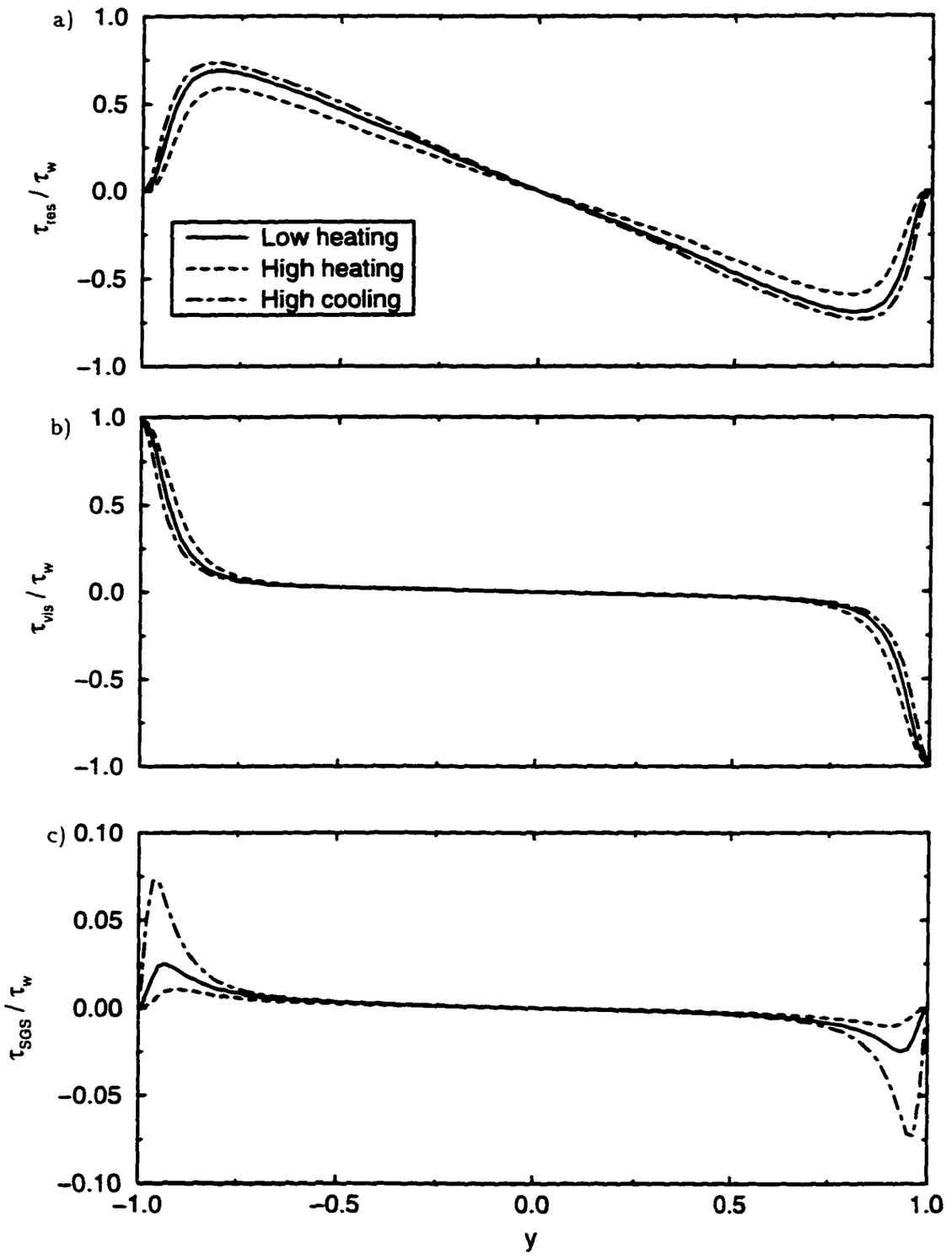

Figure 7.29 Shear stress distributions scaled by wall shear stress

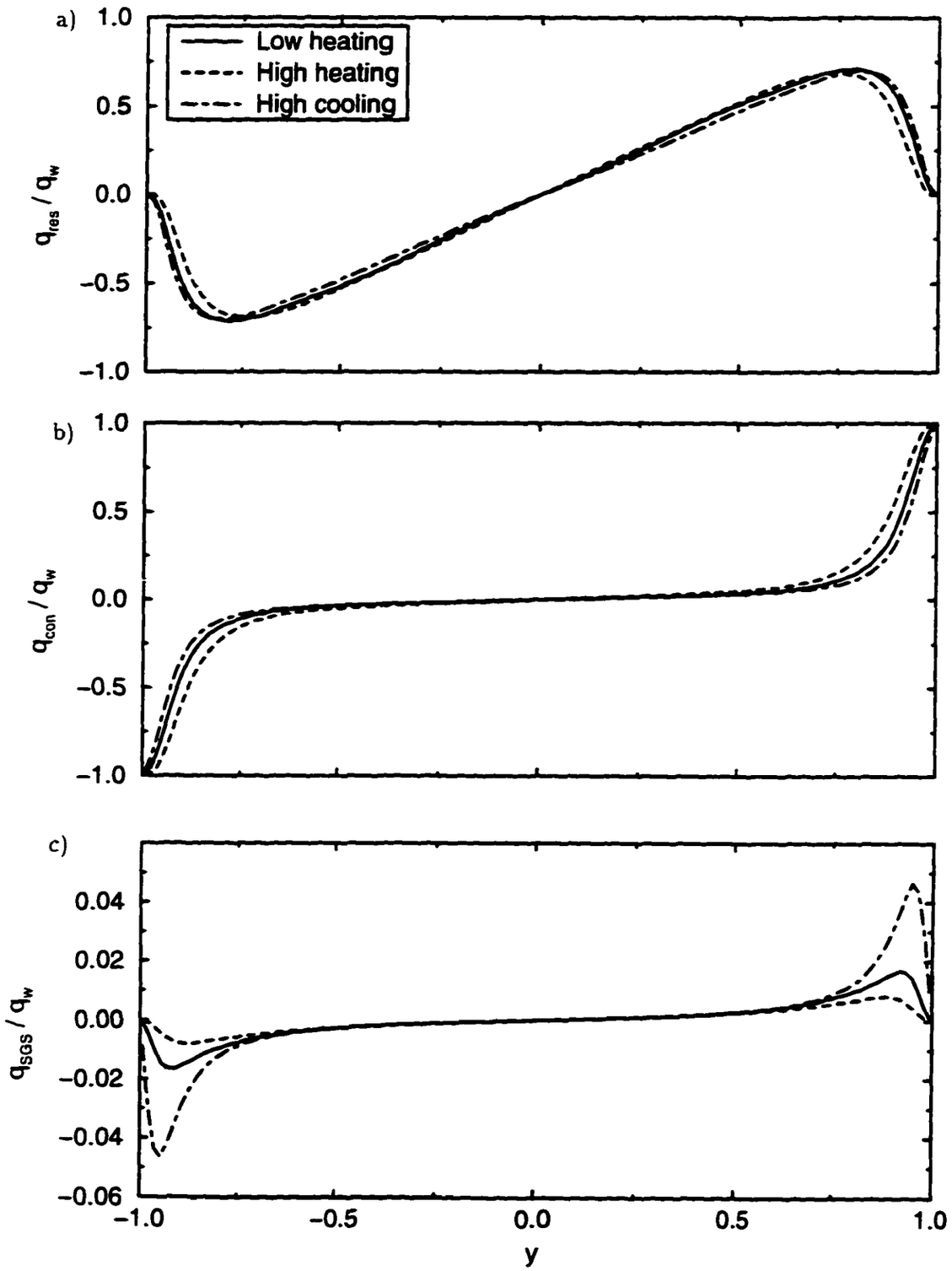

Figure 7.30 Heat flux distributions scaled by wall heat flux

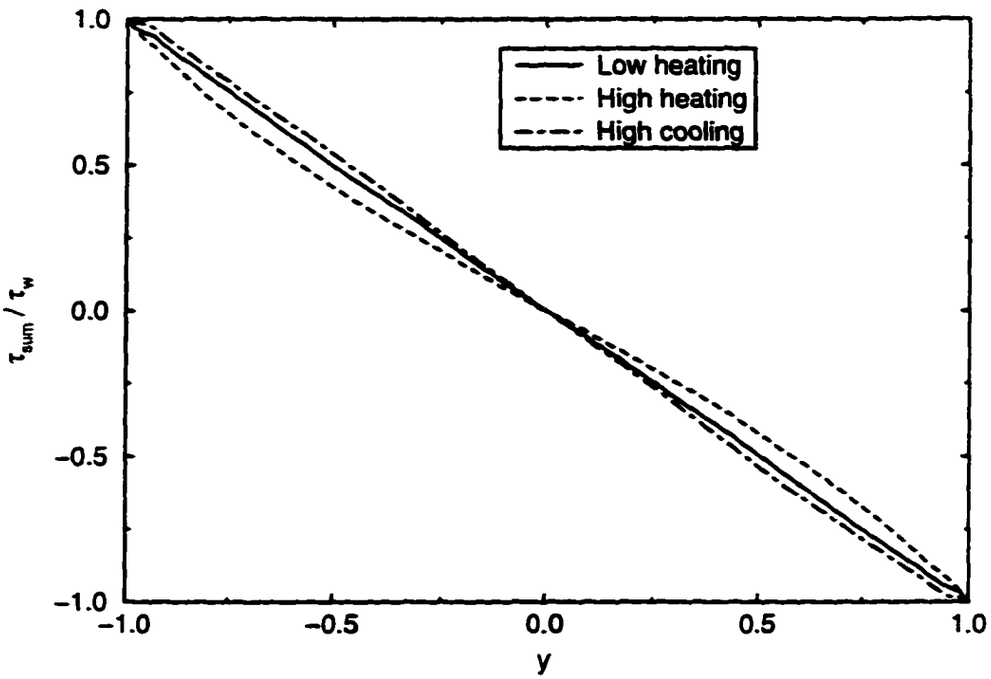

Figure 7.31 Sum of resolved, viscous, and SGS shear stress contributions scaled by wall shear stress

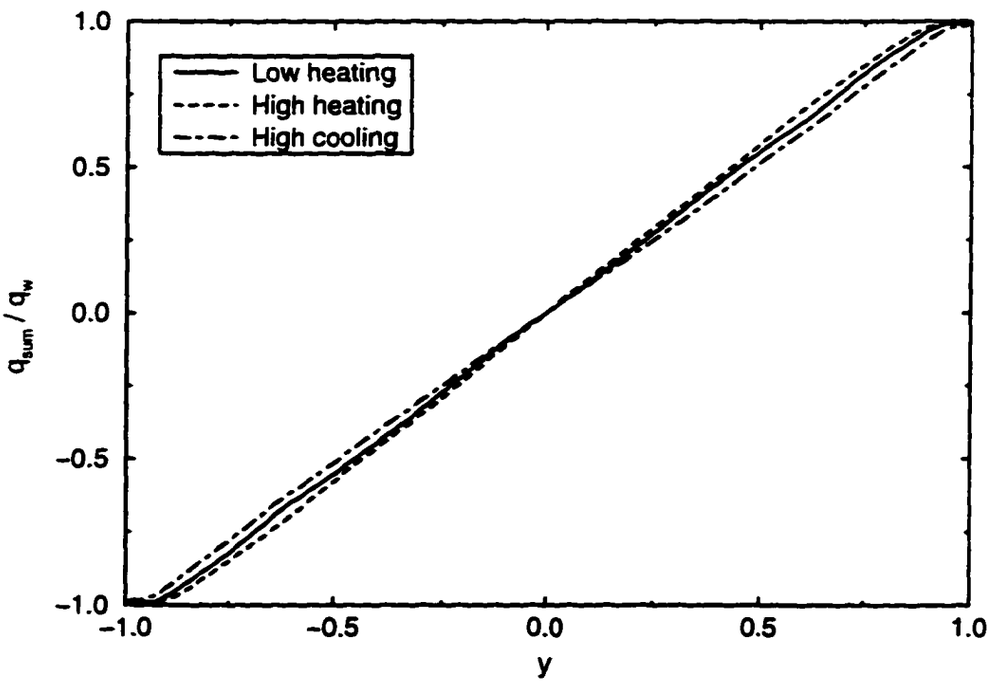

Figure 7.32 Sum of resolved, conductive, and SGS heat flux contributions scaled by wall heat flux

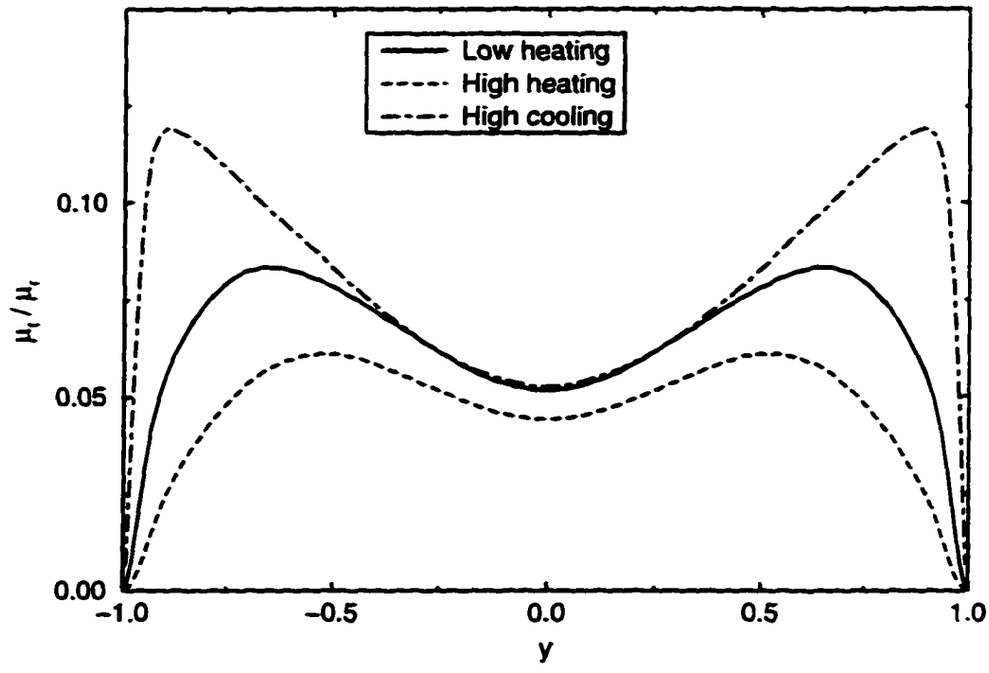

Figure 7.33 Modeled SGS turbulent viscosity scaled by reference viscosity

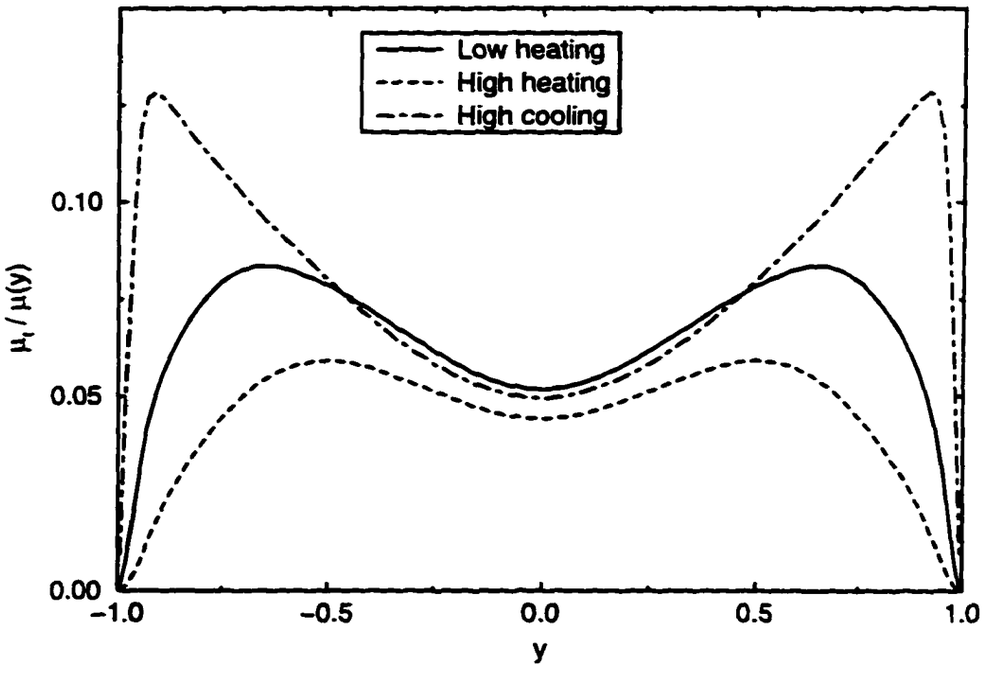

Figure 7.34 Modeled SGS turbulent viscosity scaled by local molecular viscosity

data.

7.7.1 Bursting or Ejection-Sweep Phenomenon

One particular turbulent structure of interest for solid wall bounded flows is the turbulent "bursting" phenomenon. Turbulent flows are not just random or chaotic, but contain deterministic features or coherent structures. Coherent structures in turbulence exhibit some discernible pattern in the flow, which may have many random features but nevertheless occurs with sufficient regularity, in space or time, to be recognizable as quasi-periodic or near-deterministic (McComb, 1990). For turbulent boundary layers and internal pipe or channel flows, a characteristic coherent structure that occurs is the bursting phenomenon, which is characterized by the formation of low-speed streaks near the wall, and near-periodicity of the events. This periodicity of events refers to the regular spacing in the spanwise direction of the streaks, and the cyclic way the bursts repeat in time. A schematic of the turbulent boundary layer structure near the wall is shown in Fig. 7.35.

The sequence of events involves the streaks moving out from the wall, oscillating, and finally breaking up, as depicted in Fig. 7.35. This sequence is called a "burst" in boundary layer flows, and an "ejection-sweep" cycle in pipe or channel flows.

The streaky structure of low-speed streaks forms in the viscous sublayer ($y^+ < 5$), and indicates the presence of streamwise vorticity in pairs of counter-rotating vortex filaments. This leads to a "pumping action" alternatively to and from the wall as one moves across the wall in the spanwise direction.

7.7.2 Present Results

Figures 7.36 and 7.37 show the instantaneous streamwise velocity for high heating and high cooling, respectively. The lower $x - z$ plane is at $y/\delta = -0.949$, and the upper $x - z$ plane is at $y/\delta = 0.535$. The $y - z$ plane is at $x/\delta = 5.50$. Figure 7.46 shows the corresponding contours for low heating. The low-speed streaky structure mentioned above is clearly evident in the near wall region (lower $x - z$ plane), while more isotropic structure is apparent in the

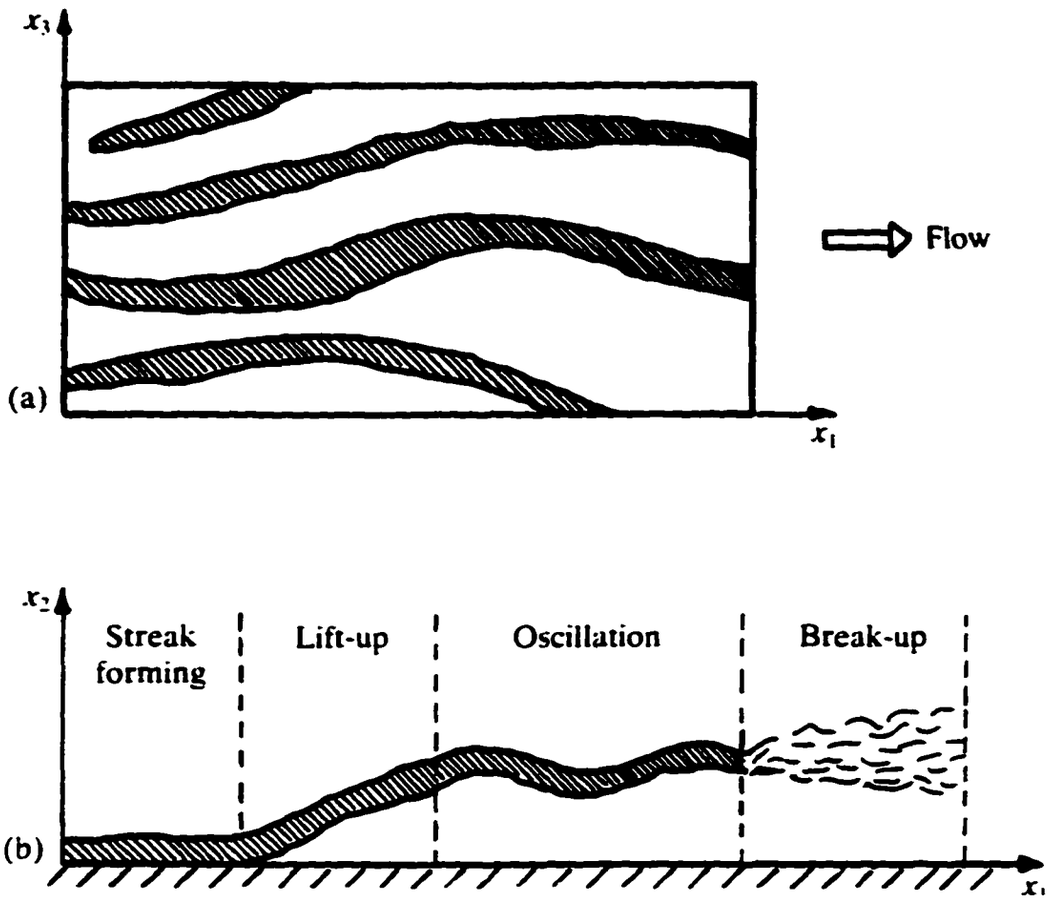

Figure 7.35 Schematic view of turbulent boundary layer structure near the wall: (a) top view of low speed streak; (b) side view of the sequence of events leading to the break-up of a streak (McComb, 1990)

upper plane away from the wall.

The instantaneous density is shown in Figures 7.38 and 7.39 for high heating and cooling, respectively. The $x-z$ plane in these and all subsequent figures is also at $y/\delta = -0.949$, and the $y-z$ plane is at $x/\delta = 5.50$. The variation in the density in the near-wall streaky structure is much more pronounced for high cooling, which corresponds to the larger observed values of the *rms* density fluctuations. However, the density fluctuations extend further into the center of the channel for high heating.

The instantaneous temperature contours are shown in Figures 7.40 and 7.41. The $x-y$

plane is at $z/\delta = 0.26$ in these and all subsequent figures. The ejection of hotter and colder fluid into the regions away from the wall due to the bursting phenomenon is apparent in the $y - z$ planes.

Figures 7.42, 7.43, and 7.47 show the instantaneous contours of the streamwise component of vorticity, $\tilde{\zeta}_x$, for cases HH, HC, and LH, respectively, where

$$\tilde{\zeta}_x = \frac{\partial \tilde{w}}{\partial y} - \frac{\partial \tilde{v}}{\partial z}. \tag{7.36}$$

Lifting of the streamwise vortex filaments is visible in these figures in the $x - y$ plane.

Finally, the instantaneous wall-normal vorticity component, $\tilde{\zeta}_y$, is shown in Figs. 7.44, 7.45, and 7.48, where

$$\tilde{\zeta}_y = \frac{\partial \tilde{u}}{\partial z} - \frac{\partial \tilde{w}}{\partial x}. \tag{7.37}$$

The counter-rotating vortex filaments are evident in the near wall region.

Coleman et al. (1995) compared contours of wall-normal vorticity at this y location, and concluded that as the Mach number was increased, the streamwise coherence was increased, which was indicated by the tendency of the contours of wall-normal vorticity to become "less wiggly". This effect was believed to be due to heat transfer or Mach number effects, and not due to Reynolds number (or viscous) effects. Slight differences in the streakiness were observed in the present results. The high cooling case shows the most coherence ("least wiggly") while the high heating appears to be less coherent ("more wiggly") compared to the low heating case. Since low Mach numbers were employed here, yet the differences in the streakiness were still observed, this study also suggests the effects must be due to heat transfer.

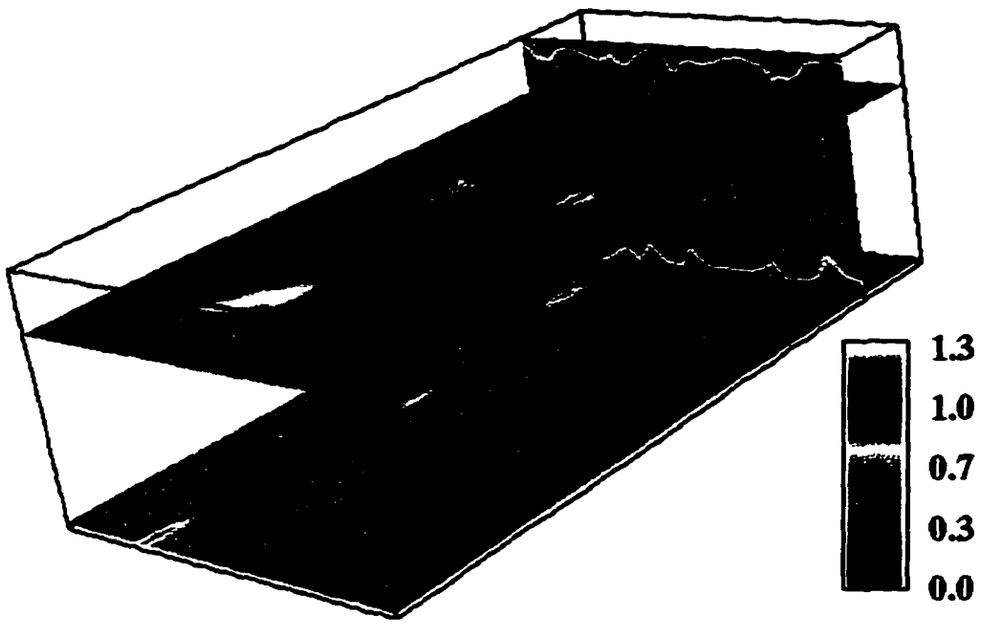

Figure 7.36 Instantaneous streamwise velocity, $\tilde{u}$, for case HH

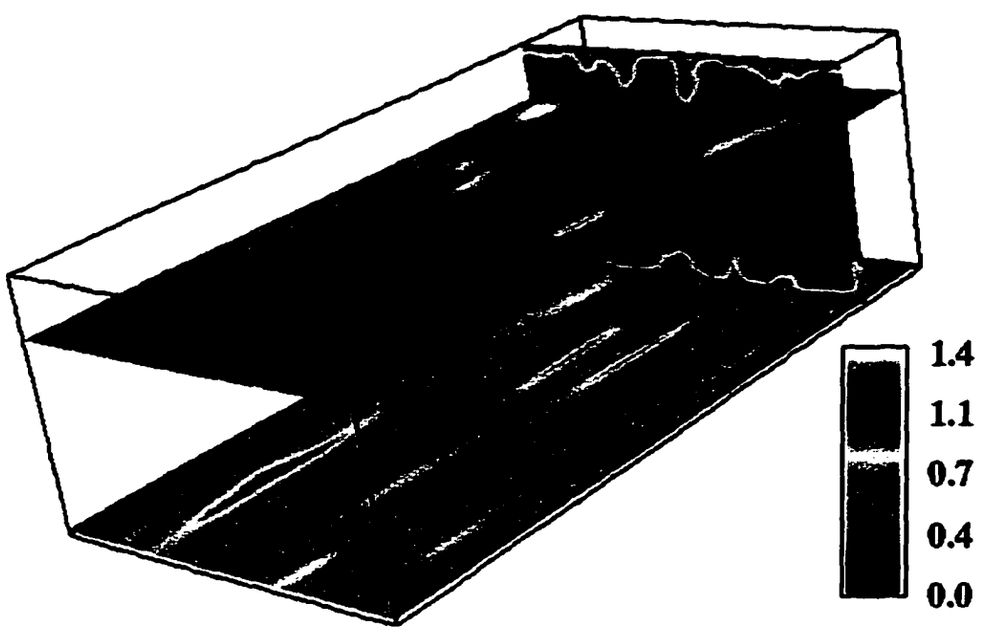

Figure 7.37 Instantaneous streamwise velocity, $\tilde{u}$, for case HC

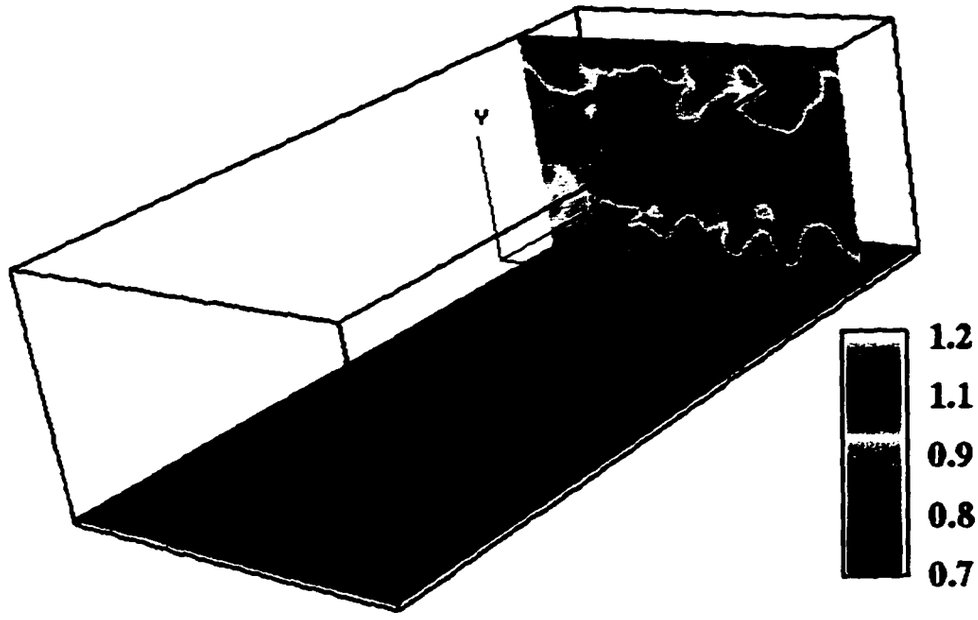

Figure 7.38 Instantaneous density, $\tilde{\rho}$, for case HH

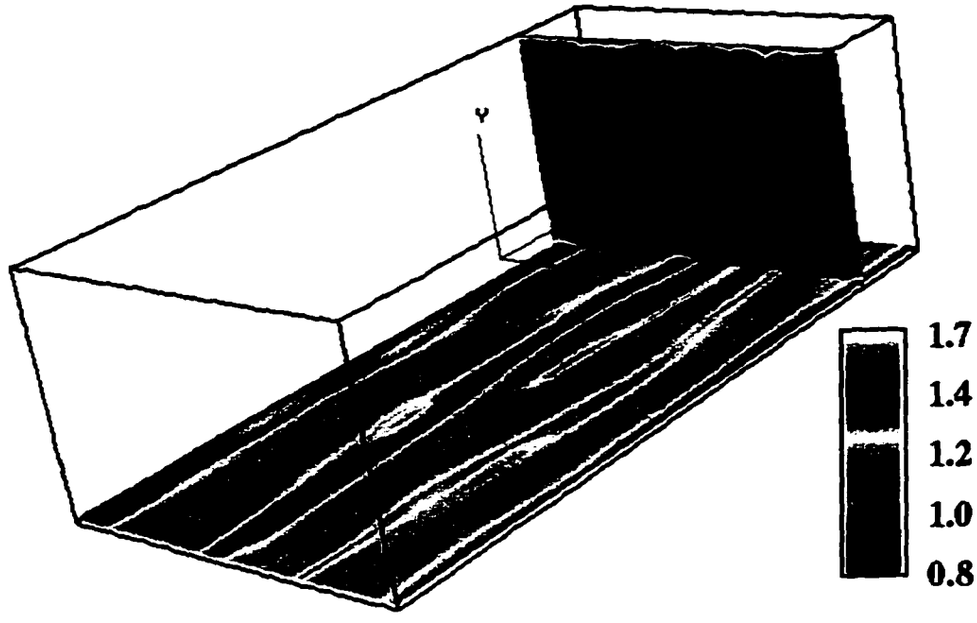

Figure 7.39 Instantaneous density, $\tilde{\rho}$, for case HC

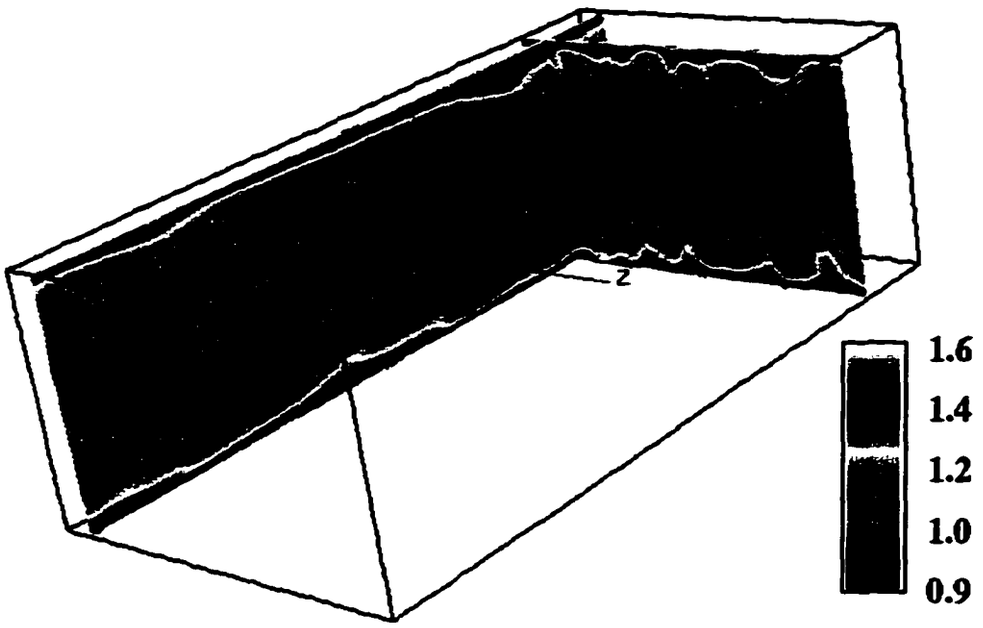

Figure 7.40 Instantaneous temperature, $\tilde{T}$, for case HH

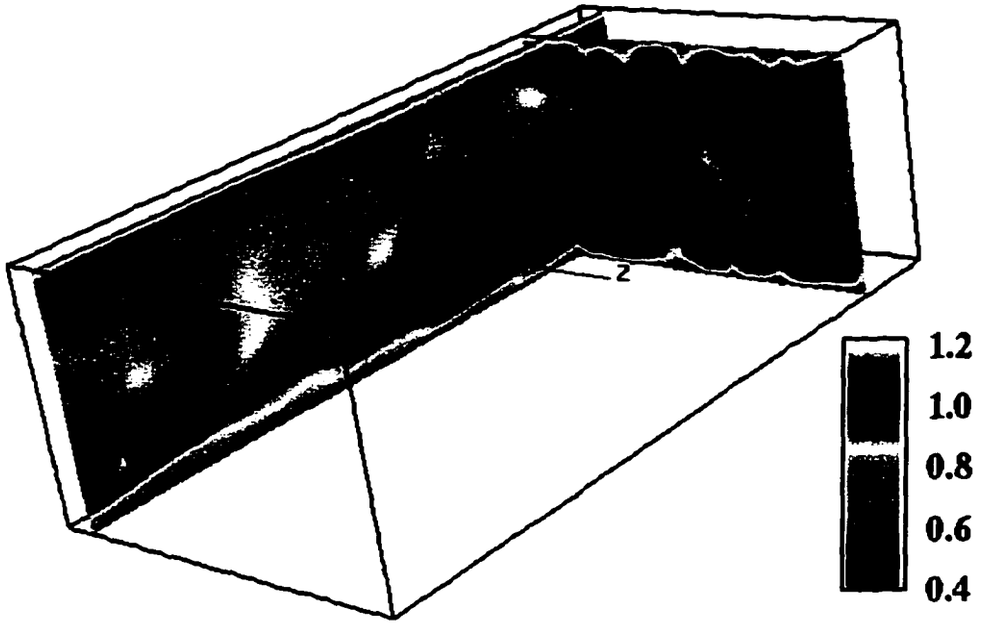

Figure 7.41 Instantaneous temperature, $\tilde{T}$, for case HC

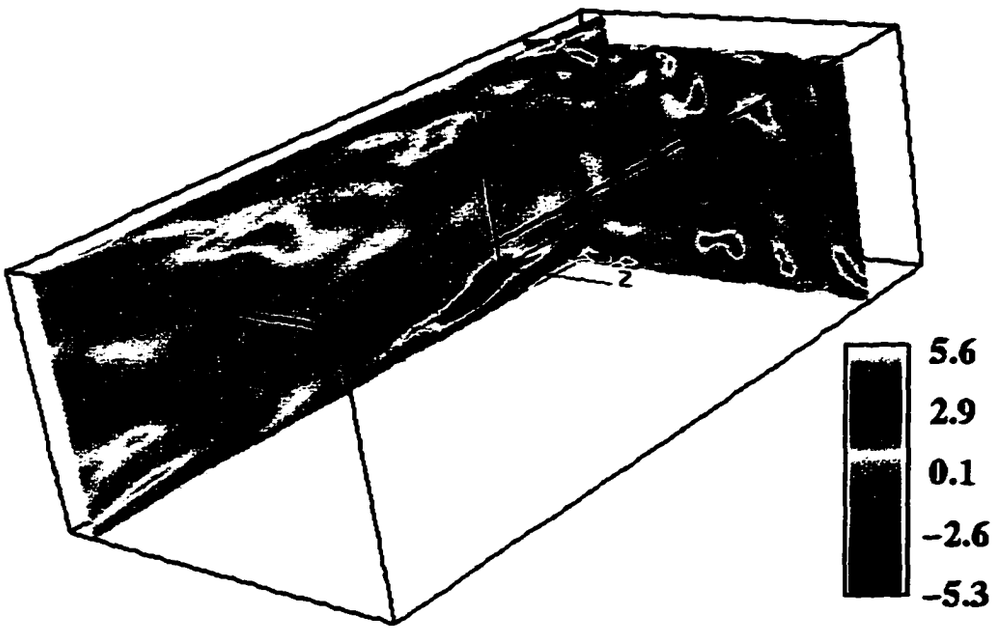

Figure 7.42 Instantaneous streamwise vorticity, $\tilde{\zeta}_x$, for case HH

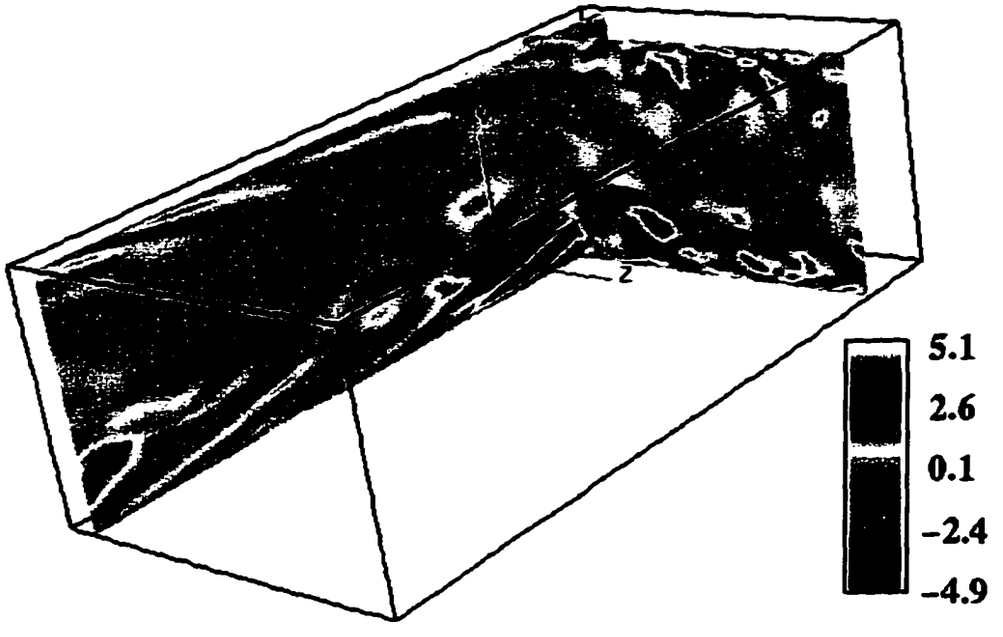

Figure 7.43 Instantaneous streamwise vorticity, $\tilde{\zeta}_x$, for case HC

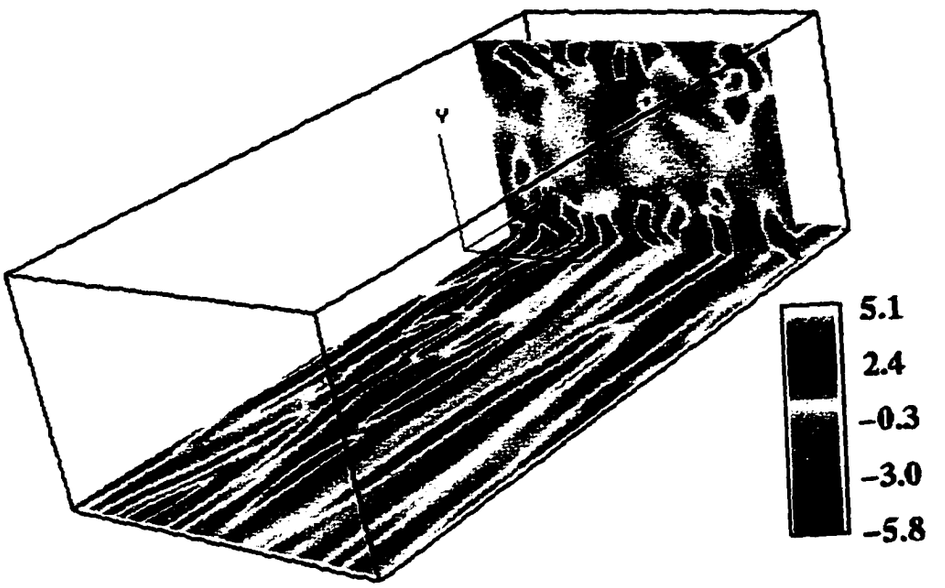

Figure 7.44 Instantaneous wall-normal vorticity, $\tilde{\zeta}_y$, for case HH

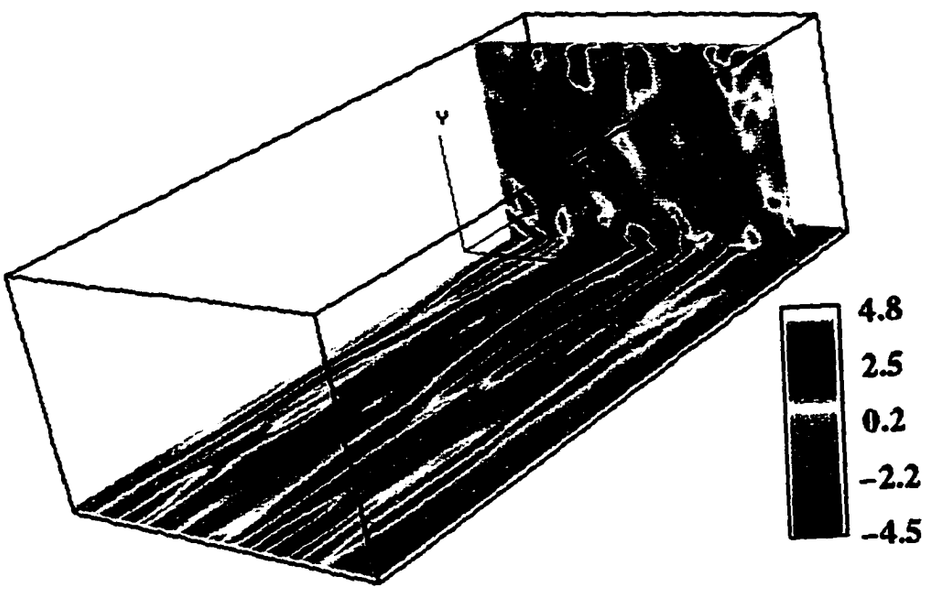

Figure 7.45 Instantaneous wall-normal vorticity, $\tilde{\zeta}_y$, for case HC

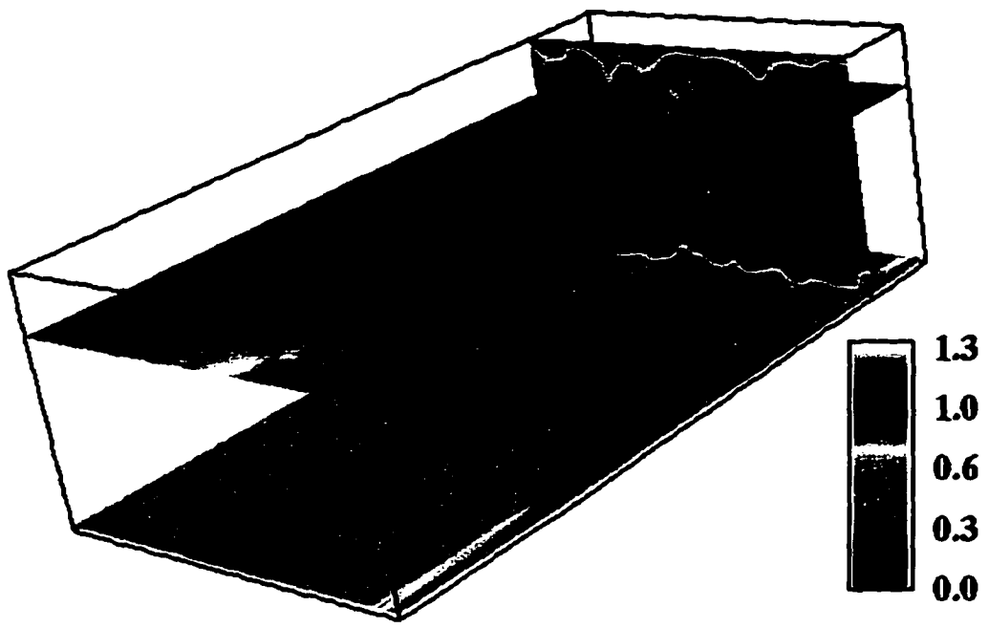

Figure 7.46 Instantaneous streamwise velocity, $\tilde{u}$, for case LH

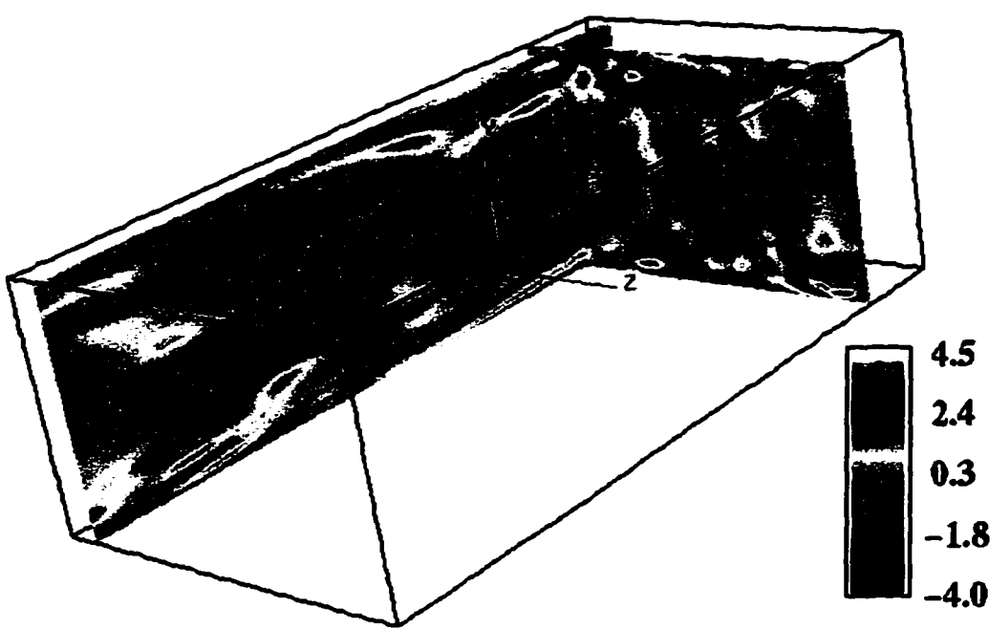

Figure 7.47 Instantaneous streamwise vorticity, $\tilde{\zeta}_x$, for case LH

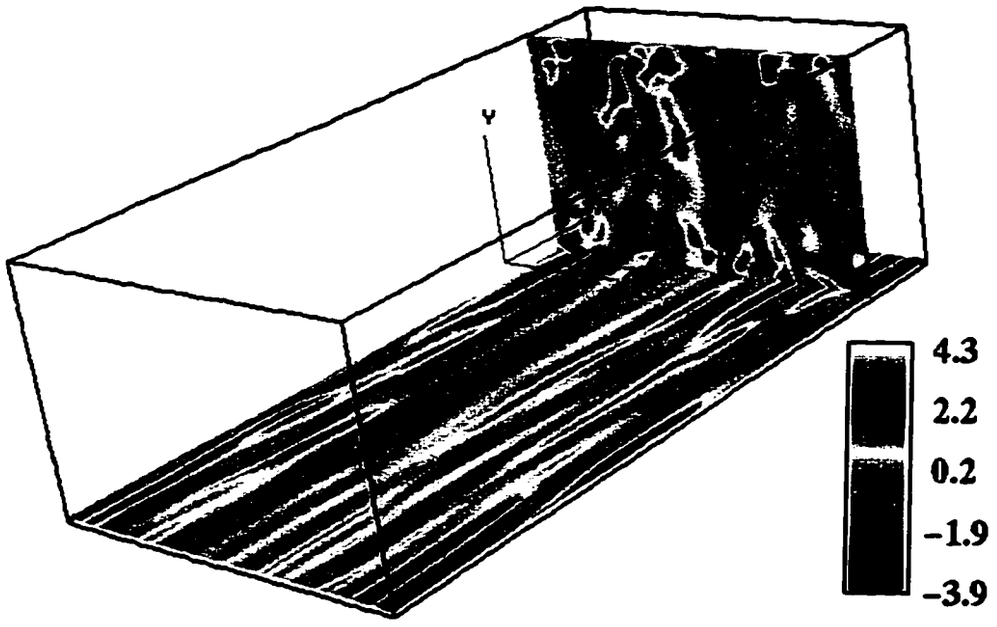

Figure 7.48 Instantaneous wall-normal vorticity, $\tilde{\zeta}_y$, for case LH

7.8 Comparison to Variable Property Correlations

In this section, the friction coefficients and Nusselt numbers are compared to several variable property empirical correlations. The two most common methods for correcting the constant property correlations for variable property effects are the reference temperature method and property ratio method. The reference temperature method involves choosing a characteristic temperature at which to evaluate properties in the constant property correlations, such that variable property behavior is obtained. The more commonly used property ratio method involves determining the properties with the bulk temperature, but the variable property effects are lumped into ratios of one property at the surface temperature to that at the bulk temperature.

For gases, the property ratio method is in terms of the wall-to-bulk temperature ratio as

$$\frac{\mathrm{Nu}}{\mathrm{Nu}_{cp}} = \left(\frac{T_w}{T_b}\right)^n \qquad \frac{f}{f_{cp}} = \left(\frac{T_w}{T_b}\right)^m, \tag{7.38}$$

where the subscript *cp* refers to the corresponding constant property correlation.

A variable property correlation given by Petukhov and Popov (1963) is

$$\begin{aligned} &\tfrac{T_w}{T_b} < 1, \quad n = -0.36 \quad \text{for cooling} \\ &\tfrac{T_w}{T_b} > 1, \quad n = -\left[0.3\log_{10}\left(\tfrac{T_w}{T_b}\right) + 0.36\right] \quad \text{for heating} \end{aligned} \tag{7.39}$$

where Nu_{cp} is given by Eq. 6.27. The correlation is valid for $0.37 < T_w/T_b < 3.1$ and $10^4 < \mathrm{Re}_D < 5.8 \times 10^6$ within ±4%. The analysis used to develop the correlation assumed the turbulent Prandtl number was unity. The friction factor exponents for variable properties are given by

$$\begin{aligned} &\tfrac{T_w}{T_b} < 1, \quad m = -0.6 + 5.6\mathrm{Re}_w^{-0.38} \quad \text{for cooling} \\ &\tfrac{T_w}{T_b} > 1, \quad m = -0.6 + 0.79\mathrm{Re}_w^{-0.11} \quad \text{for heating} \end{aligned} \tag{7.40}$$

where $\mathrm{Re}_w = u_b D_h \rho_w/\mu_w$. Equation 7.40 is valid for $0.37 < T_w/T_b < 3.7$ and $14 \times 10^3 < \mathrm{Re}_D < 10^6$ with 2 to 3% error.

Kays and Crawford (1993) recommended the following exponents with Nu_{cp} given by Eq. 6.33

$$\begin{aligned} &\tfrac{T_w}{T_b} < 1, \quad n = -0.5 \quad m = -0.1 \quad \text{for heating} \\ &\tfrac{T_w}{T_b} > 1, \quad n = 0.0 \quad m = -0.1 \quad \text{for cooling.} \end{aligned} \tag{7.41}$$

Correlations that have resulted strictly from experimental studies, the majority of which were for gas heating at constant wall temperature in circular ducts, are expressed in the form

$$\mathrm{Nu}_D = C\,\mathrm{Re}_D^{0.8}\mathrm{Pr}^{0.4}\left(\frac{T_w}{T_b}\right)^n. \tag{7.42}$$

For instance, the correlation proposed by Humble, Lowdermilk, and Desmon (1951) is

$$\mathrm{Nu}_D = 0.023\mathrm{Re}_D^{0.8}\mathrm{Pr}^{0.4}\left(\frac{T_w}{T_b}\right)^n. \tag{7.43}$$

where $n = 0$ for cooling and $n = -0.55$ for heating. The correlation is valid for $0.46 < T_w/T_b < 3.5$ and $7 \times 10^3 < \mathrm{Re}_D < 3 \times 10^5$.

A correlation given by Barnes and Jackson (1961) valid for heating only with $1.2 < T_w/T_b < 2.2$ and $4 \times 10^3 < \mathrm{Re}_D < 6 \times 10^4$ and $L/d > 60$ is

$$\mathrm{Nu}_D = 0.023\mathrm{Re}_D^{0.8}\mathrm{Pr}^{0.4}\left(\frac{T_w}{T_b}\right)^{-0.4}. \tag{7.44}$$

McEligot et al. (1965) proposed a similar correlation of

$$\mathrm{Nu}_D = 0.021\mathrm{Re}_D^{0.8}\mathrm{Pr}^{0.4}\left(\frac{T_w}{T_b}\right)^{-0.5} \tag{7.45}$$

valid for $1 < T_w/T_b < 2.5$ and $1.5 \times 10^4 < \mathrm{Re}_D < 2.33 \times 10^5$ and $L/d > 30$.

The results for the present simulations are compared to the correlations given above in Tables 7.8 through 7.11, for cases LHTW, LHQW, HH, and HC, respectively. The agreement for the low heating cases, Tables 7.8 and 7.9, is good, with differences of less than 9 percent for both the friction coefficient and Nusselt number for both cases LHTW and LHQW for all correlations. The best agreement is obtained with the correlations of Humble, Lowdermilk, and Desmon (1951) and Barnes and Jackson (1961), with less than 1.2 percent difference for the Nusselt numbers. These two correlations are valid for lower Reynolds number ranges than the other correlations.

Good agreement was also obtained with the correlations for the high cooling case, shown in Table 7.11. Best agreement is again obtained with the Humble, Lowdermilk, and Desmon correlation.

The high heating cases did not compare as favorably with the correlations, with the correlations suggesting more of a decrease in the Nusselt number due to heating than was obtained

Table 7.8 Comparison to variable property correlations for low heating with specified $T_w(x)$ (case LHTW)

Correlation	Equation	f	% error	Nu_D	% error
Present simulation	—	0.00768	—	34.5	—
Petukhov and Popov (1963)	7.39	0.00750	2.4	32.6	5.8
Humble, Lowdermilk, and Desmon (1951)	7.43	—	—	34.8	-0.8
Barnes and Jackson (1961)	7.44	—	—	34.9	-1.2
McEligot (1985)	7.45	—	—	31.8	8.5
Kays and Crawford (1993)	7.41	0.00709	8.4	32.2	7.2

Table 7.9 Comparison to variable property correlations for low heating with specified q_w (case LHQW)

Correlation	Equation	f	% error	Nu_D	% error
Present simulation	—	0.00768	—	34.3	—
Petukhov and Popov (1963)	7.39	0.00754	1.9	32.3	6.2
Humble, Lowdermilk, and Desmon (1951)	7.43	—	—	34.4	-0.3
Barnes and Jackson (1961)	7.44	—	—	34.5	-0.6
McEligot (1985)	7.45	—	—	31.4	9.1
Kays and Crawford (1993)	7.41	0.00711	8.0	31.8	7.7

with the present results. The differences ranged from 6.6 to 13.1 percent for the two low Reynolds number correlations of Humble, Lowdermilk, and Desmon and Barnes and Jackson. However, differences as high as 21.4 percent were observed with other correlations.

7.9 Comparison of Van Driest Damping Formulations

Two fine grid simulations for high heat flux turbulent channel flows were completed before an error in the definition of y^+ used in the Van Driest damping formulation was discovered. Fortunately, the utilized computer resources were not a total waste, since the simulations were used to study the sensitivity of the results to the damping formulation and SGS model.

The intended "correct" definition of y^+ is based on the wall values of density and molecular viscosity, denoted as y_w^+ in the figures in this section, and given as

$$y^+ = y_w^+ = \frac{\delta_w^* \, u_\tau^* \rho_w}{\mu_w} = \mathrm{Re}\,\frac{\delta_w \, u_\tau}{\nu_w} \tag{7.46}$$

Table 7.10 Comparison to variable property correlations for high heating (case HH)

Correlation	Equation	f	% error	Nu_D	% error
Present simulation	—	0.00782	—	30.8	—
Petukhov and Popov (1963)	7.39	0.00658	18.7	26.9	14.2
Humble, Lowdermilk, and Desmon (1951)	7.43	—	—	27.2	13.1
Barnes and Jackson (1961)	7.44	—	—	28.8	6.6
McEligot (1985)	7.45	—	—	25.3	21.4
Kays and Crawford (1993)	7.41	0.00690	13.4	25.7	20.0

Table 7.11 Comparison to variable property correlations for high cooling (case HC)

Correlation	Equation	f	% error	Nu_D	% error
Present simulation	—	0.00779	—	34.0	—
Petukhov and Popov (1963)	7.39	0.00935	-16.7	39.2	-13.2
Humble, Lowdermilk, and Desmon (1951)	7.43	—	—	34.0	-0.1
Kays and Crawford (1993)	7.41	0.00759	2.6	31.5	8.0

where the superscript asterisk denotes dimensional variables, and δ_w is the distance to the nearest wall. The earlier simulations were performed with an "incorrect" definition of y^+ based on the reference values of density and viscosity, denoted as y_r^+, and given as

$$y^+ = y_r^+ = \frac{\delta_w^* \, u_\tau^* \rho_r}{\mu_r} = \mathrm{Re}\, \delta_w \, u_\tau. \tag{7.47}$$

The two simulations were for high heating and high cooling, as presented previously in this chapter, except the definition of y^+ in the damping formulation was in error, effectively changing the damping of the modeled SGS turbulent viscosity. The high cooling simulation used a Smagorinsky coefficient of $C_s = 0.08$, the same as for the simulations presented earlier with the "correct" y^+ definition. However, the high heating simulation was simulated using a lower value of $C_s = 0.069$ because the simulations tended to laminarize (exhibited by a gradual, then sudden, decrease in turbulent kinetic energy over time). When the damping formulation was corrected, the normal value of $C_s = 0.08$ was used without any problem.

The square of the average Van Driest damping function that resulted for the four different simulations is shown in Fig. 7.49. Clearly, significant differences exist (as much as 50 percent)

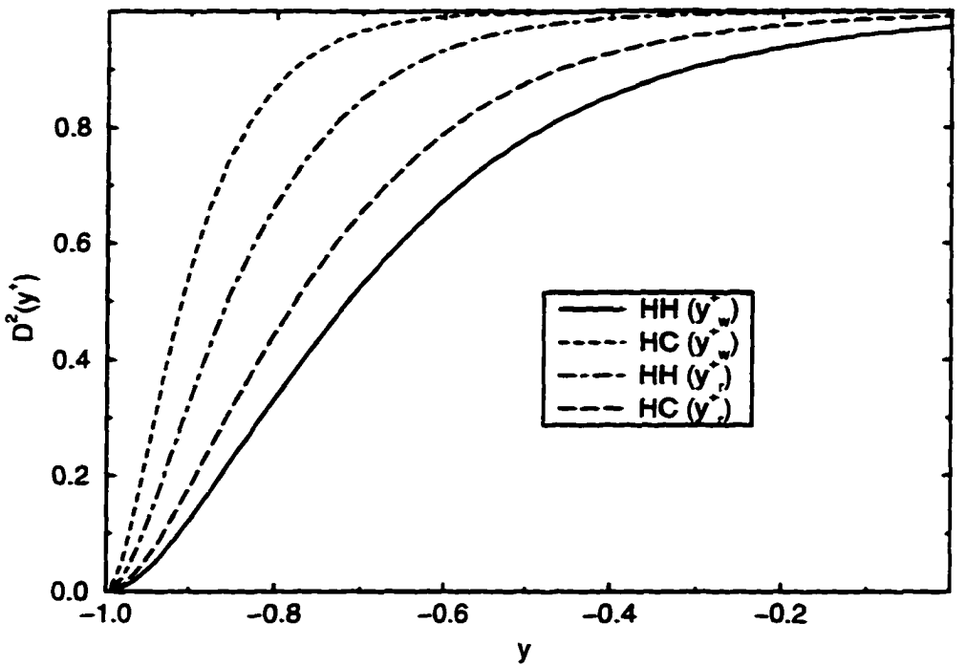

Figure 7.49 Van Driest damping function with y^+ based on wall properties, y_w^+, and on reference properties, y_r^+

between the damping formulations at the same location in the channel. For high heating, y_r^+ resulted in much less damping, while for high cooling, y_r^+ resulted in much more damping. The modeled SGS turbulent viscosity profiles are shown in Fig. 7.50. The difference was more pronounced for high cooling, which shows much lower values of μ_t near the wall with the incorrect damping. The overdamping for high heating with the incorrect y^+ definition led to the laminarizing effect described above.

Although the effects on the damping formulation and SGS model were dramatic, the effects on the resulting turbulence statistics was minimal. For instance, the mean velocity and temperature profiles, normalized by reference quantities or bulk properties, showed no noticeable difference between the two different damping formulations (and hence, were not shown here). The effect on the turbulent fluctuations was only slightly apparent, as shown in Fig. 7.51 for the velocity fluctuations, Fig. 7.52 for the turbulent kinetic energy, and Fig. 7.53 for the temperature fluctuations. The fact that the SGS turbulent viscosity was significantly different, and yet the turbulence statistics were almost unaffected, demonstrates the small contribution

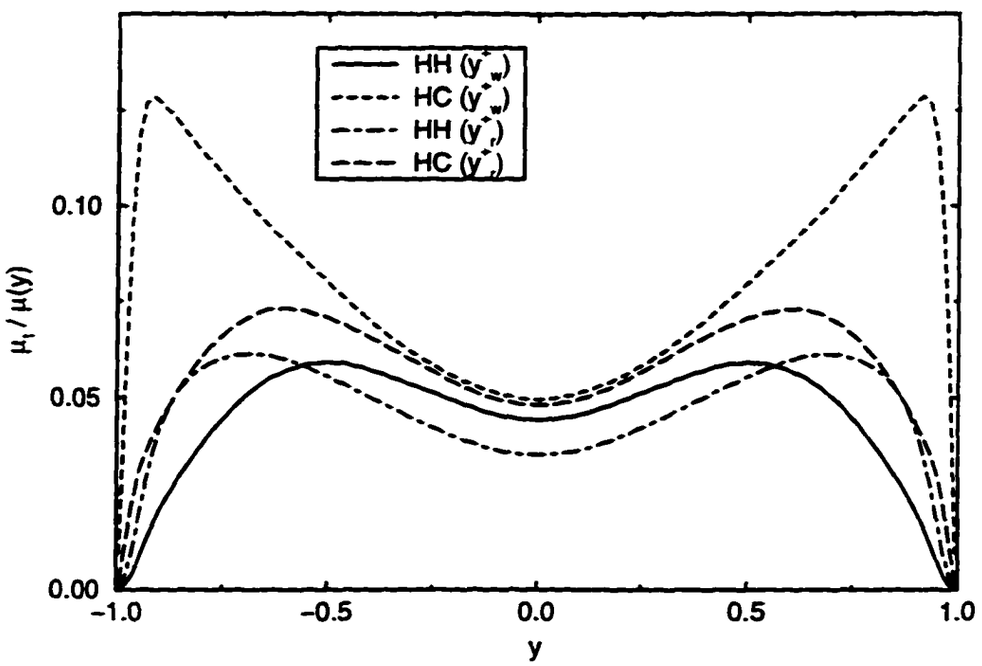

Figure 7.50 Effect of damping formulation on SGS turbulent viscosity normalized by local molecular viscosity

of the SGS model.

7.10 Summary

Two-dimensional, laminar, hydrodynamically and thermodynamically developing channel flow with constant wall heating rates was computed to study the quasi-developed region far downstream from the entrance region. A suitable set of approximate streamwise boundary conditions was found, such that the flow in the quasi-developed region could be computed in a step-wise periodic manner. The same boundary conditions were applied to the turbulent simulations.

Turbulent channel flows with constant wall heating or cooling rates of magnitudes large enough to cause significant variation in the temperature-dependent fluid properties were simulated. The simulations were performed for high heating (and cooling), with a resulting bulk temperature increase (and decrease). The results were compared to nearly incompressible sim-

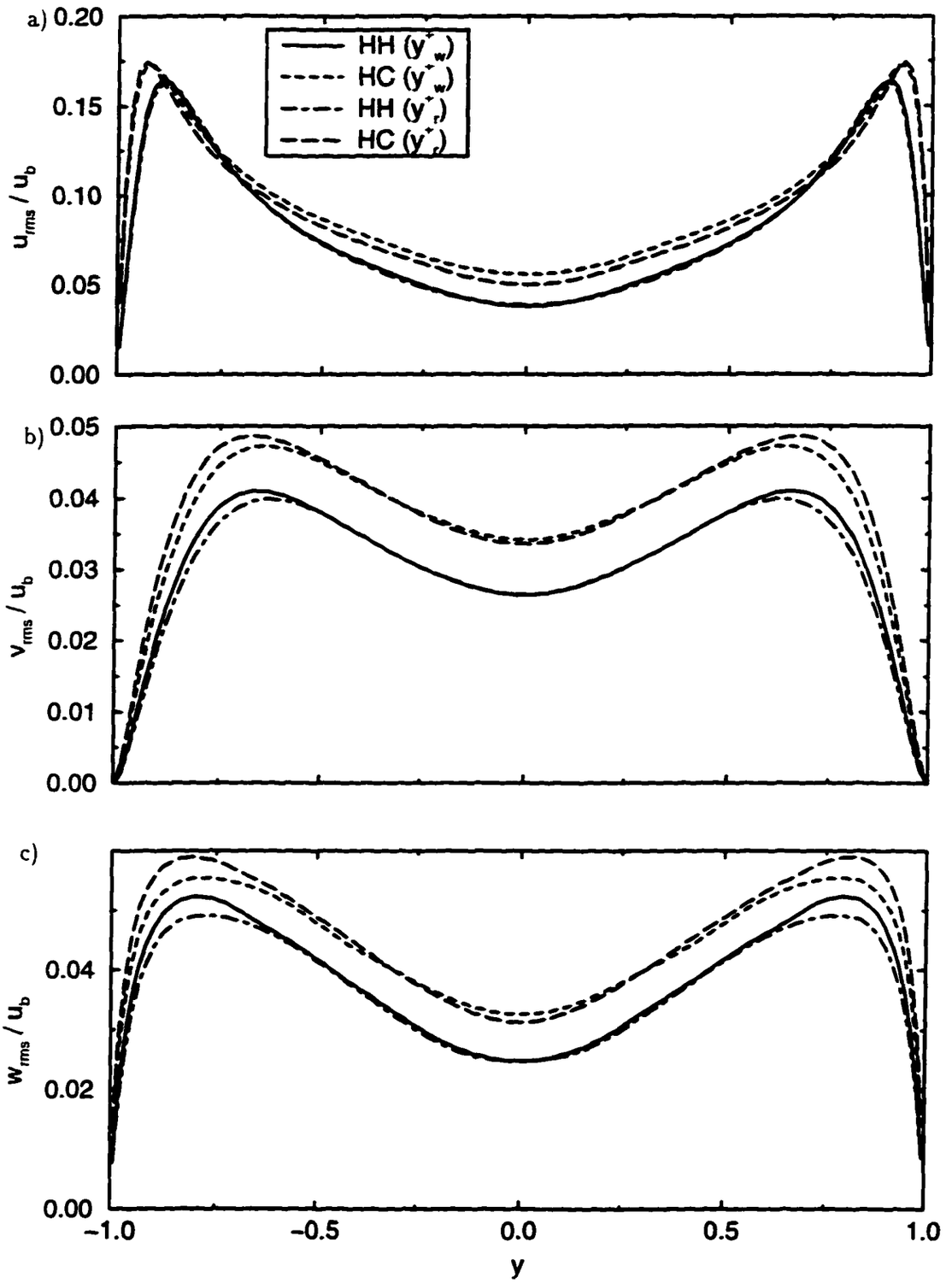

Figure 7.51 Effect of damping formulation on *rms* velocity fluctuations normalized by bulk velocity

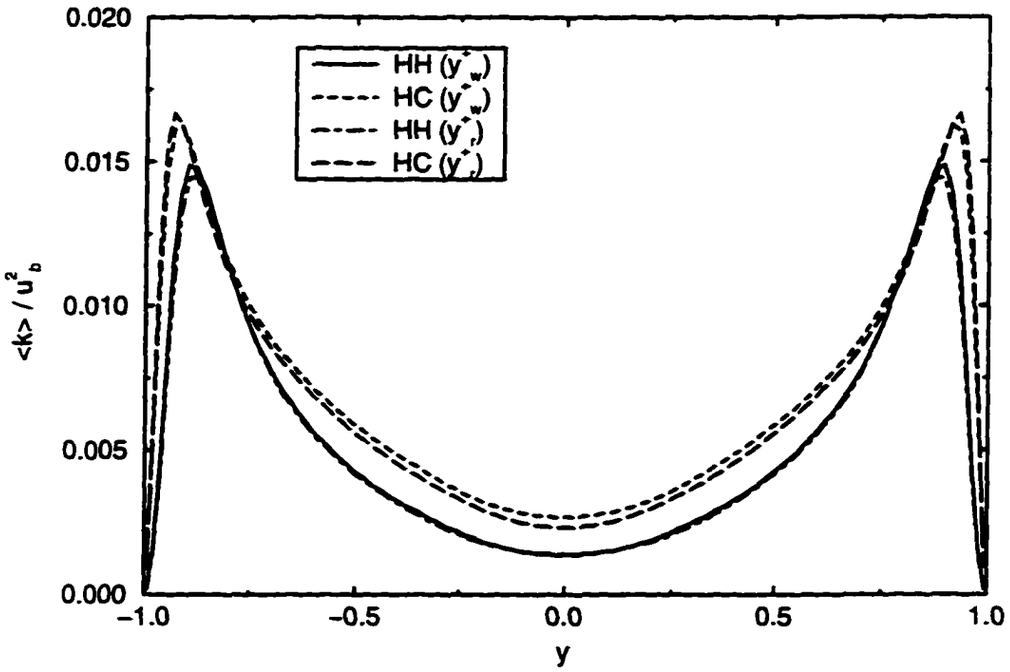

Figure 7.52 Effect of damping formulation on turbulent kinetic energy normalized by square of bulk velocity

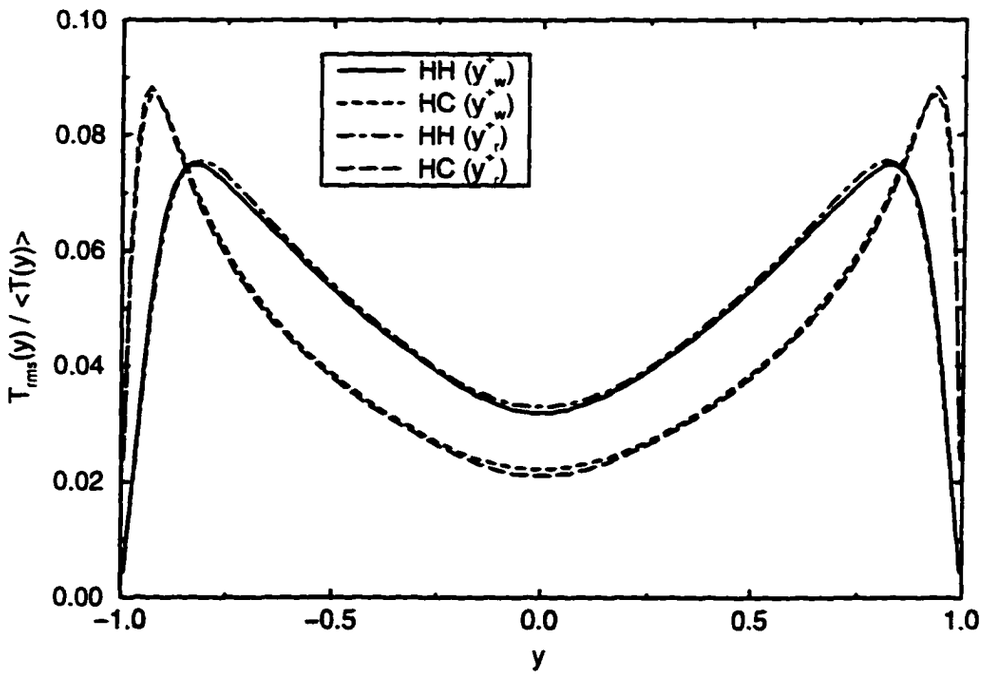

Figure 7.53 Effect of damping formulation on *rms* temperature fluctuations normalized by local mean temperature

ulations with low heating presented in Chapter 6. Comparisons were also made to LES and DNS results of other similar, but distinctly different, compressible or variable property channel flows.

In general, high heating was found to suppress turbulent velocity fluctuations, while high cooling promoted velocity fluctuations. This included the associated turbulent shear stresses and heat fluxes. The velocity fluctuations nearly collapsed to the incompressible results when plotted with semi-local coordinates, as opposed to wall coordinates. The mean velocity profiles collapsed to the incompressible log-law when plotted with the Van Driest transformation.

On a local percentage basis, the density and temperature fluctuations for high heating were larger over most of the channel compared to the high cooling results, except near the wall where the peak values were larger and shifted towards the wall for high cooling. When normalized by the wall-to-bulk temperature difference, the temperature fluctuations were nearly independent of the heating level.

The bursting or ejection-sweep phenomenon was clearly evident near the wall in the instantaneous quantities. More coherence was observed in the near-wall streaky structure for high cooling compared to low heating, while less coherence was observed for high heating. This effect has also been observed by other researchers (Coleman et al., 1995; Wang and Pletcher, 1996).

Extensive comparisons were made to empirical correlations for the friction coefficient and Nusselt number. The high cooling results compared favorably to most of the correlations, while the high heating results did not show as large a decrease in the Nusselt number as suggested by the correlations.

Finally, an alternate formulation of the Van Driest damping function in the modeled SGS turbulent viscosity was compared to the standard formulation. Although the damping had a significant effect on the SGS turbulent viscosity, little or no differences were observed in the mean flow and turbulent fluctuation profiles.

CHAPTER 8 TURBULENT FLOW AND HEAT TRANSFER FOR A RIB-ROUGHENED CHANNEL

8.1 Introduction

The turbulent flow and heat transfer was simulated for a plane channel with transverse square ribs on one wall. The objective was to evaluate the finite volume LES formulation for a more complex geometry that results in complex flow features. The rib-roughened channel was chosen as a test case because the ribbed wall provides complex flow features, such as flow separation, recirculation zones, and reattachment, and yet allows the use of periodic boundary conditions in the streamwise direction. The rib-roughened channel is of interest for cooling in gas turbine blades and other practical applications. The backward facing step provides similar complex flow features, but requires the specification of nonperiodic inflow conditions, which remains a challenge for LES.

In this chapter, the problem of interest is described, followed by a review of previous LES, DNS, and experimental investigations of similar configurations. Simulation details, such as modifications to the SGS modeling and the procedure for computing turbulence statistics are discussed. Finally, results from several simulations are presented and compared to previous LES and experimental results. Shortcomings in the present LES formulation for complex geometries are identified.

8.2 Problem Description

The problem of interest is the turbulent flow and heat transfer in a two-dimensional plane channel with a periodic array of transverse square ribs on one wall, as depicted in Fig. 8.1.

Many practical applications of rib-roughened channels have ribs on both walls, but the simplified case of ribs on one wall was used here to minimize grid requirements. The use of ribs on one wall has also been exploited in experimental studies because it simplifies detailed measurements of velocities and heat transfer parameters.

The simulation was set up such that comparisons could be made to the experimental data of Drain and Martin (1985) and Bates et al. (1983), who made detailed mean and fluctuating velocity measurements. The geometry of interest, depicted in Fig. 8.1, consisted of a periodic array of transverse, square ribs of height and width, h. The blockage ratio, which is the ratio of the rib height, h, to channel height, H, was $h/H = 0.2$. The pitch-to-height ratio of the ribs was 7.2, where the pitch, P, is the streamwise spacing of the ribs. Incidentally, this value of pitch-to-height ratio has consistently been found empirically to yield the greatest enhancement of heat transfer rates (Ciofalo and Collins, 1992). The nominal Reynolds number based on hydraulic diameter ($D_h = 4\delta$) and bulk velocity was $\mathrm{Re}_D = 20,000$.

For simulations with heat transfer, a constant heat flux, q_w, was applied to the lower wall and the upper wall was adiabatic. On the front, top, and back surfaces of the rib, a constant heat flux, $q_{w,rib}$, was applied with a magnitude that was one-third of the heat flux on the lower wall, q_w. Consequently, the total heat added to the channel was the same as for a smooth walled channel with no ribs and wall heat flux, q_w. For the simulations presented here, $q_w = 0.0009$ and $q_{w,rib} = 0.0003$.

As shown in Fig. 8.1, the computational domain only contained one rib. This section was assumed to be embedded in a periodic array of many ribs in a fully developed flow, which permitted the use of periodic boundary conditions in the streamwise direction.

8.3 Review of Previous Simulations

In this section, a review is given of known LES or DNS simulations of rib-roughened channel flows. Experimental studies and RANS computations are also briefly mentioned.

An early simulation was conducted by Kobayashi et al. (1983), who used LES to simulate the turbulent flow in a plane channel with ribs on one wall. The rib parameters were $h/H =$

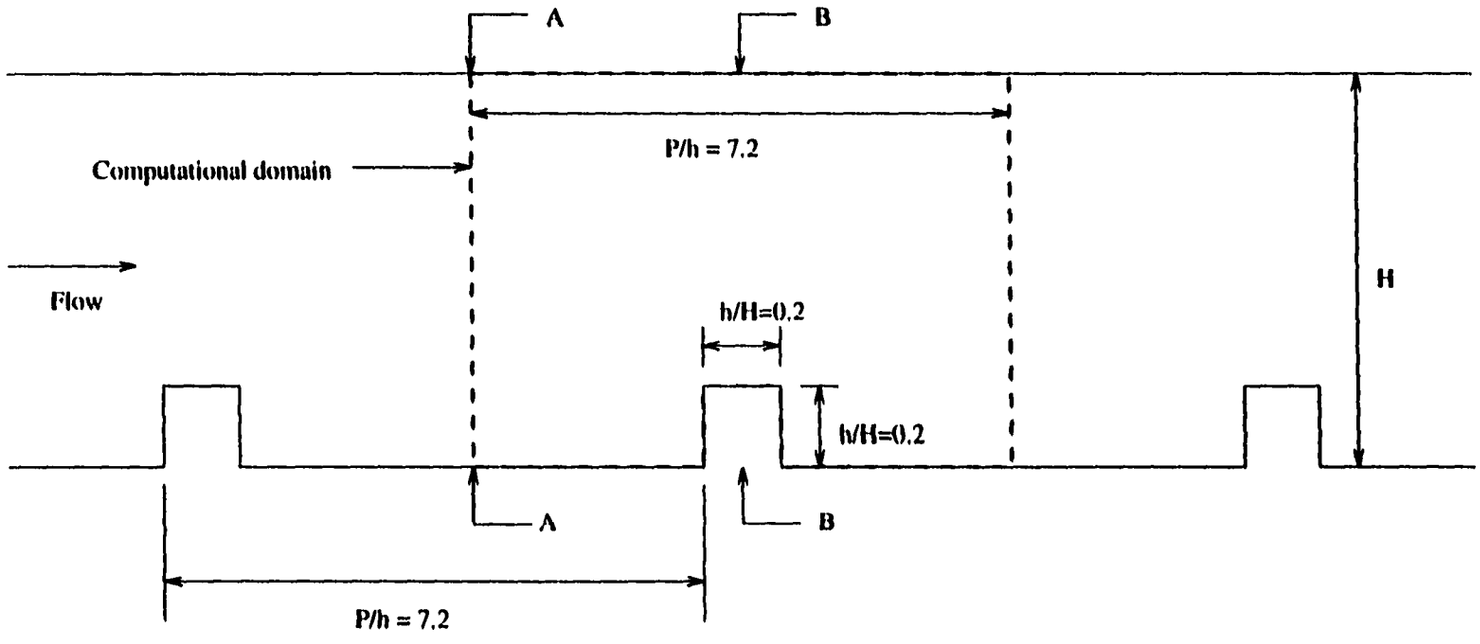

Figure 8.1 Schematic of plane channel with transverse square ribs on lower wall

0.3125. $P/h = 5.0$ and $\mathrm{Re}_D = 11.000$. A $40 \times 25 \times 9$ uniformly spaced grid was used. The filtered incompressible Navier-Stokes equations were solved with central differencing in space and the Adams-Bashforth differencing scheme in time. A transport equation for temperature was also solved with constant heat flux boundary conditions. Fair agreement was obtained compared to very limited experimental data for the temperature. In a later paper, Kobayashi et al. (1985a) compared numerical predictions obtained with a $k-\epsilon$ turbulence model to their prior LES results. More extensive experimental results were also presented. They reported good agreement between the LES and experimental results, but the $k-\epsilon$ model performed unfavorably, especially behind the turbulence promoter, or rib. In a third report, Kobayashi et al. (1985b) showed LES results after making improvements to their original SGS model.

Ciofalo and Collins (1992) also studied a similar rib-roughened channel configuration. The rib parameters were slightly different, with $h/H = 0.2$, $P/h = 7.2$ and $\mathrm{Re}_D = 20.000$. A $48 \times 24 \times 24$ grid was used for a domain that included two ribs. The filtered incompressible Navier-Stokes equations were solved with a colocated grid and the Rhie-Chow algorithm to prevent "checkerboard" oscillations. The Crank-Nicolson scheme was used for time stepping. A decoupled energy equation was solved with constant heat flux boundary conditions on the lower wall and adiabatic conditions on the upper wall. The Smagorinsky SGS model with Van Driest damping was employed. Comparisons were made to $k-\epsilon$ model predictions and experimental data. The mean flow rate and turbulence levels were slightly overpredicted, but the LES results compared more favorably to the test data than the $k-\epsilon$ predictions.

The simulation of a turbulent flow over an obstacle was performed by Yang and Ferziger (1993). The rib parameters were $h/H = 0.5$, $P/h = 62$ and $\mathrm{Re}_D = 12800$. This flow had a high blockage ratio and simulated the flow over a single obstruction as opposed to a periodic array of ribs. Yang and Ferziger performed LES and DNS with the incompressible equations, using the Smagorinsky and dynamic SGS models for LES. The central-differenced finite volume scheme was spatially second order accurate. A fractional step method was used to march in time, with the convective terms marched explicitly with a Runge-Kutta scheme, and the viscous terms marched implicitly with a Crank-Nicolson scheme. In order to keep the dynamic model stable,

Yang and Ferziger had to perform local averaging in addition to the averaging in homogeneous directions. A $112 \times 48 \times 40$ grid was used. They concluded that the dynamic model yielded better results compared to the Smagorinsky SGS model.

Numerous studies of rib-roughened channel flows have been conducted with RANS methods using mostly the $k - \epsilon$ turbulence model (Liou et al., 1992 and 1993; Chang and Mills, 1993; Acharya et al., 1993 and 1994; Stephens et al., 1995; Prakash and Zerkle, 1995; Liou and Chen, 1995). The computations typically dealt with more complex geometries (e.g., skewed ribs, non-square ribs, rotation) and higher Reynolds numbers than currently possible with LES and DNS.

Rib-roughened channel flows have also been studied extensively with experimental techniques (e.g. Burgraff, 1970; Han et al., 1978; Han, 1988). A large majority of the studies measured only simple parameters of engineering interest, such as friction factors and Nusselt numbers. The effect of rib parameters such as the blockage ratio, h/H, pitch-to-height ratio, P/h, rib geometry, skewness, and Reynolds number were thoroughly investigated.

There are relatively few experimental studies with detailed velocity and/or temperature measurements. Drain and Martin (1985) and Bates et al. (1983) both made detailed measurements of the mean and fluctuating velocities using laser-Doppler velocimetry (LDV) of fully developed water flow in a rectangular duct with one surface roughened with a periodic rib structure with $h/H = 0.2$ and $P/h = 7.2$. The configurations were similar to the one used in this research, as described in Section 8.2. The Reynolds numbers were $\mathrm{Re}_D = 64,000$ for Drain and Martin and $\mathrm{Re}_D = 50,000$ for Bates et al. Lockett and Collins (1990) used holographic interferometry to determine two-dimensional fluid isotherms as well as local heat transfer data for a similar configuration ($h/H = 0.11$, $P/h = 7.2$, $\mathrm{Re}_D = 10,000 - 30,000$). For their study, the lower wall with the ribs was heated with electrical pad resistance heaters.

A noteworthy RANS study of the turbulent flow and heat transfer for ribs on one wall was performed by Liou et al. (1993). They studied a range of Reynolds numbers, blockage ratios, and pitch-to-height ratios. Comparisons were made to the data of Drain and Martin and Lockett and Collins. Liou et al. used a $k - \epsilon$ algebraic stress (abbreviated $k - \epsilon - A$)

turbulence model, which solves transport equations for k, ϵ, the Reynolds shear stress, and the Reynolds heat flux. They obtained reasonable agreement with experimental results.

8.4 Simulation Details

The turbulent rib-roughened channel simulations were performed in much the same manner as the smooth channel simulations presented in previous chapters, with the exceptions and modifications noted below.

8.4.1 SGS Modeling

For the simulations presented in this chapter, only the Smagorinsky model with Van Driest damping was used. The Smagorinsky coefficient was $C_s = 0.08$, which corresponds to $C_d = 0.0064$. For the smooth walled channel simulations, the value of y^+ used in the damping formulation was based on the minimum distance to the upper or lower wall and the average friction velocity for both the upper and lower walls, where

$$u_{\tau,avg} = \frac{1}{2L_x}\left[\int_0^{L_x} u_\tau(x,1)\,dx\Big|_{y=1} + \int_0^{L_x} u_\tau(x,-1)\,dx\Big|_{y=-1}\right] \tag{8.1}$$

For the rib-roughened channel, the friction velocity in the definition of y^+ was also based on the average of the upper and lower walls, with the rib surfaces included as

$$u_{\tau,avg} = \frac{1}{2L_x + 2h}\left[\int_0^{L_x} u_\tau(x,1)\,dx\Big|_{\text{upper wall}} + \int_0^{L_x+2h} u_\tau(s)\,ds\Big|_{\text{lower wall}}\right] \tag{8.2}$$

where s is the distance along the lower wall including the rib surfaces. For reasons discussed later in Section 8.5, the distance to the wall, δ_y, in the definition of y^+ was computed in one of two ways: 1) δ_y was the distance to the nearest wall, including the rib surfaces, and 2) δ_y was the minimum distance to the upper and lower walls (ignoring the presence of the rib).

8.4.2 Boundary and Initial Conditions

For the solid walls, including the upper and lower walls and rib surfaces, the no-slip velocity and zero normal pressure gradient boundary conditions were enforced. The wall temperature

was determined from the specified heat flux, which was zero for the upper wall, q_w for the lower wall, and $q_w/3$ for the rib surfaces. All solution variables were assumed to be periodic in the z direction, the only homogeneous direction for this flow. In the streamwise direction, the same boundary conditions utilized for the high heat flux channels described in Chapter 7 were utilized. Namely, the x-momentum, v and w velocities, and periodic component of the pressure, p_p, were assumed to be periodic. The pressure gradient parameter, β, was adjusted at each time step to maintain the desired mass flow rate. The temperature was assumed to be stepwise periodic, with ΔT_x given by

$$\Delta T_x = \frac{q_w L_x}{2(\dot{m}/L_y L_z)} \tag{8.3}$$

where $L_y = 2$ and $L_z = \pi$.

The initial conditions for the velocities were obtained by superimposing random fluctuations with peak values of $\pm u_\tau$, where u_τ was from the smooth channel simulations, onto an initial mean flow. The initial mean flow for the velocity was zero for v and w, and the streamwise velocity was set to a parabolic profile at each streamwise location. The initial pressure and temperature fields were uniform. The smooth channel simulations required as many as 10,000 time steps for the flow to develop into a statistically stationary turbulent state. The ribbed channel, however, reached a statistically stationary turbulent state in about 1,000 time steps. The presence of the rib helped to set up a turbulent flow in much less time, even though the initial conditions were much less realistic, compared to the smooth channel simulations. Once the turbulent flow was deemed to be statistically stationary, the simulation was run another 4-6,000 time steps to compute the ensemble averaged turbulence statistics. The number of time steps required to obtain good statistics was generally less than that required for the smooth channel simulations as well.

The simulations were primarily run with the dual time-stepping LU-SGS scheme with the solution domain divided into 14 blocks. The simulations were run with 14 processors on the IBM SP-2 and required about 6–8 hours of wall clock time per 1000 time steps, depending on the number of subiterations required for each step in physical time.

8.4.3 Turbulence Statistics

The rib-roughened channel had only one homogeneous direction, the spanwise, or z–direction. Consequently, ensemble averaging was performed in the z direction and in time, leading to turbulence statistics that were two-dimensional in the $x - y$ plane.

The bulk properties were found by integrating from the lower wall (or rib surface) to the upper wall as

$$\rho_b = \frac{1}{y_2 - y_1} \int_{y_1}^{y_2} \rho \, dy, \tag{8.4}$$

$$u_b = \frac{1}{\rho_b (y_2 - y_1)} \int_{y_1}^{y_2} \rho u \, dy, \tag{8.5}$$

$$T_b = \frac{1}{\rho_b u_b (y_2 - y_1)} \int_{y_1}^{y_2} \rho u T \, dy, \tag{8.6}$$

where $y_2 = 1$, $y_1 = -1$ in regions ahead of or behind the rib, and $y_1 = -1 + h$ in the region on top of the rib.

8.4.4 Grid and Run Parameters

The dimensions of the computational domain were $7.2h \times 5h \times 7.85h$, or $2.88\delta \times 2\delta \times \pi\delta$, in the x, y, z directions, respectively. The grid was relatively coarse with $40 \times 32 \times 24$ control volumes, with 8 cells on each surface of the rib, as shown in Fig. 8.2. The grid was stretched towards the upper and lower walls, and towards the rib surfaces. The nondimensional time step was 0.0311, the same as for the smooth channel simulations.

Based on the results for coarse and fine grid simulations for the low heating smooth channel presented in Chapter 6, the grid used for the rib-roughened channel was inadequate for detailed comparisons to experimental data. However, coarse grids are able to capture the main features and structure of turbulent flows. As will be discussed in Section 8.5, several shortcomings in the present formulation for this geometry were identified. Consequently, no fine grid simulations were completed for the rib-roughened channel.

8.5 Results

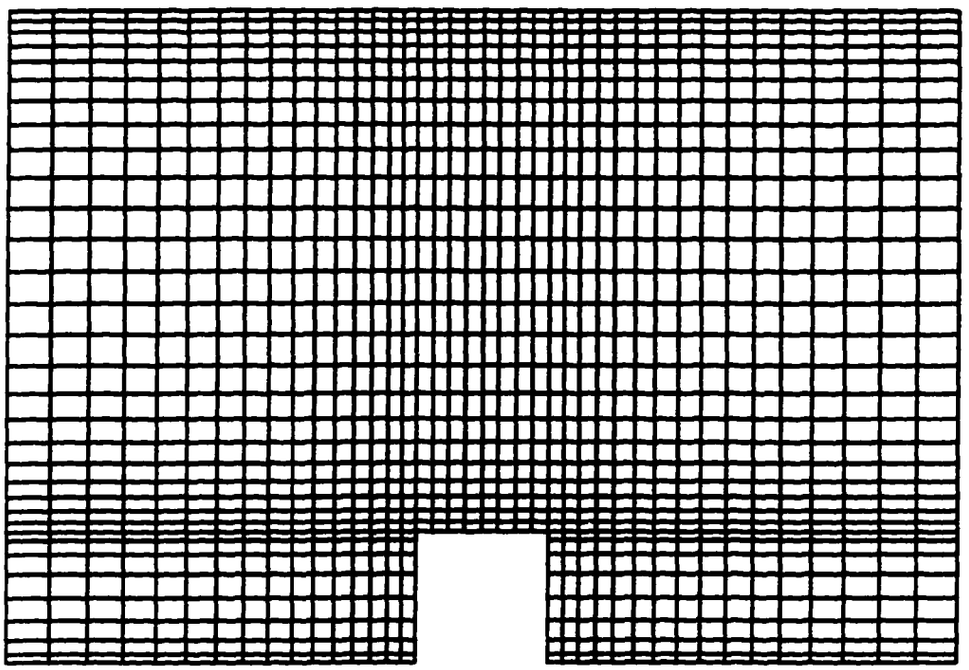

Figure 8.2 Computational grid for rib-roughened channel flow

8.5.1 Case Descriptions

Many trials of simulating the rib-roughened channel were made, but only four were selected for presentation in the thesis. The initial trials were unsuccessful: the simulations would proceed for several hundred time steps before suddenly failing due to negative temperatures or pressures. The initial trials used the LU-SGS scheme with relaxation factors $\omega = 1.0$ and $r_A = r_B = r_C = 1.0$ and no artificial dissipation. The Van Driest damping was applied with y^+ based on the distance to the nearest wall, including the rib surfaces.

The four best trials, named Cases A,B, C and D, were selected for discussion in this chapter, and are summarized below.

- **Case A.** No Van Driest damping was used in the SGS model. The LU-SGS scheme was used with relaxation factors $\omega = 1.0$ and $r_A = r_B = r_C = 1.0$. No artificial dissipation was used. The simulation ran without any failures, and $N_{stat} = 5500$ time steps were used to compute the turbulence statistics. The results from this simulation are not valid near the wall since the SGS turbulent viscosity was not damped. However, the case

provided information about the cause of the initial failures.

- **Case B.** Van Driest damping was applied, but y^+ in the Van Driest formula was based on the distance to the upper or lower channel walls only (i.e. the rib surfaces were ignored). The LU-SGS scheme was used with relaxation factors $\omega = 1.0$ and $r_A = r_B = r_C = 1.0$ and no artificial dissipation. This case also ran without failures, and $N_{stat} = 6000$ time steps were used to compute the turbulence statistics.

- **Case C.** Van Driest damping was applied with y^+ based on the distance to the nearest wall, including the rib surfaces. The simulation was stabilized by using large relaxation factors of $\omega = 25.5$ and $r_A = r_B = r_C = 2.5$ in the LU-SGS scheme. No artificial dissipation was used. This case ran for about 4,000 time steps before a negative temperature related failure was encountered. Moreover, the residuals were only decreasing by a factor of two in the subiteration process compared to an order of magnitude or more for the other cases.

- **Case D.** Van Driest damping was applied with y^+ based on the distance to the nearest wall, including the rib surfaces. The simulation was stabilized by using adaptive second order artificial dissipation with switching based on pressure and temperature gradients. The dissipation was set to zero when the switch values were below a specified threshold. The second order dissipation coefficient was $\kappa^{(2)} = 0.5$. The LU-SGS relaxation factors were $\omega = 1 - 3$ and $r_A = r_B = r_C = 1 - 2$. This case was run for about 5,900 time steps. Negative temperature failures were occasionally encountered. The LU-SGS relaxation factors were temporarily set to larger values for several hundred time steps, then returned to lower values to continue the simulation.

The switching procedure in the second order artificial dissipation for Case D was used so that the artificial dissipation was only added in regions near the rib where large gradients and the decoupling were occurring. Away from these regions, the dissipation had no direct effect. An earlier simulation was attempted with very low levels of fourth order dissipation only. Once the coefficient on the dissipation was increased to a level large enough to have an effect on the

stability problems, the turbulent fluctuations were significantly reduced, even more than for Case D. Thus, the use of fourth order dissipation was deemed unacceptable.

Table 8.1 lists the average simulation parameters for the four cases. Here, β is the ensemble averaged value of the pressure gradient parameter, k is the globally averaged turbulent kinetic energy, and $u_{\tau,avg}$ is the ensemble averaged friction velocity given by Eq. 8.2.

Table 8.1 Simulation parameters for rib-roughened channel

Case	β	u_τ	k/V_r^2	k^+
A	-0.0243	0.0532	0.0438	15.5
B	-0.0203	0.0542	0.0439	14.9
C	-0.0202	0.0533	0.0539	19.0
D	-0.0240	0.0562	0.0438	13.9

Significant odd-even decoupling of the primitive variables was evident in the solutions, especially near the rib. The failures mentioned above were probably due to these oscillations, which when superimposed on the turbulent fluctuations led to an occasional negative temperature or pressure. Case A resulted in larger effective viscosities near the rib since the turbulent viscosity was not being damped. Similarly, Case B had larger effective viscosities near the top of the rib because the damping was based on the distance to the upper and lower walls only.

Case C reduced the stability problems with large relaxation factors in the LU-SGS scheme. The simulation still produced negative temperatures, but the frequency was increased to every 1000 time steps instead of every 1–100 time steps.

Case D, and other trials with various forms of artificial dissipation, applied additional viscosity to alleviate the decoupling problem. However, as will be shown in the figures that follow, any added dissipation of magnitude sufficient to have an effect on the stability problem resulted in reduced turbulent fluctuations.

The "stability" problems mentioned here refer to the occasional failures due to negative temperatures or pressures, which were most likely due to the oscillations superimposed on the turbulent fluctuations. This is not the same as von Neumann stability theory described in textbooks, although the growth properties of errors predicted by von Neumann stability theory may be relevant to the problems observed in the present simulations.

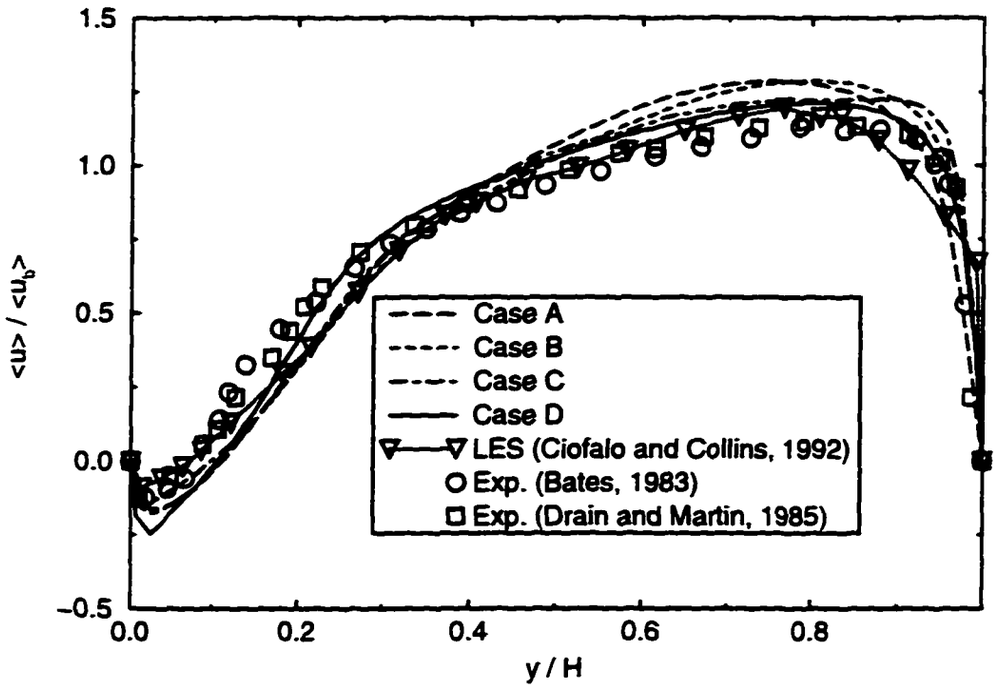

Figure 8.3 Mean streamwise velocity normalized by bulk velocity for Section A

8.5.2 Mean and Fluctuating Velocity Profiles

The mean streamwise velocity profiles, normalized by the average bulk velocity on top of the rib, are depicted in Figs. 8.3 and 8.4 at planes A and B, respectively. Plane A was located mid-way between the ribs, and plane B was located on the middle of the rib, as shown in Fig. 8.1. The profiles from the experiments of Drain and Martin (1985) and Bates et al. (1983), as well as the LES results of Ciofalo and Collins (1992) are also shown. Cases C and D gave the best agreement with the experimental results, with the exception that Case D overpredicted the velocity magnitude in the recirculation zone (Section A), and Case C overpredicted the mean velocity near the upper wall at Sections A and B. Cases A and B overpredicted the mean velocity in the mid-passage.

The corresponding root-mean-square (*rms*) of the streamwise velocity fluctuations are shown in Figs. 8.5 and 8.6 for Sections A and B, respectively. Although all four cases show the same general trends, the peak magnitude of the fluctuations was severely reduced for Cases A

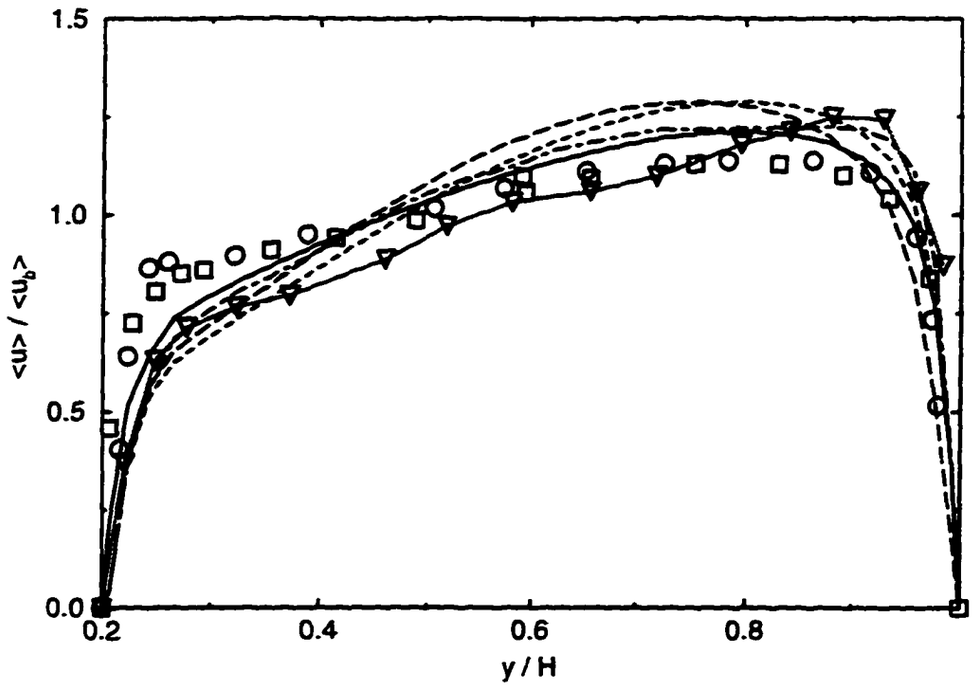

Figure 8.4 Mean streamwise velocity normalized by bulk velocity for Section B (see Fig.8.3 for label)

and B due to underdamping the SGS turbulent viscosity.

Case D, with minimal addition of artificial dissipation, also resulted in reduction of the peak fluctuation levels, although the effect was not as severe compared to cases A and B. The agreement of Case C with the experimental results was quite good, despite the seemingly insufficient drop in the residuals for each subiteration and the relatively coarse grid.

8.5.3 Heat Transfer Parameters

Heat transfer parameters were only computed for Cases C and D. Only results from Case D are presented here because the mean temperature field resulting from Case C was very poor in quality. For instance, the Nusselt numbers along some surfaces of the rib were actually negative. Recall that Case C was run with large relaxation factors, and the residuals did not decrease as much as desired in the subiteration process. Although the best agreement with the experimental velocity data was obtained with Case C, the temperature field was not fully established. Many more time steps and/or much better convergence in the subiteration process

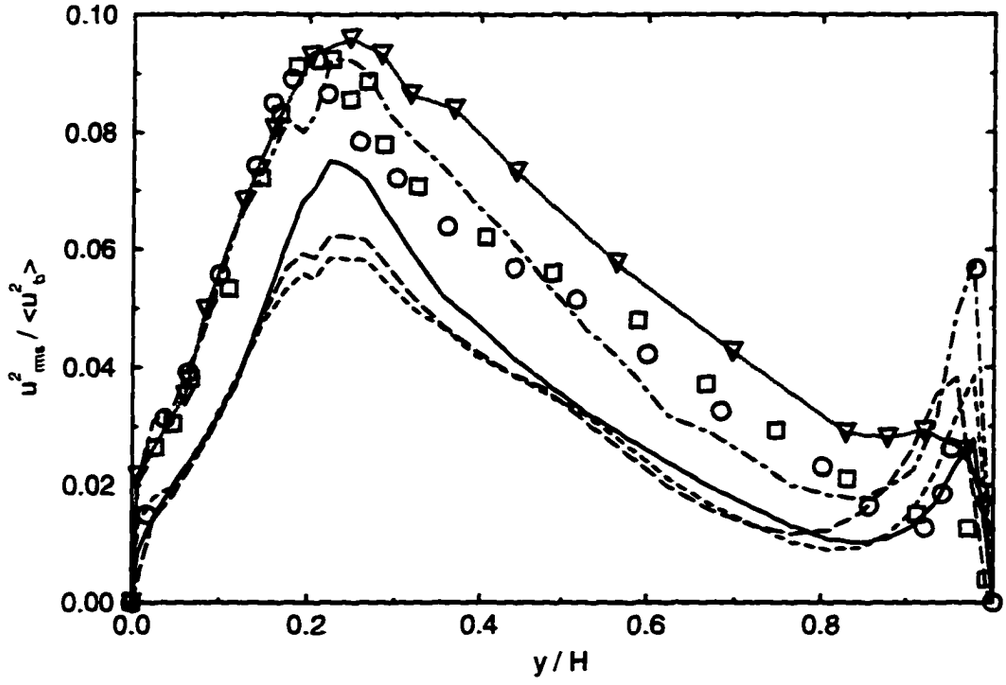

Figure 8.5 RMS streamwise velocity fluctuations normalized by bulk velocity for Section A (see Fig.8.3 for label)

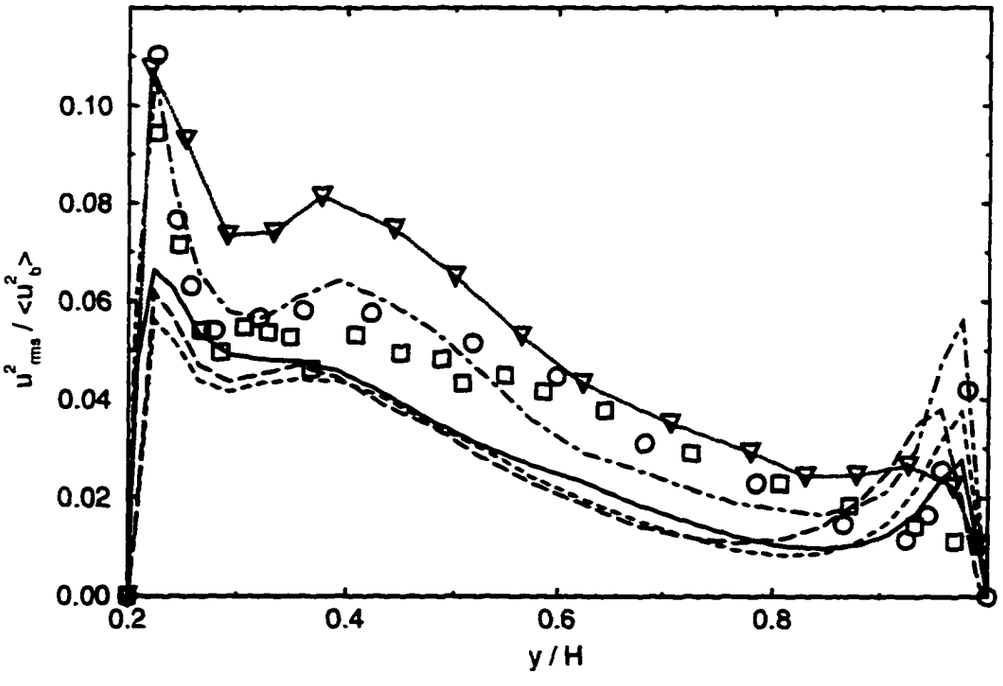

Figure 8.6 RMS streamwise velocity fluctuations normalized by bulk velocity for Section B (see Fig.8.3 for label)

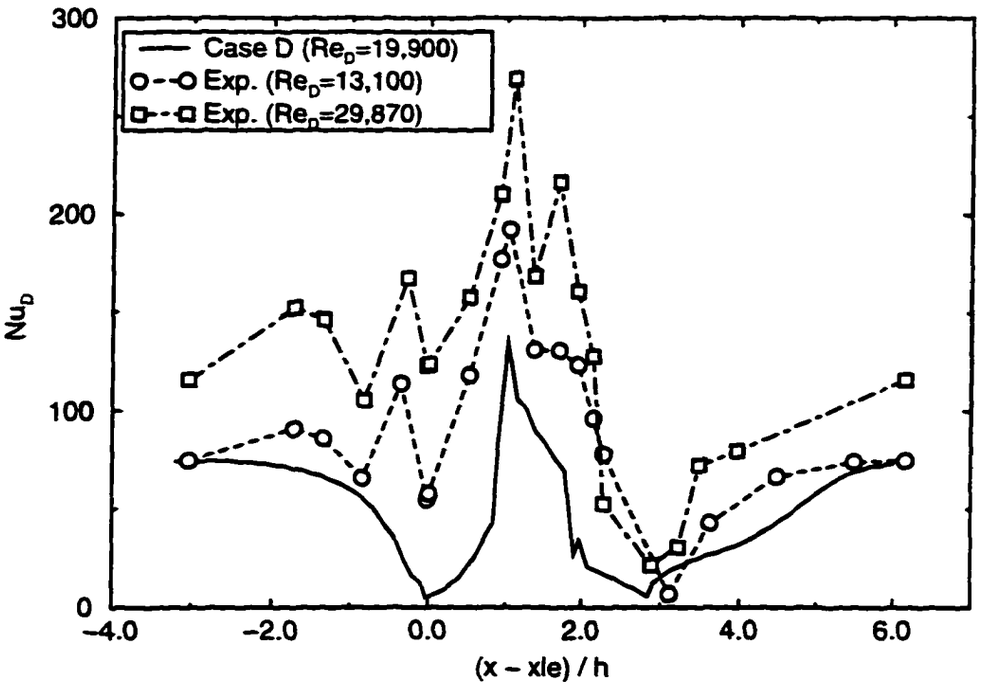

Figure 8.7 Local Nusselt number compared to experimental data of Lockett and Collins (1990)

would be needed to yield acceptable temperature results.

Case D yielded reasonable agreement with the experimental data for the velocity field, with the exception that the fluctuation levels were significantly reduced. The local Nusselt number distribution for Case D is shown in Fig. 8.7 compared to the experimental data of Lockett and Collins (1990) at two different Reynolds numbers. In Fig. 8.7 x is the distance along the lower wall of the channel, including the rib surfaces, and xle is the x location of the lower-front corner of the rib. The same distribution was normalized by the average Nusselt number, $Nu_{D,avg} = 49.6$, as shown in Fig. 8.8. The average Nusselt number was computed as

$$Nu_{D,avg} = \frac{1}{S}\int_0^S Nu_D(s)\mathrm{d}s \tag{8.7}$$

where s is the distance along the lower wall, including the rib surfaces. The normalized distributions in Fig. 8.8 allow the effects of flow features on the Nusselt number distribution to be compared for different Reynolds numbers.

The general trends in the Nusselt number distribution were obtained, but some of the local

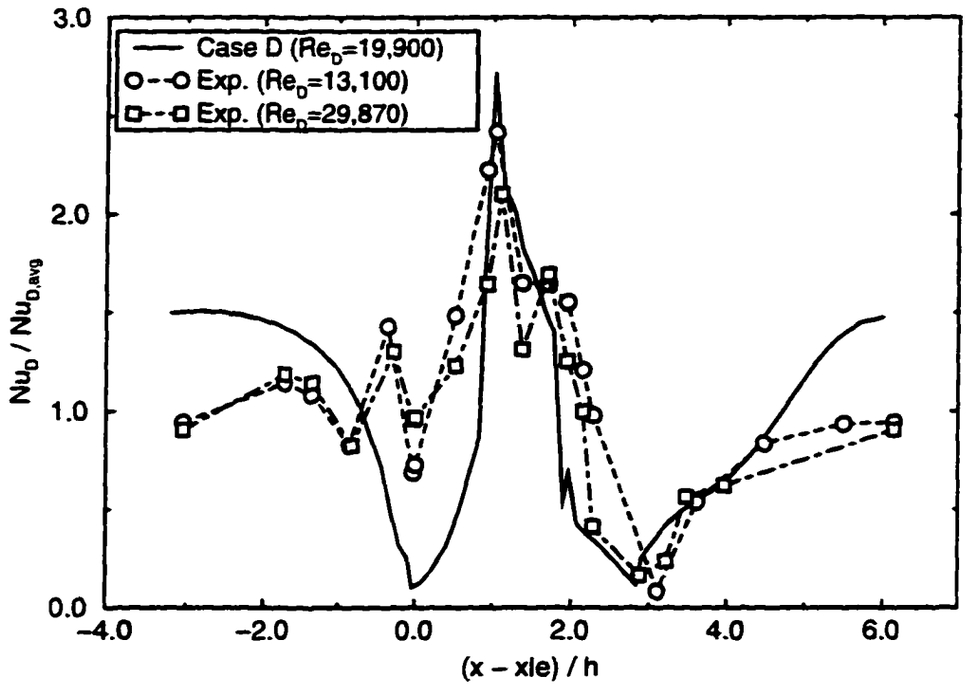

Figure 8.8 Normalized Nusselt number compared to experimental data of Lockett and Collins (1990)

features were not predicted. For instance, the experimental results indicate much larger values of Nusselt number on the front surface of the rib. The higher Reynolds number experimental results ($Re_D = 29,870$) indicate an increase in the Nusselt on top of the rib near the trailing edge, which is due to a recirculation zone that develops on top of the rib at higher Reynolds numbers. Also, the absolute level of the Nusselt number for the present results is significantly less than indicated by the experimental results. The reasons for these discrepancies are most likely due to the coarse grid used for the present simulations and the deficiencies in the SGS modeling that have been discussed previously in this chapter, including the effects of the added artificial dissipation on the turbulence fluctuations.

8.5.4 Contours of Ensemble Average Turbulence Statistics

Ensemble averaged turbulence statistics for the four cases of interest are presented in this section. Figures. 8.9, 8.10, 8.11, and 8.12 show mean velocity vectors for Cases A, B, C and D, respectively. A large recirculation zone behind the rib and a smaller recirculation zone in front

of the rib are clearly evident, although the shape and extent are slightly different for the four cases. For this pitch-to-height ratio, the recirculation region encompasses a large fraction of the region between the ribs. Drain and Martin (1985) reported a reattachment length of 4.3h, which compares well to the value of about 4.2h for Case C. Case C yielded the most favorable comparison to the experimental mean and *rms* velocity profiles shown in the previous section.

The ensemble averaged turbulent kinetic energy contours are shown in Figs. 8.13 through 8.16. The contours represent the turbulent kinetic energy computed at the cell centers of the control volumes, so k is non-zero near the wall and rib boundaries. Case C resulted in the largest magnitudes of k. The decoupling in the solutions is clearly evident, especially near the rib. The distributions from Cases A and B are quite similar, with slightly lower magnitudes for Case B. Case D produced very little decoupling or oscillations, but the magnitudes of k are significantly lower compared to Case C.

The corresponding contours of ensemble averaged uv velocity correlations, $< u'v' >$, or Reynolds stress, are shown in Figs. 8.17 through 8.20. The observations for the turbulent kinetic energy mostly apply to the $< u'v' >$ contours as well.

Contours of the ensemble averaged modeled SGS turbulent viscosity, μ_t, are shown in Figs. 8.21, 8.22 and 8.23 for Cases B, C and D, respectively. The capability to post-process μ_t was added after Case A was completed. The three cases resulted in very different distributions. Case B has very large values of μ_t near the surfaces on the upper portion of the rib. The Van Driest damping was based on the distance to the upper and lower walls only, so the turbulent viscosity near the top of the rib was not damped. The large amount of dissipation near the rib surface, where much of the decoupling occurred, allowed the computation to proceed without failures. In contrast, Case C had near-zero values of μ_t near the top of the rib, which explains why large relaxation factors were required to keep the LU-SGS scheme stable. Finally, due to the added artificial dissipation and subsequent reduction in turbulent fluctuations, the overall magnitude of μ_t was reduced for Case D. Also, very low magnitudes of μ_t were obtained near the top of the rib.

The distinct regions of low μ_t across the domain at a height equal to the rib height was due

to the grid stretching in those regions. The value of μ_t is directly related to the filter width, which is a function of the cell volume. As the grid was stretched to resolve the flow near the top of the rib, a layer of smaller control volumes resulted at all streamwise locations. This was undesirable, because it led to a variation in the size of the turbulence scales being resolved in regions where the characteristic turbulence scales were not varying greatly. The present code could be modified to handle non-Cartesian grids, so that the grid could be stretched in such a way to minimize the clustering of points away from the walls where it is not necessary.

8.6 Concluding Remarks

8.6.1 Summary

The simulation of turbulent flow and heat transfer of air in a plane channel with transverse square ribs on one wall was attempted to evaluate the finite volume LES formulation for a complex geometry and flow. Significant odd-even decoupling and oscillations were observed in the primitive variables, especially near the rib. These led to occasional negative temperatures and pressures, causing the code to fail. Several methods were tried to alleviate the problems, including modifications to the Van Driest damping in the SGS model, adding artificial dissipation, and using large relaxation factors in the LU-SGS scheme.

The modifications were effective in alleviating the failures, but led to significantly reduced turbulent fluctuations and generally less accurate results.

8.6.2 Discussion

The rib-roughened channel simulations have highlighted an apparent dilemma for using compressible central-differenced finite volume formulations for LES of complex flows. Decoupling arises due to large gradients and stagnation regions in the flow, which can potentially lead to failures associated with negative temperatures or pressures. However, any amount of artificial smoothing or modification to the SGS model can lead to significantly reduced turbulence fluctuations and generally less accurate results.

Although the decoupling was apparent in the cell-centered solution, it is not clear that the presence of oscillations is a serious drawback. The flux quantities computed at the cell faces using averaged flow quantities from the neighboring cell-centers do not exhibit oscillations, and are most likely accurate. The oscillations are nearly removed from the solution when volume weighted averaging is used to compute the solution variables at the cell vertices. For example, the turbulent kinetic energy was computed at the cell vertices for Case C, as shown in Fig. 8.24. The distribution is much smoother, and shows little oscillations.

Thus, as long as the simulation can be performed without failures due to negative temperatures or pressures, acceptable results may be possible despite the underlying oscillations in the cell-centered solution. The issue that needs to be studied is whether the averaged solution at the vertices is accurate, and whether the decoupling leads to erroneous results. For instance, it may be possible for the numerically induced oscillations due to decoupling to produce false turbulent fluctuations.

No similar problems have been reported by those who have performed turbulent simulations of similar configurations, as reviewed in Section 8.3. However, all of the simulations reviewed used incompressible formulations, whereas the present simulations used a compressible formulation. Ciofalo and Collins (1992[20]) did mention employing the Rhie-Chow algorithm to prevent "checkerboard" oscillations with their incompressible finite volume formulation with colocated grids.

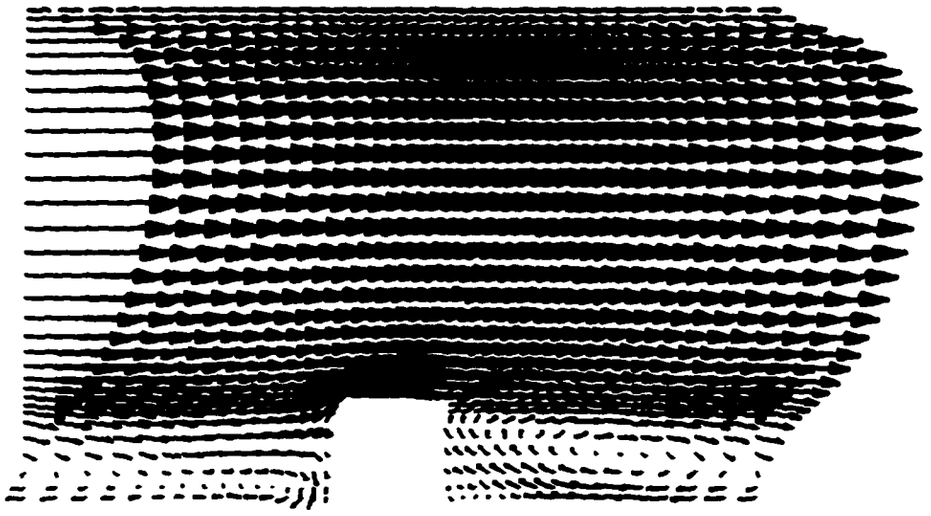

Figure 8.9 Mean velocity vectors for Case A

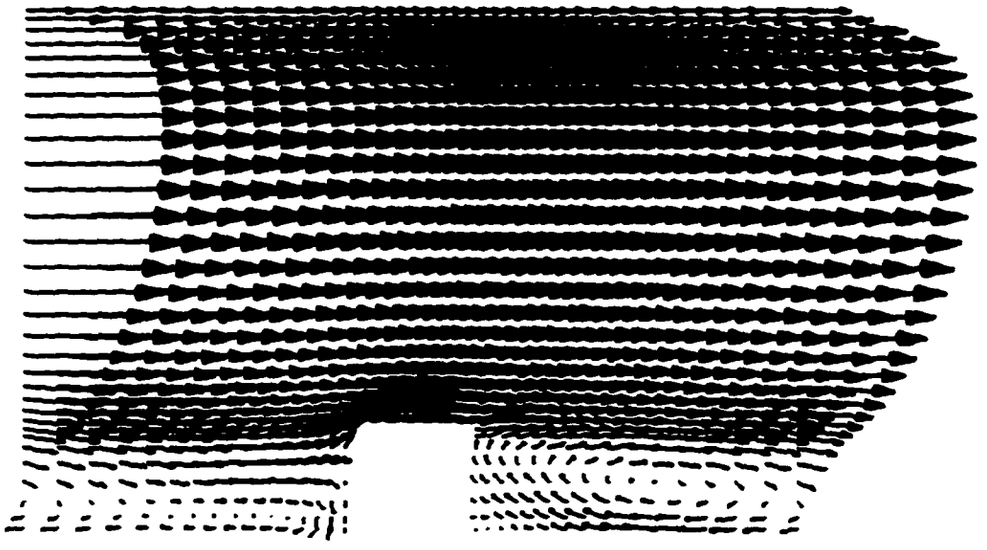

Figure 8.10 Mean velocity vectors for Case B

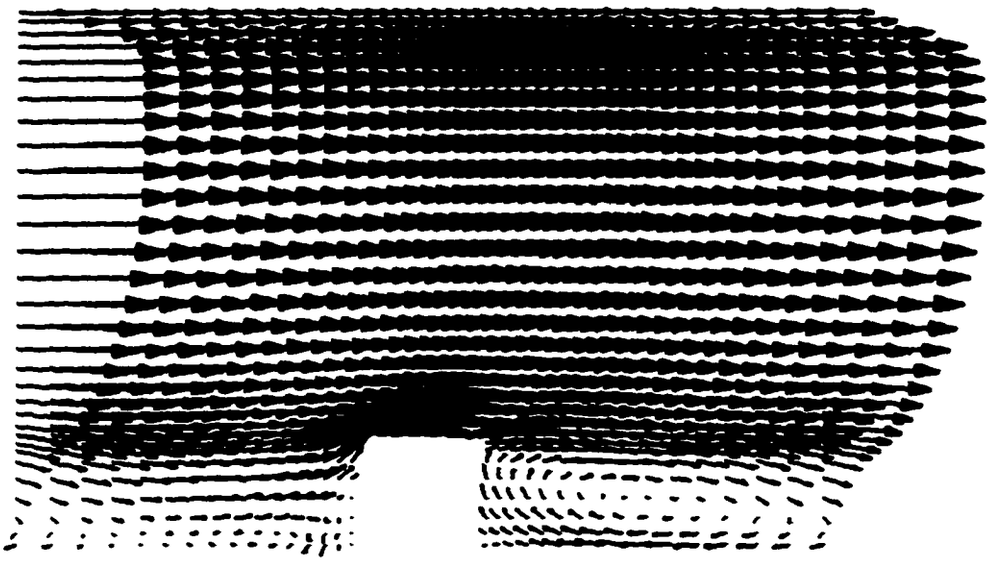

Figure 8.11 Mean velocity vectors for Case C

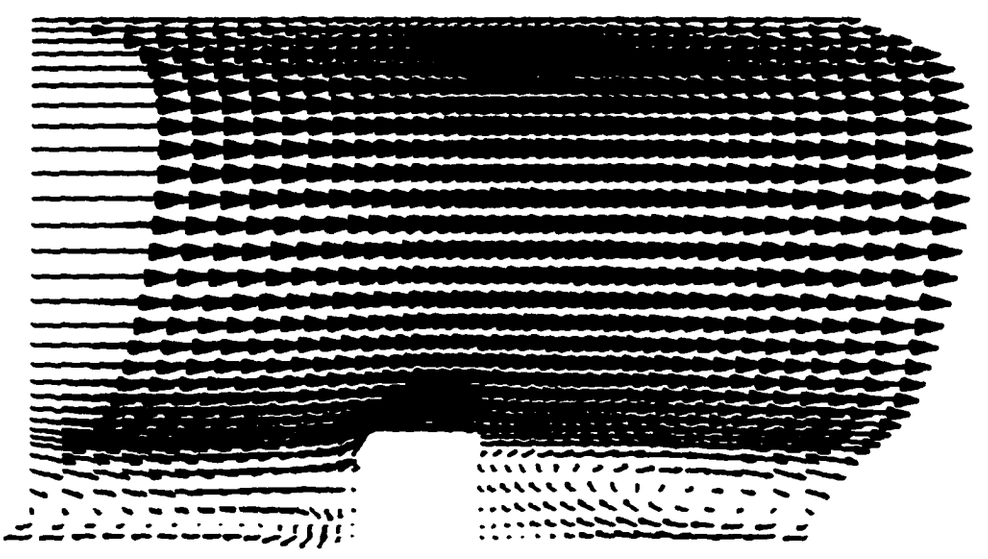

Figure 8.12 Mean velocity vectors for Case D

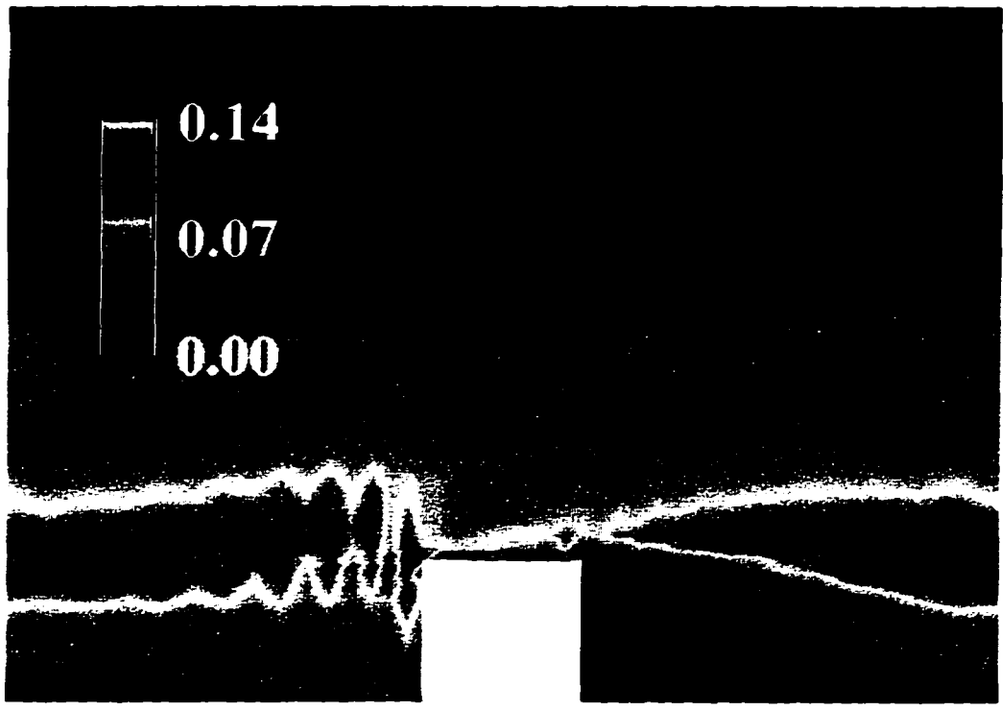

Figure 8.13 Average turbulent kinetic energy for Case A

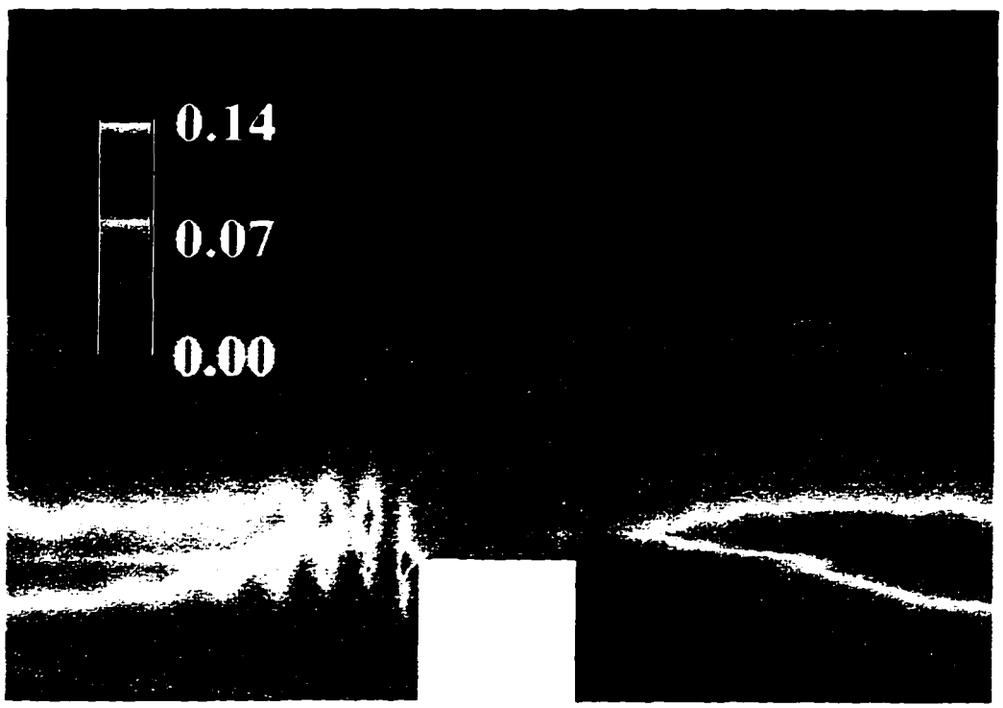

Figure 8.14 Average turbulent kinetic energy for Case B

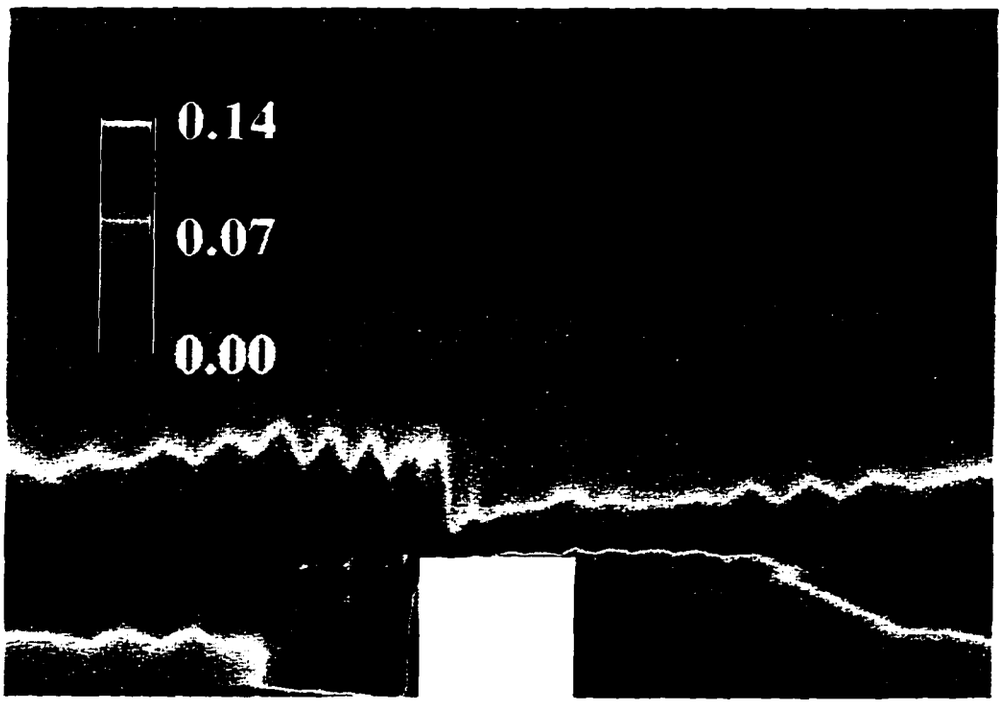

Figure 8.15 Average turbulent kinetic energy for Case C

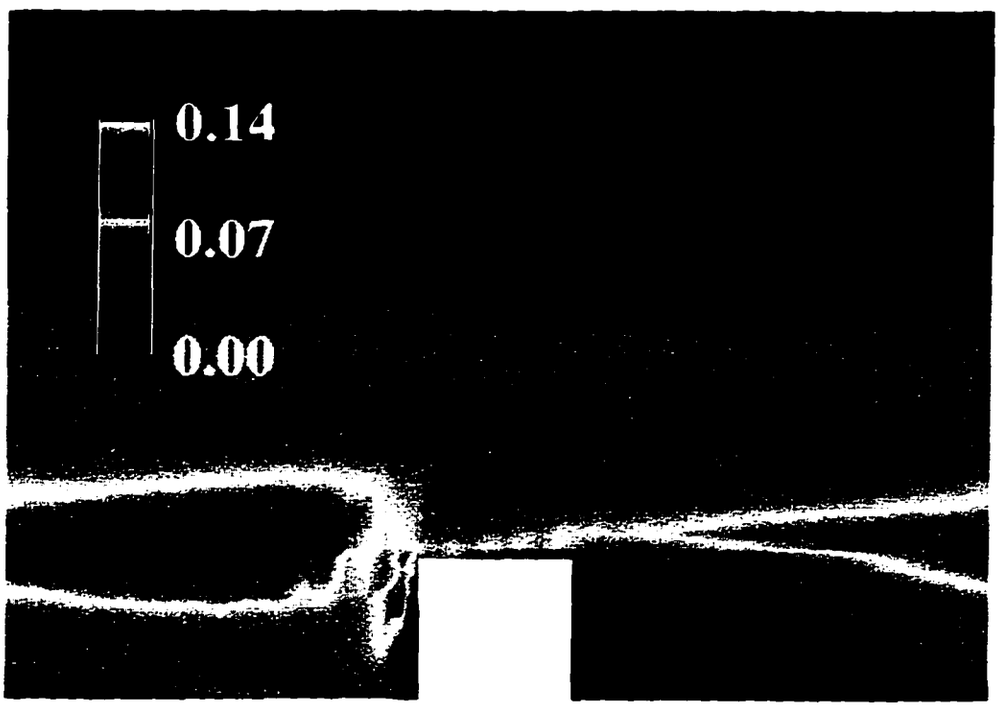

Figure 8.16 Average turbulent kinetic energy for Case D

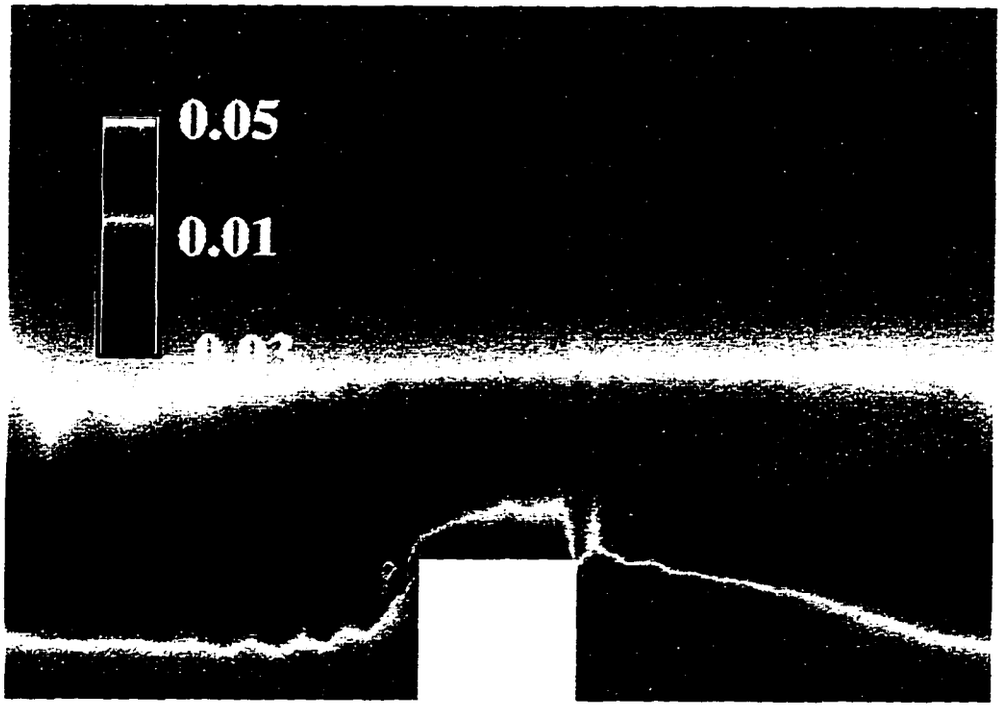

Figure 8.17 Average uv velocity correlation for Case A

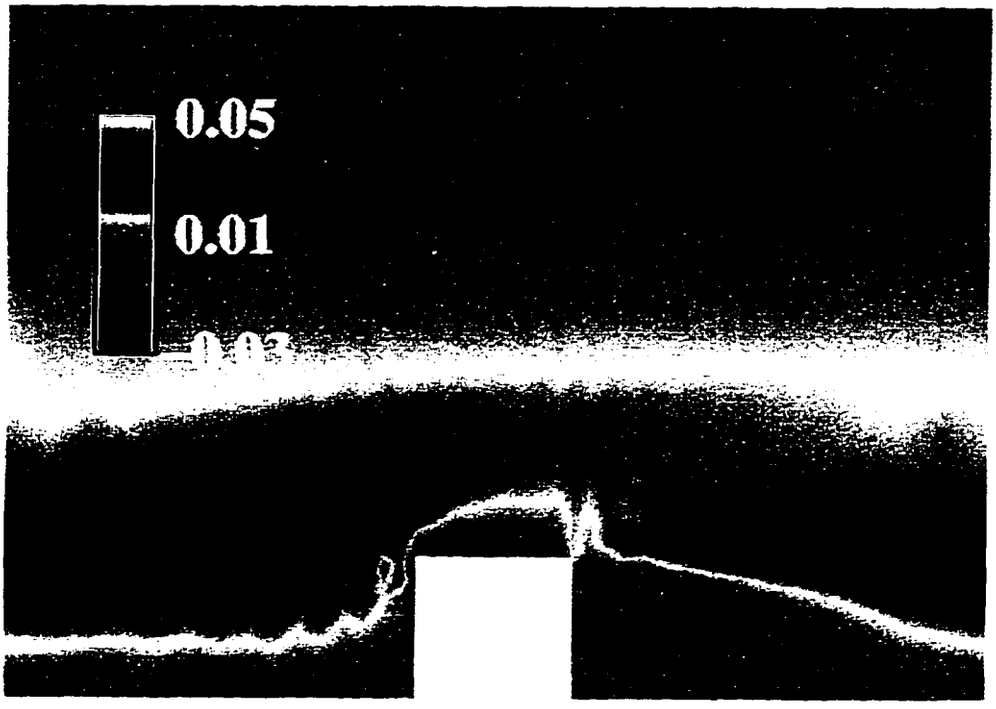

Figure 8.18 Average uv velocity correlation for Case B

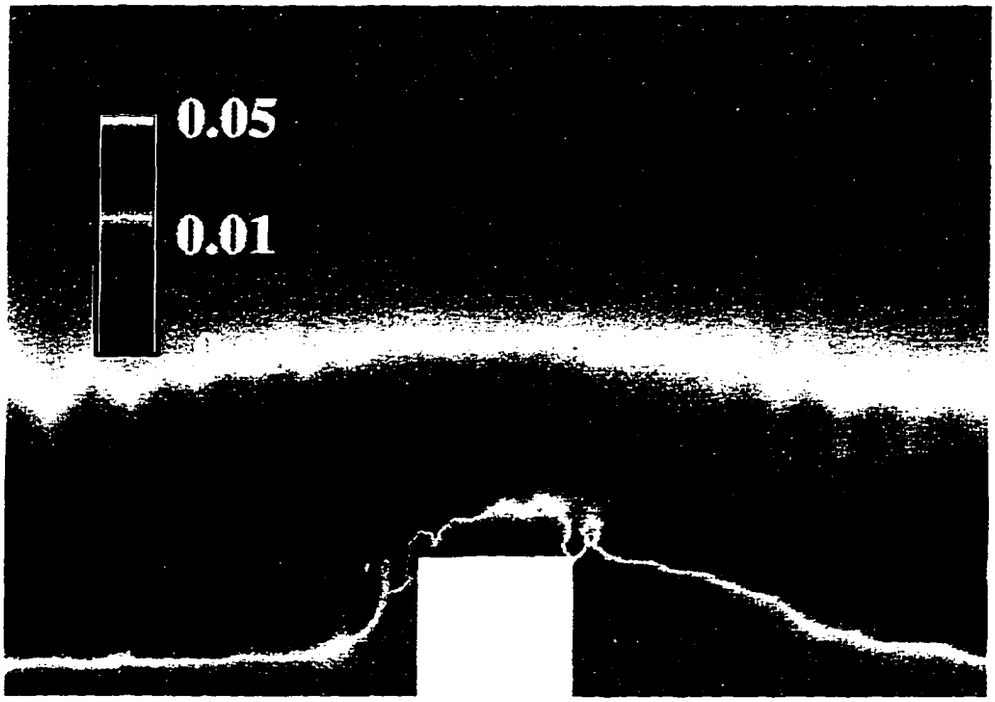

Figure 8.19 Average uv velocity correlation for Case C

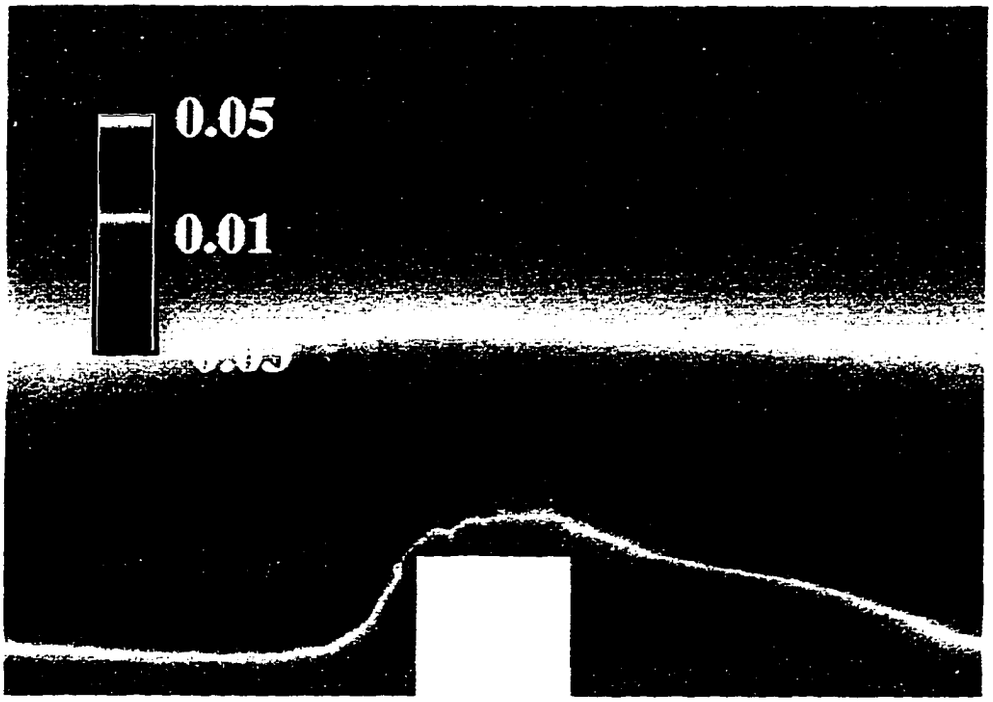

Figure 8.20 Average uv velocity correlation for Case D

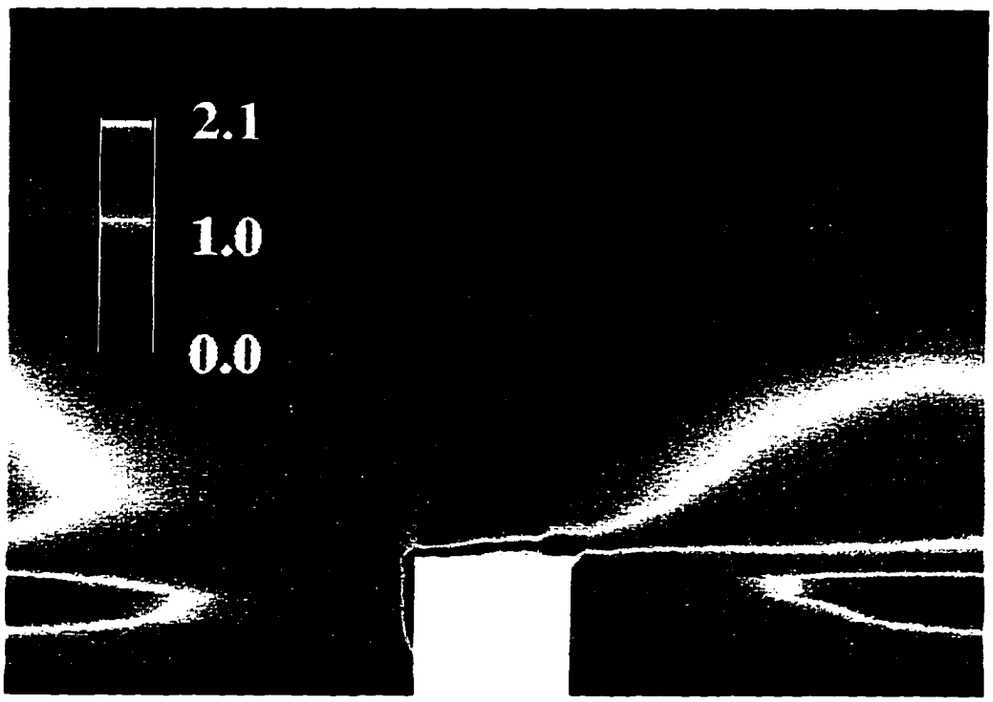

Figure 8.21 Average modeled SGS turbulent viscosity for Case B

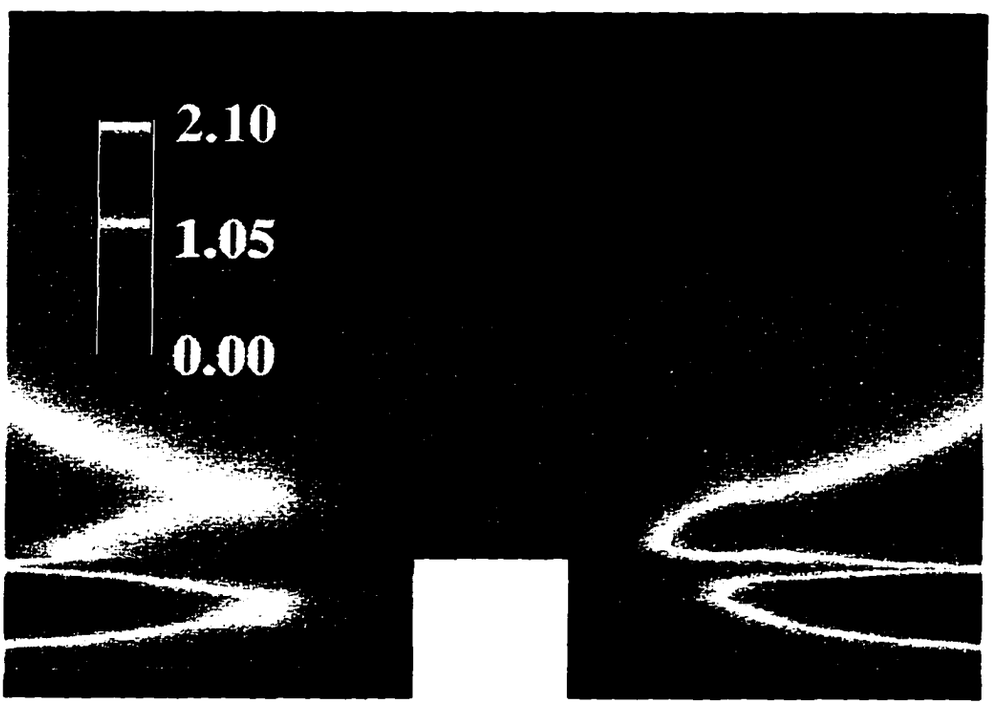

Figure 8.22 Average modeled SGS turbulent viscosity for Case C

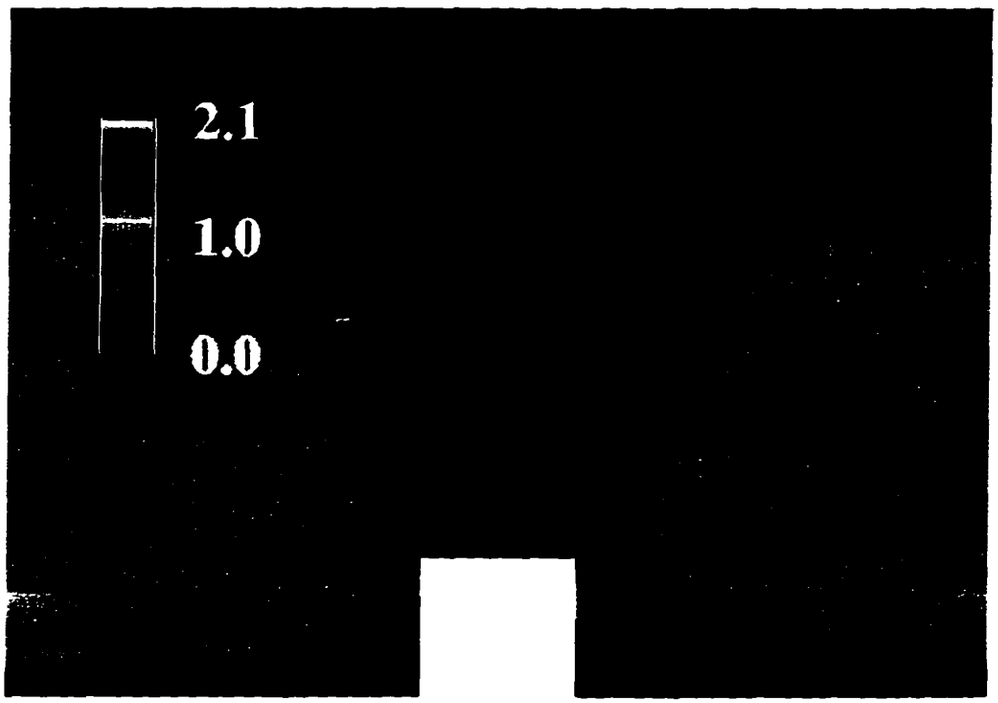

Figure 8.23 Average modeled SGS turbulent viscosity for Case D

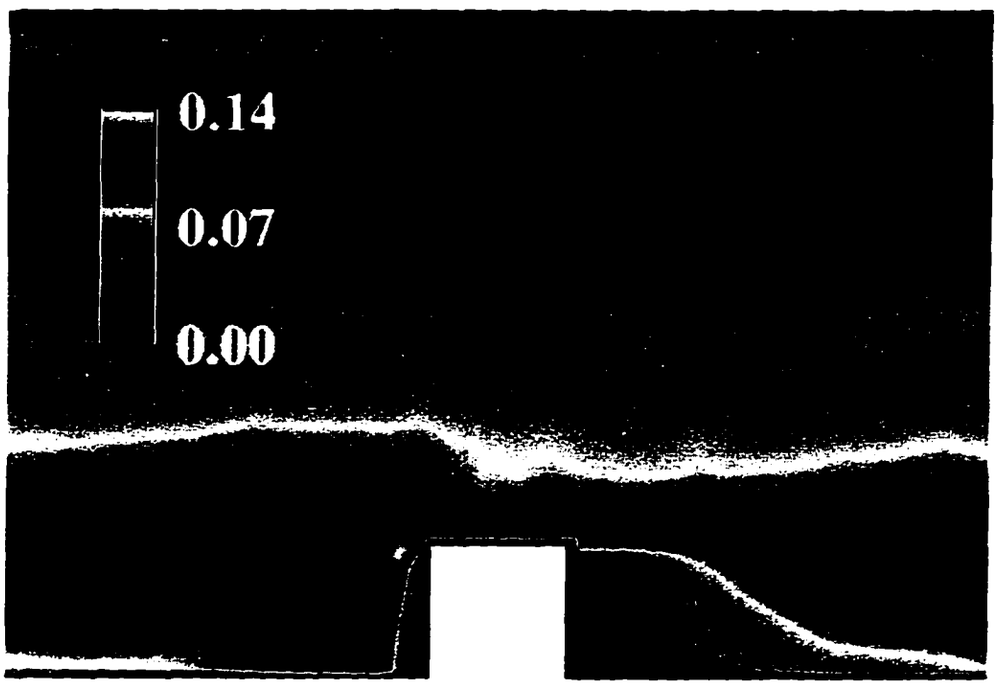

Figure 8.24 Average turbulent kinetic energy at cell vertices for Case C

CHAPTER 9 CONCLUSIONS AND RECOMMENDATIONS

A summary of the thesis is given in Section 9.1, followed by a discussion of the contributions of this work in Section 9.2. Conclusions drawn from the thesis are presented in Section 9.3. and the chapter is concluded with a discussion of recommended future work in Section 9.4.

9.1 Summary

A compressible finite volume formulation was developed for the large eddy simulation (LES) of turbulent flows with significant heat transfer. The goal was to develop an efficient, low memory scheme that would allow the simulation of more complex flows. A time-accurate explicit Runge-Kutta scheme and an implicit LU-SGS scheme were developed in a dual time stepping approach with time derivative preconditioning. The effectiveness of multigrid acceleration and time derivative preconditioning were thoroughly evaluated for time accurate flows with a two-dimensional, laminar variant of the finite volume formulation. The code was written in a multiblock framework so that it could be applied to complex geometries and to provide a means for parallelization.

The second-order accurate finite volume LES formulation was validated with simulations of turbulent incompressible benchmark flows, which included homogeneous, isotropic decaying turbulence and plane channel flow. The results were compared to experimental data and incompressible DNS results.

The LES formulation was subsequently applied to a plane channel flow with constant wall heating rates of magnitudes large enough to cause significant property variations across the channel. The results from a laminar, developing channel flow computation were compared to the results from a laminar, quasi-developed channel flow computation to validate the step-wise

periodic boundary conditions employed in the latter computation. This boundary condition treatment was subsequently used for the turbulent simulations. The effects of high heating versus high cooling on the turbulence quantities were studied and compared to the results for low heating. The results were compared to empirical correlations for the Nusselt number and friction coefficient.

Finally, the LES formulation was evaluated for a complex geometry by attempting to simulate the turbulent flow and heat transfer for a plane channel with transverse square ribs on one wall. This complex geometry results in flow separation, reattachment, recirculation zones, and stagnation points.

9.2 Contributions

Several contributions were made to the fields of CFD, in general, LES, in particular, and to the understanding of turbulent flow and heat transfer physics. The contributions are listed below.

- The LU-SGS scheme, originally developed by Yoon (1985) to solve the steady-state Euler equations, has been used in various forms, but this was the first known extension of the algorithm to a time accurate application using time derivative preconditioning in a dual time stepping approach. This combination proved to be very successful for providing a low operation count, low memory solver for LES. The present work also provided a detailed evaluation of the effectiveness of multigrid acceleration and time derivative preconditioning for this formulation, and provided a direct comparison between the explicit Runge-Kutta and implicit LU-SGS schemes. This was also one of the first multiblock applications of the LU-SGS scheme, and the convergence properties were studied with various levels of blocking.

- Second-order accurate finite volume formulations of various forms have been used with varying degrees of success for LES, but a majority of the applications have been with the incompressible form of the governing equations. Vreman et al. (1992) used a com-

pressible cell-vertex based finite volume formulation with second-order spatial accuracy to study homogeneous, isotropic decaying turbulence. Ansari and Strang (1996) used a second-order accurate unstructured grid finite volume scheme, with limited success, for turbulent mixing layers. Other compressible LES formulations have utilized various forms of upwinding, despite the fact that several researchers have determined that upwind schemes are too dissipative for LES. The present study provided a systematic evaluation of a second-order accurate, cell-centered, central differenced finite volume formulation for the compressible Favre filtered Navier-Stokes equations. The Smagorinsky and dynamic SGS models were evaluated with a coarse and fine grid for homogeneous, isotropic decaying turbulence. The formulation was then validated with plane channel flow at very low Mach numbers, so that comparisons could be made to incompressible DNS and experimental results.

- To the author's knowledge, this thesis was the first report of a turbulent simulation (LES or DNS) of a plane channel flow with constant wall heating rates leading to significant variation in the temperature-dependent fluid properties. The simulations provided additional information about the effect of large density and temperature differences on the turbulence statistics and structure due to heat transfer. There have been few LES and DNS studies of similar flows, and those that exist were set up to use homogeneous conditions in the streamwise direction. This work was also the first known application of "step-wise" periodic boundary conditions for the temperature field, so that a flow with an increasing (or decreasing) bulk fluid temperature could be simulated. Previous simulations of constant heat flux channel flows assumed constant fluid properties, and the energy equation was written in terms of a nondimensional temperature parameter that was invariant in the streamwise direction, resulting in an additional source term.

- Several turbulent simulations of turbulent rib-roughened channel or backward facing step flows have been reported in the literature, but the simulations have all utilized various incompressible formulations. This work was the first known application of a second-order accurate, cell-centered, central differenced compressible formulation to a complex

geometry such as the rib-roughened channel. The severity of odd-even decoupling was demonstrated for this type of geometry. Limitations in the grid distribution and SGS modeling used here were also identified.

9.3 Conclusions

Conclusions that can be drawn from the work presented in this thesis are listed below.

9.3.1 Development of Finite Volume Scheme

- Time-derivative preconditioning was very effective for the computation of low Mach number flows for the steady and time-accurate Runge-Kutta and LU-SGS schemes. Steady-state convergence, and the convergence in dual time stepping subiterations, was found to be nearly independent of Mach number with preconditioning.

- Time-derivative preconditioning provided a benefit for the convergence with the LU-SGS scheme even with moderate Mach numbers ($M_r > 0.3$), where preconditioning is typically not utilized. The preconditioning most likely provided a more diagonally dominant scheme, leading to convergence in fewer iterations.

- The LU-SGS scheme was superior to the Runge-Kutta scheme, yielding a lower CPU time per iteration, and requiring fewer iterations to achieve the same level of convergence. Nearly grid independent convergence was attained for some steady-state computations; conversely, the Runge-Kutta scheme demonstrated considerably slower convergence as the grid was refined.

- Multigrid acceleration provided significant speedups for steady-state convergence with the Runge-Kutta and LU-SGS schemes. The speedups for time accurate computations depended on the nature of the problem, and on the size of the time step used.

9.3.2 Evaluation of Finite Volume LES Formulation

- To achieve the same level of agreement with the data, finer grids were required for the dynamic SGS model compared to the Smagorinsky model for homogeneous, isotropic, decaying turbulence. The dynamic SGS model utilizes the resolved small-scale turbulent motion to determine the coefficients in the model. For a second-order accurate scheme on coarse grids, the small-scale motion is highly inaccurate, and the predicted coefficients are largely in error. The dynamic SGS model required significantly more computer resources compared to the Smagorinsky model. However, it may be necessary to adjust the coefficient for the Smagorinsky model from one flow to another, or for different numerics, to obtain good results.

- The second-order accurate compressible finite volume LES formulation yielded excellent results for turbulent flows with simple geometries (homogeneous, isotropic decaying turbulence and plane channel flow with smooth walls). A relatively moderate amount of grid provided excellent comparisons to experimental and DNS results.

9.3.3 Constant Heat Flux Turbulent Channel Flows

- The predicted mean temperature field was satisfactory for the constant heat flux turbulent channel flows with low heating rates. However, the temperature fluctuations in the mid-passage were grossly overpredicted. At high heating rates, this problem was not observed, and the predicted temperature fluctuations were quite acceptable. The problems were most likely due to deficiencies in the step-wise periodic treatment of the temperature. It may be possible to overcome the issue with multigrid acceleration or lower subiteration tolerance levels.

- High heating tended to reduce the velocity fluctuations, while cooling tended to promote the fluctuations. The *rms* of the velocity and temperature fluctuations and the mean velocity profiles collapsed towards the incompressible results when plotted in semi-local coordinates, as opposed to wall coordinates. The Van Driest transformation yielded mean

velocity profiles that agreed well with the incompressible log-law.

- On a local percentage basis, both the temperature and density fluctuation profiles were significantly different for high heating versus cooling. However, when normalized by a characteristic temperature difference, namely the wall-to-bulk temperature difference, the temperature fluctuations were nearly independent of the heating rate.

- There was some indication of increased coherence of the near-wall streaky structure for high cooling, while the opposite trend was observed for high heating.

- The Nusselt numbers and friction coefficients for high heating and cooling compared favorably with empirical correlations, although the reduction in the Nusselt number for high heating was less than the correlations suggested. This could be because the Reynolds numbers were on the low end of the range of validity of the correlations. It could also be due to inadequacies in the SGS modeling or other unknown effects.

9.3.4 Complex Geometry

- Problems associated with odd-even decoupling and oscillations may prohibit the application of the present LES formulation to complex geometries. Although oscillations were present in the flow, leading to occasional failures of the code due to negative temperatures or pressures, good agreement was obtained with experimental data for the mean and fluctuating streamwise velocity.

- The problem of odd-even decoupling could not be overcome by the addition of the present scalar artificial dissipation strategy. Any amount of dissipation of sufficient magnitude to have an effect on the oscillations led to an unacceptable reduction in the magnitude of the turbulent fluctuations.

- The grid stretching needed to resolve the flow near the rib led to unnecessary stretching in regions away from the rib because of the restriction to Cartesian grids. This may have adversely affected the modeled SGS turbulent viscosity, since it is a direct function of the cell volumes.

9.4 Recommendations for Future Work

The following section discusses some areas related to LES that are recommended for future work. Section 9.4.1 pertains to the work presented in this thesis. Section 9.4.2 includes the author's opinions of areas that require attention for LES, in general, based on the literature that has been reviewed and experiences with the present work.

9.4.1 Future Work Related to Present Study

Several modifications could be made to improve the finite volume formulation. Although no problems were observed for the flows considered in this thesis, it may be advantageous to include the viscous Jacobians in the implicit terms in the LU-SGS scheme for some flows. The use of implicit boundary conditions may also provide some benefit. The treatment of the LU-SGS scheme at the block interfaces could be improved, and may be necessary to achieve good performance with multigrid acceleration and multiple blocks.

The parallel efficiency and scalability of the present parallelization strategy should be improved if larger and more complex problems are to be considered. This is because more processors will be required for larger problems.

Modifications to the multigrid acceleration methodology are needed to make it effective for LES. The reason multigrid provided no speedup with LES was probably related to insufficient damping properties of the numerical scheme when no artificial dissipation is used, as discussed in Section 3.8.2 in Chapter 3. Filtering the coarse grid results or the fine grid corrections may provide the needed damping. The effectiveness of multigrid acceleration for LES is somewhat limited because large time steps cannot be used, but some improvement in convergence should be possible.

The present finite volume formulation needs to be extended to allow non-Cartesian grids so that more general geometries can be considered. As discussed in Chapter 8, non-Cartesian grids could alleviate problems related to the SGS model in regions away from the rib, where the grid was stretched unnecessarily. As noted in Chapter 3, the present formulation was developed in a general manner, but the actual coding was done by assuming Cartesian grids in

order to reduce computational costs. Extending the code to non-Cartesian grids would require minimal modifications in the flux and gradient calculations and the boundary conditions.

More complex geometries could be handled if the multiblock formulation was extended to allow noncontinuous grid lines across block boundaries. Domains could be blocked in such a way as to refine the grid only where needed. Moreover, better control of load balancing for parallel processing would be possible. Load balancing is the process of equally distributing the overall load to the processors. With the present restrictive blocking capability, processors may be assigned greatly differing block sizes. Conservative interpolation across the block interfaces, the ensemble averaging procedure for the turbulence statistics, and implementation of the dynamic SGS model are issues that would require special attention for a generalized multiblock scheme.

The PVM message passing subroutine calls in the code should be replaced with generic library message passing routines. The generic library would be linked to a number of presently available or future message passing libraries. For instance, the presently available Message Passing Interface (MPI) should be considered, because it offers improved parallel efficiency with the same portability as PVM.

It would be informative to apply the dynamic SGS model to the channel flows with high heating rates. The present constant value of the turbulent Prandtl number and Van Driest damping formulation could be compared to the turbulent Prandtl number and effective damping implied by the dynamic model.

The stability problems and SGS modeling issues need to be resolved for the rib-roughened channel flow. Many aspects of the present LES formulation need to be studied in order to successfully compute the rib-roughened channel and other similar complex geometries. One possibility is to make the code tolerant of occasional negative pressures or temperatures, by using the absolute values if they are negative, and setting a lower limit on the absolute values. It is not known if the code would converge with these modifications. It should also be determined whether odd-even decoupling can lead to inaccuracies in the vertex averaged flow field and especially the turbulence statistics.

Advanced artificial dissipation strategies could be explored to reduce the odd-even decoupling while minimizing the effect on the turbulence fluctuations. Advanced strategies include matrix dissipation (Swanson and Turkel, 1992) or the symmetric limited positive (SLIP) or upstream limited positive (USLIP) methods (Tatsumi et al., 1994), among others.

9.4.2 Future Work for LES

More research is required before LES can be applied to practical problems. A few of the many items that should be addressed are discussed in the following paragraphs.

Nonperiodic inflow and outflow boundary conditions continue to be a major limiting factor for the LES of practical internal turbulent flows, such as the flow in gas turbine blade passages. Inflow conditions must be specified as a function of time to realistically mimic the incoming turbulence energy and structure. Methods that have been tried to date are either too computationally expensive, cannot sustain a turbulent simulation, or give inaccurate results.

Models for some of the subgrid-scale terms in the compressible form of the Favre filtered energy equation need to be developed and validated. Very little research has been done in this area. The DNS of more compressible and variable property flows is needed to provide information about the relative magnitude and importance of these terms.

Present dynamic SGS models do not work well for low-order accurate finite difference (FD) and finite volume (FV) schemes, such as the one used in this thesis. The dynamic SGS model was developed and has been primarily used with spectral and pseudo-spectral codes. These codes accurately capture the high wave number, small scale turbulent motion that is used to determine the coefficients in the model. Low-order FD and FV schemes do not accurately capture the high wave number scales without a very fine grid. In order for LES to maintain its advantage over DNS, and for it to be successfully applied to complex problems, a dynamic modeling approach is needed that will work successfully on coarse grids with such schemes. The inherent numerical dissipation of FD and FV schemes acts in the same manner as the Smagorinsky model, which is why lower values of the Smagorinsky constant are typically required with FD and FV schemes compared to spectral codes. Thus, a dynamic model that

in some way utilized the numerical dissipation properties of the scheme. and considered them as an integral part of the SGS model. could potentially be more successful for FV and FD schemes.

APPENDIX A DERIVATION OF EQUATION FOR THE RESOLVED TOTAL ENERGY

Vreman et al. (1995) outlined a method for deriving a conservation law form of the energy equation in terms of the resolved total energy, $\bar{\rho}\hat{E}$, where

$$\hat{E} = \tilde{e} + \frac{1}{2}\tilde{u}_i\tilde{u}_i. \tag{A.1}$$

The equation for $\bar{\rho}\hat{E}$ can be derived from the Favre filtered continuity, momentum, and thermal energy equations (Eqs. 2.28, 2.29 and 2.30, respectively).

The terms on the left hand side of Eq. 2.29 are expanded as

$$\bar{\rho}\frac{\partial\tilde{u}_i}{\partial t} + \tilde{u}_i\left[\frac{\partial\bar{\rho}}{\partial t} + \frac{\partial(\bar{\rho}\tilde{u}_j)}{\partial x_j}\right] + \bar{\rho}\tilde{u}_j\frac{\partial\tilde{u}_i}{\partial x_j} = \cdots \tag{A.2}$$

The terms in the square brackets of Eq. A.2 are the Favre filtered continuity equation, and thus vanish. Equation A.2 is multiplied by $\tilde{u}_i$ and added to the filtered thermal energy equation, Eq. 2.30, giving

$$\begin{aligned}\frac{\partial(\bar{\rho}c_v\tilde{T})}{\partial t} + \frac{\partial(\bar{\rho}c_v\widetilde{Tu_j})}{\partial x_j} + \bar{\rho}\tilde{u}_i\frac{\partial\tilde{u}_i}{\partial t} + \bar{\rho}\tilde{u}_i\tilde{u}_j\frac{\partial\tilde{u}_i}{\partial x_j} = \\ -\overline{p\frac{\partial u_i}{\partial x_i}} - \tilde{u}_i\frac{\partial\bar{p}}{\partial x_i} + \overline{\sigma_{ij}\frac{\partial u_j}{\partial x_i}} + \tilde{u}_i\frac{\partial\hat{\sigma}_{ij}}{\partial x_j} - \tilde{u}_i\frac{\partial(\bar{\rho}\tau_{ij})}{\partial x_j} - \frac{\partial\hat{q}_j}{\partial x_j}.\end{aligned} \tag{A.3}$$

The third term on the left hand side of Eq. A.3 is rewritten as

$$\bar{\rho}\tilde{u}_i\frac{\partial\tilde{u}_i}{\partial t} = \frac{1}{2}\bar{\rho}\frac{\partial\tilde{u}_i\tilde{u}_i}{\partial t} \tag{A.4}$$

and the fourth term on the left hand side is rewritten as

$$\bar{\rho}\tilde{u}_i\tilde{u}_j\frac{\partial\tilde{u}_i}{\partial x_j} = \frac{1}{2}\bar{\rho}\tilde{u}_j\frac{\partial\tilde{u}_i\tilde{u}_i}{\partial x_j}. \tag{A.5}$$

Equations A.4 and A.5 are substituted into Eq. A.3. the filtered continuity equation is multiplied by $\frac{1}{2}\tilde{u}_i\tilde{u}_i$. and the result is added to Eq. A.3. giving

$$\frac{\partial(\bar{\rho}c_v\tilde{T})}{\partial t} + \frac{1}{2}\bar{\rho}\frac{\partial\tilde{u}_i\tilde{u}_i}{\partial t} + \frac{1}{2}\tilde{u}_i\tilde{u}_i\frac{\partial\bar{\rho}}{\partial t} + \frac{\partial(\bar{\rho}c_v\widetilde{Tu_j})}{\partial x_j} + \frac{1}{2}\bar{\rho}\tilde{u}_j\frac{\partial\tilde{u}_i\tilde{u}_i}{\partial x_j} + \frac{1}{2}\tilde{u}_i\tilde{u}_i\frac{\partial(\bar{\rho}\tilde{u}_i)}{\partial x_i} = \cdots \tag{A.6}$$

Finally. the second and third terms are combined, and the fifth and sixth terms are combined. giving

$$\frac{\partial(\bar{\rho}\hat{E})}{\partial t} + \frac{\partial(\bar{\rho}\hat{E}\tilde{u}_j)}{\partial x_j} = -\overline{p\frac{\partial u_i}{\partial x_i}} - \tilde{u}_i\frac{\partial\bar{p}}{\partial x_i} + \overline{\sigma_{ij}\frac{\partial u_j}{\partial x_i}} + \tilde{u}_i\frac{\partial\hat{\sigma}_{ij}}{\partial x_j} - \tilde{u}_i\frac{\partial(\bar{\rho}\tau_{ij})}{\partial x_j} - \frac{\partial\hat{q}_j}{\partial x_j}. \tag{A.7}$$

The subgrid-scale contributions are defined as

$$\alpha = \tilde{u}_i\frac{\partial(\bar{\rho}\tau_{ij})}{\partial x_j} \tag{A.8}$$

$$\pi = \overline{p\frac{\partial u_i}{\partial x_i}} - \bar{p}\frac{\partial\tilde{u}_i}{\partial x_i} \tag{A.9}$$

$$\epsilon = \overline{\sigma_{ij}\frac{\partial u_j}{\partial x_i}} - \hat{\sigma}_{ij}\frac{\partial\tilde{u}_i}{\partial x_j} \tag{A.10}$$

$$Q_j = c_v\bar{\rho}(\widetilde{Tu_j} - \tilde{T}\tilde{u}_j) = (\overline{pu_j} - \bar{p}\tilde{u}_j)/(\gamma - 1). \tag{A.11}$$

The final form of the equation for the resolved total energy equation is given by

$$\frac{\partial(\bar{\rho}\hat{E})}{\partial t} + \frac{\partial[(\bar{\rho}\hat{E} + \bar{p})\tilde{u}_j]}{\partial x_j} = \frac{\partial(\tilde{u}_i\hat{\sigma}_{ij})}{\partial x_j} - \frac{\partial\hat{q}_j}{\partial x_j} - \frac{\partial Q_j}{\partial x_j} - \alpha - \pi + \epsilon. \tag{A.12}$$

APPENDIX B DERIVATION OF FAVRE FILTERED TOTAL ENERGY EQUATION

Ragab and Sheen (1993) directly filtered the total energy equation, Eq. 2.3, yielding

$$\frac{\partial(\overline{\rho E})}{\partial t} + \frac{\partial(\overline{\rho E u_j})}{\partial x_j} = -\frac{\partial(\overline{pu_j})}{\partial x_j} - \frac{\partial \bar{q}_j}{\partial x_j} + \frac{\partial(\overline{\sigma_{ij} u_i})}{\partial x_j}. \tag{B.1}$$

The subgrid-scale stress, τ_{ij}, can be written as

$$\tau_{ij} = \bar{\rho}(\widetilde{u_i u_j} - \tilde{u}_i \tilde{u}_j) = L_{ij} + C_{ij} + R_{ij} \tag{B.2}$$

where L_{ij} is the Leonard stress, C_{ij} is the cross stress, and R_{ij} is the SGS Reynolds stress, defined as

$$L_{ij} = \bar{\rho}(\widetilde{\tilde{u}_i \tilde{u}_j} - \tilde{u}_i \tilde{u}_j) \tag{B.3}$$

$$C_{ij} = \bar{\rho}(\widetilde{\tilde{u}_i u_j''} + \widetilde{u_i'' \tilde{u}_j}) \tag{B.4}$$

$$R_{ij} = \bar{\rho}\widetilde{u_i'' u_j''}, \tag{B.5}$$

where u_i'' is the unresolved component of u_i. Consequently, the filtered total energy can be written as

$$\begin{aligned} \widetilde{\rho E} &= \overline{\rho(e + \frac{1}{2} u_i u_i)} \\ &= \bar{\rho}\tilde{e} + \frac{1}{2}\bar{\rho}\widetilde{u_i u_i} \\ &= \bar{\rho}\tilde{e} + \frac{1}{2}\bar{\rho}\tilde{u}_i\tilde{u}_i + \frac{1}{2}\bar{\rho}(\widetilde{u_i u_j} - \tilde{u}_i\tilde{u}_j) \\ &= \bar{\rho}\hat{E} + \frac{1}{2}q^2 \end{aligned} \tag{B.6}$$

where $\hat{E}$ is the resolved specific total energy, given by

$$\hat{E} = \tilde{e} + \frac{1}{2}\tilde{u}_i\tilde{u}_i \tag{B.7}$$

and q^2 is the unresolved, or SGS kinetic energy, given by

$$q^2 = \tau_{ii} = L_{ii} + C_{ii} + R_{ii} = \bar{\rho}(\widetilde{u_i u_i} - \tilde{u}_i \tilde{u}_i). \tag{B.8}$$

Again following the work of Ragab and Sheen (1993), the term $\overline{\rho E u_j}$ in Eq. B.1 is expanded as

$$\overline{\rho E u_j} = \overline{\rho c_v T u_j} + \frac{1}{2}\overline{\rho u_i u_i u_j}, \tag{B.9}$$

and the first term on the right hand side of Eq. B.9 is combined with the first term on the right hand side of Eq. B.1 to give

$$\overline{\rho c_v T u_j} + \overline{p u_j} = \overline{(\rho c_v T + p) u_j} = c_p \overline{\rho T u_j} = c_p \bar{\rho} \widetilde{T u_j}. \tag{B.10}$$

Equation B.10 becomes

$$c_p \bar{\rho} \widetilde{T u_j} = c_p \bar{\rho} \tilde{T} \tilde{u}_j + \gamma Q_j \tag{B.11}$$

where

$$Q_j = c_v \bar{\rho}(\widetilde{T u_j} - \tilde{T} \tilde{u}_j). \tag{B.12}$$

The second term on the right hand side of Eq. B.9 is also expanded as

$$\frac{1}{2}\overline{\rho u_i u_i u_j} = \frac{1}{2}\bar{\rho}(\widetilde{u_i u_i u_j}) = \frac{1}{2}\bar{\rho} \tilde{u}_i \tilde{u}_i \tilde{u}_j + K_j \tag{B.13}$$

where

$$K_j = \frac{1}{2}\bar{\rho}\left[(\widetilde{u_i u_i u_j}) - \tilde{u}_i \tilde{u}_i \tilde{u}_j\right]. \tag{B.14}$$

Combining the above gives the final form of the Favre filtered total energy equation as

$$\frac{\partial(\bar{\rho}\hat{E} + q^2/2)}{\partial t} + \frac{\partial[(\bar{\rho}\hat{E} + \bar{p})\tilde{u}_j]}{\partial x_j} = -\frac{\partial K_j}{\partial x_j} - \frac{\partial(\gamma Q_j)}{\partial x_j} - \frac{\partial \bar{q}_j}{\partial x_j} + \frac{\partial(\overline{\sigma_{ij} u_i})}{\partial x_j}. \tag{B.15}$$

APPENDIX C JACOBIAN MATRICES FOR FAVRE FILTERED SYSTEM OF EQUATIONS

The Jacobian matrices for the Favre filtered system of governing equations are given below.

$$[T] = \begin{bmatrix} 1/\tilde{T} & 0 & 0 & 0 & -\bar{p}/\tilde{T}^2 \\ \tilde{u}/\tilde{T} & \bar{p}/\tilde{T} & 0 & 0 & -\bar{p}\tilde{u}/\tilde{T}^2 \\ \tilde{v}/\tilde{T} & 0 & \bar{p}/\tilde{T} & 0 & -\bar{p}\tilde{v}/\tilde{T}^2 \\ \tilde{w}/\tilde{T} & 0 & 0 & \bar{p}/\tilde{T} & -\bar{p}\tilde{w}/\tilde{T}^2 \\ c_v + \frac{1}{2}(\tilde{u}^2+\tilde{v}^2+\tilde{w}^2)/\tilde{T} & \bar{p}\tilde{u}/\tilde{T} & \bar{p}\tilde{v}/\tilde{T} & \bar{p}\tilde{w}/\tilde{T} & -\frac{1}{2}(\bar{p}/\tilde{T}^2)(\tilde{u}^2+\tilde{v}^2+\tilde{w}^2) \end{bmatrix} \quad \text{(C.1)}$$

$$[\Gamma] = \begin{bmatrix} R/\tilde{T} & 0 & 0 & 0 & -\bar{p}/\tilde{T}^2 \\ R\tilde{u}/\tilde{T} & \bar{p}/\tilde{T} & 0 & 0 & -\bar{p}\tilde{u}/\tilde{T}^2 \\ R\tilde{v}/\tilde{T} & 0 & \bar{p}/\tilde{T} & 0 & -\bar{p}\tilde{v}/\tilde{T}^2 \\ R\tilde{w}/\tilde{T} & 0 & 0 & \bar{p}/\tilde{T} & -\bar{p}\tilde{w}/\tilde{T}^2 \\ R\left[c_v + \frac{1}{2}(\tilde{u}^2+\tilde{v}^2+\tilde{w}^2)/\tilde{T}\right] & \bar{p}\tilde{u}/\tilde{T} & \bar{p}\tilde{v}/\tilde{T} & \bar{p}\tilde{w}/\tilde{T} & -\frac{1}{2}(\bar{p}/\tilde{T}^2)(\tilde{u}^2+\tilde{v}^2+\tilde{w}^2) \end{bmatrix} \quad \text{(C.2)}$$

$$[A] = \begin{bmatrix} \tilde{u}/\tilde{T} & \bar{p}/\tilde{T} & 0 & 0 & -\bar{p}\tilde{u}/\tilde{T}^2 \\ \tilde{u}^2/\tilde{T}+R & 2\bar{p}\tilde{u}/\tilde{T} & 0 & 0 & -\bar{p}\tilde{u}^2/\tilde{T}^2 \\ \tilde{u}\tilde{v}/\tilde{T} & \bar{p}\tilde{v}/\tilde{T} & \bar{p}\tilde{u}/\tilde{T} & 0 & -\bar{p}\tilde{u}\tilde{v}/\tilde{T}^2 \\ \tilde{u}\tilde{w}/\tilde{T} & \bar{p}\tilde{w}/\tilde{T} & 0 & \bar{p}\tilde{u}/\tilde{T} & -\bar{p}\tilde{u}\tilde{w}/\tilde{T}^2 \\ \tilde{u}\tilde{H}/\tilde{T} & (\bar{p}/\tilde{T})(\tilde{H}+\tilde{u}^2) & \bar{p}\tilde{u}\tilde{v}/\tilde{T} & \bar{p}\tilde{u}\tilde{w}/\tilde{T} & -\frac{1}{2}(\bar{p}\tilde{u}/\tilde{T}^2)(\tilde{u}^2+\tilde{v}^2+\tilde{w}^2) \end{bmatrix} \quad \text{(C.3)}$$

$$[B] = \begin{bmatrix} \tilde{v}/\tilde{T} & 0 & \bar{\rho}/\tilde{T} & 0 & -\bar{\rho}\tilde{v}/\tilde{T}^2 \\ \tilde{v}\tilde{u}/\tilde{T} & \bar{\rho}\tilde{v}/\tilde{T} & \bar{\rho}\tilde{u}/\tilde{T} & 0 & -\bar{\rho}\tilde{v}\tilde{u}/\tilde{T}^2 \\ \tilde{v}^2/\tilde{T} + R & 0 & 2\bar{\rho}\tilde{v}/\tilde{T} & 0 & -\bar{\rho}\tilde{v}^2/\tilde{T}^2 \\ \tilde{v}\tilde{w}/\tilde{T} & 0 & \bar{\rho}\tilde{w}/\tilde{T} & \bar{\rho}\tilde{v}/\tilde{T} & -\bar{\rho}\tilde{v}\tilde{w}/\tilde{T}^2 \\ \tilde{v}\hat{H}/\tilde{T} & \bar{\rho}\tilde{u}\tilde{v}/\tilde{T} & (\bar{\rho}/\tilde{T})(\hat{H} + \tilde{v}^2) & \bar{\rho}\tilde{v}\tilde{w}/\tilde{T} & -\frac{1}{2}(\bar{\rho}\tilde{v}/\tilde{T}^2)(\tilde{u}^2 + \tilde{v}^2 + \tilde{w}^2) \end{bmatrix} \tag{C.4}$$

$$[C] = \begin{bmatrix} \tilde{w}/\tilde{T} & 0 & 0 & \bar{\rho}/\tilde{T} & -\bar{\rho}\tilde{w}/\tilde{T}^2 \\ \tilde{w}\tilde{u}/\tilde{T} & \bar{\rho}\tilde{w}/\tilde{T} & 0 & \bar{\rho}\tilde{u}/\tilde{T} & -\bar{\rho}\tilde{w}\tilde{u}/\tilde{T}^2 \\ \tilde{w}\tilde{v}/\tilde{T} & 0 & \bar{\rho}\tilde{w}/\tilde{T} & \bar{\rho}\tilde{v}/\tilde{T} & -\bar{\rho}\tilde{w}\tilde{v}/\tilde{T}^2 \\ \tilde{w}^2/\tilde{T} + R & 0 & 0 & 2\bar{\rho}\tilde{w}/\tilde{T} & -\bar{\rho}\tilde{w}^2/\tilde{T}^2 \\ \tilde{w}\hat{H}/\tilde{T} & \bar{\rho}\tilde{u}\tilde{w}/\tilde{T} & \bar{\rho}\tilde{v}\tilde{w}/\tilde{T} & (\bar{\rho}/\tilde{T})(\hat{H} + \tilde{w}^2) & -\frac{1}{2}(\bar{\rho}\tilde{w}/\tilde{T}^2)(\tilde{u}^2 + \tilde{v}^2 + \tilde{w}^2) \end{bmatrix} \tag{C.5}$$

where

$$\hat{H} = c_p\tilde{T} + \frac{1}{2}(\tilde{u}^2 + \tilde{v}^2 + \tilde{w}^2) \tag{C.6}$$

APPENDIX D DERIVATION OF DISCRETE TEST FILTERS

In this appendix, the discrete form of the top hat filtering operation is derived. The filtering operation is defined by a convolution integral as

$$\widehat{f}(\mathbf{x}, t) = \int_D \widehat{G}(\vec{x}, \vec{\xi})\, f(\vec{\xi}, t)\, d\vec{\xi} \tag{D.1}$$

where $\widehat{G}$ is the test filter function and the integration is performed over the entire domain. The top hat filter function is

$$\widehat{G}(\mathbf{x} - \xi) = \begin{cases} \frac{1}{\Delta_t^3} & \text{if } x_i - \Delta_t/2 \le \xi_i \le x_i + \Delta_t/2 \\ 0 & \text{otherwise} \end{cases} \tag{D.2}$$

where Δ_t is the test filter width.

One method for applying the filtering operation in a discrete sense is to apply a one-dimensional approximation to the integral in Eq. D.1 successively in each coordinate direction. For instance, for a grid with uniform spacing Δ and test filter width $\Delta_t = 2\Delta$, the trapezoidal rule applied at the grid points $i-1$, i, and $i+1$ gives the one-dimensional filtering operation as

$$\widehat{f_i} = \frac{1}{\Delta_t} \int_{x-\Delta_t/2}^{x+\Delta_t/2} f(\xi) d\xi = \frac{1}{4} f_{i-1} + \frac{1}{2} f_i + \frac{1}{4} f_{i+1}. \tag{D.3}$$

Similarly, Simpson's rule in one dimension gives

$$\widehat{f_i} = \frac{1}{\Delta_t} \int_{x-\Delta_t/2}^{x+\Delta_t/2} f(\xi) d\xi = \frac{1}{6} f_{i-1} + \frac{2}{3} f_i + \frac{1}{6} f_{i+1}. \tag{D.4}$$

In general, for integral approximations in terms of these three grid points, the filter operation can be expressed as

$$\widehat{f_i} = a_1 f_{i-1} + a_0 f_i + a_1 f_{i+1}. \tag{D.5}$$

where for trapezoidal integration,

$$a_0 = \frac{1}{2} \; ; \; a_1 = \frac{1}{4}, \tag{D.6}$$

and for Simpson's integration,

$$a_0 = \frac{2}{3} \; ; \; a_1 = \frac{1}{6}. \tag{D.7}$$

To filter a given quantity, the 1-D filter is applied to every grid point in the domain in three steps. In the first step, the 1-D filter in the x or i direction is applied to all points in the field. In the second step, the 1-D filter in the y or j direction is applied to all points. Finally, the 1-D filter in the z or k direction is applied to all points. The equivalent operation can be performed in a single pass with the formula given by

$$\widetilde{f_{i,j,k}} = c_0 f_{i,j,k} + c_1 \left[f_{i\pm1,j,k} + f_{i,j\pm1,k} + f_{i,j,k\pm1} \right] +$$

$$c_2 \left[f_{i\pm1,j\pm1,k} + f_{i\pm1,j,k\pm1} + f_{i,j\pm1,k\pm1} \right] + c_3 \left[f_{i\pm1,j\pm1,k\pm1} \right] \tag{D.8}$$

where

$$c_0 = a_0^3 \quad : \quad c_1 = a_0^2 a_1 \quad : \quad c_2 = a_0 a_1^2 \quad : \quad c_3 = a_1^3. \tag{D.9}$$

Consequently, for the trapezoidal filter, the coefficients are

$$c_0 = \frac{8}{64} \; : \; c_1 = \frac{4}{64} \; : \; c_2 = \frac{2}{64} \; : \; c_3 = \frac{1}{64} \tag{D.10}$$

and for the Simpson filter, the coefficients are

$$c_0 = \frac{64}{216} \; : \; c_1 = \frac{16}{216} \; : \; c_2 = \frac{4}{216} \; : \; c_3 = \frac{1}{216}. \tag{D.11}$$

An alternate method for finding approximate discrete forms of the filtering operation involve using assumed functions (or basis functions) for f. For instance, the Simpson filter above can also be derived by assuming that $f(x, y, z)$ is a second order polynomial of the form

$$f(x,y,z) = \alpha_1 + \alpha_2 x + \alpha_3 y + \alpha_4 z + \alpha_5 x^2 + \alpha_6 y^2 + \alpha_7 z^2 + \alpha_8 xy + \alpha_9 xz + \alpha_{10} yz +$$

$$\alpha_{11} x^2 y + \alpha_{12} x y^2 + \alpha_{13} x^2 z + \alpha_{14} x z^2 + \alpha_{15} y^2 z + \alpha_{16} y z^2 + \alpha_{17} xyz +$$

$$\alpha_{18} x^2 y^2 + \alpha_{19} x^2 z^2 + \alpha_{20} y^2 z^2 + \alpha_{21} xyz^2 + \alpha_{22} xy^2 z + \alpha_{23} x^2 yz +$$

$$\alpha_{24}x^2y^2z + \alpha_{25}x^2yz^2 + \alpha_{26}xy^2z^2 + \alpha_{27}x^2y^2z^2 \tag{D.12}$$

where $(x, y, z) = (0, 0, 0)$ at point (i, j, k). The coefficients α_i are determined by applying Eq. D.12 to the 27 points surrounding and including point (i, j, k). This gives 27 equations for the 27 unknown coefficients, which can be put in matrix form and solved using algebraic software such as MAPLE©. Equation D.12 is then substituted into the filtering integral, Eq. D.1, and integrated exactly. For a uniform grid with spacing Δ and filter width Δ_t, the integral becomes

$$\begin{aligned}\widetilde{f_{i,j,k}} = \frac{1}{13824}\Bigg\{ &\left(13824 - 3456\left[\frac{\Delta_t}{\Delta}\right]^2 + 288\left[\frac{\Delta_t}{\Delta}\right]^4 - 8\left[\frac{\Delta_t}{\Delta}\right]^6\right) f_{i,j,k} \\ &+ \left(576\left[\frac{\Delta_t}{\Delta}\right]^2 - 96\left[\frac{\Delta_t}{\Delta}\right]^4 + 4\left[\frac{\Delta_t}{\Delta}\right]^6\right)\left[f_{i\pm1,j,k} + f_{i,j\pm1,k} + f_{i,j,k\pm1}\right] \\ &+ \left(24\left[\frac{\Delta_t}{\Delta}\right]^4 - 2\left[\frac{\Delta_t}{\Delta}\right]^6\right)\left[f_{i\pm1,j\pm1,k} + f_{i\pm1,j,k\pm1} + f_{i,j\pm1,k\pm1}\right] \\ &+ \left[\frac{\Delta_t}{\Delta}\right]^6\left[f_{i\pm1,j\pm1,k\pm1}\right]\Bigg\}. \end{aligned} \tag{D.13}$$

The advantage to this approach is that values of $\frac{\Delta_t}{\Delta}$ other than 2 are valid, although for values much larger than 2, the interpolation function will not be as accurate. Note that for $\frac{\Delta_t}{\Delta} = 2$, the filter operation given by Eq. D.13 is equivalent to the filter given by the Simpson integration technique derived previously, with coefficients given by Eq. D.11.

Other filtering operations can be derived with different interpolation functions. For instance, a seven point filter is derived by only using the first seven terms in Eq. D.12. This gives an expression for the filtered quantity as

$$\widetilde{f_{i,j,k}} = \left[1 - \frac{1}{4}\left(\frac{\Delta_t}{\Delta}\right)^2\right] f_{i,j,k} + \frac{1}{24}\left(\frac{\Delta_t}{\Delta}\right)^2\left[f_{i+1,j,k} + f_{i-1,j,k} + f_{i,j+1,k} + f_{i,j-1,k} + f_{i,j,k+1} + f_{i,j,k-1}\right]. \tag{D.14}$$

For the commonly used ratio $\frac{\Delta_t}{\Delta} = 2$, this formula simplifies to an average of the six points neighboring the point of interest as

$$\widetilde{f_{i,j,k}} = \frac{1}{6}\left[f_{i+1,j,k} + f_{i-1,j,k} + f_{i,j+1,k} + f_{i,j-1,k} + f_{i,j,k+1} + f_{i,j,k-1}\right]. \tag{D.15}$$

APPENDIX E DERIVATION OF STEPWISE PERIODIC BOUNDARY CONDITION FOR TEMPERATURE

In this appendix, the stepwise periodic boundary condition for temperature in the streamwise direction is derived for the downstream, or quasi-developed region of a constant heat flux channel flow. Given the assumptions of negligible axial conduction and viscous dissipation, integration of the energy equation around the solution domain gives the bulk temperature rise as

$$\Delta T_b = \frac{q_w}{\dot{m}/A_c} L_x. \tag{E.1}$$

The wall temperature is specified as

$$T_w(x) = T_w(0) + \frac{dT_w}{dx} x \tag{E.2}$$

and the streamwise temperature difference from the channel inlet to outlet, ΔT_x, is approximated as a linear function of y as

$$\Delta T_x(y) = c_1|y| + c_2. \tag{E.3}$$

Equation E.3 was obtained from the results of the laminar calculations of developing channel flow discussed in Chapter 7.

The constants, c_1 and c_2, were found by applying the conditions

$$\Delta T_x(\pm 1) = \Delta T_w = \frac{dT_w}{dx} L_x \tag{E.4}$$

and

$$\Delta T_b = \frac{1}{2\rho_b u_b} \int_{-1}^{1} \rho u T dy \Big|_{x=L_x} - \frac{1}{2\rho_b u_b} \int_{-1}^{1} \rho u T dy \Big|_{x=0} = \frac{q_w}{\dot{m}/A_c} L_x. \tag{E.5}$$

Equations E.3 and E.4 give

$$\Delta T_x(\pm 1) = c_1 + c_2 = \Delta T_w. \tag{E.6}$$

Equation E.5 can be expanded as

$$\Delta T_b = \frac{1}{2\rho_b u_b}\left[\int_{-1}^{1} \rho u[T(0,y)+\Delta T_x(y)]dy - \int_{-1}^{1} \rho u[T(0,y)]dy\right] \tag{E.7}$$

or

$$\Delta T_b = \frac{1}{2\rho_b u_b}\int_{-1}^{1} \rho u \Delta T_x(y)dy. \tag{E.8}$$

Substitution of Eq. E.3 into Eq. E.8 gives

$$\frac{1}{2\rho_b u_b}\int_{-1}^{1} \rho u \Delta T_x(y)dy = \tag{E.9}$$

$$\frac{1}{2\rho_b u_b}\int_{-1}^{1} \rho u[c_1|y| + c_2]dy = \tag{E.10}$$

$$\frac{1}{2\rho_b u_b}\left[c_1\int_{-1}^{1} \rho u|y|dy + c_2\int_{-1}^{1} \rho u dy\right] \tag{E.11}$$

or

$$\Delta T_b = c_1 I_{\rho uy} + c_2, \tag{E.12}$$

where

$$I_{\rho uy} = \frac{1}{2\rho_b u_b}\int_{-1}^{1} \rho u|y|dy. \tag{E.13}$$

Using Eqs. E.6 and E.12 to solve for c_1 and c_2 gives

$$c_1 = \frac{\Delta T_b - \Delta T_w}{I_{\rho uy} - 1} \tag{E.14}$$

and

$$c_2 = \frac{I_{\rho uy}\Delta T_w - \Delta T_b}{I_{\rho uy} - 1}. \tag{E.15}$$

For constant property flows, where $\Delta T_w = \Delta T_b$, the constants become $c_1 = 0$ and $c_2 = \Delta T_w = \Delta T_b = \Delta T_x$, which is the desired result.

Alternatively, a quadratic distribution can be assumed as $\Delta T_x(y) = c_1 y^2 + c_2$. The same equations for c_1 and c_2 (Eqs. E.14 and E.15) then apply with the integral term replaced by

$$I_{\rho uy} = \frac{1}{2\rho_b u_b}\int_{-1}^{1} \rho u y^2 dy. \tag{E.16}$$

BIBLIOGRAPHY

Acharya. S.. Dutta. S., Myrum, T.A.. and Baker, R.S., 1993. "Periodically Developed Flow and Heat Transfer in a Ribbed Duct," *International Journal of Heat and Mass Transfer*. Vol. 36. pp. 2069-2082.

Acharya. S.. Dutta. S., Myrum, T.A.. and Baker, R.S. , 1994. "Turbulent Flow Past a Surface-Mounted Two-Dimensional Rib," *Journal of Fluids Engineering*, Vol. 116, pp. 238-246.

Alonso. J.J. and Jameson, A., 1994. "Fully-Implicit Time-Marching Aeroelastic Solutions." AIAA Paper 94-0056.

Alonso. J.J.. Martinelli. L., and Jameson. A.. 1995. "Multigrid Unsteady Navier-Stokes Calculations With Aeroelastic Applications." AIAA Paper 95-0048.

Alonso. J.J.. Mitty. T.J., Martinelli. L. and Jameson. A.. 1994. "A Two-Dimensional Multigrid-Driven Navier-Stokes Solver for Multiprocessor Architectures," presented at the Parallel CFD '94 Conference. Kyoto. Japan.

Ansari. A. and Strang, W.Z.. 1996. "Large-Eddy Simulation of Turbulent Mixing Layers," AIAA Paper 96-0684.

Arnone. A.. Liou. M.-S., and Povinelli. L.A.. 1993, "Multigrid Time-Accurate Integration of Navier-Stokes Equations," AIAA Paper 93-3361.

Balaras. E.. Benocci, C. and Piomelli. U., 1996. "Two-Layer Approximate Boundary Conditions for Large-Eddy Simulations." *AIAA Journal*, Vol. 34. pp. 1111-1119.

Bankston. C.A. and McEligot, D.M., 1970. "Numerical Solutions for Turbulent and Laminar Thermal Entries With Gas Property Variations," *International Journal of Heat and Mass Transfer*, Vol. 13, pp. 319-344.

Bardina. J.. Ferziger, J.H. and Reynolds, W.C., 1984. "Improved Turbulence Models Based on LES of Homogeneous Incompressible Turbulent Flows." Report No. TF-19, Department of Mechanical Engineering, Stanford University.

Barnes, J.F. and Jackson, J.D., 1961, "Heat Transfer to Air, Carbon Dioxide and Helium Flowing through Smooth Circular Tubes under Conditions of Large Surface / Gas Temperature Ratio," *Journal of Mechanical Engineering Science*, Vol. 3, pp. 303-314.

Bates, C.J., Yeoman, M.L. and Wilkes, N.S., 1983, "Non-Intrusive Measurements and Numerical Comparison of the Axial Velocity Components in a Two-Dimensional Flow Channel for a Backward-Facing Step and a Rib-Roughened Surface," Harwell Report AERE-R 10787.

Benocci, C. and Pinelli, A., 1990, "The Role of the Forcing Term in the Large Eddy Simulation of Equilibrium Channel Flow," *Engineering Turbulence Modeling and Experiments*, Rodi, W. and Ganic, E.N, eds., Elsevier Science Ltd., New York, pp. 287-296.

Blazek, J., 1994, "A Multigrid LU-SSOR Scheme for the Solution of Hypersonic Flow Problems," AIAA Paper 94-0062.

Bradshaw, P. and Huang, G.P., 1995, "The Law of the Wall in Turbulent Flow," *Proceedings of the Royal Society of London A*, Vol. 451, pp. 165-188.

Brandt, A., 1977, "Multi-Level Adaptive Solutions to Boundary-Value Problems," *Mathematics of Computation*, Vol. 31, pp. 333-390.

Breuer, M. and Rodi, W., 1994, "Large-Eddy Simulation of Turbulent Flow Through a Straight Square Duct and a 180° Bend," *Direct and Large Eddy Simulation*, Kluwer Academic Publishers, Hingham, MA.

Broeze, J., Geurts, B., Kuerten, H. and Streng, M., 1996, "Multigrid Acceleration of Time-Accurate DNS of Compressible Turbulent Flow," *Seventh Copper Mountain Conference on Multigrid Methods*, Vol. CP3339, Nelson, N.D., Manteuffel, T.A., McCormick, S.F., and Douglas, C.C., eds., NASA, Hampton, VA, pp. 109-121.

Burgraff, F., 1970, "Experimental Heat Transfer and Pressure Drop With Two Dimensional Turbulence Promoters Applied to Two Opposite Walls of a Square Tube," *Augmentation of Convective Heat and Mass Transfer*, Bergles, A.E. and Webb, R.L., eds., ASME, New York, pp. 70-79.

Calhoon, Jr., W.H. and Menon, S., 1996, "Subgrid Modeling for Reacting Large Eddy Simulations," AIAA Paper 96-0516.

Cebeci, T. and Smith, A.M.O., 1974, *Analysis of Turbulent Boundary Layers*, Academic Press, New York.

Chang, B.H. and Mills, A.F., 1993, "Turbulent Flow in a Channel With Transverse Rib Heat Transfer Augmentation," *International Journal of Heat and Mass Transfer*, Vol. 36, pp. 1459-1469.

Chen, K.-H., 1990, "A Primitive Variable, Strongly Implicit Calculation Procedure for Two and Three-Dimensional Unsteady Viscous Flows: Applications to Compressible and Incompressible Flows Including Flows With Free Surfaces," Ph.D. Thesis, Iowa State University, Ames, IA.

Chen, K.-H. and Pletcher, R.H., 1991, "Primitive Variable, Strongly Implicit Calculation Procedure for Viscous Flows at All Speeds," *AIAA Journal*, Vol. 29, pp. 1241-1249.

Chen, K.-H. and Shuen, J.-S., 1994, "Three Dimensional Coupled Implicit Methods for Spray Combustion Flows at All Speeds," AIAA Paper 94-3047.

Chenoweth, D.R. and Paolucci, S., 1986, "Natural Convection in an Enclosed Vertical Air Layer With Large Horizontal Temperature Differences," *Journal of Fluid Mechanics*, Vol. 169, pp. 173-210.

Choi, Y.-H. and Merkle, C.L., 1993, "The Application of Preconditioning in Viscous Flows," *Journal of Computational Physics*," Vol. 105, pp. 207-223.

Chwalowski, P. and Taylor, A.C., 1991, "Use of a Generalized Set of Field Variables in Fluid Flow Calculations," AIAA Paper 91-0240.

Ciofalo, M., 1994, "Large-Eddy Simulation: A Critical Survey of Models and Applications," *Advances in Heat Transfer*, Vol. 25, pp. 321-419.

Ciofalo, M. and Collins, M.W., 1992, "Large-Eddy Simulation of Turbulent Flow and Heat Transfer in Plane and Rib-Roughened Channels," *International Journal for Numerical Methods in Fluids*, Vol. 15, pp. 453-489.

Coleman, G.N., Kim, J., and Moser, R.D., 1995, "A Numerical Study of Turbulent Supersonic Isothermal-Wall Channel Flow," *Journal of Fluid Mechanics*, Vol. 305, pp. 159-183.

Comte-Bellot, G. and Corrsin, S., 1971, "Simple Eulerian Time Correlation of Full- and Narrow-Band Velocity Signals in Grid-Generated, 'Isotropic' Turbulence," *Journal of Fluid Mechanics*, Vol. 48, pp. 273-337.

Currie, I.G., 1974, *Fundamental Mechanics of Fluids*, McGraw-Hill, Inc., New York.

Dailey, L.D. and Pletcher, R.H., 1996, "Evaluation of Multigrid Acceleration for Preconditioned Time-Accurate Navier-Stokes Algorithms," *Computers & Fluids*, Vol. 25, pp. 791-811.

Dailey, L.D. and Pletcher, R.H., 1998, "Large Eddy Simulation of Constant Heat Flux Turbulent Channel Flow With Property Variations," AIAA Paper 98-0791.

Dailey, L.D., Simons, T. A., and Pletcher, R. H., 1996, "Large Eddy Simulation of Isotropic Decaying Turbulence With Structured and Unstructured Grid Finite Volume Methods," FED-Vol. 242, Proceedings of the ASME Fluids Engineering Division, Atlanta, GA, pp. 245-252.

Deissler, R.G. and Presler, A.F., 1966. "Analysis of Developing Laminar Flow and Heat Transfer in a Tube for a Gas With Variable Properties," *Proceedings of the Third International Heat Transfer Conference*, Vol. 1, pp. 250-256.

Drain, L.E. and Martin, S., 1985, "Two Component Velocity Measurements of Turbulent Flow in a Ribbed-Wall Flow Channel," *Proceedings of the International Conference on Laser Velocimetry - Advances and Applications*, Manchester, U.K.

Erlebacher, G. and Hussaini, M.Y., 1993. "Direct Numerical Simulation and Large Eddy Simulation of Compressible Turbulence," *Large Eddy Simulation of Complex Engineering and Geophysical Flows*, Galperin, B. and Orszag, S.A., eds., Cambridge University Press, New York, pp. 231-253.

Erlebacher, G., Hussaini, M.Y., Kreiss, H.O., and Sarkar, S., 1990, "The Analysis and Simulation of Compressible Turbulence," *Theoretical Computational Fluid Dynamics*, Vol. 2, pp. 73-95.

Erlebacher, G., Hussaini, M.Y., Speziale, C.G. and Zang, T.A., 1992, "Toward the Large-Eddy Simulation of Compressible Turbulent Flows," *Journal of Fluid Mechanics*, Vol. 238, pp. 155-185.

Favre, A., 1983, "Turbulence: Space-Time Statistical Properties and Behavior in Supersonic Flows," *Physics of Fluids*, Vol. 26, pp. 2851-2863.

Feng, J. and Merkle, C.L., 1990, "Evaluation of Preconditioning Methods for Time-Marching Methods," AIAA Paper 90-0016.

Ferziger, J.H., 1977, "Large Eddy Numerical Simulations of Turbulent Flows," *AIAA Journal*, Vol. 15, pp. 1261-1267.

Germano, M., Piomelli, U., Moin, P. and Cabot, W.H., 1991, "A Dynamic Subgrid-Scale Eddy Viscosity Model," *Physics of Fluids A*, Vol. 3, pp. 1760-1765.

Ghia, U., Ghia, K.N. and Shin, C.T., 1982, "High-Re Solutions for Incompressible Flow Using the Navier-Stokes Equations and a Multigrid Method," *Journal of Computational Physics*, Vol. 48, pp. 387-411.

Gnielinski, V., 1976, "Neue Gleichungen für den Wärme- und den Stoffübergang in Turbulent durchströmenten Rohren und Kanalen," *International Chemical Engineering*, Vol. 16, pp. 359-368.

Grasso, F. and Marini, M., 1991, "LU Implicit TVD Scheme for the Solution of Viscous Two Dimensional High Speed Flows," AIAA Paper 91-1573.

Han, J.C., 1988, "Heat Transfer and Friction Characteristics in Rectangular Channels With Rib Turbulators," *Journal of Heat Transfer*, Vol. 110, pp. 321-328.

Han, J.C., Glickman, L.R. and Rohsenow, W.M., 1978, "An Investigation of Heat Transfer and Friction for Rib-Roughened Surfaces," *International Journal of Heat Mass Transfer*, Vol. 21, pp. 1143-1156.

Huang, P.G. and Coleman, G.N., 1994, "Van Driest Transformation and Compressible Wall-Bounded Flows," *AIAA Journal*, Vol. 32, pp. 2110-2113.

Huang, P.G., Coleman, G.N., and Bradshaw, P., 1995, "Compressible Turbulent Channel Flow – A Close Look Using DNS Data," AIAA Paper 95-0584.

Humble, L.V., Lowdermilk, W.H., and Desmon, L.G., 1951, "Measurement of Average Heat Transfer and Friction Coefficients for Subsonic Flow of Air in Smooth Tubes at High Surface and Fluid Temperatures," NACA Report 1020.

Incropera, Frank P., and DeWitt, David P., 1996, *Fundamentals of Heat and Mass Transfer*, 4th ed., John Wiley and Sons, New York.

Jameson, A., 1991, "Time Dependent Calculations Using Multigrid, With Applications to Unsteady Flows Past Airfoils and Wings," AIAA Paper 91-1596.

Jameson, A. and Alonso, J.J., 1996, "Automatic Aerodynamic Optimization on Distributed Memory Architectures," AIAA Paper 96-0409.

Jameson, A. and Turkel, E., 1981, "Implicit Schemes and LU Decompositions," *Mathematics of Computation*, Vol. 37, pp. 385-397.

Jorgenson, P.C.E. and Pletcher, R.H., 1994, "An Implicit Numerical Scheme for the Simulation of Internal Viscous Flows on Unstructured Grids," AIAA Paper 94-0306.

Kader, B.A., 1981, "Temperature and Concentration Profiles in Full Turbulent Boundary Layers," *International Journal of Heat and Mass Transfer*, Vol. 24, pp. 1541-1544.

Kakaç, S., 1987, "The Effect of Temperature-Dependent Fluid Properties on Convective Heat Transfer," *Handbook of Single-Phase Convective Heat Transfer*, Kakac, S., Shah, R.K., and Aung,W., eds., John Wiley and Sons, New York, pp. 18.1-18.56.

Kasagi, N., Kuroda, A., Hirata, M., 1989, "Numerical Investigation of Near-Wall Turbulent Heat Transfer Taking Into Account the Unsteady Heat Conduction in the Solid Wall," *Journal of Heat Transfer*, Vol. 111, pp. 385-392.

Kasagi, N., Tomita, Y., and Kuroda, A., 1992, "Direct Numerical Simulation of Passive Scalar Field in a Turbulent Channel Flow," *Journal of Heat Transfer*, Vol. 114, pp. 598-606.

Kays, W.M. and Crawford, M.E., 1993, *Convective Heat and Mass Transfer*, 3rd ed., McGraw-Hill, Inc., New York.

Kim, J. and Moin, P., 1989, "Transport of Passive Scalars in a Turbulent Channel Flow," *Turbulent Shear Flows 6*, Springer-Verlag, Berlin, pp. 85-96.

Kim, J., Moin, P., and Moser, R., 1987, "Turbulence Statistics in Fully Developed Channel Flow at Low Reynolds Number," *Journal of Fluid Mechanics*, Vol. 177, pp. 133-166.

Kobayashi, T., Kano, M. and Ishihara, T., 1984, "Prediction of Turbulent Flow in Two-Dimensional Channel With Turbulence Promoters (1st Report, Numerical Prediction by Large Eddy Simulation)," *Bulletin of JSME*, Vol. 27, pp. 1893-1898.

Kobayashi, T., Kano, M., Ishihara, T. and Saga, T., 1985, "Prediction of Turbulent Flow in Two-Dimensional Channel With Turbulence Promoters (2nd Report, Numerical Prediction by $k-\epsilon$ Model and Comparison With Experimental Results)," *Bulletin of JSME*, Vol. 28, pp. 2940-2947.

Kobayashi, T., Kano, M. and Ishihara, T., 1985, "Prediction of Turbulent Flow in Two-Dimensional Channel With Turbulence Promoters (3rd Report, Improvement of Large Eddy Simulation and Formation of Streaklines)," *Bulletin of JSME*, Vol. 28, pp. 2948-2953.

Kwak, D., Reynolds, W.C., and Ferziger, J.H., 1975, "Three-Dimensional Time Dependent Computation of Turbulent Flow," Report No. TF-5, Stanford University.

Lee, D.L. and van Leer, B., 1993, "Progress in Local Preconditioning of the Euler and Navier-Stokes Equations," AIAA Paper 93-3328-CP.

Lee, S., 1992, "Large Eddy Simulation of Shock Turbulence Interaction," *Annual Research Briefs*, Center for Turbulence Research, Stanford University, pp. 73-84.

Leonard, A., 1974, "Energy Cascade in Large-Eddy Simulations of Turbulent Fluid Flows," *Advances in Geophysics*, Vol. 18A, p. 237-248.

Lesieur, M., 1990, *Turbulence in Fluids*, Kluwer Academic Publishers, Norwell, MA.

Lilly, D.K., 1966, "On the Application of the Eddy Viscosity Concept in the Inertial Subrange of Turbulence," Report NCAR-123, National Center for Atmospheric Research, Boulder, CO.

Lilly, D.K., 1992, "A Proposed Modification of the Germano Subgrid-Scale Closure Method," *Physics of Fluids A*, Vol. 4, pp. 633-635.

Liou, T.-M. and Chen, S.-H., 1995, "Computation of Spatially Periodic Turbulent Fluid Flow and Heat Transfer in a Channel With Various Rib Shapes," ASME Paper 95-GT-23.

Liou, T.-M., Hwang, J.-J., and Chen, S.-H., 1992, "Turbulent Transport Phenomena in a Channel With Periodic Rib Turbulators," *Journal of Thermophysics and Heat Transfer*, Vol. 6, pp. 513-521.

Liou, T.-M., Hwang, J.-J., and Chen, S.-H., 1993. "Simulation and Measurement of Enhanced Turbulent Heat Transfer in a Channel With Periodic Ribs on One Principal Wall." *International Journal of Heat and Mass Transfer*, Vol. 36, pp. 507-517.

Liu, F. and Ji, S., 1995, "Unsteady Flow Calculations With a Multigrid Navier-Stokes Method," AIAA Paper 95-2205.

Lockett, J.F. and Collins, M.W., 1990. "Holographic Interferometry Applied to Rib-Roughness Heat Transfer in Turbulent Flow." *International Journal of Heat and Mass Transfer*, Vol. 33, pp. 2439-2449.

Lyons, S.L. and Hanratty, T.J., 1991, "Direct Numerical Simulation of Passive Heat Transfer in a Turbulent Channel Flow," *International Journal of Heat and Mass Transfer*, Vol. 34, pp. 1149-1161.

Manhart, M. and Wengle, H., 1994, "Large-Eddy Simulation of Turbulent Boundary Layer Flow over a Hemisphere," *Direct and Large Eddy Simulation*, Kluwer Academic Publishers, Hingham, MA.

Martinelli, L. and Jameson, A., 1988, "Validation of a Multigrid Method for Reynolds Averaged Equations," AIAA Paper 88-0414.

Maxwell, M.J. and Ghajar, A.J., 1985, "Laminar Forced-Convective Heat Transfer With Varying Properties in the Entrance Region of Flat Rectangular Ducts," *Heat Transfer Engineering*, Vol. 6, pp. 31-37.

McAdams, W.H., 1954, *Heat Transmission*, 3rd ed., McGraw-Hill, New York.

McEligot, D.M., 1985, "Convective Heat Transfer in Internal Gas Flows With Temperature-Dependent Properties." *Advances in Transport Processes*, Vol. 4, pp. 113-200.

McEligot, D.M., Magee, P.M., and Leppert, G., 1965, "Effect of Large Temperature Gradients on Convective Heat Transfer: The Downstream Region." *Journal of Heat Transfer*, Vol. 87, pp. 67-76.

McEligot, D.M., Smith, S.B., and Bankston, C.A., 1970, "Quasi-Developed Turbulent Pipe Flow With Heat Transfer," *Journal of Heat Transfer*, Vol. 92, pp. 641-650.

Melson, N.D., Sanetrik, M.D., and Atkins, H.L., 1993, "Time-Accurate Navier-Stokes Calculations With Multigrid Acceleration," *Proceedings of the Sixth Copper Mountain Conference on Multigrid Methods*, Copper Mountain, Colorado.

Menon, S. and Yeung, P.-K., 1994, "Analysis of Subgrid Models Using Direct and Large Eddy Simulations of Isotropic Turbulence," presented at the 74th AGARD Fluid Dynamics Panel Symposium on Application of Direct and Large Eddy Simulation to Transition and Turbulence, Chania, Greece, April 18-21.

Mittal, R., 1995, "Large-Eddy Simulation of Flow Past a Circular Cylinder," *Annual Research Briefs*, Center for Turbulence Research, Stanford University, pp. 107-116.

Mittal, R., 1996, "Progress on LES of Flow Past a Circular Cylinder," *Annual Research Briefs*, Center for Turbulence Research, Stanford University, pp. 233-241.

Moin, P. and Jimenez, J., 1993, "Large Eddy Simulation of Complex Turbulent Flows," AIAA Paper 93-3099.

Moin, P. and Kim, J., 1982, "Numerical Investigation of Turbulent Channel Flow," *Journal of Fluid Mechanics*, Vol. 118, pp. 341-377.

Moin, P., Squires, K., Cabot, W. and Lee, S., 1991, "A Dynamic Subgrid-Scale Model for Compressible Turbulence and Scalar Transport," *Physics of Fluids A*, Vol. 3, pp. 2746-2757.

Niederschulte, M.A., Adrian, R.J., and Hanratty, T.J., 1990, "Measurements of Turbulent Flow in a Channel at Low Reynolds Numbers," *Experiments in Fluids*, Vol. 9, pp. 222-230.

Perkins, H.C. and Worsoe-Schmidt, P., 1965, "Turbulent Heat and Momentum Transfer for Gases in Circular Tube at Wall to Bulk Temperature Ratios to Seven," *International Journal of Heat and Mass Transfer*, Vol. 8, pp. 1011-1031.

Petukhov, B.S., 1970, "Heat Transfer and Friction in Turbulent Pipe Flow With Variable Physical Properties," *Advances in Heat Transfer*, J.P. Hartnett and T.F. Irvine, eds., Academic, New York, Vol. 6, pp. 504-564.

Petukhov, B.S. and Popov, V.N., 1963, "Theoretical Calculation of Heat Exchange and Frictional Resistance in Turbulent Flow in Tubes of an Incompressible Fluid With Variable Physical Properties," *High Temperature*, Vol. 1, pp. 69-83.

Piomelli, U., 1994, "Large-Eddy Simulation of Turbulent Flows," TAM Report No. 767, Theoretical and Applied Mechanics Department, University of Illinois at Urbana-Champaign, Urbana, IL.

Pletcher, R.H. and Chen, K.-H., 1993, "On Solving the Compressible Navier-Stokes Equations for Unsteady Flows at Very Low Mach Numbers," AIAA Paper 93-3368.

Prakash, C. and Zerkle, R., 1995, "Prediction of Turbulent Flow and Heat Transfer in a Ribbed Rectangular Duct With and Without Rotation," *Journal of Turbomachinery*, Vol. 117, pp. 255-264.

Ragab, S.A. and Sheen, S.-C., 1993, "Large Eddy Simulation of Mixing Layers," *Large Eddy Simulation of Complex Engineering and Geophysical Flows*, Galperin, B. and Orszag, S.A., eds., Cambridge University Press, New York, pp. 231-253.

Rai, M.M. and Chakravarthy, S., 1993, "Conservative High-Order-Accurate Finite Difference Methods for Curvilinear Grids," AIAA Paper 93-3380.

Rai and Moin, 1989, "Direct Simulations of Turbulent Flow using Finite-Difference Schemes," AIAA Paper 89-0369.

Ridder, J.P., 1992, "Large Eddy Simulation of Compressible Channel Flow," Ph.D. Thesis, University of Illinois at Urbana-Champaign, Urbana, IL.

Rieger, H. and Jameson, A., 1988, "Solution of Steady Three Dimensional Compressible Euler and Navier Stokes Equations by an Implicit LU Scheme," AIAA Paper 88-0619.

Rizzi, A., Eliasson, P., Lindblad, I., Hirsch, C., Lacor, C., and Haeuser, J., 1993, "The Engineering of Multiblock/Multigrid Software for Navier-Stokes Flows on Structured Meshes," *Computers & Fluids*, Vol. 22, pp. 341-367.

Rosenfeld, M., 1993, "Validation of Numerical Simulation of Incompressible Pulsatile Flow in a Constricted Channel," *Computers & Fluids*, Vol. 22, pp. 139-156.

Rossow, C.-C., 1992, "Efficient Computation of Inviscid Flow Fields Around Complex Configurations Using a Multiblock Multigrid Method," *Communications in Applied Numerical Methods*, Vol. 8, pp. 735-747.

Schade, K.W. and McEligot, D.M., 1971, "Cartesian Graetz Problems With Air Property Variation," *International Journal of Heat and Mass Transfer*, Vol. 14, pp. 653-666.

Schade, K.W. and McEligot, D.M., 1971, "Turbulent Flow Between Parallel Plates With Gas Property Variation," ASME Paper 71-FE-38.

Schumann, U., 1975, "Subgrid Scale Model for Finite Difference Simulations of Turbulent Flows in Plane Channels and Annuli," *Journal of Computational Physics*, Vol. 18, pp. 376-404.

Shannon, R.L. and Depew, C.A., 1969, "Forced Laminar Flow Convection in a Horizontal Tube With Variable Viscosity and Free-Convection Effects," *Journal of Heat Transfer*, Vol. 91, pp. 251-258.

Sheng, C., Taylor, L., and Whitfield, D., 1995, "Multiblock Multigrid Solution of Three-Dimensional Incompressible Turbulent Flows about Appended Submarine Configurations," AIAA Paper 95-0203.

Shuen, J.-S., Chen, K.-H., and Choi, Y., 1992, "A Time-Accurate Algorithm for Chemical Non-Equilibrium Viscous Flows at All Speeds," AIAA Paper 92-3639.

Shuen, J.-S., Chen, K.-H., and Choi, Y., 1993, "A Coupled Implicit Method for Chemical Non-Equilibrium Flows at All Speeds," *Journal of Computational Physics*, Vol. 106, pp. 306-318.

Shumway, R.W. and McEligot, D.M., 1971, "Heated Laminar Gas Flow in Annuli With Temperature-Dependent Transport Properties," *Nuclear Science and Engineering*, Vol. 46, pp. 394-407.

Smagorinsky, J., 1963, "General Circulation Experiments With the Primitive Equations: Part I. The Basic Experiment," *Monthly Weather Review*, Vol. 91, pp. 99-164.

Speziale, C.G., Erlebacher, G., Zang, T.A., and Hussaini, M.Y., 1988, "The Subgrid-Scale Modeling of Compressible Turbulence," *Physics of Fluids*, Vol. 31, pp. 940-942.

Spyropoulos, E.T. and Blaisdell, G.A., 1995, "Evaluation of the Dynamic Subgrid-Scale Model for Large Eddy Simulations of Compressible Turbulent Flows," AIAA Paper 95-0355.

Spyropoulos, E.T. and Blaisdell, G.A., 1997, "Large-Eddy Simulation of a Spatially Evolving Compressible Boundary Layer Flow," AIAA Paper 97-0429.

Squires, K.D., 1991, "Dynamic Subgrid-Scale Modeling of Compressible Turbulence," *Annual Research Briefs*, Center for Turbulence Research, Stanford University, pp. 207-223.

Steinthorsson, E. and Ameri, A.A., 1995, "Computations of Viscous Flows in Complex Geometries Using Multiblock Grid Systems," AIAA Paper 95-0177.

Stephens, M.A., Shih, T.I-P., and Civinskas, K.C., 1995, "Computation of Flow and Heat Transfer in a Rectangular Channel With Ribs," AIAA Paper 95-0180.

Swanson, R.C. and Radespiel, R., 1991, "Cell Centered and Cell Vertex Multigrid Schemes for the Navier-Stokes Equations," *AIAA Journal*, Vol. 29, pp. 697-703.

Swanson, R.C. and Turkel, E., 1987, "Artificial Dissipation and Central Difference Schemes for the Euler and Navier-Stokes Equations," AIAA Paper 87-1107.

Swanson, R.C. and Turkel, E., 1992, "On Central-Difference and Upwind Schemes," *Journal of Computational Physics*, Vol. 101, pp. 292-306.

Swanson, R.C. and Turkel, E., 1993, "Aspects of a High Resolution Scheme for the Navier-Stokes Equations," AIAA Paper 93-3372.

Swearingen, T.B. and McEligot, D.M., 1971, "Internal Laminar Heat Transfer With Gas-Property Variation," *Journal of Heat Transfer*, Vol. 93, pp. 432-440.

Tatsumi, S., Martinelli, L., and Jameson, A., 1994, "Design, Implementation, and Validation of Flux Limited Schemes for the Solution of the Compressible Navier-Stokes Equations," AIAA Paper 94-0647.

Teitel, M. and Antonia, R.A., 1993, "Heat Transfer in Fully Developed Turbulent Channel Flow: Comparison Between Experiment and Direct Numerical Simulations," *International Journal of Heat and Mass Transfer*, Vol. 36, pp. 1701-1706.

Turkel, E., 1987, "Preconditioned Methods for Solving the Incompressible and Low Speed Compressible Equations," *Journal of Computational Physics*, Vol. 72, pp. 277-298.

Turkel, E., 1992, "Review of Preconditioning Methods for Fluid Dynamics," NASA-CR-189712 or ICASE Report No. 92-47.

Van Driest, E.R., 1951, "Turbulent Boundary Layer in Compressible Fluids," *Journal of Aeronautical Science*, Vol. 18, pp. 145-160.

Vatsa, V.N. and Wedan, B.W., 1990, "Development of a Multigrid Code for 3-D Navier-Stokes Equations and Its Applications to a Grid-Refinement Study," *Computers & Fluids*, Vol. 18, pp. 391-403.

Venkateswaran, S. and Merkle, C.L., 1995, "Dual Time Stepping and Preconditioning for Unsteady Computations," AIAA Paper 95-0078.

Vreman, B., Geurts, B. and Kuerten, H., 1995, "Subgrid-Modeling in LES of Compressible Flow," *Applied Scientific Research*, Vol. 54, pp. 191-203.

Vreman, A.W., Geurts, B.J., Kuerten, J.G.M., and Zandbergen, P.J., 1992, "A Finite Volume Approach to Large Eddy Simulation of Compressible, Homogeneous, Isotropic, Decaying Turbulence," *International Journal for Numerical Methods in Fluids*, Vol. 15, pp. 799-816.

Wang, W.-P., 1995, "Coupled Compressible and Incompressible Finite Volume Formulation for the Large Eddy Simulation of Turbulent Flow With and Without Heat Transfer," Ph.D. Thesis, Iowa State University, Ames, IA.

Wang, W.-P. and Pletcher, R.H., 1995, "Evaluation of Some Coupled Algorithms for Large Eddy Simulation of Turbulent Flow Using a Dynamic SGS Model," AIAA Paper 95-2244.

Wang, W.-P. and Pletcher, R.H., 1996, "On the Large Eddy Simulation of a Turbulent Channel Flow With Significant Heat Transfer," *Physics of Fluids*, Vol. 8, pp. 3354-3366.

Wang, Z.J. and Yang, H.Q., 1994, "Unsteady Flow Simulation Using a Zonal Multi-Grid Approach With Moving Boundaries," AIAA Paper 94-0057.

Weiss, J.M. and Smith, W.A., 1994, "Preconditioning Applied to Variable and Constant Density Time Accurate Flows on Unstructured Meshes," AIAA Paper 94-2209.

White, F.M., 1991, *Viscous Fluid Flow*, McGraw-Hill, Inc., New York.

Withington, J.P., Shuen, J.S., and Yang, V., 1991, "A Time Accurate, Implicit Method for Chemically Reacting Flows at All Mach Numbers," AIAA Paper 91-0581.

Worsoe-Schmidt, P.M. and Leppert, G., 1965, "Heat Transfer and Friction for Laminar Flow of Gas in a Circular Tube at High Heating Rate," *International Journal of Heat and Mass Transfer*, Vol. 8, pp. 1281-1301.

Wu, X. and Squires, K., 1997, "Large Eddy Simulation of an Equilibrium Three-Dimensional Turbulent Boundary Layer," *AIAA Journal*, Vol. 35, pp. 67-74.

Yadlin, Y. and Caughey, D.A., 1991. "Block Multigrid Implicit Solution of the Euler Equations of Compressible Fluid Flow," *AIAA Journal*, Vol. 29, pp. 712-719.

Yadlin, Y. and Caughey, D.A., 1992. "Parallel Computing Strategies for Block Multigrid Implicit Solution of the Euler Equations," *AIAA Journal*, Vol. 30, pp. 2032-2038.

Yang, K.-S. and Ferziger, J.H., 1993. "Large-Eddy Simulation of Turbulent Obstacle Flow Using a Dynamic Subgrid-Scale Model," *AIAA Journal*, Vol. 31, pp. 1406-1413.

Yoon, S., 1985, "Numerical Solution of the Euler Equations by Implicit Schemes With Multiple Grids," Ph.D. Thesis, Department of Mechanical and Aerospace Engineering, Princeton University.

Yoon, S. and Jameson, A., 1987, "An LU-SSOR Scheme for the Euler and Navier-Stokes Equations," AIAA Paper 87-600.

Yoon, S., Jameson, A., and Kwak, D., 1995, "Effect of Artificial Diffusion Schemes on Multigrid Acceleration," AIAA Paper 95-1670-CP.

Yoshizawa, A., 1986, "Statistical Theory for Compressible Turbulent Shear Flows, With the Application to Subgrid Modeling," *Physics of Fluids A*, Vol. 29, pp. 2152-2164.

Zang, Y., Street, R.L. and Koseff, J.R., 1993, "A Dynamic Mixed Subgrid-Scale Model and Its Application to Turbulent Recirculating Flows," *Physics of Fluids A*, Vol. 5, pp. 3186-3196.

ACKNOWLEDGMENTS

The support of a National Defense Science and Engineering Graduate (NDSEG) Fellowship sponsored by the U.S. Department of Defense, is gratefully acknowledged. I would like to thank the Department of the Army, Army Research Office, and especially W. Davis Hein, Army NDSEG Program Manager, for administering the fellowship.

I would like to thank General Electric Aircraft Engines for allowing me to attend Iowa State University while on an educational leave of absence, and for providing support after the fellowship tenure expired.

My sincere gratitude is offered to my major professor, Dr. Richard H. Pletcher. His guidance and assistance in technical and career matters have been invaluable. I would also like to thank Drs. Richard Hindman, Ted Okiishi, Gene Takle, and John Tannehill for serving on my Program of Study Committee.

The majority of this research was conducted using the computational resources at the Cornell Theory Center (CTC) and the Maui High Performance Computing Center (MHPCC). The CTC receives major funding from the National Science Foundation (NSF) and New York State, with additional support from the National Center for Research Resources at the National Institutes of Health (NIH), IBM Corporation, and other members of the center's Corporate Partnership Program. The MHPCC is supported by the Air Force Research Laboratory, Air Force Materiel Command, USAF. In addition, resources were utilized at the Numerical Aerospace Simulation (NAS) Facility at NASA Ames Research Center, the Lewis Advanced Cluster Environment (LACE) at NASA Lewis Research Center, and the US Army Corps of Engineers Waterways Experiment Station (CEWES). The use of all resources is greatly appreciated.

The many hours spent in the basement of Black Engineering (both in person and across

the Internet wires) were made tolerable by colleagues Todd Simons, Ravikanth Avancha, Chidambaram Narayanan, and Rob Cupples. Our discussions about LES, CFD, and the world were always lively and informative. Special thanks go to Todd Simons for assistance with making animations, and for being a great companion on our journey to Cajun country.

Finally, I would like to offer my profound gratitude to my family: my wife, Laura, my son, Calvin, and my crazy dog, Sierra. Your love, support, and patience are greatly appreciated.

VITA

NAME OF AUTHOR: Lyle D. Dailey

DATE AND PLACE OF BIRTH: February 12, 1967, Anderson, Indiana

DEGREES AWARDED:

B.S. in Aeronautical and Astronautical Engineering, Purdue University, 1990
M.S. in Aerospace Engineering, University of Cincinnati, 1993

HONORS AND AWARDS:

Sigma Xi, The Scientific Research Society, 1996
National Defense Science and Engineering Graduate Fellowship, 1993-1996
Herbert F. Rogers Scholarship, Purdue University, 1990
Henry Ford II Scholarship, Purdue University, 1989
Sigma Gamma Tau Aerospace Honor Society, 1988

PROFESSIONAL EXPERIENCE:

Engineer, General Electric Aircraft Engines
Analytical Aero and Cooling Technology, 1996-present
Computational Turbomachinery Aerodynamics, 1992-1993
Engineering Development Program, 1990-1992
Teaching Assistant, Iowa State University, 1996
Engineer, Allison Gas Turbine Division of General Motors
Co-operative Education Program, 1987-1989

PROFESSIONAL PUBLICATIONS:

Dailey, L.D. and Pletcher, R.H., 1998, "Large Eddy Simulation of Constant Heat Flux Turbulent Channel Flow with Property Variations," AIAA Paper 98-0791.

Dailey, L.D. and Pletcher, R.H., 1997, "Evaluation of a Second-Order Accurate Compressible Finite Volume Formulation for the Large Eddy Simulation of Turbulent Flow," presented at the First AFOSR International Conference on DNS and LES, August 4-8, 1997, Ruston, LA.

Dailey, L.D., Simons, T.A., and Pletcher, R.H., 1996, "Large Eddy Simulation of Isotropic Decaying Turbulence with Structured and Unstructured Grid Finite Volume Methods," FED-Vol. 242, Proceedings of the ASME Fluids Engineering Division, Atlanta, GA, pp. 245-252.

Dailey, L.D. and Pletcher, R.H., 1996, "Evaluation of Multigrid Acceleration for Preconditioned Time-Accurate Navier-Stokes Algorithms," *Computers & Fluids*, Vol. 25, pp. 791-811.

Dailey, L.D., Jennions, I.K., and Orkwis, P.D., 1995, "Simulation of Laminar-Turbulent Transition with an Explicit Navier-Stokes Flow Solver," *Journal of Propulsion and Power*, Vol. 11, pp. 1187-1194.